
**Joint Ground/Space Observations of Transient
Phenomena Associated with the Polar Cusp.**

Thesis submitted for the degree of
Doctor of Philosophy
at the University of Leicester

Iain Jonathan Rae

Radio and Space Plasma Physics Group
Department of Physics and Astronomy
University of Leicester

December 2000

UMI Number: U141485

All rights reserved

INFORMATION TO ALL USERS

The quality of this reproduction is dependent upon the quality of the copy submitted.

In the unlikely event that the author did not send a complete manuscript and there are missing pages, these will be noted. Also, if material had to be removed, a note will indicate the deletion.



UMI U141485

Published by ProQuest LLC 2013. Copyright in the Dissertation held by the Author.
Microform Edition © ProQuest LLC.

All rights reserved. This work is protected against
unauthorized copying under Title 17, United States Code.



ProQuest LLC
789 East Eisenhower Parkway
P.O. Box 1346
Ann Arbor, MI 48106-1346

Joint Ground/Space Observations of Transient Phenomena Associated with the Polar Cusp.

Iain Jonathan Rae

Abstract

This thesis concerns the study of solar wind entry into the near-Earth environment via the process of time-varying reconnection. Specifically, the plasma signatures associated with this magnetic flux transfer were investigated in the context of the upstream interplanetary conditions. This study is primarily accomplished with the Polar spacecraft, situated in the mid-altitude cusp, but also utilises low-altitude spacecraft and ground-based instrumentation to trace solar wind entry into the near-Earth space environment.

A detailed case study is presented of the energy-dispersed pulsed particle signatures (PPS) observed in the mid-altitude cusp by Polar. Two discrete time-scales of PPS were observed and linked to the prevailing IMF conditions. The simultaneous observation of two different frequency components has not previously been reported in the mid-altitude cusp.

A second, complementary case study was conducted utilising the definitions outlined in the previous study to relate PPS to the low-altitude and ionospheric signatures of transient reconnection. Although there is no direct 1:1 relationship between the mid-, low-altitude and ionospheric signatures of reconnection in this case study, the ionospheric footprints of all three signatures are closely located in time and space.

Finally, the location and occurrence statistics of PPS observed in the magnetosphere and traced into the ionosphere are investigated with respect to IMF orientation and the solar wind dynamic pressure. PPS were found to occur over a wide range of latitudes and local times, and also found to favour southward IMF in terms of increased numbers and percentage occurrence, than its positive B_z counterpart. Increased solar wind dynamic pressure also permits increased numbers of PPS to be observed at a wider range of latitudes and local times, through magnetospheric compression allowing Polar to sample differing volumes of the cusp. The statistical results provide further evidence that PPS are the plasma signatures of transient reconnection.

To my parents

Acknowledgements

I would like to thank the following people for their roles in the compilation of this thesis:

PPARC for funding my Ph. D. and Professor Stan Cowley for allowing me the opportunity to study in the Radio and Space Plasma Physics Group.

Next comes Dr. Mark Lester for the caffeine-conferences on football, cricket, life and science in that order! Also a special thanks to the man who taught me grammar, and the use of the semicolon, a vastly underrated punctuation mark.

Thanks also to Dr. Tim Yeoman for his unique perspective on science and a second year viva grilling. Then there's Dr. Alan Rodger for making me think, which, although painful, is in the end quite gratifying.

Also Drs. Jackie Davies and Steve Milan for their ridiculous knowledge of programming, in their own inimitable styles, without which this thesis would surely be lighter. Also thanks to Jackie and Steve for teaching me the proper use of the semicolon.

The Polar instrument teams for their data provision and constructive criticism. In particular, Ted Fritz (CMMICE PI) and the respective PIs of the Hydra, CEPPAD and MFE instruments. Also thanks to Barry Kellett and Chris Perry at R.A.L and Jeremy Faden at the University of Iowa for their programming expertise and data provision.

To "the Group", past and present, for copious amounts of coffee, beer, friendship, and all-round amusement value on a whole range of levels. And to my friends "up north" for all of the above and more.

Thanks also to Bill Gates, for if I never use Microsoft Office again, it will be too soon.

To my parents, this is for you. And me sis, did you think I'd forget?

And to Lisa. Thank you most of all.

Contents

Chapter 1 Solar-Terrestrial Relations

1.1	Introduction	1
1.2	Solar Physics	1
1.2.1	The Sun	1
1.2.2	Solar wind structure and the IMF	2
1.3	The near-Earth environment	4
1.3.1	The Earth's Magnetosphere	4
1.3.2	The Earth's Ionosphere	5
1.4	Thesis aims	7
1.5	Summary	7

Chapter 2 Review of the polar cusps and dayside reconnection

2.1	Background	9
2.2	“Viscous” Interaction	10
2.3	Magnetic Reconnection	10
2.3.1	The role of IMF B_z	11
2.3.2	The role of IMF B_y	13
2.3.3	Control of ionospheric convection pattern by IMF	14
2.4	Signatures of transient reconnection	15
2.4.1	Magnetopause signatures of transient reconnection	15
2.4.2	Mid-altitude signatures of transient reconnection	17
2.4.3	Low-altitude signatures of transient reconnection	18
2.4.4	Ionospheric and ground-based signatures of transient reconnection	19
2.5	Theories of transient reconnection	21
2.5.1	Fossil flux tube model	21
2.5.2	Two-Dimensional (2-D) reconnection pulse model	22
2.5.3	Multiple X line model	23
2.5.4	Magnetosheath pressure pulse model	24
2.6	Discussion and Summary	24

Chapter 3 Instrumentation

3.1	Introduction	26
-----	--------------	----

3.2	The Polar spacecraft	26
3.2.1	The Charge and Mass Magnetospheric Ion Composition Experiment (CAMMICE)	27
3.2.2	The Hot Plasma Analyser (Hydra)	28
3.2.3	The Comprehensive Energetic Particle and Pith Angle Distribution Experiment (CEPPAD)	29
3.2.4	The Magnetic Fields Experiment (MFE)	31
3.3	The Wind spacecraft	32
3.3.1	The Magnetic Fields Instrument (MFI)	32
3.3.2	The Solar Wind Experiment (SWE)	33
3.4	The ACE spacecraft	34
3.4.1	The ACE magnetometer (MAG)	34
3.4.2	The ACE Solar Wind Ion Composition Sensor (SWICS)	34
3.5	The DMSP satellite network	35
3.6	The Co-Operative Twin Located Auroral Sounding System (CUTLASS)	36
3.6.1	The CUTLASS HF radar system	36
3.6.2	HF propagation	36
3.7	Discussion and Summary	37

Chapter 4 Polar observations of the time-varying cusp

4.1	Introduction	38
4.2	Observations –29 th October 1996	38
4.2.1	The Interplanetary Magnetic Field (IMF)	38
4.2.2	Polar spacecraft data	39
4.3	Further Cusp Crossings	42
4.3.1	12 th October 1996	42
4.3.2	20 th October 1996	43
4.4	Discussion	45
4.5	Summary	50

Chapter 5 Pulsed cusp particles and their ionospheric flow signatures

5.1	Introduction	52
5.2	Instrumentation Set-up	52
5.3	Observations – 24 th April 1999	53
5.3.1	Wind spacecraft data	53

5.3.2	Polar spacecraft observations	54
5.3.3	DMSP observations	55
5.3.4	CUTLASS Finland observations	55
5.4	CUTLASS/Polar comparison	58
5.5	Discussion	58
5.6	Summary	62
Chapter 6	Pulsed Particle Signature Statistics	
6.1	Introduction	64
6.2	Statistical Criteria	64
6.3	Magnetospheric PPS location characteristics	66
6.3.1	All IMF orientations	67
6.3.2	Effect of B_z on PPS location	68
6.3.3	Effect of B_y on PPS location	70
6.3.4	Effect of both B_y and B_z together on PPS location	71
6.3.5	Effect of solar wind dynamic pressure on PPS location	73
6.4	Ionospheric location of PPS	75
6.4.1	The Tsyganenko 89c model (T89c)	75
6.4.2	All IMF	77
6.4.3	Effect of B_z on PPS location	78
6.4.4	Effect of B_y on PPS location	79
6.4.5	Effect of solar wind dynamic pressure on PPS location	80
6.5	Discussion	81
6.6	Summary	88
Chapter 7	Summary and Conclusions	
7.1	Introduction	90
7.2	Summary of Results	91
7.2.1	29 th October 1996	91
7.2.2	24 th April 1999	92
7.2.3	Statistical Study	93
7.3	Suggestions for Future Work	94
References		97

CHAPTER 1

Solar-Terrestrial Relations

1.1 Introduction

This thesis investigates the solar wind entry into the Earth's magnetosphere and ionosphere. This topic falls within the general area of Solar-Terrestrial Physics and it is the aim of this chapter to briefly summarise the solar surroundings, and its interaction with the near-Earth space environment. In particular, the entry of solar wind into the magnetosphere-ionosphere system is discussed. An outline of the research that this thesis documents is then presented. The specifics of solar wind-magnetosphere-ionosphere coupling will be discussed in more detail in Chapter 2.

1.2 Solar Physics

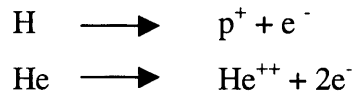
1.2.1 The Sun

To an astronomer, the sun is merely an average star of spectral type G2V and absolute magnitude 4.8. However, the sun is still 330,000 times greater than the Earth in terms of mass ($\sim 10^{30}$ kg), with a radius 109 times larger than that of the Earth (*Priest, 1995*). Under its own gravitational attraction, solar material is compressed to such a high central density and temperature that nuclear reactions take place. These nuclear reactions are the source of the energy which is continuously radiated into space and which drives solar activity. The main constituents of the sun comprise Hydrogen ($\sim 90\%$) and Helium ($\sim 10\%$), with $\sim 1\%$ heavy elements completing the composition.

A relatively small core contains most of the mass and is almost entirely responsible for the sun's luminosity. The central sphere of the sun is one quarter the solar radius, where one half of the solar mass is found, and $\sim 99\%$ of the sun's emitted energy is generated. At the very

centre, the sun's temperature is 15 million degrees Kelvin and its pressure ~250 billion atmospheres (*Gibson, 1972*). A diagram of the sun's interior is shown in Figure 1.1.

The sun's atmosphere is composed of three different layers; the photosphere, chromosphere and corona. The photosphere has a density of 10^{23} m^{-3} and is a thin skin 500 km in thickness, from which the greatest component of the sun's light is emitted. Above the photosphere lies the more transparent chromosphere, which has a density of the order of 10^{17} m^{-3} , and the sun's corona, which has a density of the order of 10^{14} m^{-3} . At peak coronal temperatures ($\sim 2 \times 10^6 \text{ K}$) the average particle energies are $\sim 260 \text{ eV}$, much bigger than the ionisation potential for H^+ (13.6 eV) or He^{++} (25 eV for the first electron; 54 eV for the second electron).



Collisional processes result in the formation of a fully ionised plasma.

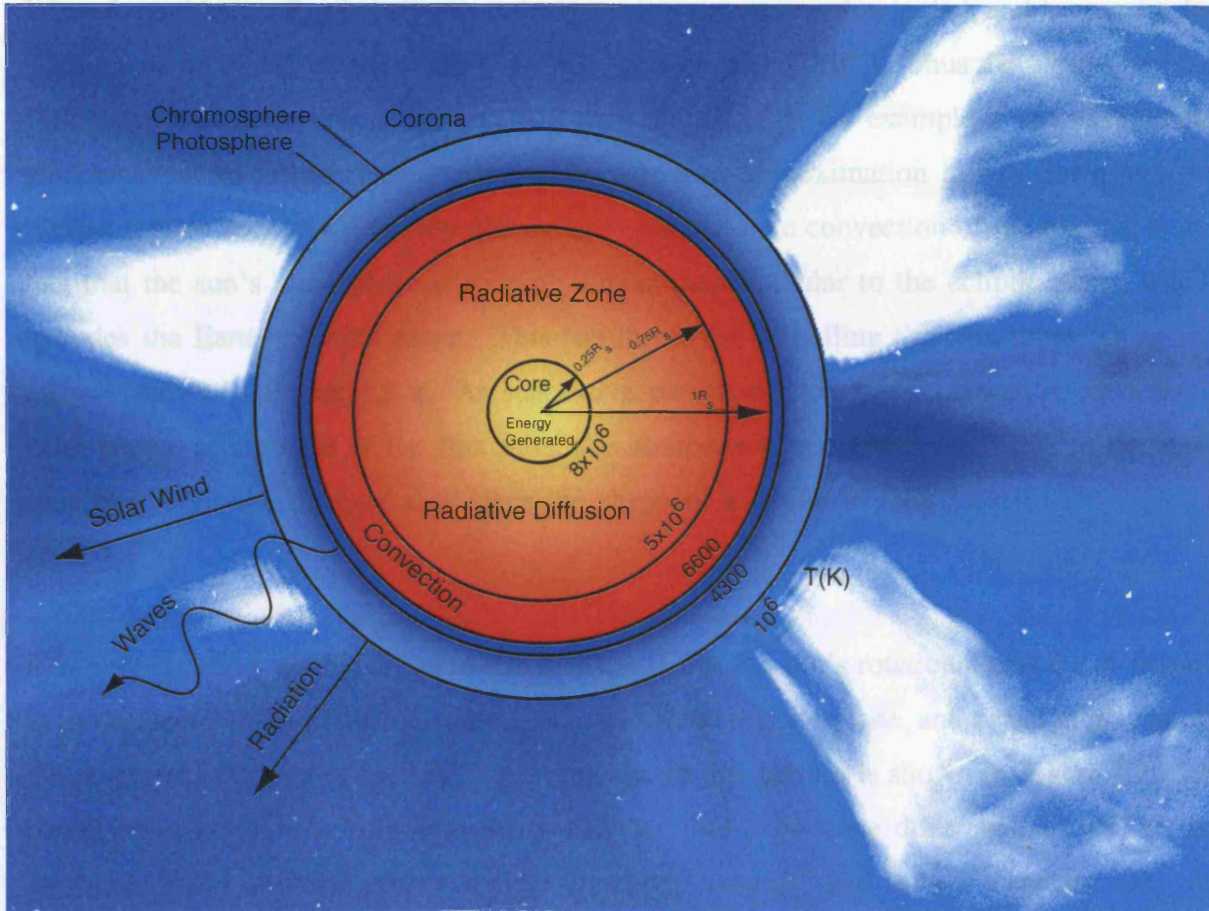
1.2.2 Solar wind structure and the IMF

Why does the solar wind blow away from the sun? Is the sun not sufficiently massive such that the ionised hydrogen should be gravitationally bound to it? The answers are deceptively simple. The flow is produced by the large pressure difference between the hot, dense material in the solar atmosphere, and the cold tenuous gas in the interstellar medium. This pressure difference dwarfs the effect of solar gravitational pull on the plasma, and the high electrical conductivity of the plasma forces part of the sun's magnetic field to be pulled outwards as if it were "frozen in" the plasma. This field, called the Interplanetary Magnetic Field (IMF), acts like a cosmic glue forcing the plasma to behave collectively as a hydrodynamic fluid.

The Magnetic Reynolds number, R_m , gives an indication of how well the plasma and IMF are coupled together. It is defined as the ratio of convective and diffusive terms in a time-varying magnetic field from the diffusion equation, and is given by

$$R_m = \mu_0 \sigma v L$$

where μ_0 is the permeability of free space, σ the conductivity of the medium, v the characteristic velocity of the medium, and L is the scale length for magnetic variations, or the characteristic scale length of the plasma.



At solar minimum, the sun behaves as an inclined dipolar body, and the Earth experiences a two-sector pattern. However, as solar maximum approaches, four-sector patterns have been observed (Fronz et al., 1990), implying that there is a significant quadrupolar element to the sun. The orientation of the current sheet is the main influence of the X (radial) and Y (Dawn-Dusk) components of the IMF. The Z-component (North-South) of the IMF is more susceptible to the noisy perturbations that the sun creates which are effectively superposed on the Parker speed. These perturbations include Coronal Mass Ejections (CMEs), shocks,

FIGURE 1.1: The solar interior and atmosphere (adapted from Priest, 1985) superimposed on an image of a Coronal Mass Ejection event courtesy of SOHO/LASCO consortium. SOHO is a project of international cooperation between ESA and NASA.

The plasma and "frozen-in" IMF are accelerated at distances up to 10 solar radii from the sun from Parker's solution for the expanding solar wind, after which the velocity remains between ~ 300 - 600 km s⁻¹ and density 10^8 - 10^7 m⁻³ though through coronal holes, velocities can approach 1000 km s⁻¹ and densities of 5×10^7 m⁻³ at 1 AU (e.g. Gosine et al., 1976, 1978).

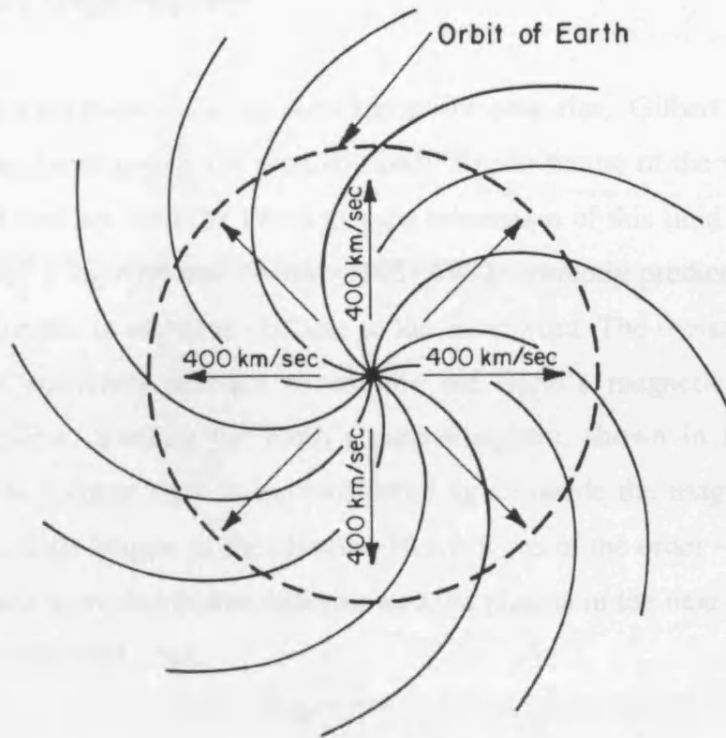
where μ_0 is the permittivity of free space, σ the conductivity of the medium, v the characteristic velocity of the medium, and L is the scale length for magnetic variations, or the characteristic scale length of the plasma.

When L (and hence R_m) is large, then the system is convection dominated, and for most solar phenomena on global length scales ($\sim 10^6$ m), R_m is huge (10^6 - 10^{12}). Thus the plasma and the IMF move together. When L is so small such that $R_m \leq 1$, for example in the exceptional circumstances of intense current sheets, the frozen-in approximation breaks down and the plasma regime becomes diffusion dominated. Added to the convection of the plasma, is the fact that the sun's atmosphere is rotating almost perpendicular to the ecliptic plane, which includes the Earth's orbital plane. This has the effect of pulling the flux tubes out in the fashion shown in Figure 1.2 a. As successive parcels of flux move outward from a fixed solar source at the base of the flux tube, this source will move beneath it due to the solar rotation. Thus the trace of flux takes the shape of a spiral, as first identified by *Parker* [1958].

However, a further complication to this scenario is that the sun's rotational axis is not aligned to its dipole axis. This tilts the current sheet out of the ecliptic plane, and hence greatly alters the magnetic structure of the IMF. A schematic of this picture is shown in Figure 1.2b. A planet on or around the solar equator would therefore experience different "sectors" of the magnetic field - alternate magnetic field direction "towards" and "away" from the sun. At solar minimum, the sun resembles an inclined dipolar body, and the Earth experiences a two-sector pattern. However, as solar maximum approaches, four-sector patterns have been observed (*Yeoman et al.*, 1990), implying that there is a significant quadrupolar element to the sun. The orientation of the current sheet is the main influence of the X (radial) and Y (Dawn-Dusk) components of the IMF. The Z-component (North-South) of the IMF is more susceptible to the many perturbations that the sun creates which are effectively superposed on the Parker spiral. These perturbations include Coronal Mass Ejections (CMEs), shocks, tangential discontinuities, solar flares and Magnetohydrodynamic (MHD) waves.

The plasma and "frozen in" IMF are accelerated at distances up to 10 solar radii from the sun from Parker's solution for the expanding solar wind, after which the velocity remains between ~ 300 - 600 kms^{-1} and density 10^6 - 10^7 m^{-3} though through coronal holes, velocities can approach 1000 kms^{-1} and densities of 5×10^7 m^{-3} at 1 AU (e.g. *Gosling et al.*, 1976; 1978).

(a)



(b)

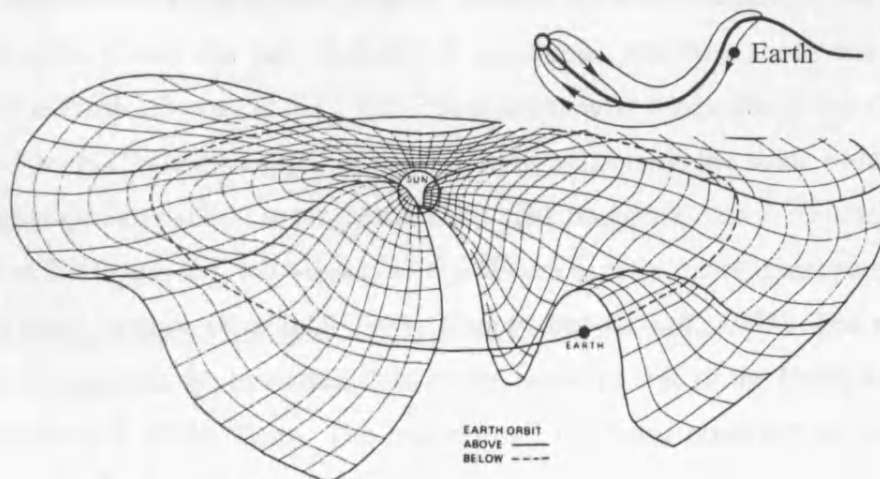


FIGURE 1.2: The Parker spiral. Figure 1.2a shows the overall configuration of the solar magnetic field in the ecliptic plane [adapted from *Parker, 1963*]. Figure 1.2b displays a three-dimensional sketch of the equatorial current sheet. When the sun rotates, an observer near the ecliptic plane would alternately be above and below the current sheet. The inset shows the meridional cross-section with the Earth below the current sheet (taken from *Kelley, 1989*).

1.3 The near-Earth Environment

1.3.1 The Earth's Magnetosphere

That the Earth has a magnetic field has been known for centuries. Gilbert showed as early as 1600, in his treatise *De Magnete*, the predominantly dipolar nature of the terrestrial magnetic field. However, it was not until the 1930s that the interaction of this field and solar radiation was first explained. *Chapman and Ferraro* [1931;1932] correctly predicted that a planetary magnetic field provides an effective obstacle to the solar wind. The dynamic pressure of the solar wind exerts sufficient pressure to confine the Earth's magnetic field to a cavity surrounding the planet, forming the Earth's magnetosphere, shown in Figure 1.3. If the Magnetic Reynolds number were to be considered again inside the magnetospheric cavity, with characteristic scale lengths of the plasma $\sim 10 R_E$, R_m is of the order $\sim 10^{17}$. This implies that convection once more dominates diffusion and the plasma in the near-Earth environment is tied to the terrestrial field lines.

Because the solar wind is super-Alfvénic ($\geq 300 \text{ kms}^{-1}$), which vastly exceeds the Alfvén velocity ($\sim 50 \text{ kms}^{-1}$), then a shock wave (bow shock) forms. This has the effect of deflecting the solar wind around the magnetospheric cavity, in much the same manner as that in front of a supersonic aircraft. Under the vast majority of conditions, the bow shock lies 13-15 R_E upstream from the Earth (*Peredo et al.*, 1995). Behind the bow shock, the plasma is slowed, compressed and heated forming a layer of turbulent plasma outside the solar wind/terrestrial boundary (magnetopause) called the magnetosheath. The magnetopause is routinely situated 9-11 R_E from the Earth (*Roelof and Sibeck*, 1993). Where exactly the magnetopause lies is a question of pressure balance (*Fairfield*, 1971, *Walker and Russell*, 1995). The solar wind pressure, which compresses the terrestrial field on the sunward side of the Earth, also creates a long tail antisunward of the Earth. The *magnetotail* has been observed up to 1000 R_E downstream from the Earth (*Villante*, 1975).

A defining feature of the Chapman-Ferraro picture is the presence of two magnetic null points in the terrestrial field. These null points are called the *polar cusps*, labelled c in Figure 1.3, and it is the aim of this thesis to attempt in some way to further our understanding of these cusps (see review by *Smith and Lockwood*, 1996). To this end, Chapter 2 will go into extensive detail as to the role of these null points, with respect to the magnetospheric and ionospheric dynamics, and their coupling processes.

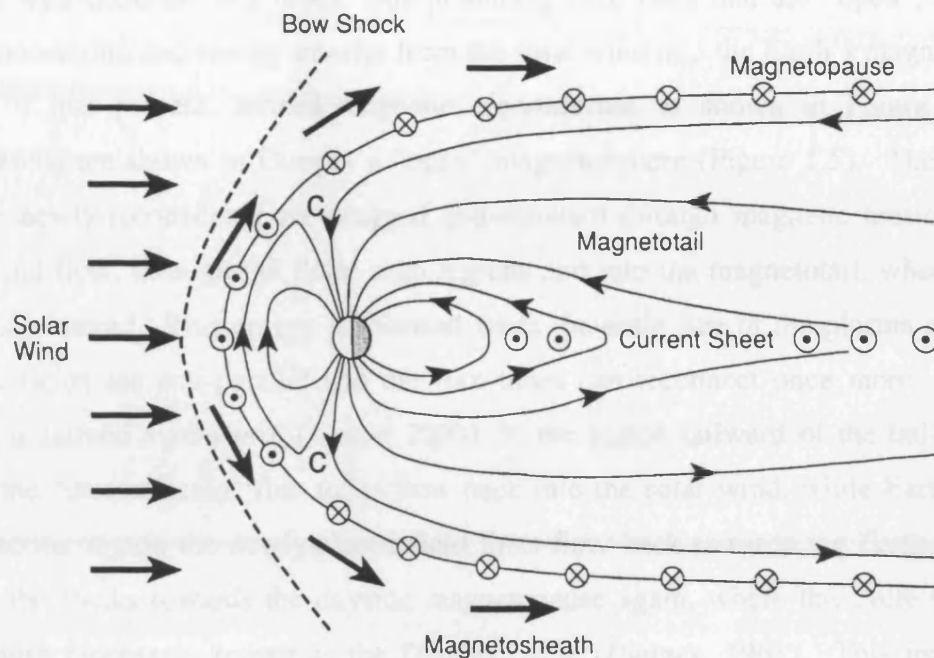


FIGURE 1.3: Cross-section of the simplest model of the magnetosphere. In this "closed" model, the geomagnetic field is perfectly confined by the sheet currents flowing on the magnetopause. The solar wind flow is deflected at the bow shock and flows around the flanks of the magnetosphere, forming the magnetosheath (adapted from *Hughes, 1995*). The regions marked c are the polar cusps, null points in the terrestrial field.

There are very few regions in the magnetosphere where the frozen-in approximation breaks down. However, when it does it is in crucial regions. At the boundary between the IMF and the geomagnetic field, an intense current sheet is formed, and hence the scale size of the plasma is sufficiently small that the frozen-in approximation breaks down, and the plasma regime is diffusion-dominated. This allows the field lines from both regimes to break and re-connect with different flux tubes, thus producing field lines that are “open”, and allowing mass, momentum and energy transfer from the solar wind into the Earth’s magnetosphere. A sketch of this process, termed magnetic reconnection, is shown in Figure 1.4 and the implications are shown in Dungey’s “open” magnetosphere (Figure 1.5). These field lines that are newly-reconnected are dragged anti-sunward through magnetic tension forces and solar wind flow, through the Polar cusp regions and into the magnetotail, where the energy and flux is stored. This energy is released when the scale size of the plasma again is small and the fields are anti-parallel and the flux tubes can reconnect once more. This energy release is termed a substorm (*Lester, 2000*). In the region tailward of the tail-reconnection region the “disconnected” flux tubes flow back into the solar wind, while Earthward of the reconnection region the newly-closed field lines flow back towards the Earth, and convect around the flanks towards the dayside magnetopause again, where the cycle repeats itself. This entire process is known as the Dungey cycle (*Dungey, 1961*). This magnetospheric convection cycle is communicated to the ionosphere and drives a twin-cell convection pattern at high-latitudes in the ionosphere (*Cowley, 1982*).

Of course, this depiction is for one particular IMF orientation, and the highly variable nature of the IMF has already been discussed in Section 1.2.2. The picture for oppositely directed (northward) IMF and the influence of IMF B_x and B_y will be discussed in Chapter 2.

1.3.2 The Earth’s Ionosphere

The existence of the Earth’s ionosphere was not confirmed until the 1920’s, when *Breit and Tuvé* [1925] recorded echoes from radio waves transmitted near vertically. Solar radiation is incident on the Earth’s upper atmosphere in the ultraviolet (UV) and extreme ultraviolet (EUV) ranges. These frequencies provide the photons to ionise the neutral atmosphere. This is known as *photoionisation*. An additional ionisation mechanism is energetic particle precipitation, known as *impact ionisation*. Ionising particles can come from a number of sources, such as cosmic rays, the magnetosphere, or from the ionosphere if local ion or electron acceleration mechanisms are involved. The rate at which electrons are produced is

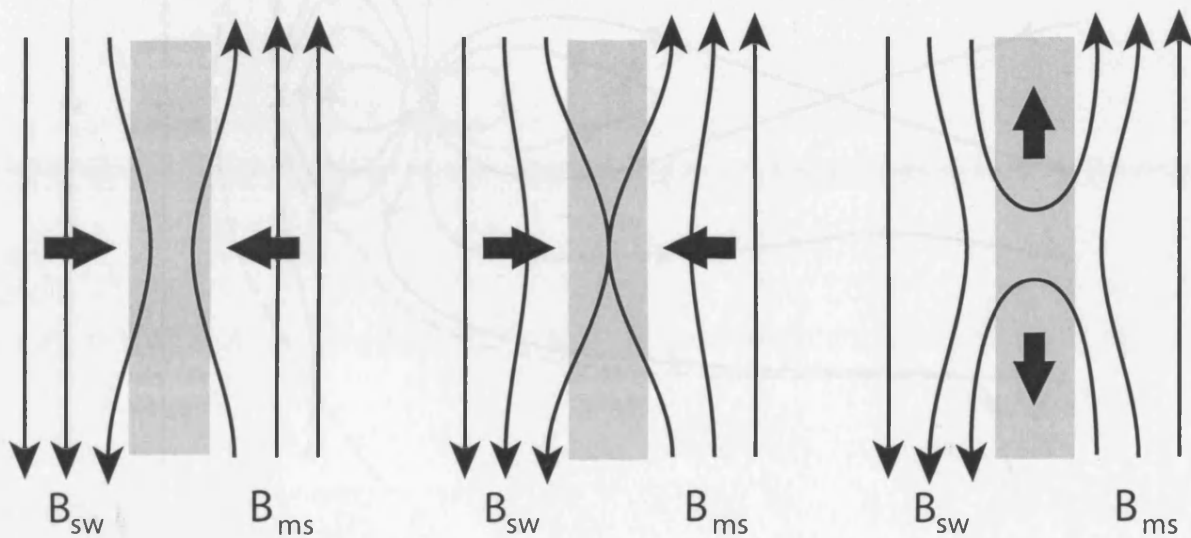


FIGURE 1.4: A sketch showing the effect of the process of magnetic reconnection at the magnetopause. Field lines diffuse through the current layer from both sides and "re-connect", producing "open" field lines that thread the magnetosheath-magnetosphere boundary. The magnetic tension forces on the field lines result in field and plasma flows away from the reconnection site and along the current sheet.

...of the density of the gas and the intensity of the magnetic field. The Earth's ...
 ...is described in more detail by such authors as Schindler (1987) and ...

...of the ...
 ...of the ...

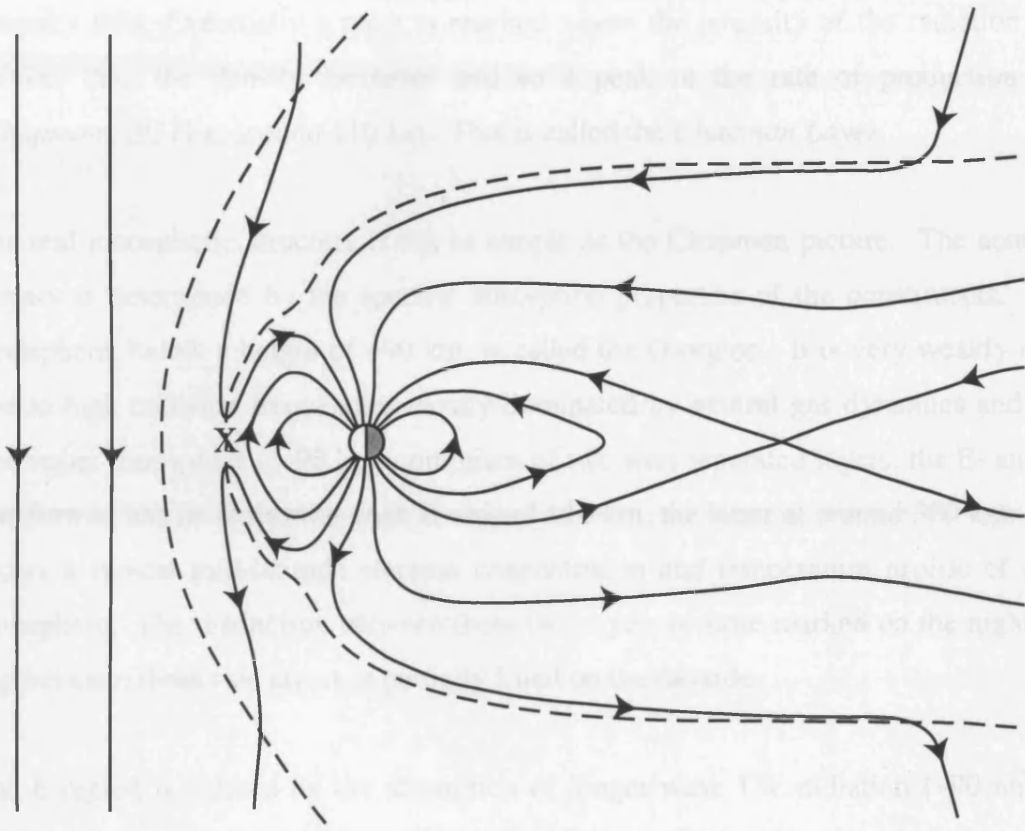


FIGURE 1.5: Dungey's "open" magnetosphere. Field lines reconnect at the low-latitude magnetopause (X), and are dragged anti-sunward into the magnetotail. Energy and flux is stored in the tail until these field lines become anti-parallel once more, reconnect again, and become closed again. In the region tailward of the tail-reconnection region the "disconnected" flux tubes flow back into the solar wind, while Earthward of the reconnection region the newly-closed field lines flow back towards the Earth, and convect around the flanks towards the dayside magnetopause again, where the cycle repeats itself.

proportional to the density of the gas and the intensity of the ionising radiation. The Earth's ionosphere is reviewed in some detail by such authors as *Schunk (1983)* and *Rishbeth (1988)*.

Of course, gas concentration reduces with increasing height and so at high altitudes the rate of production is small. As the radiation passes into denser atmosphere the production rate increases. Because more radiation is being absorbed in the denser atmosphere the radiation intensity falls. Eventually a point is reached where the intensity of the radiation falls away quicker than the density increases and so a peak in the rate of production is formed (*Chapman, 1931*) at around 110 km. This is called the *Chapman Layer*.

The real ionospheric structure is not as simple as the Chapman picture. The actual electron density is determined by the specific absorption properties of the constituents. The lower ionosphere, below a height of ~90 km, is called the D-region. It is very weakly ionised and due to high collision frequencies mostly dominated by neutral gas dynamics and chemistry. The upper ionosphere (> 90 km) comprises of two well separated layers: the E- and F-region. The former has its ionisation peak at around 110 km, the latter at around 300 km. Figure 1.6 shows a typical mid-latitude electron concentration and temperature profile of the Earth's ionosphere. The distinction between these two layers is more marked on the nightside as the gap between these two layers is partially filled on the dayside.

The E-region is formed by the absorption of longer wave UV radiation (~90 nm) which is attenuated as it passes through the atmosphere until the density of molecular Oxygen becomes sufficiently high, and thus the E-region is dominated by O_2^+ and NO^+ ions. At high-latitudes, ionisation due to precipitating energetic electrons and protons contributes significantly to the formation of the E-region.

The F-region splits into two sub-layers on the dayside. The F1-layer has an ionisation peak at ~200 km and the F2-layer at ~300 km. The former is the product of shorter wavelength (20-80 nm) dayside UV radiation. The latter is formed due to the height variation of the neutral densities and recombination and attachment rates for different atmospheric constituents. In the lower F2-region, O^+ ionisation and recombination are dominant. At higher altitudes the decreasing neutral density and attachment limit the increase in electron density. In this manner, the F2-peak is at the height that these two processes balance, and produces electron densities of the order 10^{12} m^{-3} .

1.4 Thesis Aims

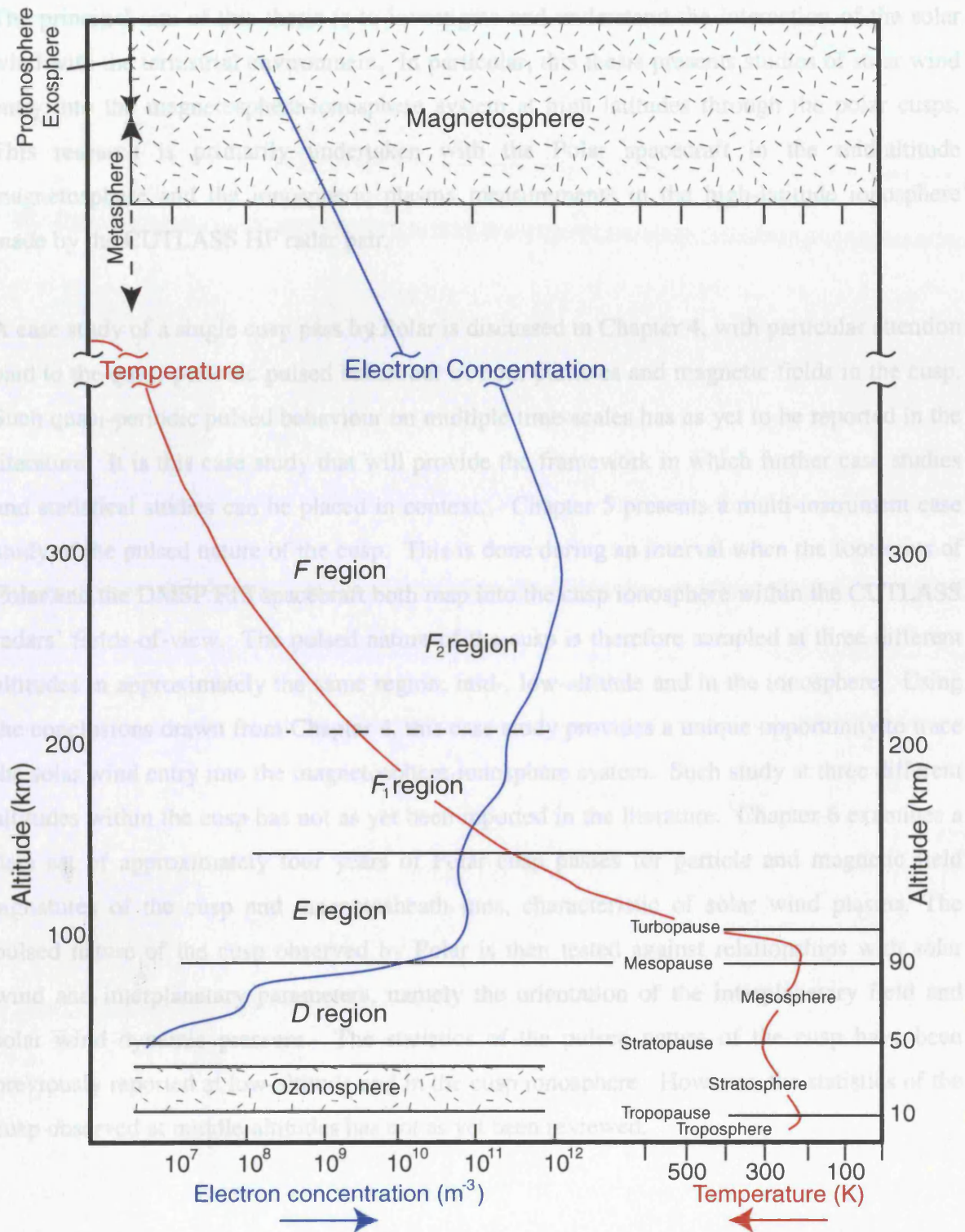


FIGURE 1.6: Typical mid-latitude electron concentration and temperature profiles of the Earth's ionosphere.

1.5 Summary

A brief overview of the interaction of the solar and terrestrial environments has been presented in this chapter. The dynamics of the interaction of the solar wind, magnetosphere and ionosphere have been reviewed, though some elements will be discussed in greater detail

1.4 Thesis Aims

The principal aim of this thesis is to investigate and understand the interaction of the solar wind with the terrestrial environment. In particular, this thesis presents studies of solar wind entry into the magnetosphere-ionosphere system at high latitudes through the polar cusps. This research is primarily undertaken with the Polar spacecraft in the mid-altitude magnetosphere and the ionospheric plasma measurements in the high-latitude ionosphere made by the CUTLASS HF radar pair.

A case study of a single cusp pass by Polar is discussed in Chapter 4, with particular attention paid to the quasi-periodic pulsed behaviour of both particles and magnetic fields in the cusp. Such quasi-periodic pulsed behaviour on multiple time-scales has as yet to be reported in the literature. It is this case study that will provide the framework in which further case studies and statistical studies can be placed in context. Chapter 5 presents a multi-instrument case study of the pulsed nature of the cusp. This is done during an interval when the footprints of Polar and the DMSP F13 spacecraft both map into the cusp ionosphere within the CUTLASS radars' fields-of-view. The pulsed nature of the cusp is therefore sampled at three different altitudes in approximately the same region; mid-, low-altitude and in the ionosphere. Using the conclusions drawn from Chapter 4, this case study provides a unique opportunity to trace the solar wind entry into the magnetosphere-ionosphere system. Such study at three different altitudes within the cusp has not as yet been reported in the literature. Chapter 6 examines a data set of approximately four years of Polar cusp passes for particle and magnetic field signatures of the cusp and magnetosheath ions, characteristic of solar wind plasma. The pulsed nature of the cusp observed by Polar is then tested against relationships with solar wind and interplanetary parameters, namely the orientation of the interplanetary field and solar wind dynamic pressure. The statistics of the pulsed nature of the cusp have been previously reported at low-altitude and in the cusp ionosphere. However, the statistics of the cusp observed at middle-altitudes has not as yet been reviewed.

1.5 Summary

A brief overview of the interaction of the solar and terrestrial environments has been presented in this chapter. The dynamics of the interaction of the solar wind, magnetosphere and ionosphere have been reviewed, though some elements will be discussed in greater detail

in Chapter 2. Finally, the contents of the thesis is discussed, and the motivations behind this research reviewed.

CHAPTER 2

Review of the polar cusps and dayside reconnection

This chapter reviews the interaction of the terrestrial field with the solar wind, and the mechanisms that allow the transfer of mass, momentum and energy into the near-Earth environment. As the primary mechanism to accomplish this transfer is by magnetic reconnection, as previously discussed in Section 1.3.1, this chapter scrutinises the process of magnetic reconnection, the role of the cusps and the various models for this magnetic and plasma flux transfer. Furthermore, the signatures of the reconnection process throughout the magnetosphere-ionosphere system are reviewed. The impact on the ionospheric convection flows generated by dayside reconnection is also discussed.

2.1 Background

It has been previously discussed in Section 1.3.1 that the terrestrial field and the IMF are not mutually exclusive (*Dungey, 1961*). Therefore the interaction between these two fields has come under intense scrutiny over the last 40 years. However, reconnection is not the only mechanism that has been suggested as an explanation for high-latitude ionospheric plasma flows. The application of the theory of magnetic reconnection was pioneered by *Dungey* in the early 1950s, which he applied to solar wind-magnetosphere coupling processes in the early 1960s (*Dungey, 1961*). The fundamental aspect of this is that the field lines can thread the magnetopause and be attached to the ionosphere and the solar wind concurrently. However *Axford and Hines* [1961] proposed an alternative mechanism, “viscous interaction”, that did not directly invoke reconnection, but could provide the necessary means to generate these high-latitude ionospheric flows without resorting to the breakdown of the frozen-in approximation. It was later shown that this method could not adequately describe the plasma flows and features observed, while reconnection could. For completeness, however, a brief overview of viscous interaction is included in Section 2.2.

2.2 “Viscous” Interaction

Only months after Dungey had proposed the theory of reconnection, *Axford and Hines* [1961] suggested that viscous interaction occurring between the solar wind and magnetosphere was responsible for the plasma flows observed in the Earth’s ionosphere. The exact nature of this interaction was not discussed, but the most likely type of interaction is a Kelvin-Helmholtz “wave over water” type instability. This instability is caused by a velocity shear in magnetised plasmas. The magnetosheath plasma is flowing along the magnetopause around the magnetosphere, and it is easy to imagine that any contact between the flow and the magnetospheric field may cause ripples on the boundary to evolve. A schematic of this process is illustrated in Figure 2.1. These magnetospheric ripples translate to an ionospheric flow pattern, shown in Figure 2.2a (*Axford and Hines*, 1961). When the rotation of the Earth is taken into account, then this picture becomes slightly more distorted, and is shown in Figure 2.2b. To summarise, unspecified instabilities at the magnetopause coerce the magnetospheric plasma to convect in the near-circular pattern shown in Figures 2.1 and with the ionospheric footprints of this convection pattern shown in Figure 2.2.

However, this scenario did not explain many of the features observed in the ionosphere, such as the variation in the convection pattern observed. Neither does this model explain the “open” nature of the field lines over the polar cap regions of the Earth, that is to say, the presence of magnetosheath plasma and the drainage of magnetospheric plasma on these “open” field lines. Dungey’s reconnection model, however, does.

2.3 Magnetic Reconnection

When *Dungey* [1961] published his theories on the breakdown of the frozen-in approximation, it was greeted with a mixed reception. However, during the last 40 years, his theories have, for the most part, been proven to be correct. In Section 1.3.1 the reconnection process was briefly touched upon, but this Section will go into the details, characteristics and possible locations of reconnection sites.

The “frozen-in approximation” was discussed in Section 1.2.2. To recap, it is a consequence of the electrical conductivity of the plasma being sufficiently large that the plasma and the field lines convect together. Magnetic reconnection is a process that can only ensue when

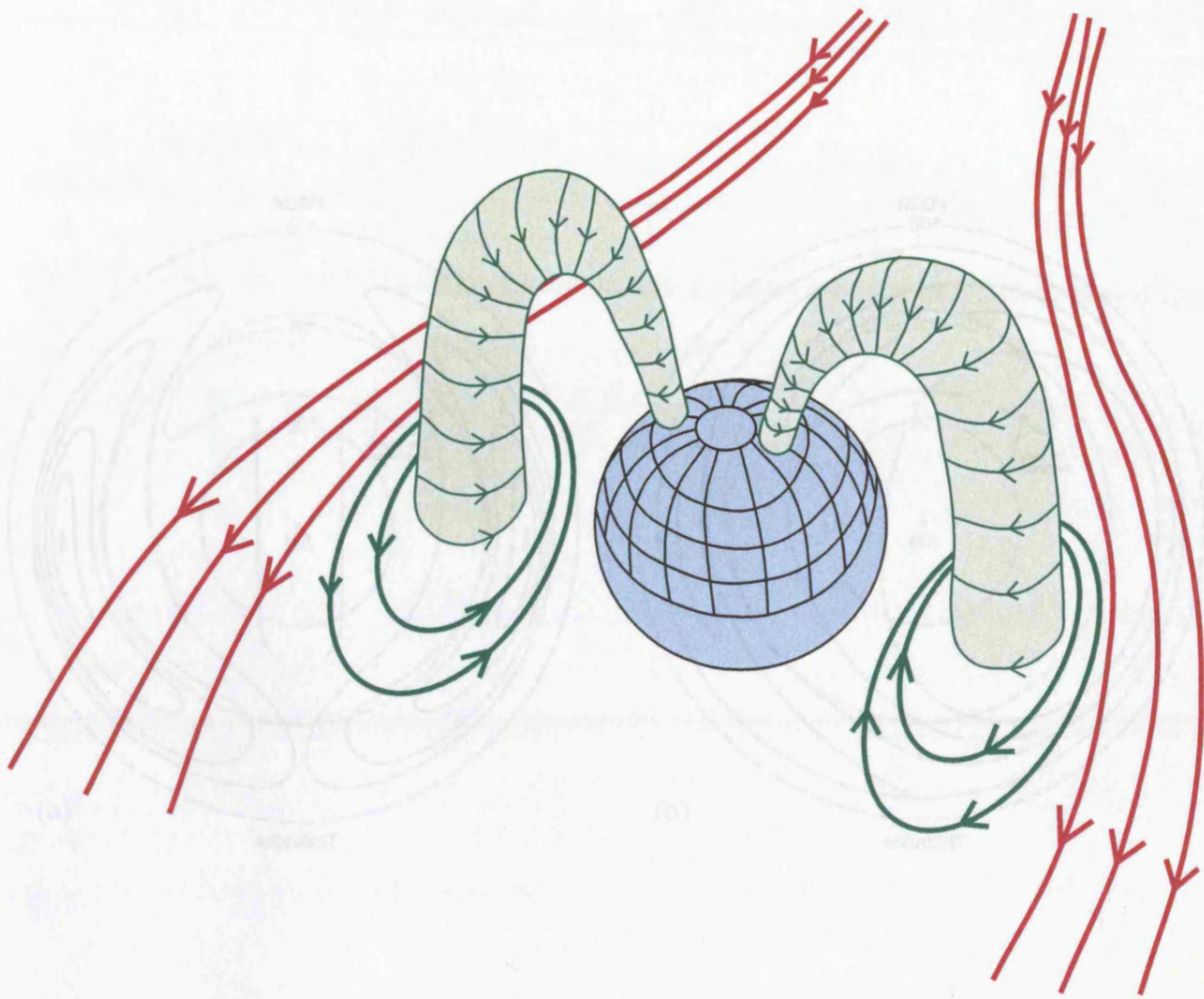


FIGURE 2.1 The ionospheric convection patterns according to *Axford and Hines* [1961] (a) in the Earth's rest frame, and (b) with the Earth's rotation incorporated.

FIGURE 2.1: A schematic of the magnetospheric configuration of the "viscous" interaction process as proposed by *Axford and Hines* [1961]. Ionospheric convection patterns are thought to be generated via Kelvin-Helmholtz type instabilities at the magnetopause.

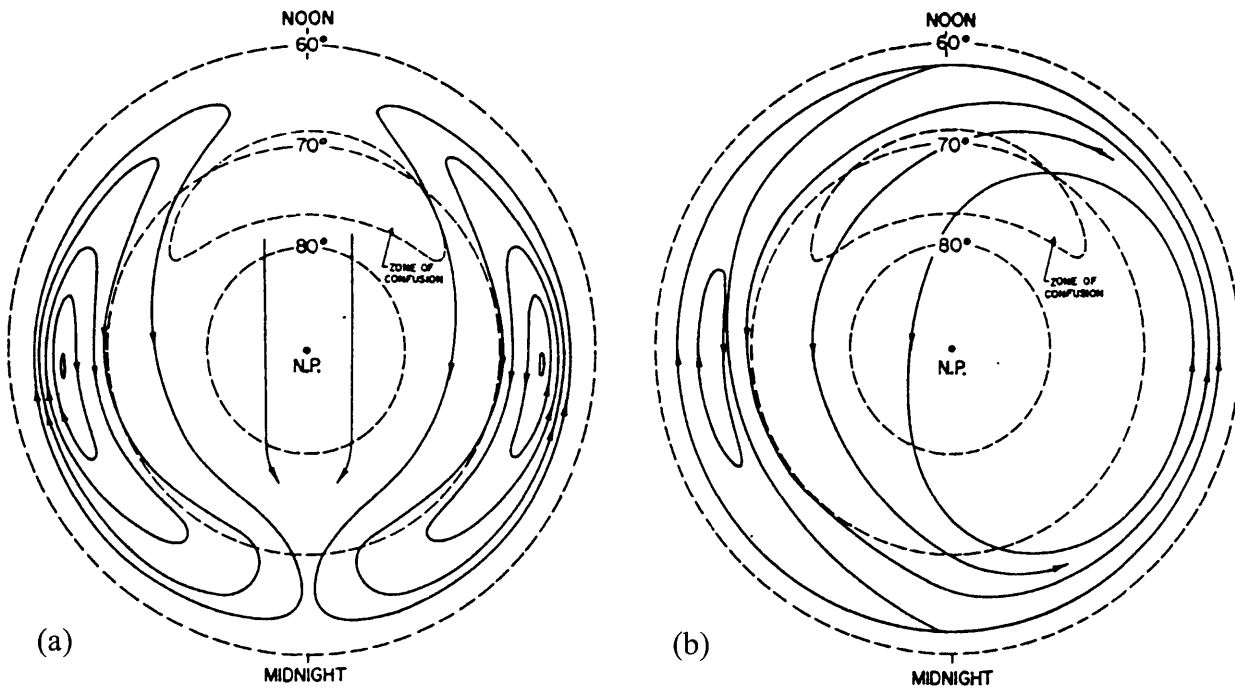


FIGURE 2.2: The ionospheric convection patterns according to *Axford and Hines* [1961] (a) in the Earth's rest frame, and (b) with the Earth's rotation incorporated.

this criterion breaks down. This is not likely in the collisionless plasma of space, where the Reynolds numbers are huge. However, a direct consequence of the frozen-in approximation is that thin boundaries can form between different plasma regimes. One such boundary is the magnetopause where the interplanetary field and the terrestrial field encounter one another. In this case a current sheet forms between the oppositely directed fields and the scale length of the plasma is small such that R_m is less than unity. As R_m is the ratio of convective and diffusive terms in a time-varying magnetic field, then $R_m < 1$ implies that diffusion dominates convection, and thus MHD can and does break down locally (see Figure 1.4) at the point on the magnetopause where these two fields are anti-parallel. This presents a fundamentally different picture, as magnetic flux tubes can now enter the diffusion region, where R_m is less than unity, and instead of being annihilated, can leave from the top and bottom of the picture. In the process the flux tubes are “cut” and “reconnected” to different partners as illustrated in Figure 2.3. Plasma on these new flux tubes, coming from different regions, now finds itself on a single flux tube in total violation of the frozen-in flux theorem. Reconnection was first proposed by *Dungey* [1958] to explain the internal processes of a solar flare, in terms of the boundary between different plasma regimes inside such an event. The magnetopause current sheet is another such location of a boundary between different plasma regimes, and as discussed earlier, this has three major implications. As has been stated in Section 1.3.3, solar wind momentum can be efficiently transferred into the magnetosphere, through the anti-sunward solar wind flow. Secondly, plasma particles can cross the magnetopause and into the magnetosphere on a routine basis. Thirdly, as the flux tubes are subject to magnetic tension forces along the magnetopause boundary, the plasma on these flux tubes is accelerated and heated.

2.3.1 The role of IMF B_z

The simplest case for reconnection in the Sun-Earth system is with a purely southward IMF, though obviously the IMF can assume any orientation. It is the southward case that is discussed first. Figure 2.3 illustrates the situation. When the southward IMF approaches the northward directed terrestrial magnetic field magnetic reconnection can occur. The numbered field lines illustrate the magnetospheric flow, or convection, driven by magnetic reconnection, with the inset portraying the ionospheric footprint of this convection which has a double-vortex type pattern. Instead of a purely geomagnetic field line with both ends attached to the Earth and an interplanetary field line with both ends on the Sun, there are now two field lines, each with a footpoint in one hemisphere of the Earth and the other end

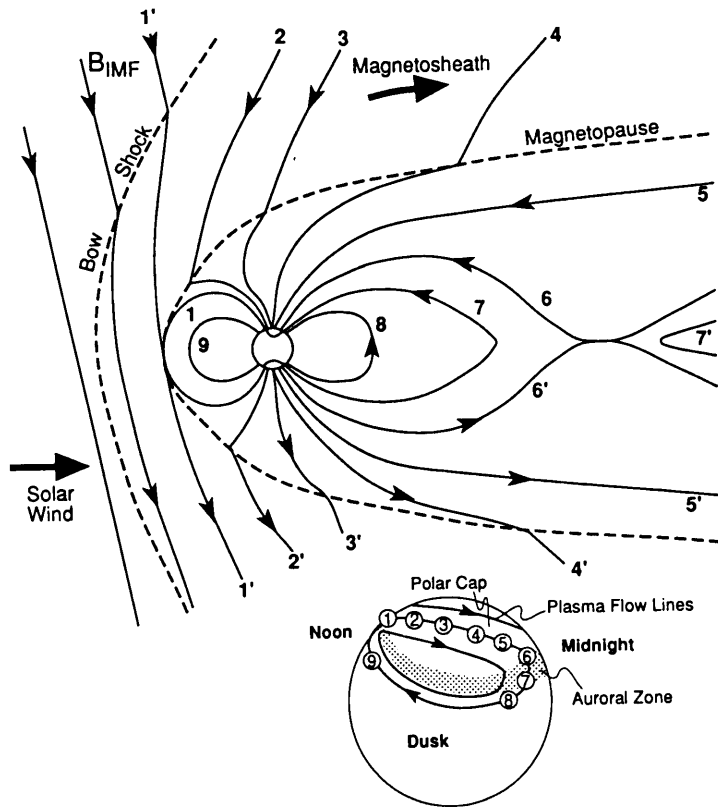
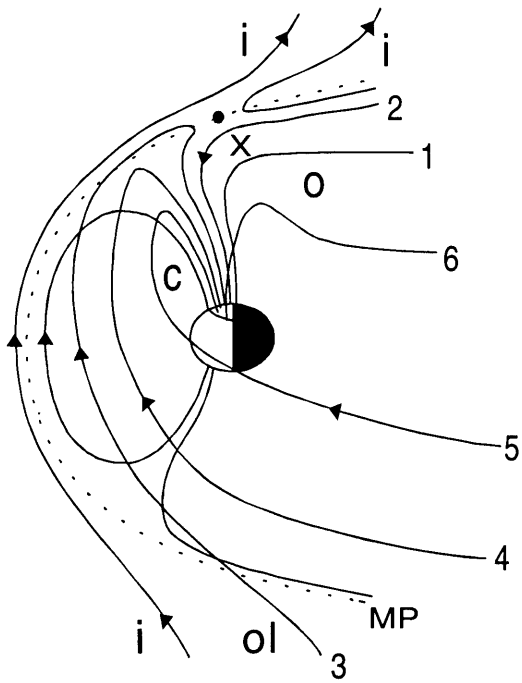


FIGURE 2.3: Flow of flux tubes within the magnetosphere (convection) driven by magnetic reconnection. The numbered field lines are indicative of the successive configurations the reconnected flux tubes assume after reconnection with field line 1' at the low-latitude magnetopause. Field lines 6 and 6' reconnect in the geomagnetic tail, thus allowing the field lines to return towards the dayside at lower latitudes. The inset depicts the ionospheric footprint of these numbered field lines and the resultant plasma flows; anti-sunward flow at high-latitudes, and return flow at lower-latitudes (taken from *Hughes*, 1995).

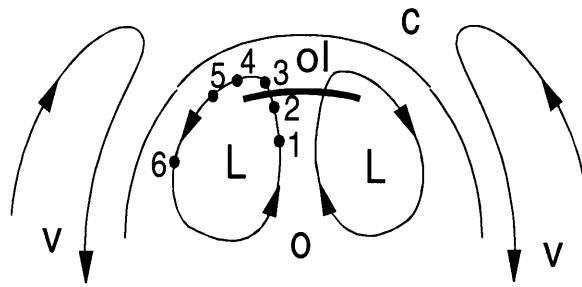
stretching into interplanetary space. The field line is dragged anti-sunwards by the solar wind flow and the convection electric field, $\mathbf{E} = -\mathbf{v}_{sw} \times \mathbf{B}_{sw}$. In steady-state the force associated with the electric field, directed from dawn-dusk, drives the flow from noon to midnight, as observed. Thus the field lines move successively through the numbered locations in Figure 2.3, and the solar wind naturally draws out the flux tubes to form the geomagnetic tail.

Of course, this process cannot go on indefinitely without a method of returning this flux to a “closed” state, as this would result in the entire terrestrial field connecting to the IMF. This is achieved by reconnection at another X-line in the geotail. This results in the destruction of the two “open” field lines and results in a newly-closed geomagnetic field line and a new interplanetary field line. The new interplanetary field line contains plasma of a magnetospheric origin and is distorted and stressed and can flow anti-sunward and rejoin the solar wind flow. The new geomagnetic field line is also stressed and endeavours to flow and relax earthward, though this flow can be retarded somewhat by the plasma pressure on the flux tube. Eventually the circuit in the flow of the field lines is completed when these field lines flow around the flanks of the Earth back towards the dayside, much like the inset picture of Figure 2.3.

There are several possible scenarios for the interaction between a purely northward IMF and the geomagnetic field. Note that there are two potential reconnection locations for a northward oriented magnetosheath field, one in either hemisphere, where the fields can become anti-parallel. As a consequence, the magnitude and direction of the B_x and B_y components of the interplanetary field are critical in the location of any reconnection sites. Figure 2.4 shows two possible portrayals of what is known as *lobe reconnection* (taken from Lockwood, 1998). Figure 2.4a is a representation of reconnection taking place in only the northern hemisphere between an interplanetary field line, draped in the magnetosheath (i) and the open flux of the tail lobe (o). Note that in this illustration the open flux was produced by a prior period of southward IMF and thus threads the boundary further down the tail and has a different orientation in the sheath and interplanetary space to i (Russell, 1972). Field lines evolve sequentially as shown in the illustration. This is known as *lobe stirring*, as the old open field lines such as 1 evolve towards the reconnection site (to 2) before being reconfigured at X so that they thread the dayside magnetopause (like the “open” over-draped field line 3) (Crooker, 1992) before returning to the tail lobe via magnetosheath flow. This is essentially a slower convection as magnetic tension and curvature forces will be retarded somewhat by the sheath flow as they are effectively acting in opposite directions. This

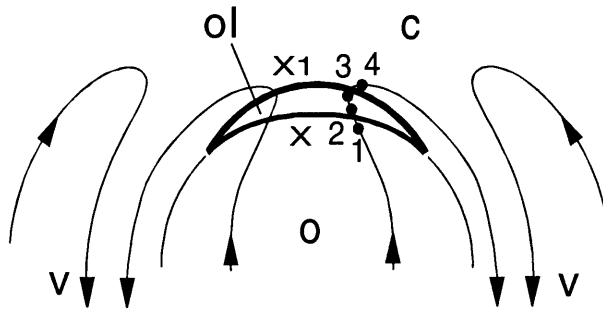
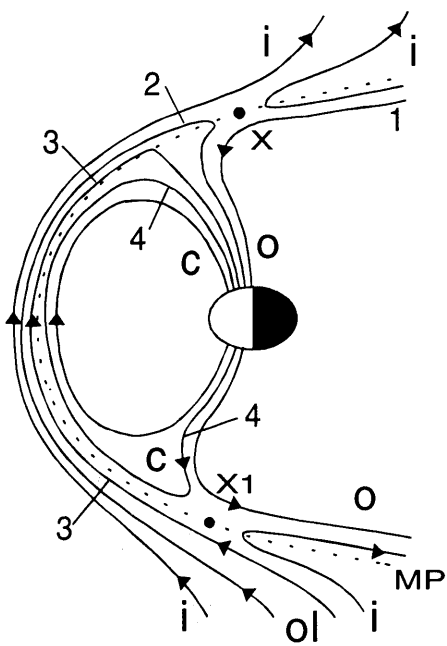


a). IMF $B_z > 0$



v = "viscously-driven" flow
L = lobe flow cell

b). IMF $B_z > 0$



i = interplanetary field line
o = open field line
c = closed field line
ol = overdraped lobe field line
(here northern hemisphere ionosphere only)

FIGURE 2.4: A schematic of two possible reconnection scenarios for IMF $B_z > 0$ as seen from the dusk flank, with their corresponding ionospheric patterns in the northern hemisphere for $B_y \sim 0$ (adapted from *Lockwood, 1998*). Field lines and regions that are open (o), closed (c), and interplanetary (i) are marked.

depiction can be steady-state, as the field lines can, in principle, circulate round the lobe cell, L, within the open field line region, as in Figure 2.4a. However, in practice, the flux tubes lifetime is far less than the time that would elapse in circulation, and therefore the circulation of these flux tubes will not persist. This is simply due to the scale sizes of the changes in the IMF. If, for example, the lobe cell occupies 10 degrees of invariant latitude (~ 1200 km), at a velocity of 500 ms^{-1} a flux tube would take ~ 120 minutes to circulate all the way round. It is unlikely that the IMF would maintain a northward direction for that length of time, and so it is most likely that the IMF orientation will change before it has time to complete a lobe circuit (*M. Lockwood*, private communication).

Figure 2.4b depicts two reconnection sites, one in either hemisphere, which are reconnected at different times. The overdraped flux produced by reconnection of 1 and i, to produce a field line such as 3, is itself reconnected at X1 to produce a field line like 4. This is remarkably similar to the picture first envisioned by Dungey, and recently revisited by *Song and Russell* [1992], as a way of producing a closed LLBL containing magnetosheath plasma, but is more realistic in that the field lines are not simultaneously reconnected at both sites. Note that the ionospheric flow cells generated now actually cross the open-closed field line boundary (henceforth termed OCFLB), as compared to Figure 2.4a. If the reconnection rates at X1 exceeds that at X, the northern hemisphere overdraped lobe flux will decay, the northern cusp would essentially disappear, and X1 would produce an overdraped lobe connected to the southern hemisphere.

2.3.2 The role of IMF B_y

As has been mentioned earlier it is not just IMF B_z that is important in the process of reconnection. To a large extent, it is the magnitude and direction of IMF B_y that controls the location and evolution of the reconnection site(s). Reconnection is at its strongest when there is maximum shear between the fields, but can theoretically occur when there is any shear between them. As the IMF angle relative to north in the Y-Z GSM plane, or *IMF clock angle*, varies then reconnection rates vary. For clock angles less than 45° in magnitude (strongly northward IMF), lobe reconnection occurs in either one (or both) hemispheres as discussed in Section 2.3.1 and illustrated in Figure 2.4. This will cause either lobe stirring in the former case as in Figure 2.4a, or the closure of open flux in the latter, as in Figure 2.4b. As the clock angle increases to a magnitude of 45° - 90° , reconnection can occur at both the low-latitude magnetopause and the lobes (*Sandholt et al.*, 1998a), thus producing the twin-

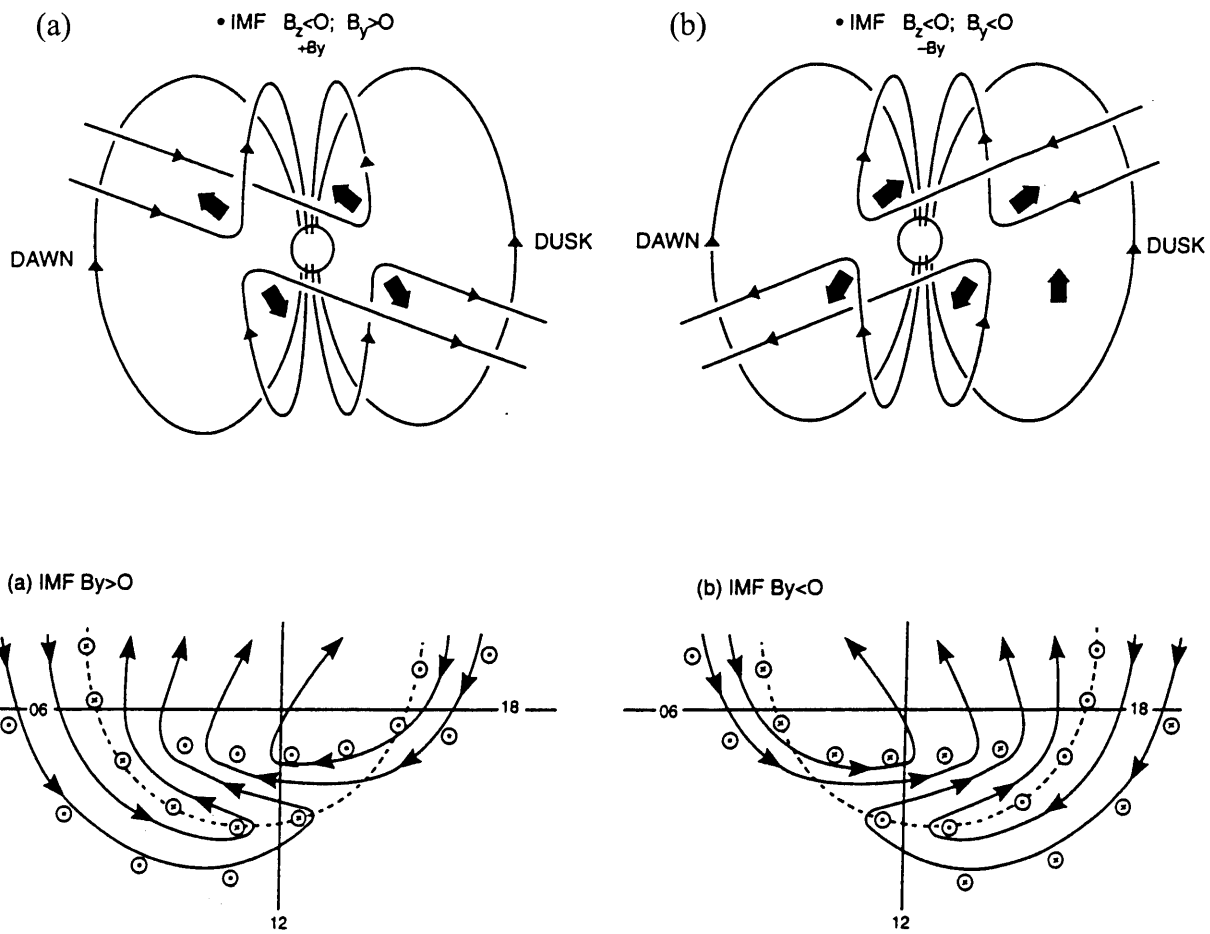


FIGURE 2.5: The effect of a non-zero B_y on reconnection site location (Gosling *et al.*, 1990), and ionospheric convection (taken from Cowley *et al.*, 1991). Figure 2.3.3(a) shows newly opened field lines as seen from the sun for IMF $B_z < 0$ and $B_y > 0$ and (b) shows $B_z < 0$ and $B_y < 0$, with corresponding ionospheric convection patterns in the northern hemisphere below.

vortical cell pattern as discussed in Section 2.3.1 together with the lobe-stirring generated flows due to lobe reconnection. When the IMF clock angle is greater than 90° , then lobe reconnection must cease due to the elimination of the anti-parallel field criterion, and subsolar reconnection can occur and twin-cell convection can dominate in the ionosphere. *Svalgard* [1968] and *Mansurov* [1969] were the first to comment on the effect of IMF B_y on the location and characteristics of the magnetic signature of the cusp. They interpreted the dependence of the cusp location on the dawn/dusk component of the IMF as the magnetic signature of an azimuthal flow driving a Hall current in the opposite direction to the flow along the poleward edge of the open/closed separatrix (*Friis-Christensen and Wilhelm, 1975; Cowley, 1981, 1984*). Figure 2.5 illustrates the positive and negative B_y orientations for the magnetospheric configurations for $B_z < 0$ (*Gosling et al., 1990*) with corresponding ionospheric flow patterns that are excited (*Cowley et al., 1991a*).

2.3.3 Control of the ionospheric convection pattern by IMF

The control of ionospheric convection by the IMF is a well-understood process (e.g. *Reiff and Burch, 1985; Cowley and Lockwood, 1997*). In summary, the typical “steady-state” ionospheric convection patterns for different orientations of IMF B_z and B_y are shown in Figure 2.6. As has been discussed in Sections 2.3.1 and 2, and illustrated in Figures 2.4 and 2.5, under southward IMF conditions, a simple two-cell convection pattern exists, with the non-zero B_y acting to distort the flow pattern such that one cell becomes dominant, depending on the sign of B_y . There is also a shift of the polar cap, the region of the ionosphere threaded by open magnetic flux, towards dusk (dawn) for negative (positive) B_y in the northern hemisphere (*Lester and Cowley, 2000*). Under northward IMF conditions, the convection pattern shrinks. Three or four cells exist, two solely on closed field lines due to the viscous interaction of the magnetosheath plasma moving past the magnetopause (e.g. *Reiff and Burch, 1985*). One or two convection cells are also present due to reconnection, which occurs on already open flux, and thus does not produce more open flux, called lobe-stirring. There are several points to note about this steady-state picture. Firstly, that the southward IMF convection pattern extends to lower latitudes, which is a direct consequence of a greater amount of open flux being present, and thus a larger polar cap. Secondly, this is, as previously stated, a steady-state model, and hence no time-dependent processes are considered. This is important on several levels; flow will naturally evolve from the rotation of the B_z component of the IMF, which occurs on timescales of minutes to hours, and thus the amount of open flux will vary; tail reconnection, most likely controlled by substorm activity

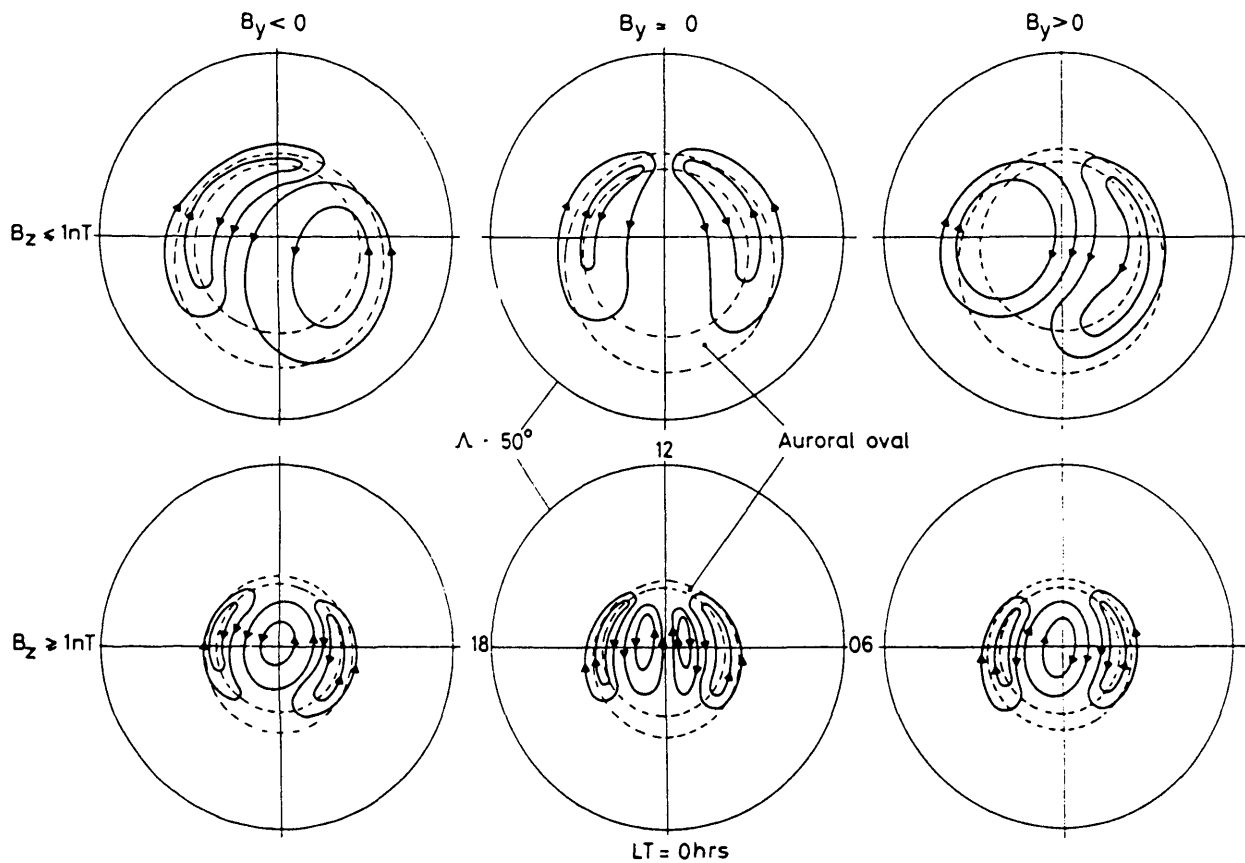


FIGURE 2.6: The inferred ionospheric steady-state convection pattern (Lockwood, 1993) in the Northern hemisphere as a function of IMF orientation. Solid lines with arrows represent the plasma streamlines, and the central circle to open closed field line boundary. The dashed portions represent the merging gap sites, which map back to the reconnection sites.

will destroy open flux; and time-varying reconnection at the low-latitude magnetopause will add a varying amount of flux to the polar cap.

2.4 Signatures of transient reconnection

2.4.1 Magnetopause signatures of transient reconnection

Time-dependent dayside reconnection (e.g. *Russell and Elphic*, 1979) has been postulated for many years. In Dungey's original picture it was thought that following the onset of dayside reconnection, nightside reconnection would ultimately ensue. This led to the proposal (*Petschek*, 1964; *Levy et al.*, 1964) that reconnection was a static, large-scale process, in which dayside and nightside reconnection processes were very much inter-linked. However, there were several discrepancies in observed measurements compared to this theory. *Russell* [1972] and *Russell and McPherron* [1973] suggested that differential reconnection occurred, that is dayside and nightside reconnection were two separate time-dependent processes. The first observations of transient reconnection were published by *Haerendel et al.* [1978], using HEOS-2 measurements, which traversed the magnetopause on many occasions. The term "flux transfer event" (FTE) was coined to describe an individual magnetopause reconnection pulse, as identified in ISEE-1 and -2 spacecraft observations by *Russell and Elphic* [1978,1979]. They observed a characteristic bipolar magnetic field signature normal to the magnetopause using the "boundary normal" co-ordinate system as illustrated in Figure 2.7. The N component is chosen to be in the direction normal to the magnetopause, the L component is tangentially northward along the magnetospheric field and the M component is tangential to the boundary toward dawn, and completes the right-handed Cartesian set. Figure 2.8 depicts one such interval identified by these authors, with multiple bipolar B_N oscillations occurring. They also identified a rough MLT dependence of FTE signatures, in that they occur between 9 and 15 MLT, and a large dependence on IMF B_z . These FTEs were observed almost exclusively when the IMF points southward, as measured in the interplanetary medium (*Berchem and Russell*, 1984) and mostly observed when the magnetosheath field points southward (*Rijnbeek et al.*, 1984). Subsequently the magnetic signature of FTEs were found to be accompanied by a characteristic plasma signature related to particles accelerated by the reconnection process; plasma of mixed magnetosheath and magnetospheric origin will typically exist on these flux tubes (e.g. *Klumpar et al.*, 1990; *Le et al.*, 1999).

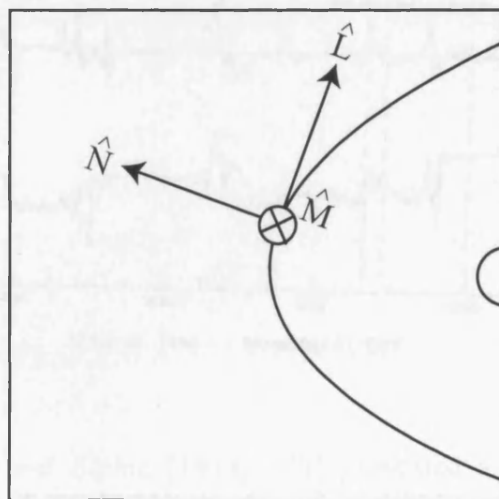
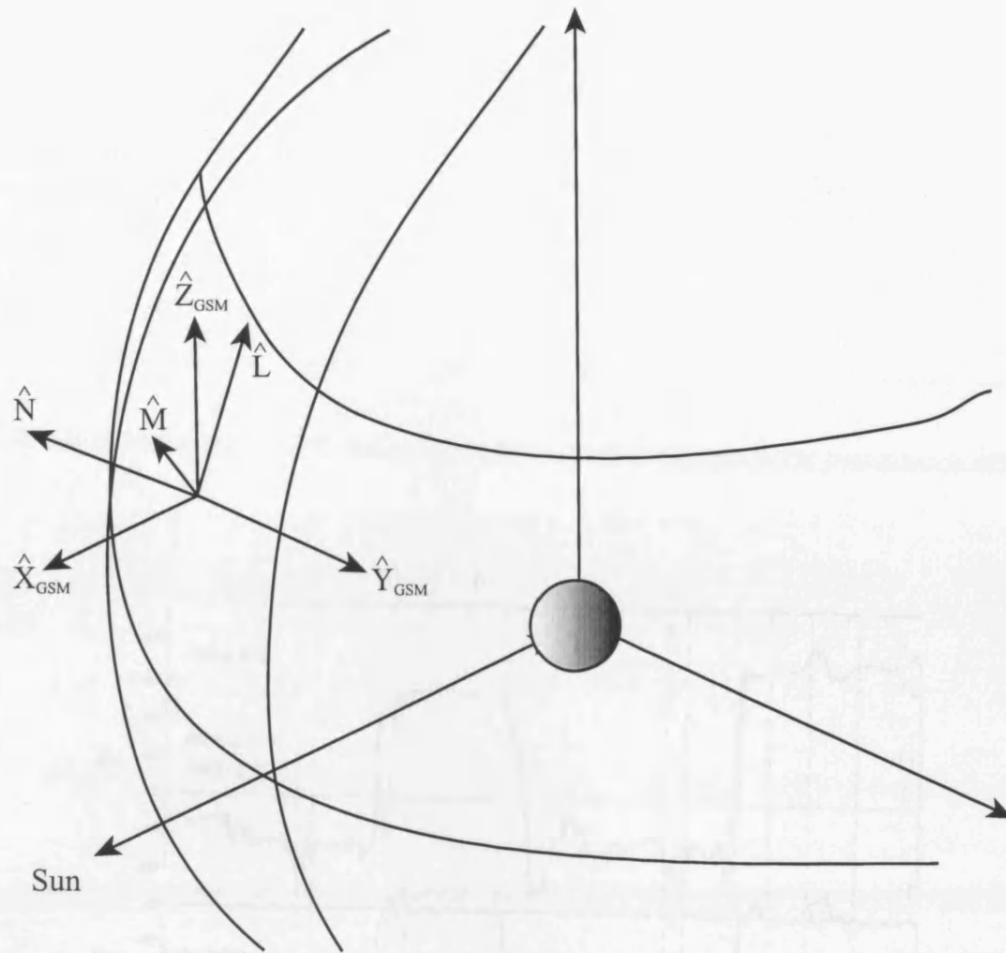


FIGURE 2.7: The "boundary normal" co-ordinate system (adapted from *Elphic and Russell, 1979*). The N component is chosen to be in the direction normal to the magnetopause, the L component is tangentially northward along the magnetospheric field and the M component is tangential to the boundary toward dawn, and completes the right-handed Cartesian set. The inset depicts the boundary normal co-ordinate system from the dusk flank through the noon-midnight meridian.

Since the early identification of a bipolar variation in the boundary normal magnetic field component there has been a variety of single and multi-point observations by various low altitude spacecraft. These have revealed the complex structure of the boundary and the effects of the solar wind on the magnetosphere. The first multi-point observations of the dayside magnetosphere were obtained by *Interplanetary Magnetic Field* (IMF) and *Interplanetary Electric Field* (IPEF) by the *Interplanetary Magnetic Field* (IMF) and *Interplanetary Electric Field* (IPEF) spacecraft. The first multi-point observations of the dayside magnetosphere were obtained by *Interplanetary Magnetic Field* (IMF) and *Interplanetary Electric Field* (IPEF) by the *Interplanetary Magnetic Field* (IMF) and *Interplanetary Electric Field* (IPEF) spacecraft. The first multi-point observations of the dayside magnetosphere were obtained by *Interplanetary Magnetic Field* (IMF) and *Interplanetary Electric Field* (IPEF) by the *Interplanetary Magnetic Field* (IMF) and *Interplanetary Electric Field* (IPEF) spacecraft.

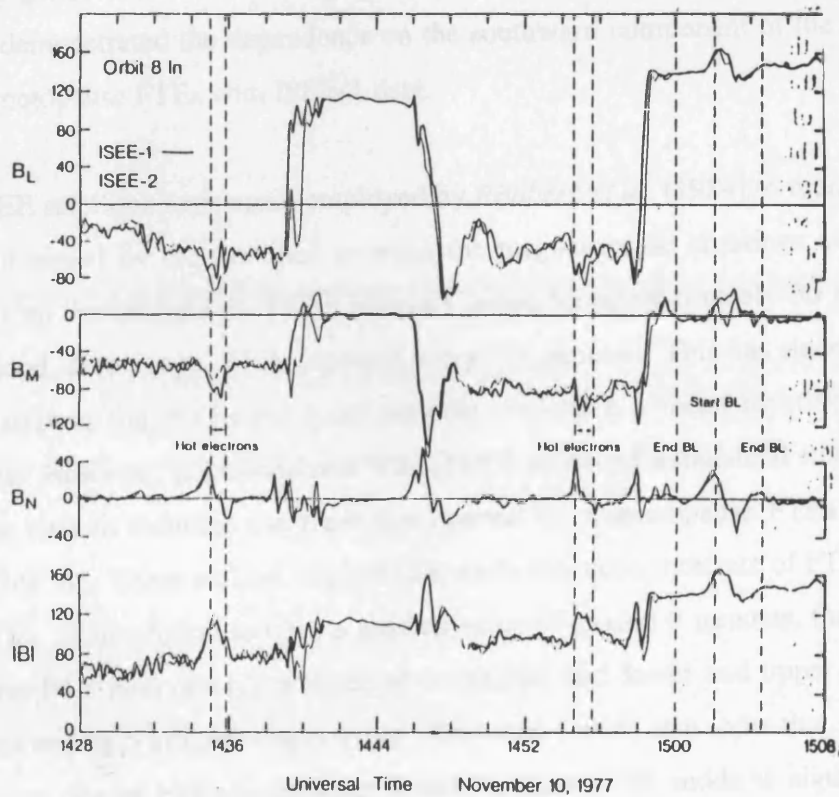


FIGURE 2.8: Russell and Elphic [1978;1979] presented a series of FTE signatures as observed by ISEE-1 and -2, marked by the dashed vertical lines.

Since the early identification of a bipolar variation in the boundary normal magnetic field component, there has been a variety of single, and multi-point observations by a whole host of spacecraft, though none traversed the magnetopause with the regularity of ISEE-1 and -2 and HEOS-2. Further evidence that time-varying reconnection occurred on the dayside was presented by *Paschmann et al.* [1982] who observed strong plasma flow bursts against the background plasma flow with ISEE-1 and -2 during 5 separate crossings of the magnetopause. *Le et al.* [1999] revisited the ISEE-2 dataset and showed that the plasma distribution functions of the magnetosheath FTE cores were composed of a mixture of magnetosheath and magnetospheric plasma. This was in contrast to those detected in the magnetosphere when the hot magnetospheric plasma has drained off. *Kawano and Russell* [1997] demonstrated the dependence on the southward component of the interplanetary field on magnetopause FTEs with ISEE-1 data.

The ISEE satellites were again employed by *Rijnbeek et al.* [1984] to report on the number of FTEs observed by the satellites between the magnetopause crossings and the FTE furthest away from the boundary. These intervals lasted for approximately 30 minutes, and during this period, on average, FTEs repeated every 7-9 minutes. This has since been interpreted as demonstrating that FTEs are quasi-periodic, and have a mean repetition rate of around 8 minutes. However, *Lockwood and Wild* [1993] produced a statistical study of ISEE-1 and -2 satellite data to examine the repetition interval of magnetopause FTEs and its dependence upon IMF B_z . These authors suggest that while the recurrence rate of FTEs (or the inter-FTE period) is indeed found to have a median value of around 8 minutes, that the distribution of the inter-FTE intervals has a mode of 3 minutes, and lower and upper decile values of 1.5 minutes and 18.5 minutes respectively. *Kuo et al.* [1995] also show that, although the median repetition rate of FTEs is between 7 and 8 minutes, the mode is significantly less than 8 minutes, at around 4 minutes. These results are illustrated in Figure 2.9, alongside observational evidence of ground-based and ionospheric evidence of flux transfer, as discussed in Sections 2.4.4 (taken from *McWilliams et al.*, 2000).

Sanny et al. [1998] presented a statistical study of AMPTE magnetopause crossings, and discovered that in cases close to the magnetic equator, the classical bipolar B_N was distorted into an asymmetric signature. This implies that the asymmetric signature evolves into the classical symmetric B_N signature as it evolves from the X line. More recent studies include *Safrankova et al.* [1998], who reported on two-point INTERBALL measurements of transient reconnection signatures. A study was also performed by *Phan et al.* [2000], who, with the

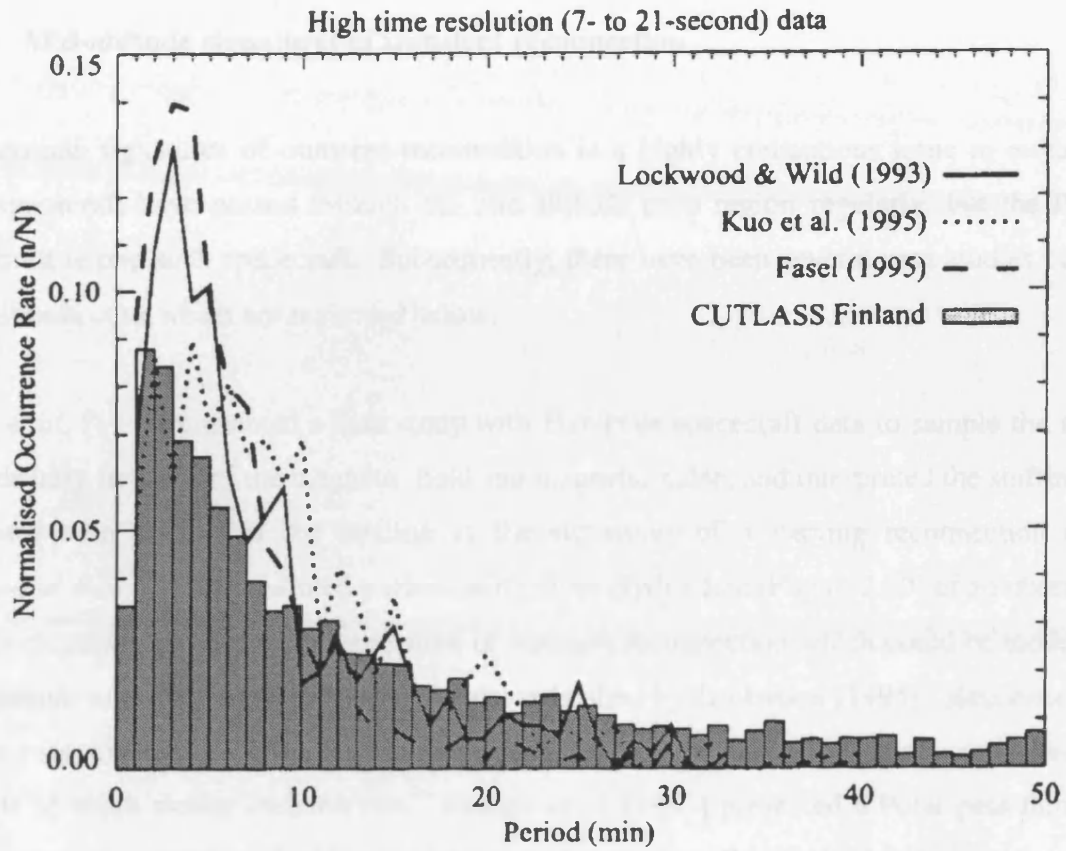


FIGURE 2.9: The occurrence rate of various signatures of Flux Transfer Events taken from *McWilliams et al.* [2000]. The shaded bars represent high-time resolution (7-21s) CUTLASS Finland I-o-s velocity data. Inter-FTE intervals from the ISEE spacecraft from *Lockwood and Wild* [1993] (solid line) and *Kuo et al.* [1995] (dotted line) are also included. The dashed line is the distribution of the time between optical measurements of PMAFs (*Fasel et al.*, 1995).

combined satellite measurements of Equator-S and Geotail measured the inferred bi-directional plasma and field jets in the B_L direction, another signature of transient reconnection.

2.4.2 Mid-altitude signatures of transient reconnection

Mid-altitude signatures of transient reconnection is a highly contentious issue in research. Few spacecraft have passed through the mid-altitude cusp region regularly, but the Polar spacecraft is one such spacecraft. Subsequently, there have been several case studies of the mid-altitude cusp which are reviewed below.

Chen et al. [1997] presented a case study with Hawkeye spacecraft data to sample the mid-altitude cusp in terms of the magnetic field and magnetic noise, and interpreted the shifting of the cusp with respect to the satellite as the signatures of a varying reconnection rate. *Lockwood et al.* [1998] presented a study using Polar Hydra data (Figure 2.10) of an observed energy-dispersed pulsed particle signature of transient reconnection which could be modelled by a simple time-varying reconnection model published by *Lockwood* [1995]. Reconnection in this case was found to be occurring almost exclusively in a series of pulses, separated by periods of much slower reconnection. *Grande et al.* [1997] presented a Polar pass through the cusp under northward IMF conditions and with the CAMMICE MICS instrument observed a spatially extended region of magnetosheath plasma of almost 5° width in magnetic latitude.

Zhou and Russell [1997] and *Zhou et al.* [1999] investigated the magnetic signature of the cusp with the instruments onboard Polar. These authors found that the cusp was detected as a structured depression in the local magnetic field, which was interpreted and discussed in terms of field aligned current signatures, which in turn could be interpreted as those pertaining to the reconnection process, as discussed in Section 2.5.

One contrary view of the time-varying cusp is presented by *Trattner et al.* [1999], who, with the Polar TIMAS instrument and a favourable position of the Interball-Aurora satellite found that the features observed by Polar were essentially reproducible by Interball-Aurora passing through the same MLT/MLAT some 90 minutes later. In another case study with the two spacecraft 35 minutes apart, similar features were reproduced at both spacecraft. The authors interpreted this as a spatial structure existing in the cusp.

To the best of the author's knowledge, there has been little observation of the mid-auroral cusp on a routine basis, and it is the aim of this thesis to address this gap in the observations.

2.4.3 Low-altitude signatures of transient reconnection

Low-altitude signatures of transient reconnection were first identified by *Newell and Meng* [1988]. The low-altitude observations come from the fleet of DMSP satellites, primarily weather satellites, but with particle sensors designed to measure plasma properties along the spacecraft tracks. *Newell and Meng* [1988, 1992] produced a MLT/MLAT map of the dayside

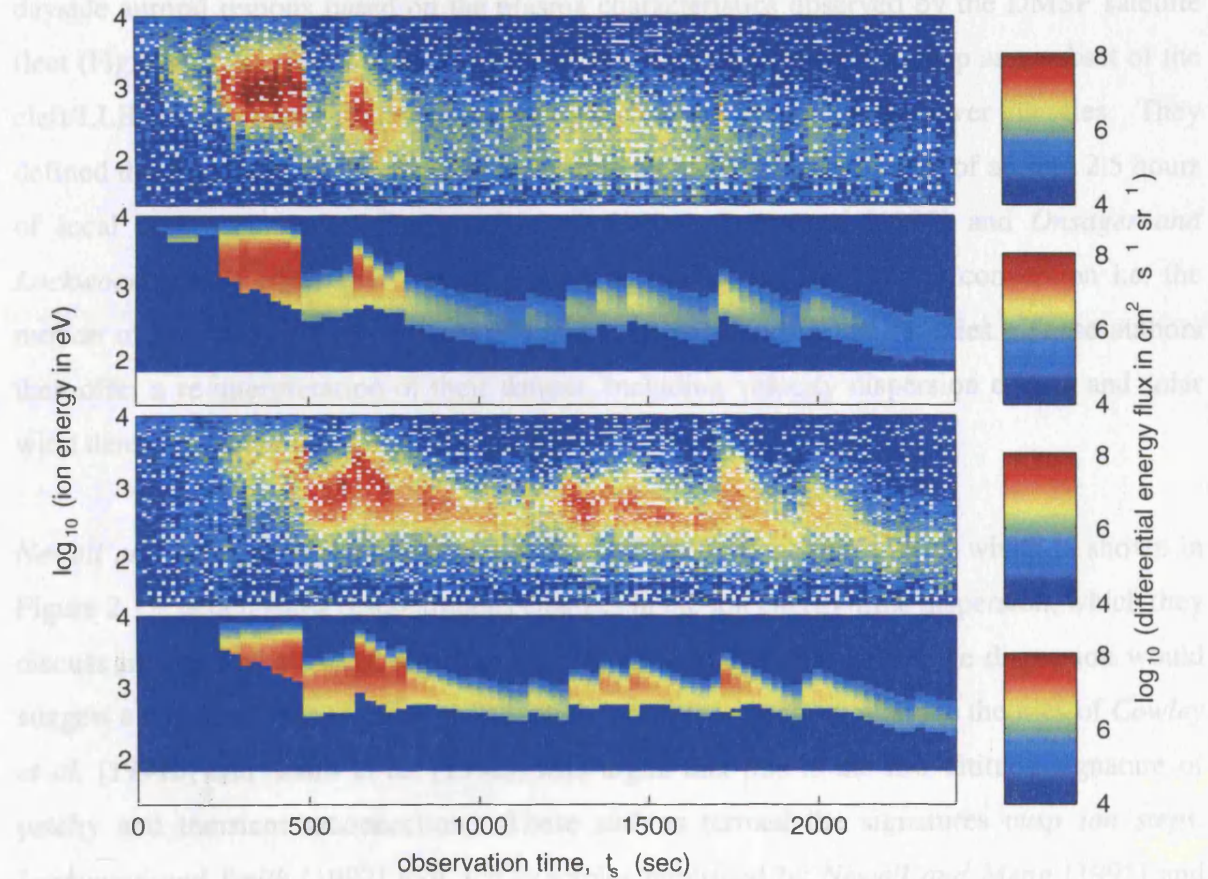


FIGURE 2.10: The observed and modelled ion differential energy flux spectrograms, as measured by the Polar HYDRA instrument and modelled from *Lockwood* [1995]. From top to bottom; observed down-going ions, modelled down-going ions, observed up-going ions and modelled up-going ions (taken from *Lockwood et al.*, 1998).

To the best of the author's knowledge, there has been little observation of the mid-altitude cusp on a routine basis, and it is the aim of this thesis to address this gap in the observations.

2.4.3 Low-altitude signatures of transient reconnection

Low-altitude signatures of ephemeral reconnection were first identified by *Newell and Meng* [1988]. The low-altitude observations come from the fleet of DMSP satellites, primarily weather satellites, but with particle sensors designed to measure plasma properties along the spacecraft tracks. *Newell and Meng* [1988; 1992] produced a MLT/MLAT map of the dayside auroral regions based on the plasma characteristics observed by the DMSP satellite fleet (Figure 2.11). Based upon this data set, the authors describe the cusp as a subset of the cleft/LLBL, with higher fluxes of magnetosheath particles at slightly lower energies. They defined the cusp as being localised to near noon and with a typical width of around 2.5 hours of local time. However, *Lockwood et al.* [1996], *Lockwood* [1997] and *Onsager and Lockwood* [1997] argue that *Newell and Meng* do not include plasma convection i.e. the motion of particles in a crossed electric and magnetic field in their studies. These authors then offer a re-interpretation of their dataset, including velocity dispersion effects and solar wind densities on the precipitating particles.

Newell and Meng [1991] published a series of DMSP F7 passes, one of which is shown in Figure 2.12, which show discontinuous changes in the ion energy-time dispersion, which they discuss in terms of a spatial structure existing in the cusp. However, the dispersion would suggest a temporal change rather than spatial, which is in keeping with the theories of *Cowley et al.* [1991b] and *Smith et al.* [1992], who argue that this is the low-altitude signature of patchy and transient reconnection. These authors termed the signatures *cusp ion steps*. *Lockwood and Smith* [1992] took the examples published by *Newell and Meng* [1991] and applied the theories of *Cowley et al.* and *Smith et al.* and from this evaluated the variations in the reconnection rate, which is implicitly defined as the rate of flux transfer.

A case study by *Yeoman et al.* [1997] presented simultaneous observations of the cusp in DMSP, HF radar, and optical data. *Lockwood et al.* [1995] present a DMSP F10 pass which detects such a cusp ion step, between two poleward moving events of enhanced electron temperature observed by the EISCAT incoherent scatter radar in the ionosphere.

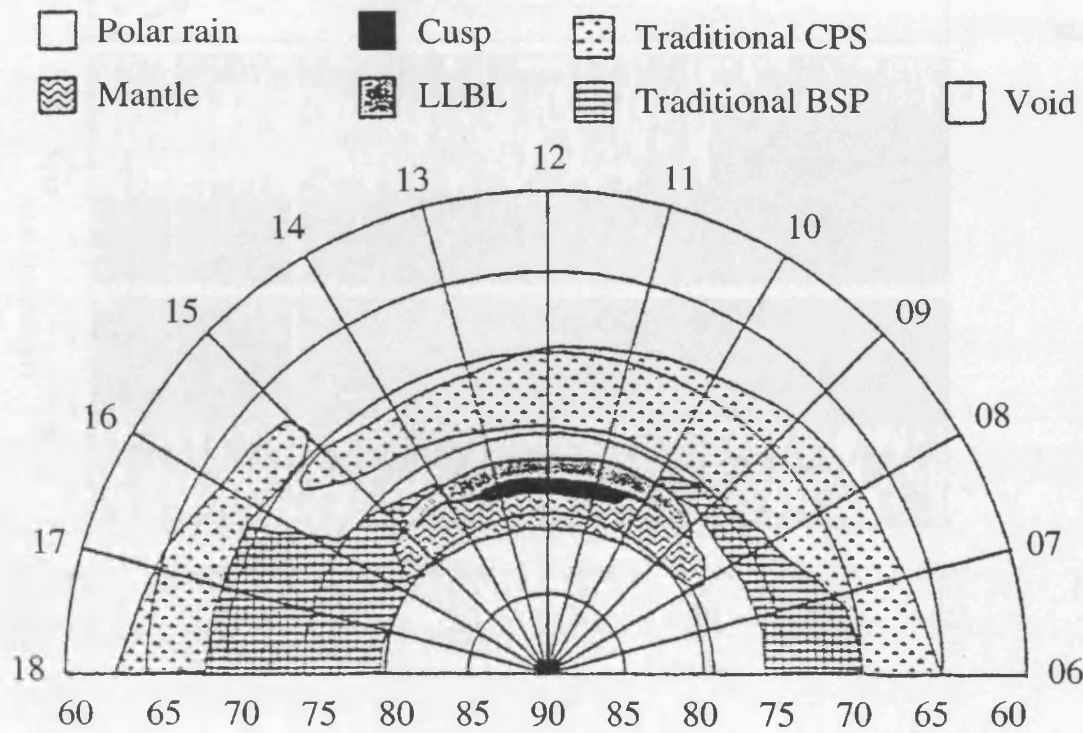


FIGURE 2.11: A map of the high-latitude ionosphere constructed from DMSP passes over several years (taken from *Newell and Meng, 1992*) based on plasma characteristics.

2.4.4 Ionospheric and ground-based signatures of transient reconnection

It took several years before ground-based signatures of flux transfer events was published.

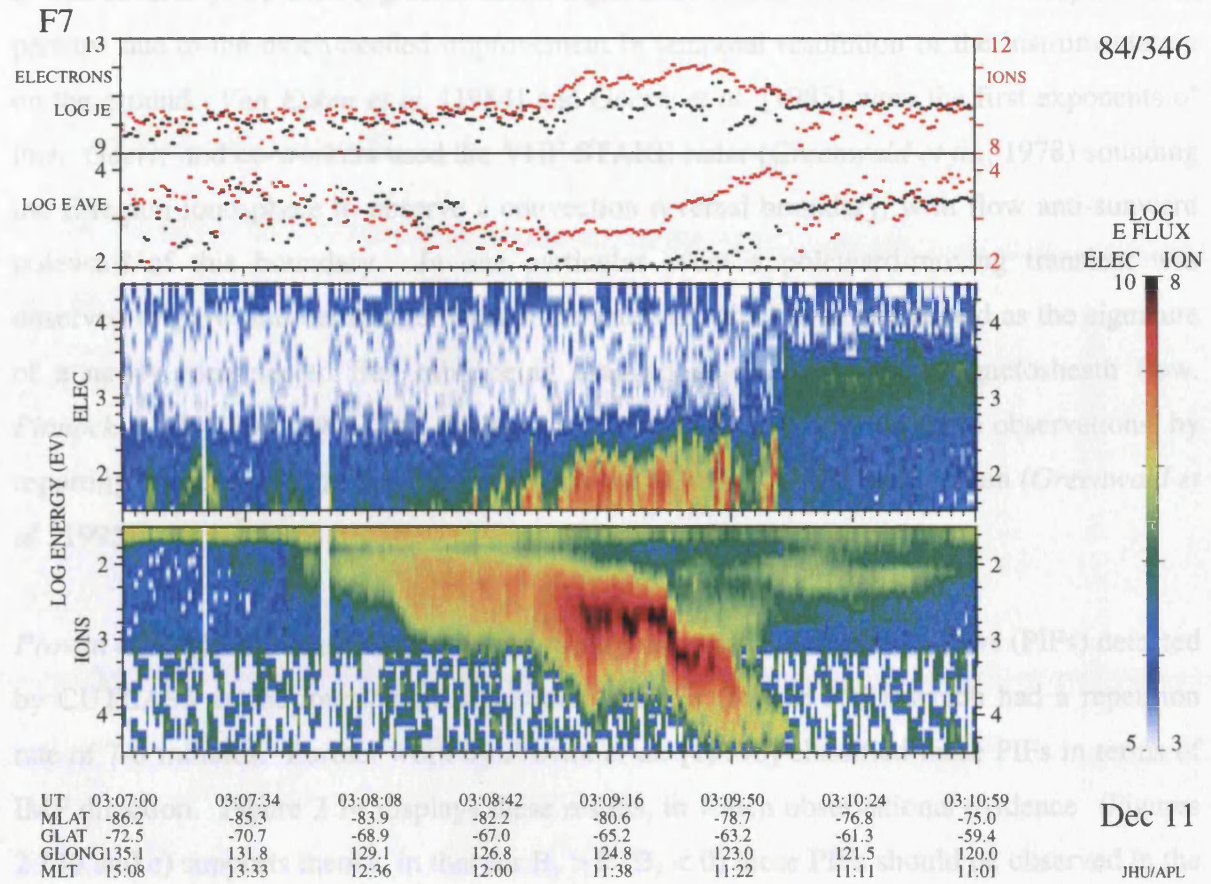


FIGURE 2.12: A DMSP F7 pass of the low-altitude cusp region (taken from *Newell and Meng, 1991*). A "classical cusp ion step" is observed in the bottom panel, consistent with the observation of a reconnection burst.

Elphic et al. [1990] and *Newberg et al. [1999]* report the only direct evidence linking magnetopause FTE signatures into the ionosphere, using ISF P-1 and -2 and the EISCAT VHF Radar, and Equator-S and the CUTLASS HF radar, respectively. The case study presented by *Elphic et al. (1990)* is shown in Figure 2.15. Isolated FTE signatures (denoted by vertical lines) are detected by the EISCAT radar in the ionosphere as westward and poleward moving plasma flow bursts. The case study presented by *Newberg et al. [1999]* is shown in Figure 2.16. Equator-S observed an isolated bipolar boundary normal oscillation in conjunction with an enhanced flow channel event (FCE) observed by the CUTLASS Fineduc HF radar. Since then, *Newberg et al. [2000]* have produced a survey of magnetopause FTE

2.4.4 Ionospheric and ground-based signatures of transient reconnection

It was several years before ground-based signatures of flux transfer events was published, perhaps due to the much-needed improvement in temporal resolution of the instrumentation on the ground. *Van Eyken et al.* [1984] and *Goertz et al.* [1985] were the first exponents of this. *Goertz* and co-workers used the VHF STARE radar (*Greenwald et al.*, 1978) sounding the E-region ionosphere to observe a convection reversal boundary, with flow anti-sunward poleward of this boundary. In one particular event a poleward-moving transient was observed to grow and decay over a 4 minute interval, which was interpreted as the signature of a newly reconnected flux tube being dragged poleward by the magnetosheath flow. *Pinnock et al.* [1993; 1995] and *Rodger and Pinnock* [1997] built on these observations, by reporting on poleward moving transients with the SuperDARN HF radar chain (*Greenwald et al.*, 1995).

Provan et al. [1998] identified the poleward-moving pulsed ionospheric flows (PIFs) detected by CUTLASS as the ionospheric signatures of FTEs (Figure 2.13), which had a repetition rate of 7-8 minutes. Further work by *Provan et al.* [1999b] classified these PIFs in terms of IMF direction. Figure 2.14 displays these results, in which observational evidence (Figures 2.14b and c) supports theory, in that for $B_y > 0$ ($B_y < 0$) these PIFs should be observed in the shaded regions pre (post) noon (Figures 2.14d and e). Therefore the change in ionospheric convection due to reconnection (PIFs) is in agreement with the average east-west controlled tilt of the cusp throat flow. *McWilliams et al.* [2000] demonstrated that there was no biasing in the CUTLASS radar sample set by performing a statistical study of both the IMF B_y and B_z components, and while there is a 67% bias towards southward IMF, there is no dependence of detection on IMF B_y .

Elphic et al. [1990] and *Neudegg et al.* [1999] report the only direct evidence linking magnetopause FTE signatures into the ionosphere, using ISEE-1 and -2 and the EISCAT VHF Radar, and Equator-S and the CUTLASS HF radars, respectively. The case study presented by *Elphic et al.* [1990] is shown in Figure 2.15. Isolated FTE signatures (denoted by vertical lines) are detected by the EISCAT radar in the ionosphere as westward and poleward moving plasma flow bursts. The case study presented by *Neudegg et al.* [1999] is shown in Figure 2.16. Equator-S observed an isolated bipolar boundary normal oscillation in conjunction with an enhanced flow channel event (FCE) observed by the CUTLASS Finland HF radar. Since then, *Neudegg et al.* [2000] have produced a survey of magnetopause FTE

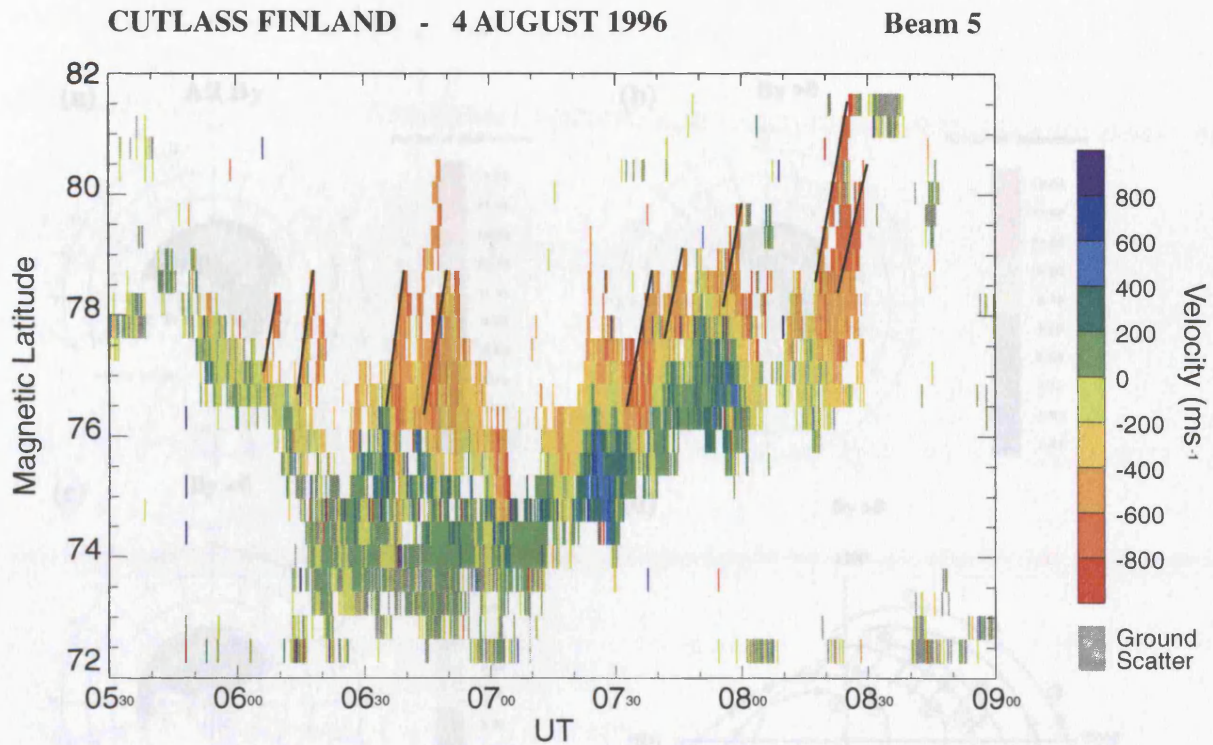


FIGURE 2.13: Latitude Time Velocity (LTV) plot of beam 5 of the CUTLASS Finland radar. The line-of-sight Doppler velocities are colour-coded with red denoting l-o-s velocity away from the radar and blue denoting towards the radar. Several of the poleward-moving pulsed ionospheric flows (PIFs) are traced with black lines (taken from *Provan and Yeoman, 1999*).

FIGURE 2.14: (a) Occurrence distribution of PIF signatures as observed by high-time resolution data from the CUTLASS Finland HF radar, and (b) and (c) show the occurrences for $B_y > 0$ and $B_y < 0$ respectively. Figures (d) and (e) show sketches of the dayside ionospheric convection pattern for $B_y > 0$ and $B_y < 0$ respectively (taken from *Provan et al., 1999*).

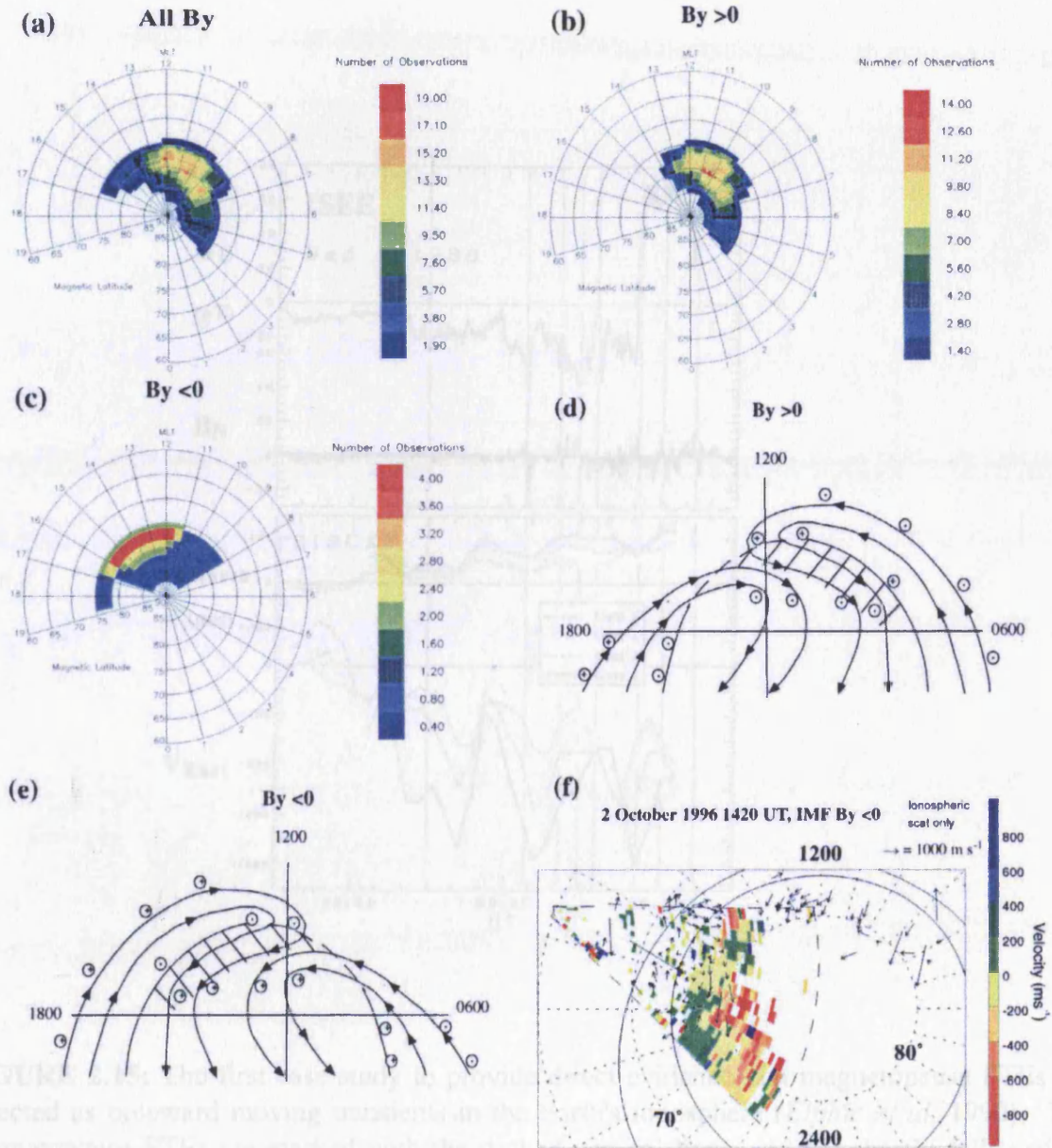


FIGURE 2.14: (a) Occurrence distribution of PIF signatures as observed by high-time resolution data from the CUTLASS Finland HF radar, and (b) and (c) show the occurrences for $B_y > 0$ and $B_y < 0$ respectively. Figures (d) and (e) show sketches of the dayside ionospheric convection pattern for $B_y > 0$ and $B_y < 0$ respectively (taken from Provan *et al.*, 1999)

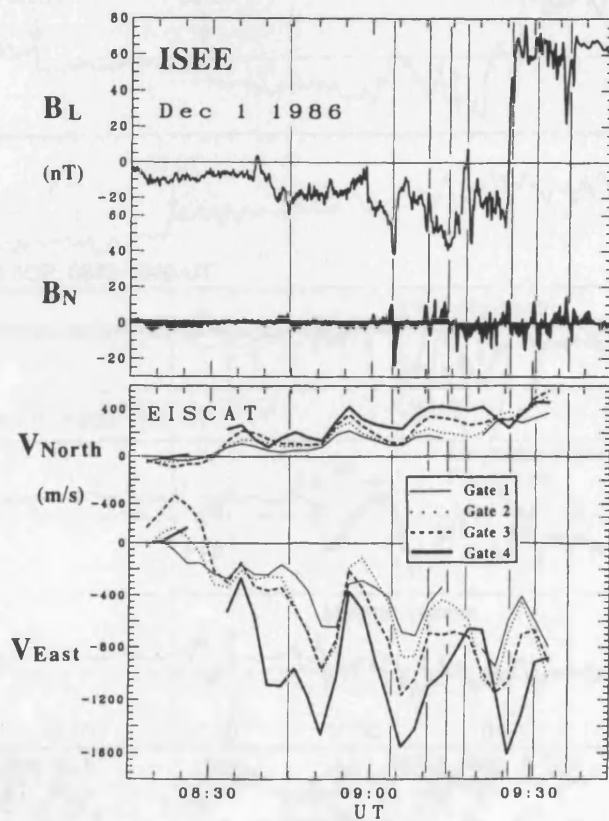


FIGURE 2.15: The first case study to provide direct evidence that magnetopause FTEs are detected as poleward moving transients in the Earth's ionosphere (*Elphic et al, 1990*). The magnetopause FTEs are marked with the dashed vertical lines, and are shortly followed by their ionospheric signature, that of a poleward (and in this case westward) moving ionospheric plasma flow bursts.

signature with Equator-S and their associated flow bursts in the ionosphere, and found a correlation of ~ -0.7 between the two signatures.

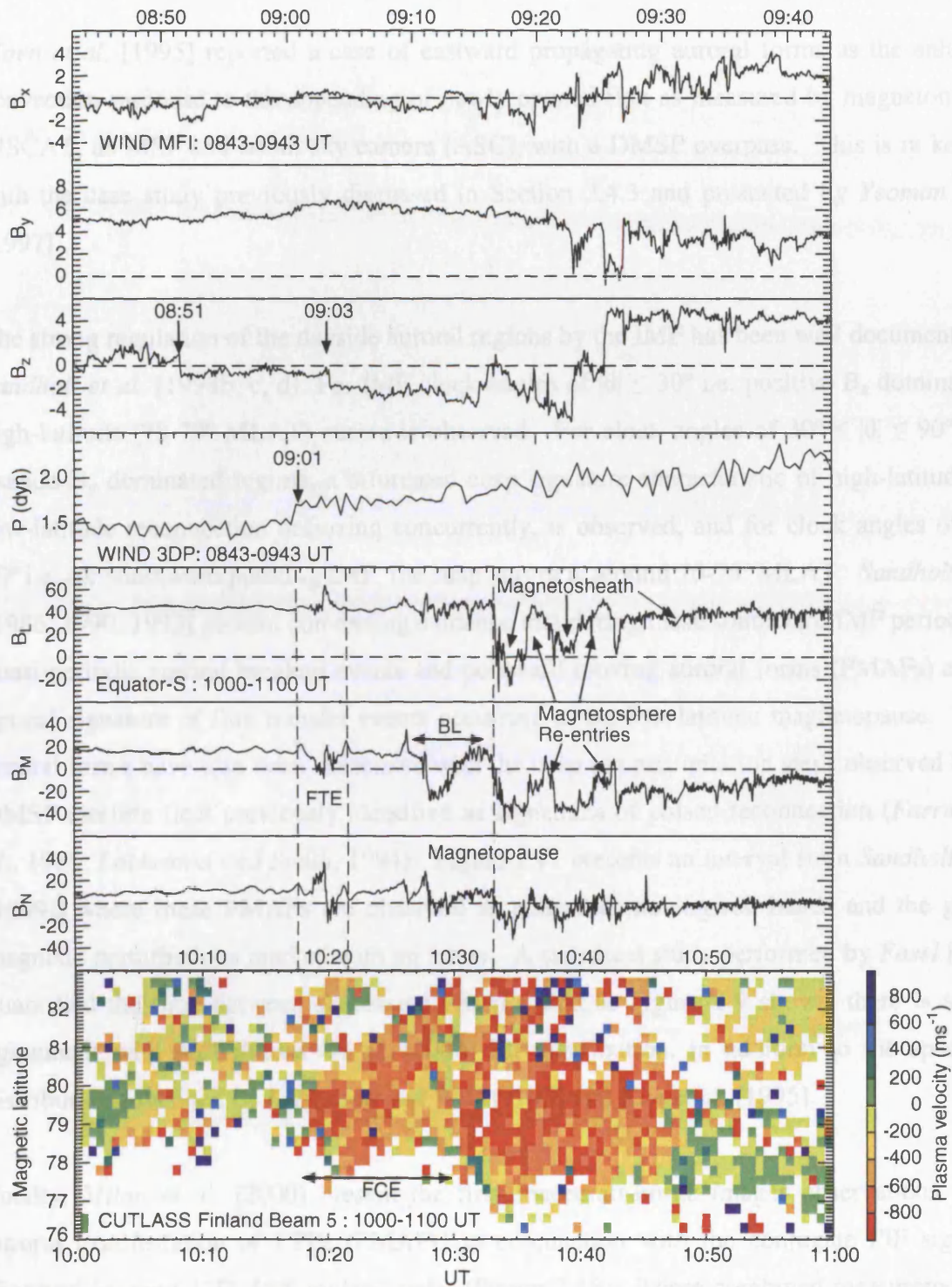


FIGURE 2.16: From top to bottom, B_x , B_y and B_z (in GSM co-ordinates) and dynamic pressure from the WIND spacecraft, and B_L , B_M , and B_N from Equator-S. Bottom is Beam 5 of the CUTLASS Finland HF radar. A single isolated FTE signature (a bipolar oscillation of B_N) is observed which is coincident with a channel of enhanced plasma velocity (a flow channel event, FCE, or pulsed ionospheric flow, PIF), taken from *Neudegg et al.* [1999].

signatures with Equator-S and their associated flow bursts in the ionosphere, and found a correlation of ~80% between the two signatures.

Moen et al. [1995] reported a case of eastward propagating auroral forms as the enhanced convection response to the appending of newly opened flux as measured by magnetometers, EISCAT, an MSP and an all sky camera (ASC), with a DMSP overpass. This is in keeping with the case study previously discussed in Section 2.4.3 and presented by *Yeoman et al.* [1997].

The strong regulation of the dayside auroral regions by the IMF has been well documented by *Sandholt et al.* [1998b, c, d]. For IMF clock angles of $|\theta| \leq 30^\circ$ i.e. positive B_z dominates, a high-latitude (78-79° MLAT) aurora is observed. For clock angles of $30^\circ \leq |\theta| \leq 90^\circ$ i.e. a pseudo- B_y dominated regime, a bifurcated cusp signature characteristic of high-latitude and low-latitude reconnection occurring concurrently, is observed, and for clock angles of $|\theta| \geq 90^\circ$ i.e. for southward pointing IMF, the cusp aurora is around 70-75° MLAT. *Sandholt et al.* [1986, 1990, 1993] present convincing evidence that during these southward IMF periods, the quasi-periodic auroral breakup events and poleward moving auroral forms (PMAFs) are the optical signature of flux transfer events occurring at the low-latitude magnetopause. These auroral forms have also been associated with the cusp ion precipitation steps observed by the DMSP satellite fleet previously identified as signatures of pulsed reconnection (*Farrugia et al.*, 1988; *Lockwood and Smith*, 1994). Figure 2.17 presents an interval from *Sandholt et al.* [1999], where these PMAFs are observed as poleward moving red bands and the ground magnetic perturbations marked with an arrow. A statistical study performed by *Fasel* [1995] quantified the time between successive PMAFs, and as Figure 2.9 shows, there is a good agreement with *McWilliams' et al.* [2000] PIF distribution, in addition to the spacecraft distributions obtained by *Lockwood and Wild* [1993] and *Kuo et al.* [1995].

Finally, *Milan et al.* [2000] present the first spacecraft-borne imager observations of the auroral manifestation of FTEs (PMAFs) in conjunction with the conjugate PIF signature observed by the CUTLASS Finland radar (Figure 2.18). These combined measurements of the bifurcation of the auroral oval and the evolution duskwards provide an indication that the PMAFs can extend up to 3500 km or 7 hours of MLT in length. The anti-sunward movement of the bifurcation of the oval was interpreted as the expansion of the reconnection X line along the dusk flank of the magnetopause.

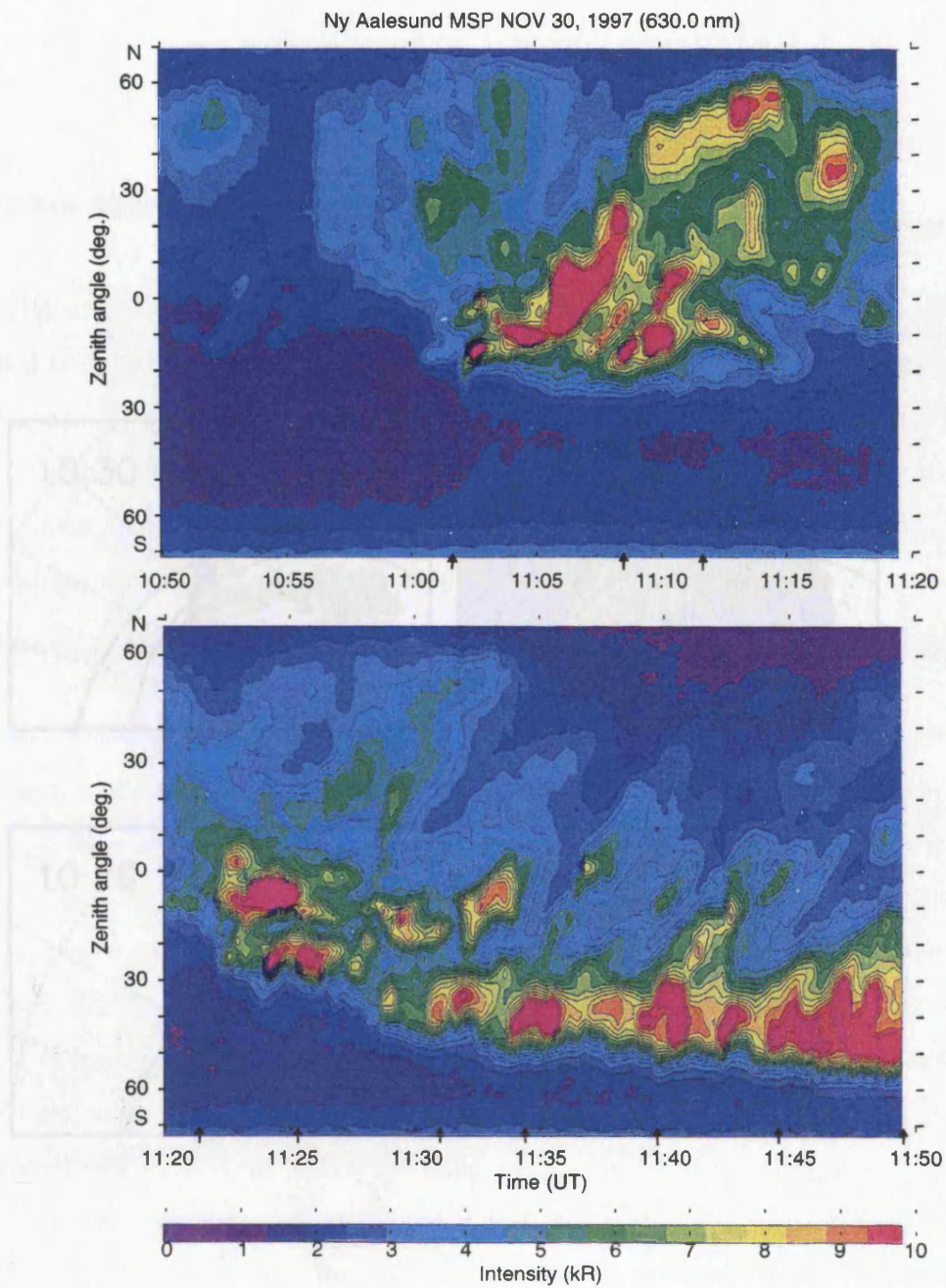


FIGURE 2.15: A comparison of the intensity of auroral emission as seen by the Polar UVT

FIGURE 2.17: Colour-coded contour plot of Ny Ålesund meridian scanning photometer (MSP) observations of 630 nm emissions (taken from *Sandholt et al., 1999*). PMAFs are seen as poleward moving red bands.

2.5 Theories of transient reconnection

The theories of the mechanism of flux transfer have been the subject of discussion since the discovery of time-dependent reconnection. The most comprehensive survey of the means of transient reconnection is given in Lockwood and Hapgood (1998).

2.5.1 Fossil Flux Tube Model

Russell and Elphic (1978) proposed an FTE model based on a pulse of reconnection being invoked at a sharp ($-1R_p$) reconnection X line (Figure 2.19). These newly opened flux tubes

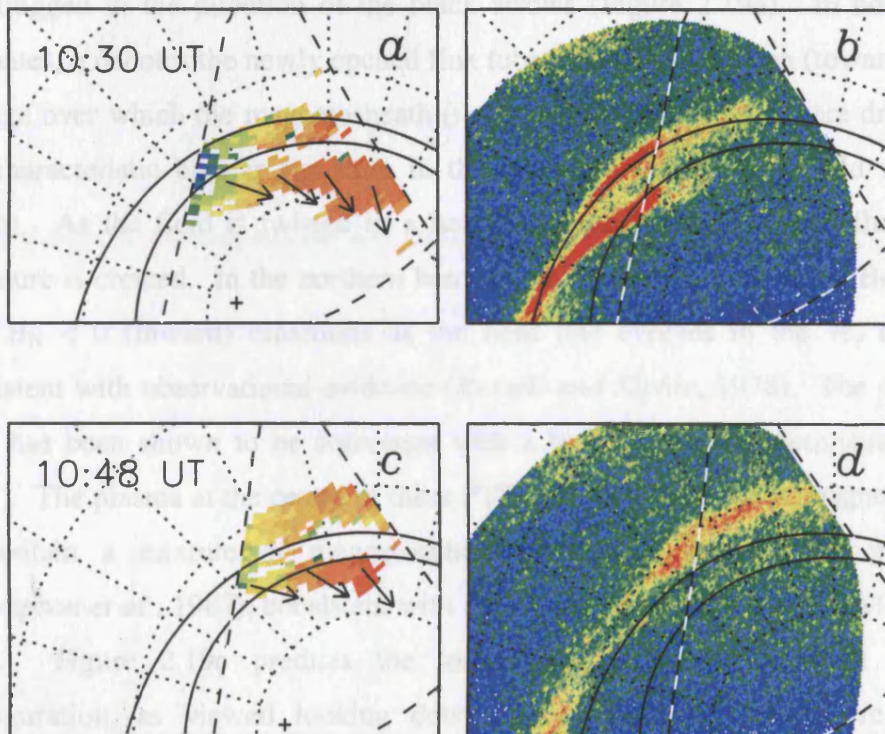


FIGURE 2.18: A comparison of the location of auroral emission as seen by the Polar UVI instrument (right panels) and simultaneous CUTLASS Finland radar backscatter (left panels). The poleward moving features observed by CUTLASS Finland are an extension of the poleward portion of the bifurcation of the main auroral oval, which is identified as PMAFs (taken from Milan *et al.*, 2000).

one of the following models:

To conclude, then, the fossil flux tube model invokes patchy, time-dependent reconnection, which results in newly-opened flux tubes being dragged across an *in-situ* spacecraft. The

2.5 Theories of transient reconnection

The theories of the mechanism of flux transfer have been the subject of discussion since the discovery of time-dependent reconnection. The most comprehensive survey of the means of transient reconnection is given in *Lockwood and Hapgood* [1998].

2.5.1 Fossil Flux Tube Model

Russell and Elphic [1978] proposed an FTE model based on a pulse of reconnection being invoked at a short ($\sim 1R_E$) reconnection X line (Figure 2.19). These newly opened flux tubes are dragged in the direction of the black arrows (Figure 2.19a). In boundary normal coordinates, o denotes the newly opened flux tube in the $-M$ direction (towards dusk) and forms a bulge over which the magnetosheath (i) and closed field lines (c) are draped, thus creating the characteristic bipolar signature in the boundary normal, B_N , field component (Figure 2.19b). As the field is twisted in a helical fashion inside the open flux region a bipolar signature is created. In the northern hemisphere the field points in the $B_N > 0$ (outward) and then $B_N < 0$ (inward) directions as the field line evolves in the $+L$ direction, which is consistent with observational evidence (*Russell and Elphic*, 1978). The draping of the field lines has been shown to be consistent with a bulge in the magnetopause (*Farrugia et al.*, 1987). The plasma at the centre of these FTEs, on both sides of the magnetopause, are shown to contain a mixture of magnetospheric and magnetosheath-like plasma populations (*Thompson et al.*, 1987), consistent with the hypothesis that they are newly reconnected field lines. Figure 2.19c predicts the ionospheric signatures of such a magnetospheric configuration, as viewed looking down on the northern hemisphere, which was first postulated by *Goertz et al.* [1985] and *Southwood* [1985; 1987]. The circular footprint of the newly-reconnected flux tube moves anti-sunward as the field line evolves away from the reconnection site under magnetic tension and magnetosheath flow. As this footprint is moving faster than the background flow, it will excite plasma flow in the direction of the arrows, thus producing field aligned currents into and out of the ionosphere at the edges of the event. Many attempts have been made to identify this sort of ionospheric signature (*Goertz et al.*, 1985; *Todd et al.*, 1986) but have been inconclusive, and better explained by one of the following models.

To conclude, then, the fossil flux tube model invokes patchy, time-dependent reconnection, which results in newly-opened flux tubes being dragged across an in-situ spacecraft. The

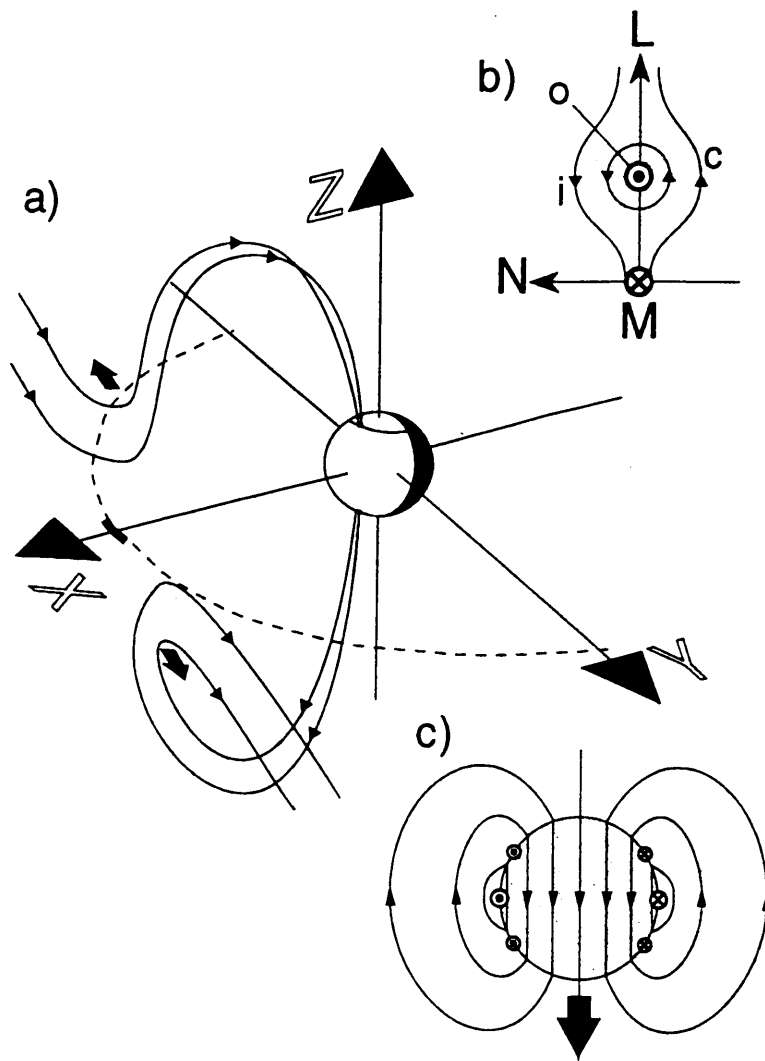


FIGURE 2.19: The fossil flux tube model of flux transfer. (a) shows a view of the magnetosphere from mid-latitude and -afternoon in GSM coordinates, with the dashed line denoting the low-latitude magnetopause, with a short ($\sim 1R_E$) X line (solid line). (b) shows a cross-section of the magnetopause in boundary normal LMN coordinates, where *i* denotes the magnetosheath, *c* the closed terrestrial field lines, which are draped over the twisted open field lines (*o*) of the flux tube. (c) is a view looking down on the Earth's ionosphere (with the top representing the sunward direction), with the predicted flow lines (arrows) and field aligned current structure (dots and crosses denoting directions out of and into the page respectively) that this model infers (taken from *Lockwood and Hapgood, 1998*).

spacecraft does not measure reconnection but rather that the spacecraft is observing reconnected flux tubes as they are contracting under field tension and are dragged anti-sunwards across it. It is by definition a 3-D model, and explains many features of flux transfer, from magnetopause FTEs, their occurrences, and several ionospheric signatures of flux transfer.

2.5.2 Two-Dimensional (2-D) reconnection pulse model

The 2-D reconnection model first envisaged by *Saunders* [1983], pursued by *Southwood et al.* [1988] and simulated through MHD by *Scholer* [1988a,b; 1989] is similar to the fossil flux tube model. However, there are significant differences insofar as this model explains the bulge in the magnetopause as a pulse of enhanced reconnection at an X line of unspecified length. Figure 2.20 illustrates this model in the same format as Figure 2.19. The longitudinally extended reconnection X line allows no M component to the FTE. An M component has been added to Figure 2.20a, which produces a twisting of the flux tubes (*Southwood et al.*, 1988). The satellite will only see those flux tubes that were reconnected at one point of the reconnection line unless the flow streamlines tangential to the magnetopause alters. Hence no information about the extent of the FTE or the X line can be gleaned (*Newell and Sibeck*, 1993), and so the transpolar voltage cannot have much added to it by FTEs. *Lockwood et al.* [1995] surmised that if these events are not longitudinally extensive, then there must be many events simultaneously occurring at different local times to explain the occurrence statistics over such a wide range of local times.

Figure 2.20c portrays the ionospheric signatures that this model predicts (*Cowley et al.*, 1991b; *Lockwood*, 1994). Essentially, this is the same pattern as the fossil flux tube model predicts, but with the facility to now incorporate a longitudinally extended event, and also allows evolution of the shape of the newly opened flux as it is appended to the geomagnetic tail. Successive reconnection pulses can also be appended to each other in an adjoining location, thus producing a series of discontinuous step-like features so commonly observed in the cusp region, and discussed in Section 2.4.

Figure 2.20d is a simplified schematic of the *Southwood et al.* (1988)/*Scholer* (1988) FTE production model (taken from *Lockwood and Wild*, 1993) in 2-D in the noon-midnight meridian in which reconnection occurs in a burst-like fashion. X denotes the longitudinally extended reconnection line at the dayside magnetopause. When reconnection ceases at this

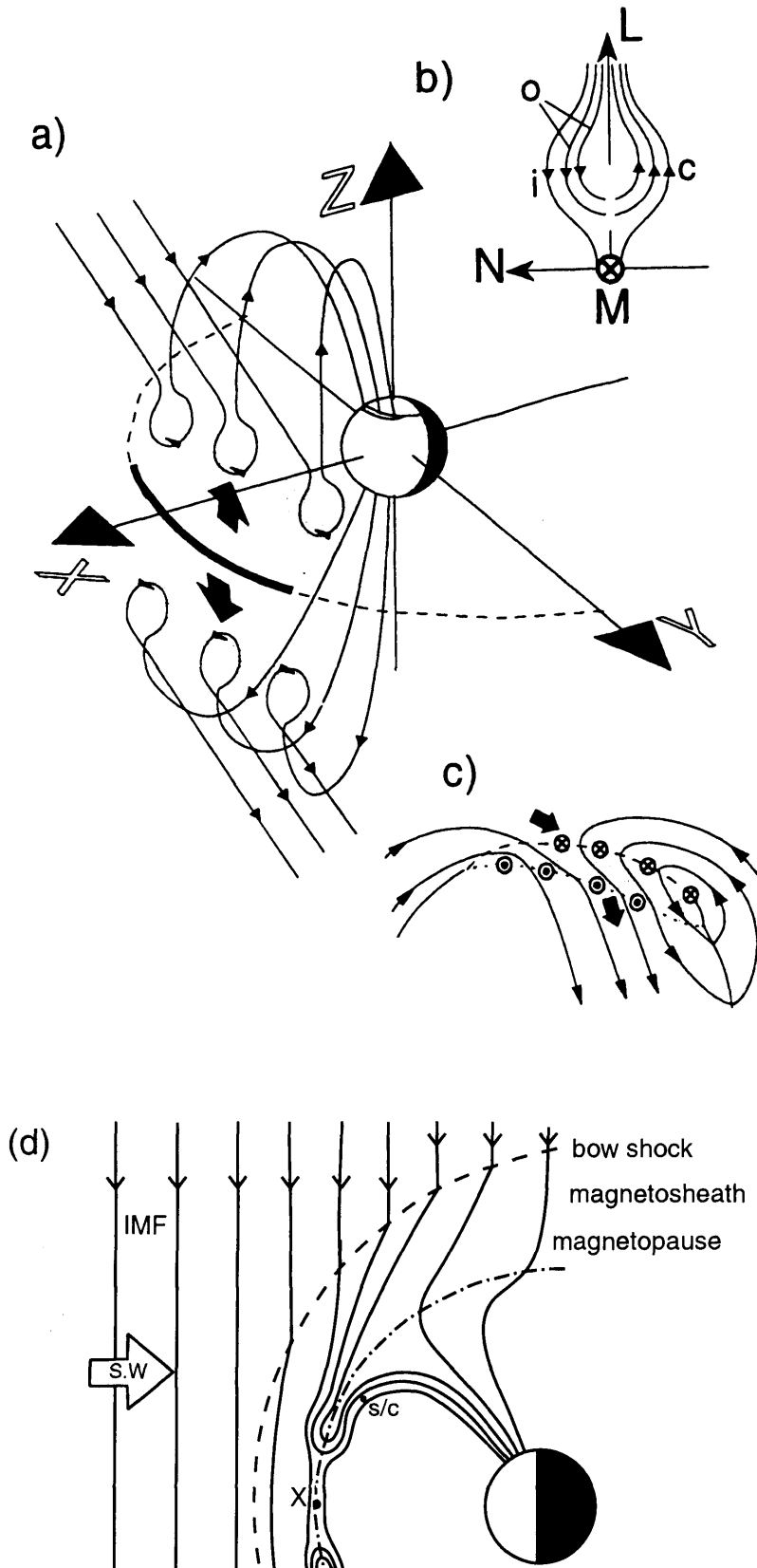


FIGURE 2.20: The 2-D reconnection pulse model, as in the same format as Figure 2.19. The longitudinal extent of the X line or the FTE is unspecified. Figure 2.20d shows the noon-midnight cross-section through the reconnection region. A spacecraft situated at s/c would see the flux tube sweep over it and record the characteristic bipolar B_N magnetic field signature.

location, the individual flux tubes are 'pinched', and move over the magnetopause surface, carrying plasma of a mixed magnetosheath and magnetospheric origin. It is these plasma 'bubbles' that are termed FTEs, and which give the characteristic bipolar magnetic signature as the field lines convect over the spacecraft, *s/c*. In this way, particle signatures in the cusp region are modulated by the bursts of reconnection taking place at the low-latitude magnetopause.

In the 2-D Reconnection Pulse Model, the draped field lines can map back to an active X line, whereas the fossil flux tube model cannot. This can be invoked to explain counterstreaming of electrons on the borders of the FTE (*Scholer et al.*, 1992; *Southwood et al.*, 1988). In many ways, this model is an improved version of the fossil flux tube model, and can thus reproduce and explain many more features of the signatures of transient reconnection.

2.5.3 Multiple X line model

Lee and Fu [1985] proposed the multiple X line model as illustrated in Figure 2.21. Multiple reconnection sites are linked by twisted field lines, which, like previous models, can explain the dependence on IMF B_z , and the mixture of magnetosheath and magnetospheric plasma inside an FTE. It cannot, however, explain the accelerated plasma signatures on the trailing edge of the FTE, which has to occur if the field lines evolve away from the reconnection site (*Ma et al.*, 1994). In addition to this, if the characteristic B_N bipolar signature were to be observed then both the reconnection lines and the bulges between them (Figure 2.21b) must evolve anti-sunward. This in turn would not give the isolated B_N signature so commonly observed (*Lockwood and Wild*, 1993; *Kuo et al.*, 1995), but would give a continuous sequence of B_N oscillations (e.g. *Elphic and Southwood*, 1987; *Elphic et al.*, 1990). It is clear, therefore, that some events can be described in terms of a multiple X line scenario, but the majority of reported observations cannot.

Figure 2.21c is the interpretation of *Lee* (1986), where the twisted field lines produce a coaxial field aligned current structure. An untwisting flux tube moving over a ground station is envisaged to produce a combination of Figures 2.19 and 2.20 (*Lockwood et al.*, 1990). Ground-based observations of such a current structure are usually attributed to part of a travelling convection vortex (TCV) structure as discussed in Section 2.5.4. However, dayside

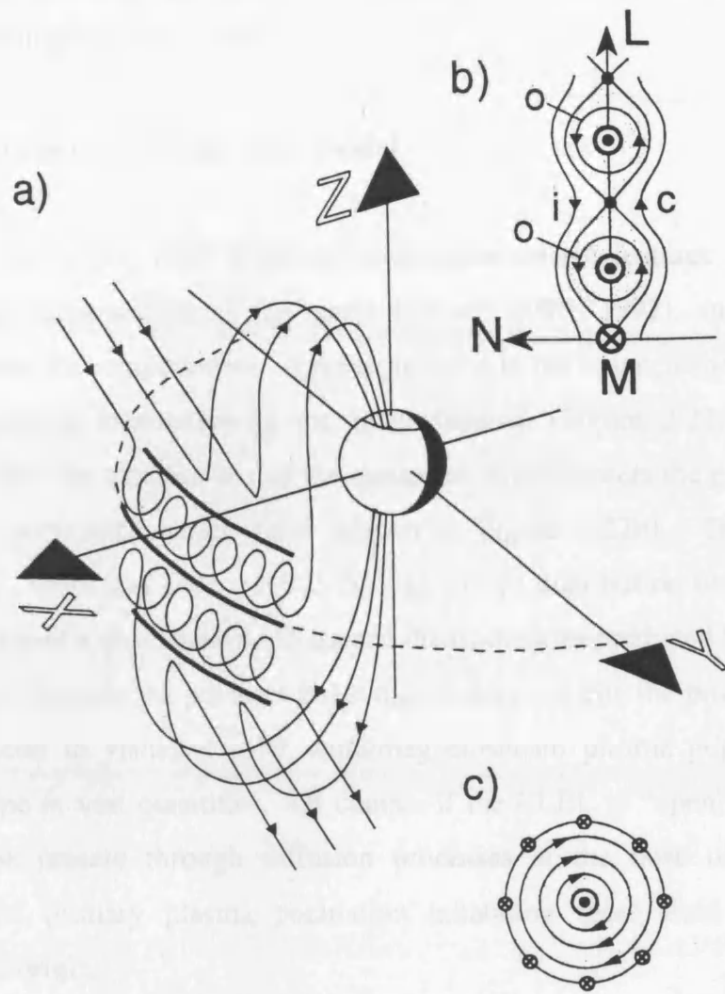


FIGURE 2.21: The multiple X line model, shown in the same format as Figure 2.19 (taken from *Lockwood and Hapgood, 1998*).

2.5 Discussion and Summary

This chapter discusses the magnetospheric structure for a coronal configuration such as that described above. A pair of field-aligned current channels and associated IMF and ICV structures are presented, where the former (ICV) structure is in the form of a pair of current sheets. The latter structure is in the form of a pair of current sheets. The latter structure is in the form of a pair of current sheets. The latter structure is in the form of a pair of current sheets.

auroral transient brightenings have been reported by *Fasel et al.* [1993] as a possible signature of a multiple X line scenario.

2.5.4 Magnetosheath pressure pulse model

An alternative model has been proposed to describe certain features of FTEs that do not invoke transient reconnection as the cause (*Sibeck*, 1990; 1992), and must therefore be discussed in order for completeness. A pressure pulse in the magnetosheath was envisaged to produce a travelling indentation in the magnetopause (Figure 2.22a). This moves the magnetopause over the satellite so that the spacecraft briefly enters the plasma depletion layer (PDL), during northward sheath field (shown in Figure 2.22b). This is not borne out observationally (*Smith and Owen*, 1992) through in situ distribution function measurements. These authors found a characteristic D-shaped distribution as predicted by *Cowley* [1982] for an open LLBL. Because the pressure pulse model does not cite the process of reconnection, then it is difficult to visualise solar wind/magnetosheath plasma populations in the flux transfer envelope in vast quantities. Of course, if the LLBL is “open” then magnetosheath plasma may be present through diffusion processes at the nose of the magnetopause, nevertheless the primary plasma population inhabiting these field lines would be of magnetospheric origin.

Figure 2.22c shows the predicted ionospheric signature for a pressure pulse event such as that described above. A pair of field aligned currents (*Kivelson and Southwood*, 1991) produce a pair of travelling convection vortices (TCVs), though how is a matter of contention. *Kivelson and Southwood* [1991] suggest that the TCV is created due to a simple change in magnetopause position, whereas *Glaßmeier* [1992] envisages an in-out (or vice versa) motion of the magnetopause. Both, however, agree on the signature of the TCV.

2.6 Discussion and Summary

This chapter discusses the processes in which solar wind plasma can and does enter the magnetosphere-ionosphere system. Firstly, the process of magnetic reconnection was examined, and then its variable and transient nature discussed. Secondly the observational evidence at various locations reviewed; from spacecraft measurements at or near the magnetopause, to mid- and low-altitude measurements of reconnection in the polar cusp, to

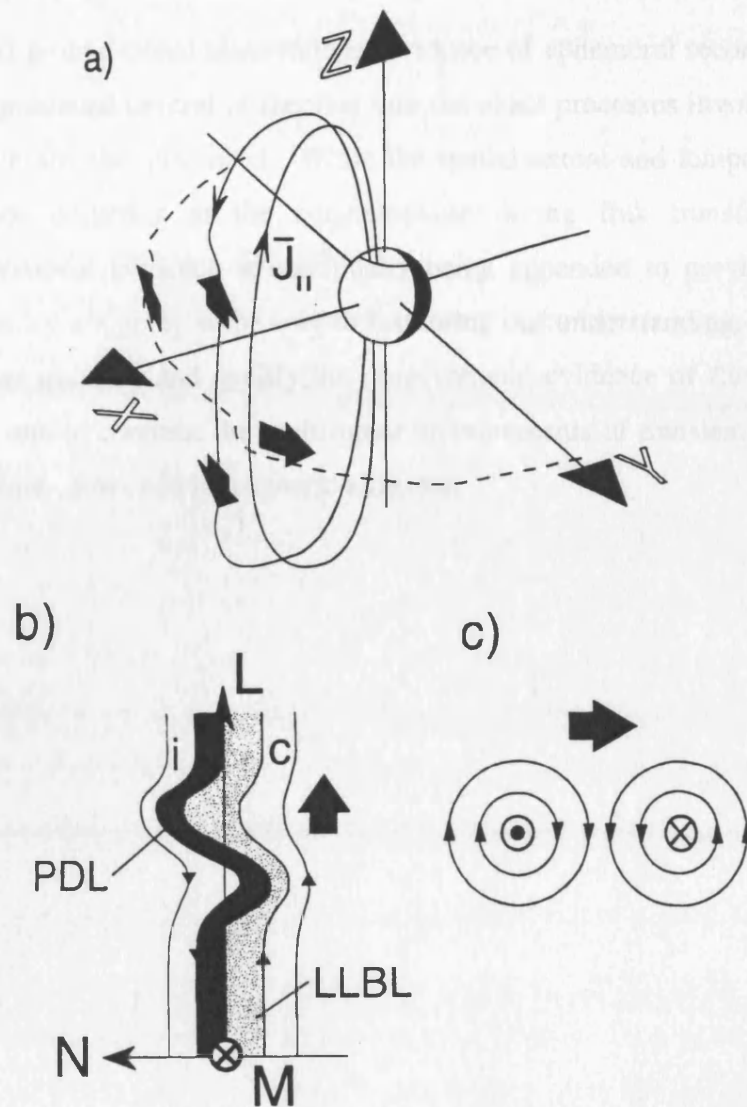


FIGURE 2.22: The magnetosheath pressure pulse model, shown in the same format as Figure 2.19 (taken from *Lockwood and Hapgood, 1998*).

the ionospheric and ground-based observational evidence of ephemeral reconnection. These observations then produced several of theories into the exact processes involved in transient reconnection, which are also discussed. While the spatial extent and temporal variation of reconnection pulses occurring at the magnetopause during flux transfer is not fully understood, observational evidence is continually being appended to previous knowledge, and advances in theory are going some way to furthering our understanding. It is the aim of this thesis to further quantify and qualify the observational evidence of flux transfer in the published domain, and to continue the multi-point measurements of transient reconnection in the cusp region at mid-, low- and ionospheric altitudes.

CHAPTER 3

Instrumentation

3.1 Introduction

When embarking on a study such as this, one must consider carefully the merits of probing the region of interest by various methods and with various instruments. It is the intention of this chapter to review the main methods of probing the polar cusps with a variety of complimentary instrumentation in an attempt to further understanding of the solar wind-magnetosphere-ionosphere coupling process. During the process of this investigation, there has always been one overriding question; are the features being observed spatial structures, or temporal ones – the so-called spatial/temporal problem. For example, if a single spacecraft flies through a region of interest, then it is difficult to ascertain if the region of interest is there permanently (i.e. a spatial structure) or there for a fleeting time (i.e. a temporal structure). Conversely, ground-based instrumentation is at a fixed point on the ground, rotating with the Earth, and cannot sample the variety of regions that an orbiting spacecraft can. Hence a variety of well-chosen spacecraft and ground-based instrumentation can be used to attempt to trace the solar wind plasma entry into the magnetosphere-ionosphere system.

3.2 The Polar spacecraft

The Polar spacecraft was developed under the auspices of NASA's Global Geospace Science (GGS) mission (*Acuña et al.*, 1995). Polar was the second component of this programme, with the Wind spacecraft being the first (see Section 3.3), although the intention was to launch these two satellites concurrently. Figure 3.1 shows the spacecraft pre-launch to give a perspective on how large Polar is. An artist's impression of Polar is displayed in Figure 3.2 with the locations of the instruments included. Polar was launched at precisely 06:23:59.997 EST on February 24th, 1996 from Space Launch Complex 2 at Vandenberg Air Force Base, shown in Figure 3.3. Launched into an elliptical orbit of $\sim 1.8 \times 9 R_E$, Polar's apogee was

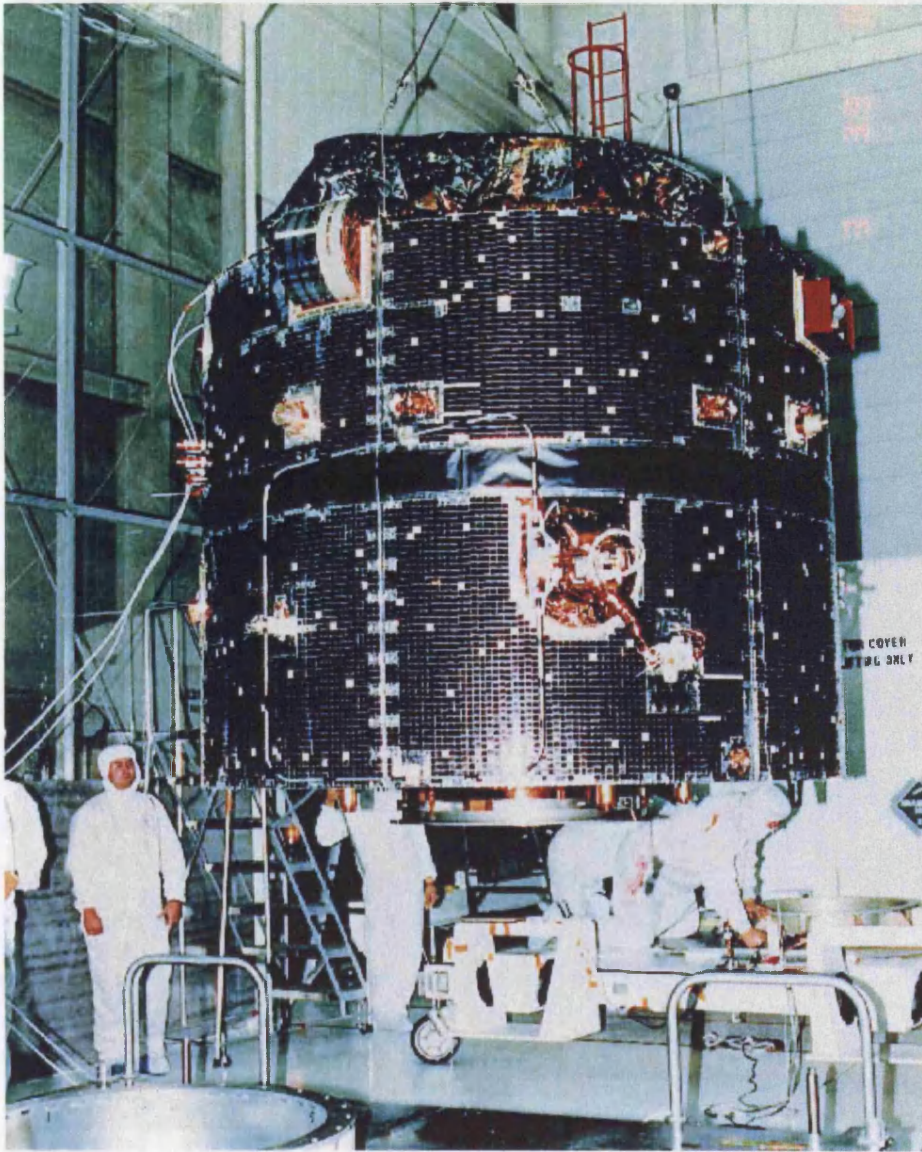


FIGURE 3.1: An early version of the Polar spacecraft, with the main instrument suite installed.

FIGURE 3.1: The Polar spacecraft in its final testing stages pre-launch at Vandenberg Air Force Base.

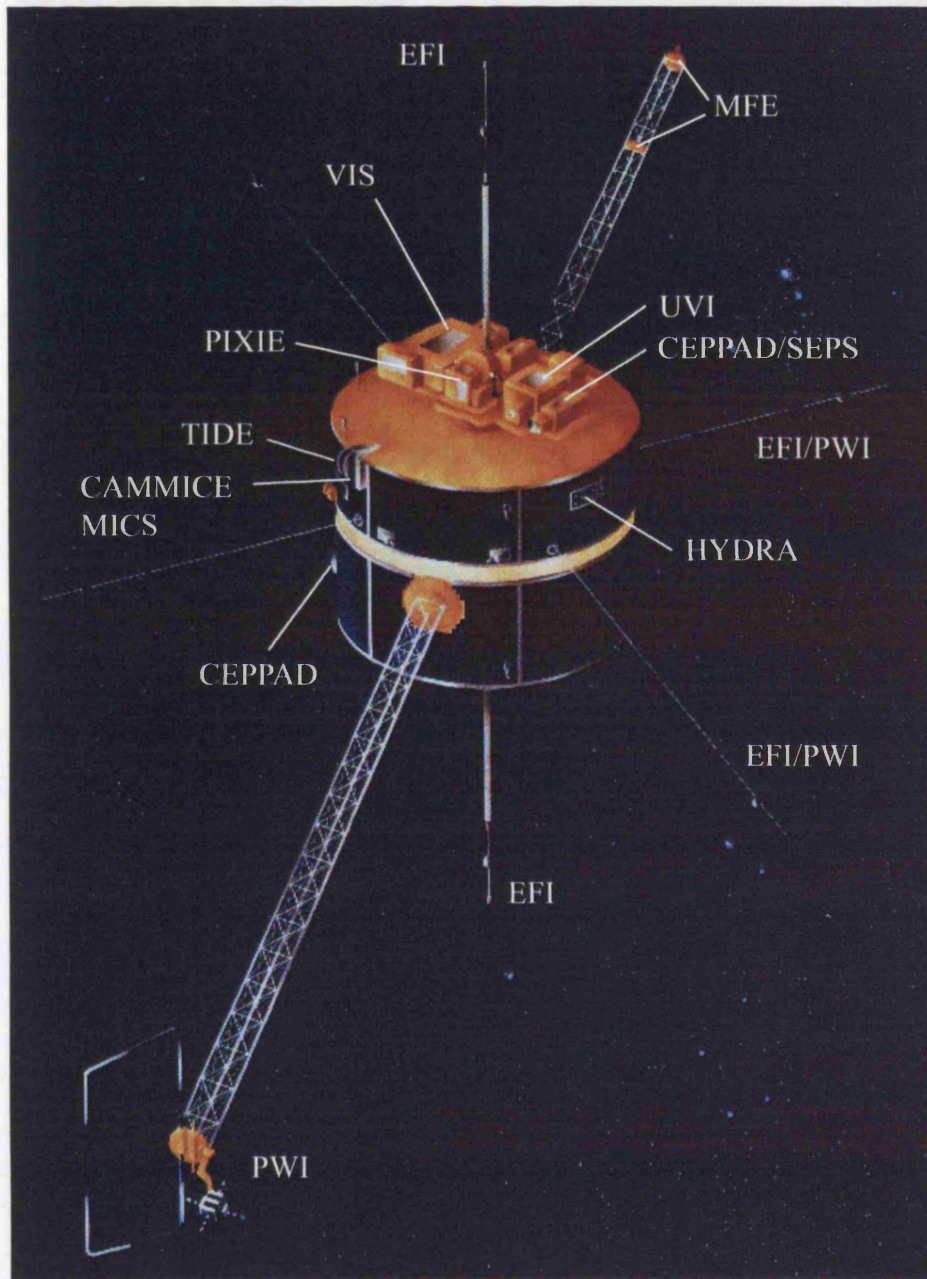


FIGURE 3.2: An artist's impression of the Polar spacecraft, with the main instrumentation labelled.

FIGURE 3.3: The launch of the Polar spacecraft from Vandenberg Air Force Base mounted upon the Delta 235, a 1925 Delta II launch vehicle, launched at precisely 06:23:49.997 EST on February 24th, 1996 from Space Launch Complex 2.



FIGURE 3.3: The launch of the Polar spacecraft from Vandenberg Air Force Base mounted upon the to Delta 233, a 7925 Delta II launch vehicle, launched at precisely 06:23:59.997 EST on February 24th, 1996 from Space Launch Complex 2 .

initially situated over the North Pole, but has been steadily advancing towards the equator at $\sim 15^\circ$ per year. Figure 3.4a depicts the Polar orbit and variation with each passing year. As the Earth orbits the Sun, the spacecraft orbit varies with respect to the Sun. Thus, as Figure 3.4b illustrates, during spring the spacecraft passes up through the dayside and down through the nightside, and in autumn this is reversed as the spacecraft passes up through the nightside and down through the dayside of the Earth's magnetosphere. This presents a slightly different view of the dayside cusps depending on season, though Polar is travelling slowly during this section of its orbit and so will effectively be quasi-stationary for long periods of time throughout this region. In the following sections, the instruments of choice to study the cusp are detailed. Note that the energy ranges of the instruments are such that the three chosen instruments effectively sit on top of each other and overlap to a degree. This effectively creates a single instrument (of differing energy and temporal resolution admittedly) with a huge energy range, 1 eV – 1MeV, which permits the tracing of features throughout this energy range.

3.2.1 The Charge and Mass Magnetospheric Ion Composition Experiment (CAMMICE)

CAMMICE consists of two sensor systems, the Heavy Ion Telescope (HIT), and MICS, the Magnetospheric Ion Composition Sensor, designed to measure the charge and mass composition of ions contained within the magnetospheric plasma over the energy range ~ 1 keV/Q to 60 MeV/Q. Unfortunately, in July 1997, the high energy element of CAMMICE, the HIT sensor, failed and so this thesis will concentrate on the MICS sensor array, which measures ion composition in the ~ 1 -425 keV/Q range. This instrument is based upon a similar instrument on the CRRES spacecraft (*Wilken et al.*, 1992). A photograph of MICS onboard Polar is shown in Figure 3.5.

A schematic of the MICS detector assembly is shown in Figure 3.6. The opening of the Electrostatic Analyser (ESA) is an annulus of inner radius 74.5mm, with an outer radius of 77.5 mm. Prior to entering the deflecting plate gap the incident ions are collimated to reduce scattering inside the ESA and to suppress particles with oblique trajectories. The collimator half-angle is 2.2° , and the aperture $0.07 \text{ cm}^2 \text{ sr}$. This method gives an excellent means to fully and accurately characterise the particle's incident direction and hence its pitch angle (PA). The addition of an ESA, which accepts only particles with a defined energy per charge E/Q ratio, allows the determination of the ionic charge Q. To improve sensitivity and charge

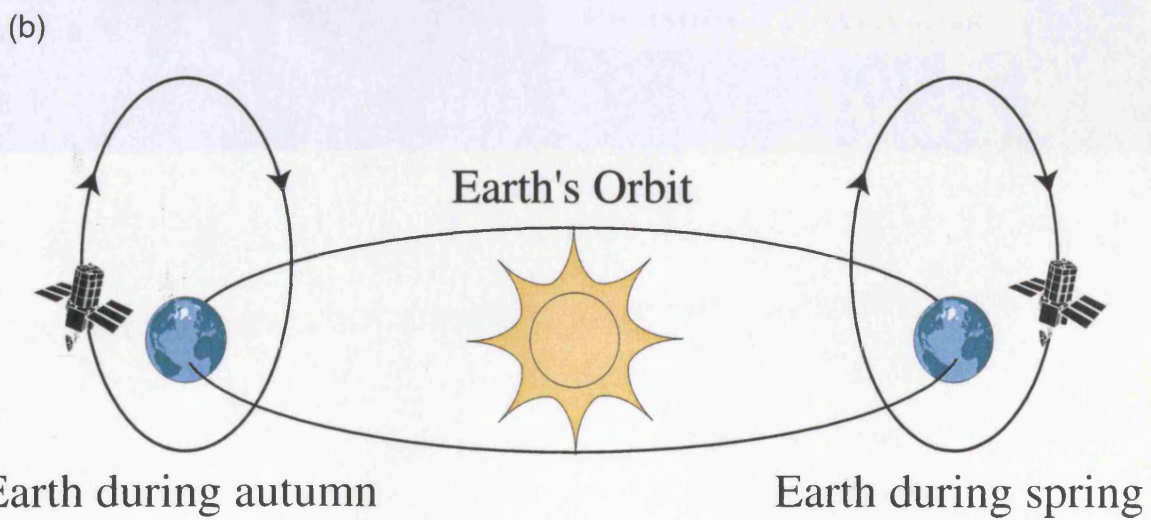
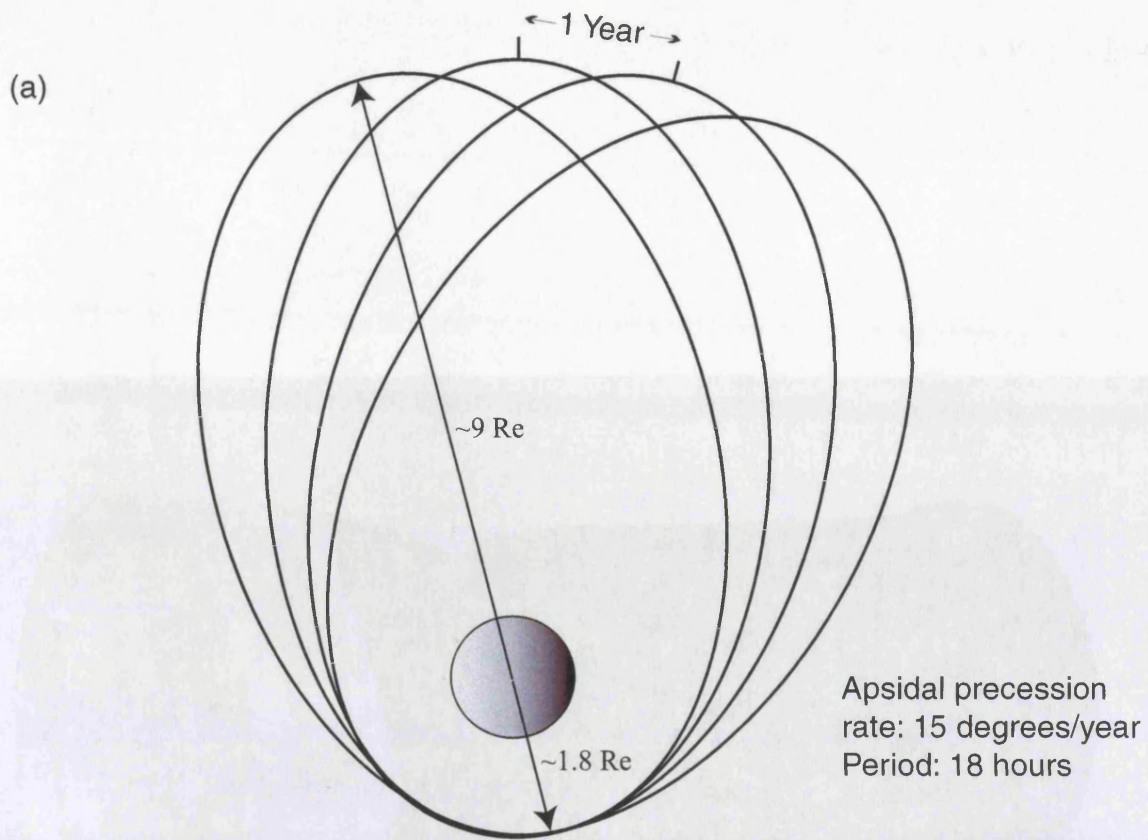


FIGURE 3.4: Schematic representation of the Polar orbit. (a) showing the precession and period (b) showing the seasonal variation with respect to the Sun.

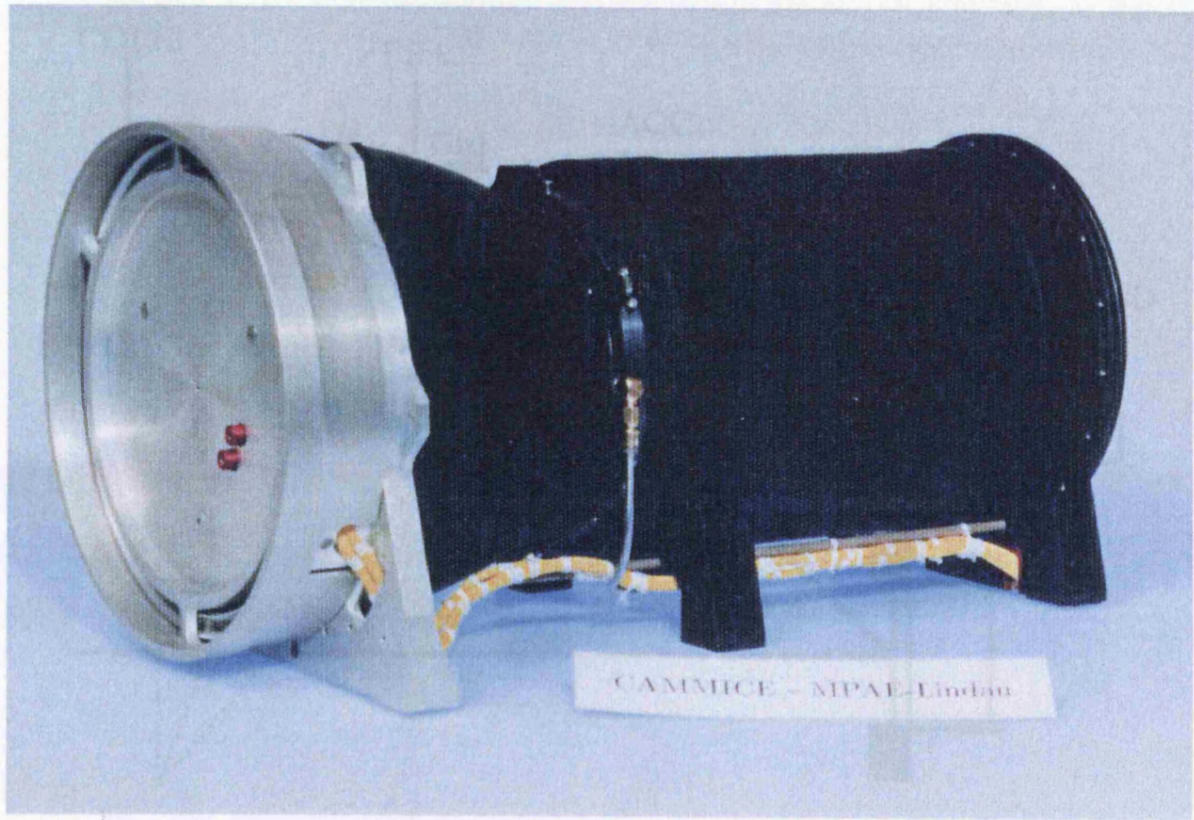


FIGURE 3.5: Photograph of the CAMMICE MICS detector assembly pre-launch.

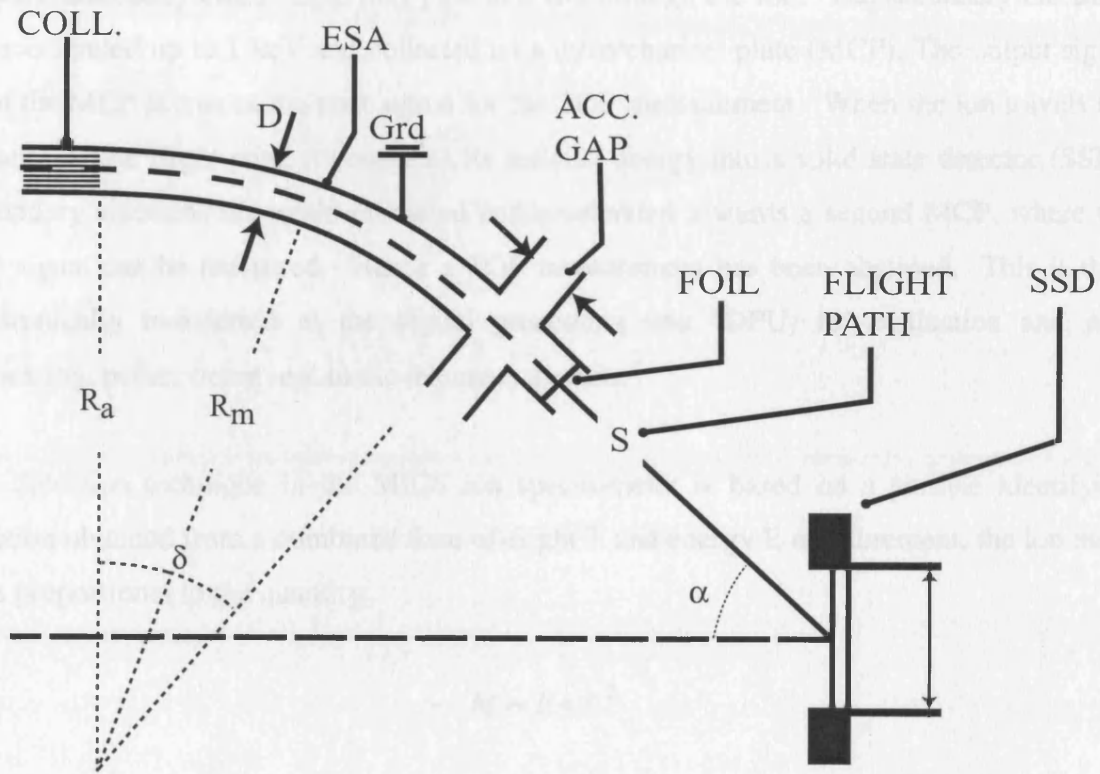


FIGURE 3.6: Schematic of the MICS analyser/detector assembly [from *Wilken et al.*, 1992].

resolution of the instrument at low particle energies, a post-accelerating voltage U is applied between the ESA and the detector system. The detected particle energy E is then $E = E_0 + UQ = Q [(E_0/Q) + U]$ with E_0 denoting the incident particle energy.

Ions now enter the time-of-flight (TOF) part of the instrument. Entry to this part of the instrument is shielded by a $\sim 5\mu\text{g}/\text{cm}^2$ carbon foil. Incident ions with sufficient energy produce secondary electrons as they pass into and through the foil. The secondary electrons are accelerated up to 1 keV and collected on a microchannel plate (MCP). The output signal from the MCP serves as the start signal for the TOF measurement. When the ion travels the distance S , the flight path, it dissipates its residual energy into a solid state detector (SSD). Secondary electrons are again produced and accelerated towards a second MCP, where the stop signal can be measured. Hence a TOF measurement has been obtained. This is then electronically transferred to the digital processing unit (DPU) for evaluation and pre-processing, before being sent to the telemetry system.

The detection technique in the MICS ion spectrometer is based on a particle identifying function obtained from a combined time-of-flight T and energy E measurement; the ion mass M is proportional to the quantity

$$M \propto E \cdot T^2$$

As the ESA steps in multiples of E/Q , then the ionic charge can be found. Therefore, the incident ions are fully characterised in terms of mass, M , energy, E , charge, Q , and Pitch angle, PA . This procedure has a temporal resolution of 197.5 seconds in normal mode, with a PA resolution of 11° . In routine service, MICS should logarithmically sweep 32 energy levels covering 1.2-427 keV/ Q , but telemetry problems in the ESA imposed a realistic limit of 24 stepped energy levels after launch. In summary then, the CAMMICE MICS instrument provides an excellent means of tracing solar wind plasma into the magnetosphere-ionosphere system as it resolves ion species at energies appropriate to this transfer process.

3.2.2 The Hot Plasma Analyser (Hydra)

An instrument to investigate and sample the velocity space of electrons and ions between ~ 2 keV/ q and 35 keV/ q in three dimensions routinely at a temporal resolution of 0.5s (*Scudder et al.*, 1995) is Hydra. The Hydra instrument is split into five packages located at various points

around the experimental platforms of Polar, shown in Figure 3.7. These are the Data Processing Unit (DPU); two sets of Electrostatic Analysers (ESAs) called the DuoDeca Electron Spectrometer (DDEIS), and two parallel plate imaging analysers (PPAs). The DDEIS sensors, diagonally opposed, contain 12 narrow (10° FW) fields of view (defined by 127° cylindrical ESAs) to sample the electrons and ions (and photographed in Figure 3.8). The second pair of diagonally opposed sensors are the PPAs, each with a conical (30° FW) field of view. The energy selection required by the PPAs is performed by a parallel plate ESA (at a much higher angular resolution than its counterpart of the DDEIS assembly). The individual ESAs of the DDEIS unit 1 and the centre line of the PPA unit 1 are pointed downwards in the $-Z_{SC}$ direction (labelled “down” in Figure 3.7) and parallel to the spacecraft spin equator, and the ESAs of DDEIS unit 2 and the centre line of the PPA unit 2 are upwards in the $+Z_{SC}$ direction (labelled “up” in Figure 3.7) and parallel to the spacecraft spin equator. In this way, then, the instrument can sample 4π steradians each energy level. As the spacecraft rotates, a full energy-angle distribution can be obtained in the desired 0.5s. In this manner then, electron and ion fluxes are measured at a routine temporal resolution of ~ 12 s, and with a full pitch angle characterisation.

The Hydra instrument is an excellent complement to the CAMMICE MICS instrument. Sampling at a vastly superior temporal resolution, the fine-scale structure associated with flux transfer into the near-Earth environment can be resolved, in addition to Hydra providing the lower-energy complement to MICS, and thus features can be traced to lower energies.

3.2.3 The Comprehensive Energetic Particle and Pitch Angle Distribution Experiment (CEPPAD)

The CEPPAD experiment (*Blake et al.*, 1995) consists of four sensors for investigating energetic particles on the Polar spacecraft. These sensors provide 3-D proton and electron angular distributions in the energy range of ~ 20 keV to ~ 1 MeV, energetic proton and electron measurements extending to energies greater than ~ 10 MeV, high angular and time resolution in the source/loss-cone and data on energetic neutral particles. All sensors operate in conjunction with special on-board data processing units that control sensor data acquisition modes while performing in-flight data processing, data compression, and telemetry formatting.

HYDRA EXPERIMENT - POLAR SPACECRAFT

Relative angular location of the boxes mounted on the experiment shelves

Boxes in this quadrant are mounted on the bottom of the bottom shelf and all detectors point down

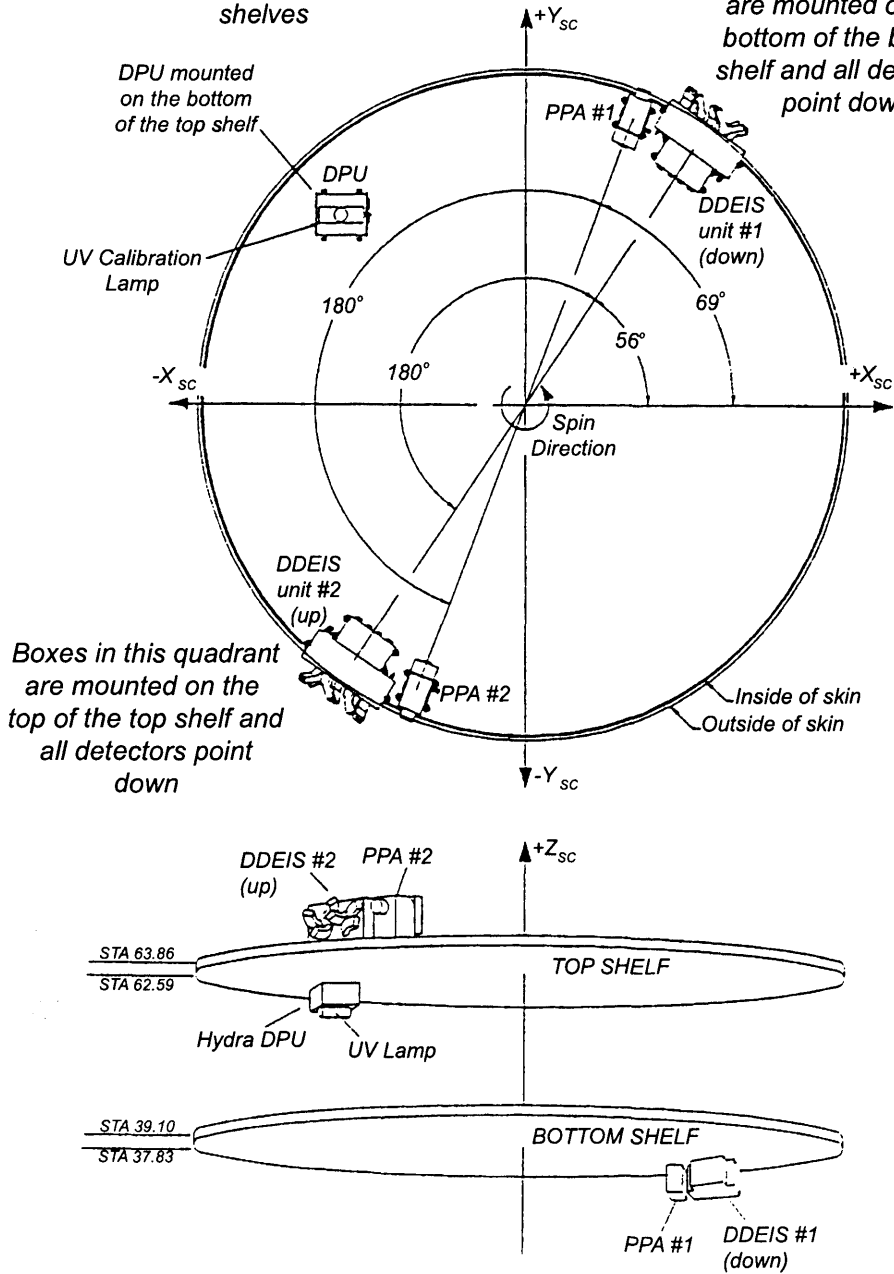


FIGURE 3.7: Shelf isometric of spacecraft equipment decks locating Hydra boxes [taken from Scudder *et al.*, 1995].

The four detectors are the Imaging Proton Sensor (IPS), the Imaging Electron Sensor (IES),

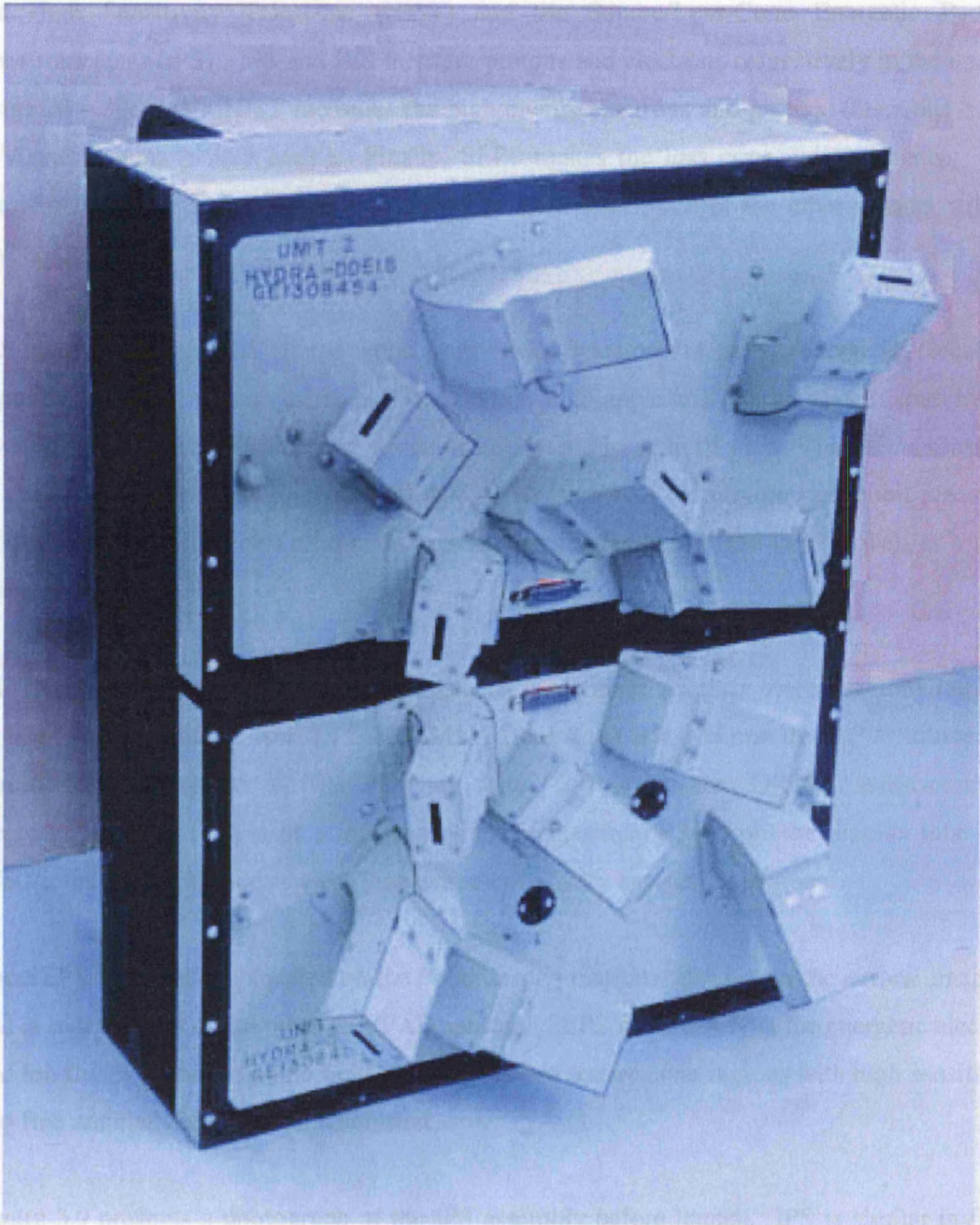


FIGURE 3.8: Photograph of the two DDEIS detector assemblies before launch.

The large pixels marked 0, 2 and 4 in Figure 3.10b are sized to yield equal geometric factors for particles incident through the collector assembly. Pixel 1 monitors penetrating radiation and pixel 3

The four detectors are the Imaging Proton Sensor (IPS), the Imaging Electron Sensor (IES), the High Sensitivity Telescope (HIST) and the Source/Loss-Cone Energetic Particle Spectrometer (SEPS). IPS and IES measure protons and electrons respectively in the energy range 20 – 500 keV. HIST measures the high-energy electrons and protons (electrons ≥ 350 keV and protons ≥ 3.25 MeV). Finally, SEPS makes the loss cone measurements. This thesis only makes use of IPS and so only a general description of the other sensors will be given.

IES uses ion-implanted silicon solid state strip detectors to sense energetic electrons. Simultaneous flux measurements as a function of pitch-angle and energy are achieved by the novel geometry of the IES sensor, which has a $180 \times 35^\circ$ field of view. The IES is sensitive to energetic electrons ranging from 30 keV to 500 keV. An aluminium mylar foil placed in front of each strip detector eliminates protons of energies below 350 keV as well as a light response.

HIST (located under the IES) uses three detector elements to measure electrons from 350 keV to 10 MeV and protons from 2.15 to 80 MeV. Detector A is a 300 mm thick, 300 square mm surface-barrier. Detector B is a 2000 μm thick, 200 square mm ORTEC surface-barrier. Detector C is a Bicron plastic scintillator with a Hamamatsu R3668 photomultiplier tube. The HIST attempts to provide a "clean" measurement of very energetic electrons.

The SEPS instrument is located on the Polar despun platform along with the auroral imagers, and is independent of the other CEPPAD sensors. SEPS measures both the energetic electron and ion fluxes in the magnetic field-aligned loss and source cone regions with high sensitivity and fine angular and temporal resolution.

Figure 3.9 presents a photograph of the IPS assembly before launch. IPS is similar in form and function to the IES. The IPS uses a monolithic ion-implanted solid-state detector that is discretely segmented into multiple pixels. The detector sits behind a collimation stack at the "focal plane" of a "pin-hole camera", thereby imaging a slice of phase space. Three identical heads, each with three non-overlapping look directions ($20^\circ \times 12^\circ$) provide collectively an instantaneous snapshot of a $180^\circ \times 12^\circ$ wedge of phase space. Figure 3.10 presents a schematic of one of the detector heads and the detector board assembly. The large pixels marked 0, 2 and 4 in Figure 3.10b are sized to yield equal geometric factors for particles incident through the collimator assembly. Pixel 1 monitors penetrating radiation and pixel 3

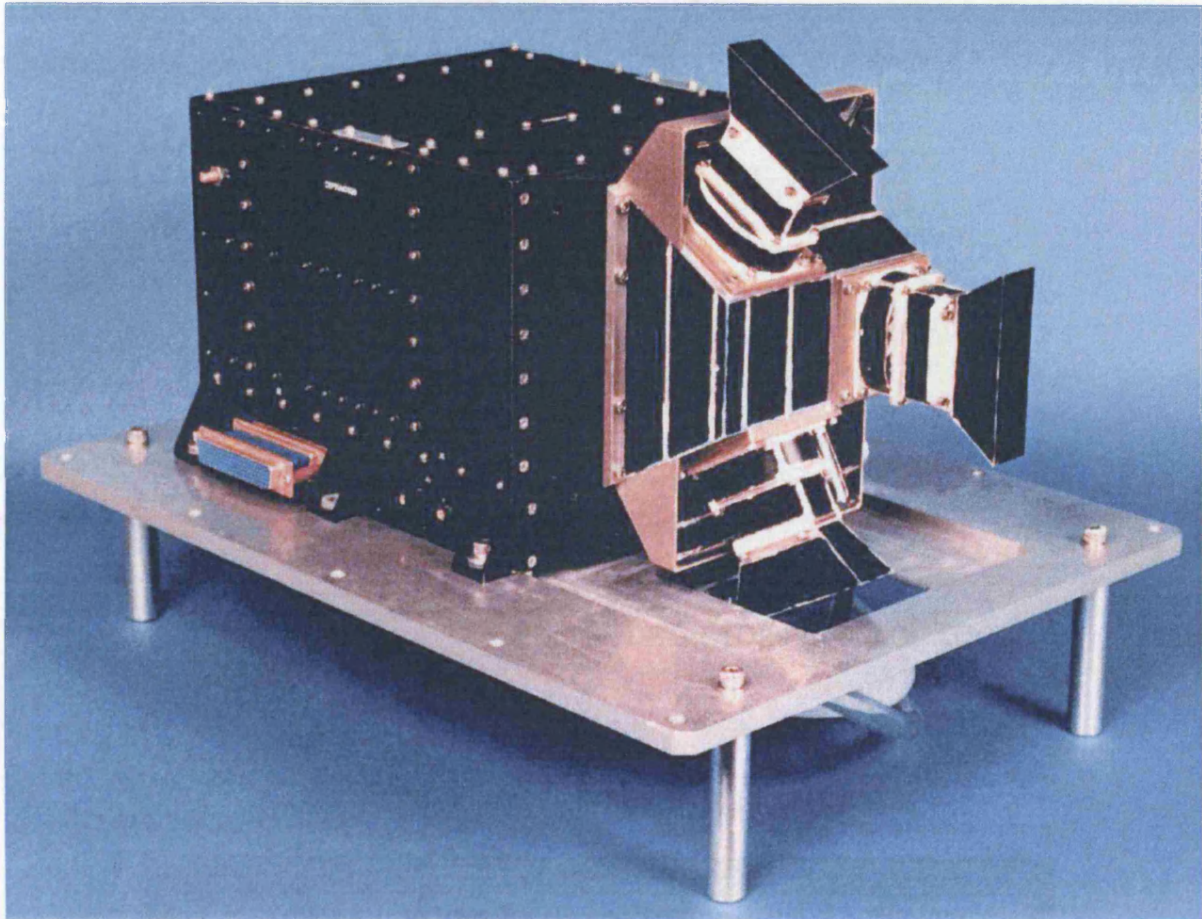
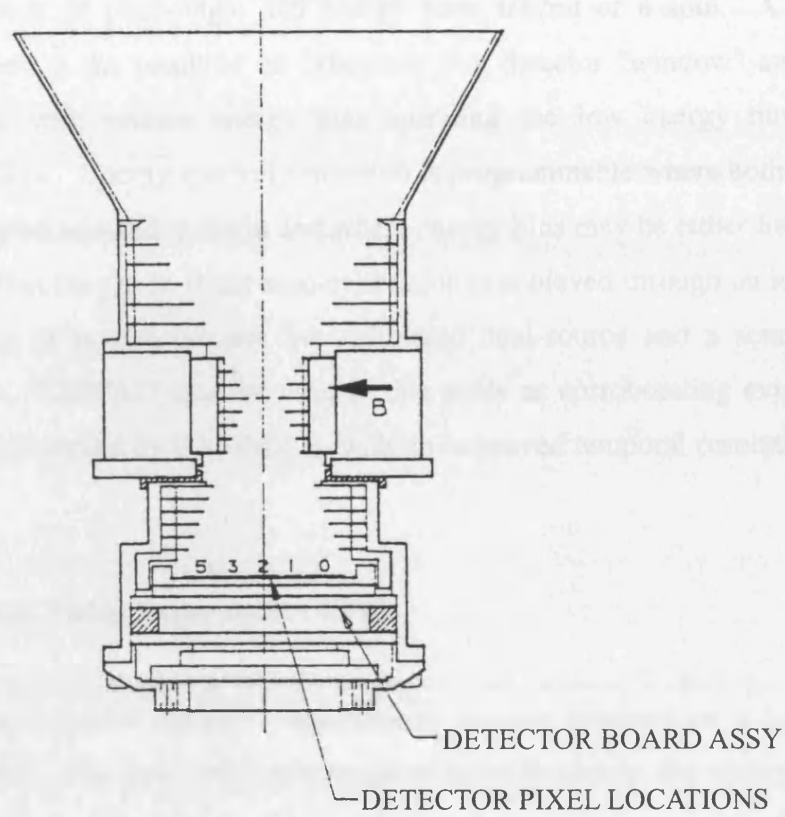


FIGURE 3.9: Photograph of the IPS detector assembly before launch. Of particular note are the three sensor heads located at the front, designed to measure incident particles of differing pitch angles.



MICRON DETECTOR SCHEMATIC LAYOUT

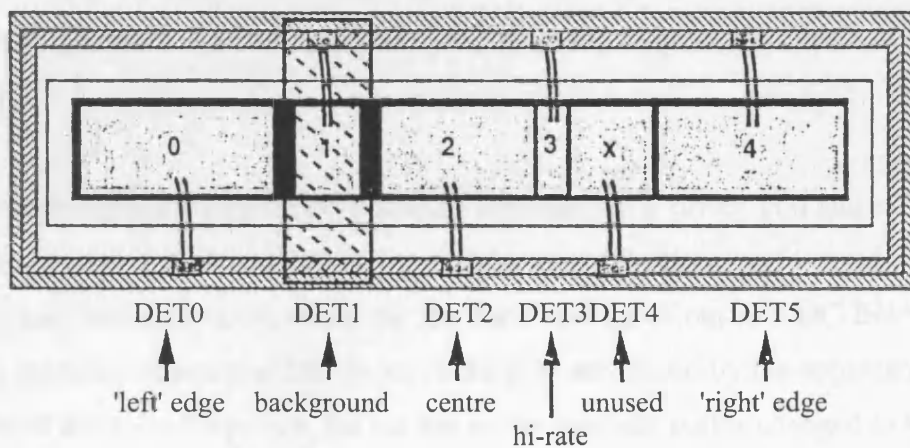


FIGURE 3.10: The IPS detector. (a) Assembly drawing showing one of the IPS heads. (b) a schematic of a single IPS detector showing the six panels surrounded by the guard ring [from *Blake et al.*, 1995].

can be used under conditions of high counting rate. As a consequence of spacecraft rotation, the IPS maps out a full 4π sr image within a single 6 s spin period. Flux measurements are obtained as a function of pitch-angle and energy each 1/32nd of a spin. A low energy threshold of ~ 12 keV is the result of an extremely thin detector "window" and low-noise support electronics, with sixteen energy bins spanning the low energy threshold to a maximum of ~ 1.5 MeV. Energy spectral resolution is programmable where both the low and high thresholds may be selected in-flight and where energy bins may be either linear or semi-logarithmic across that range. In-flight auto-calibration is achieved through an internal pulse generator consisting of both a discrete but calibrated dual-source and a semi-continuous uncalibrated source. CEPPAD data are used in this study as corroborating evidence of the region and features observed by CAMMICE, with an improved temporal resolution for more exact timing.

3.2.4 The Magnetic Fields Experiment (MFE)

MFE consists of two triaxial fluxgate magnetometer sensors mounted on a 6-metre boom (*Russell et al., 1995*). The dual configuration provides redundancy, the ability to measure different ranges of magnetic field, and also permits the accurate removal of the dipolar portion of the spacecraft's internal field. All other instruments onboard Polar were minimised with respect the internal fields they generated to 2 nT at 1m, to diminish the inaccuracies that the magnetometer is subject to. The instrument was designed to measure the vector magnetic field at the spacecraft location in three ranges: ± 700 nT, ± 5700 nT, and ± 47000 nT.

The fluxgate sensors are ring core-types; each composed of a 'driver' coil and a 'feedback' coil surrounding a ring-shaped magnetically permeable core. The drive coil is used to periodically drive the core into saturation, while the feedback coil zeros out any DC field in the core. When the presence of external 'DC' fields in the core are sensed by the appearance of second harmonics of the drive frequency, the current in the feedback coil is changed to keep the core field near zero. Three orthogonal sensors make each of the two fluxgate units. 'Flippers' can mechanically change a sensor in the spacecraft spin plane with the one along the spin axis in order to determine any zero-level offsets in the measured fields. The magnetometer is a fully redundant system with duplicate processors, analogue-digital converters, spacecraft interface electronics, power conversion circuits and two independent basic magnetometers, one

designed to measure fields up to 47,000 nT and one designed to measure fields up to 5500 nT.

3.3 The Wind spacecraft

The Wind spacecraft is very similar to Polar in many ways, barring the lack of imaging experiments onboard, and hence there was no need for a despun platform. The launch of Wind occurred at 04:31:00.057 EST on November 1st, 1994, from Launch Complex 17, Pad B at the Kennedy Space Centre in Florida (Figure 3.11). A schematic of the spacecraft is shown in Figure 3.12.

The initial orbit selected for Wind is based on a general class of orbits commonly known as “double lunar swing-by” (*Farquhar, 1991*). This is due to the fact that the gravitational attraction of the moon is used periodically to maintain the semi-major axis of the Wind orbit roughly aligned with the Earth-Sun direction during the entire mission (illustrated in Figure 3.13). The orbital pattern was selected to provide radial mapping of the interplanetary medium and the Earth’s foreshock region in the first stage of the mission, before being placed in a ‘halo’ orbit around the Lagrangian (L1) point between the Earth and the sun (*Farquhar, 1970*). This is the same orbit as employed by ESA’s SOHO spacecraft as it allows continuous monitoring of the Sun’s corona and photosphere without the periodic perturbations induced by the Earth’s rotation that ground-based observatories suffer from.

The two most commonly used instruments, and also the ones used primarily in this thesis, are the Magnetic Field Instrument (MFI) and Solar Wind Experiment (SWE), both of which will be described in the subsections below. These two instruments provide the upstream interplanetary condition monitor, which can be used to predict the time that any upstream interplanetary conditions will impinge upon, and affect the near-Earth environment.

3.3.1 The Magnetic Fields Instrument (MFI)

MFI consists is a boom-mounted dual tri-axial fluxgate magnetometer (*Lepping et al., 1995*), very similar in nature to the MFE experiment onboard Polar (see Section 3.3.3). The dual configuration again provides redundancy and also permits the accurate removal of the dipolar portion of the spacecraft’s internal field. The magnetometer is capable of measuring a wide

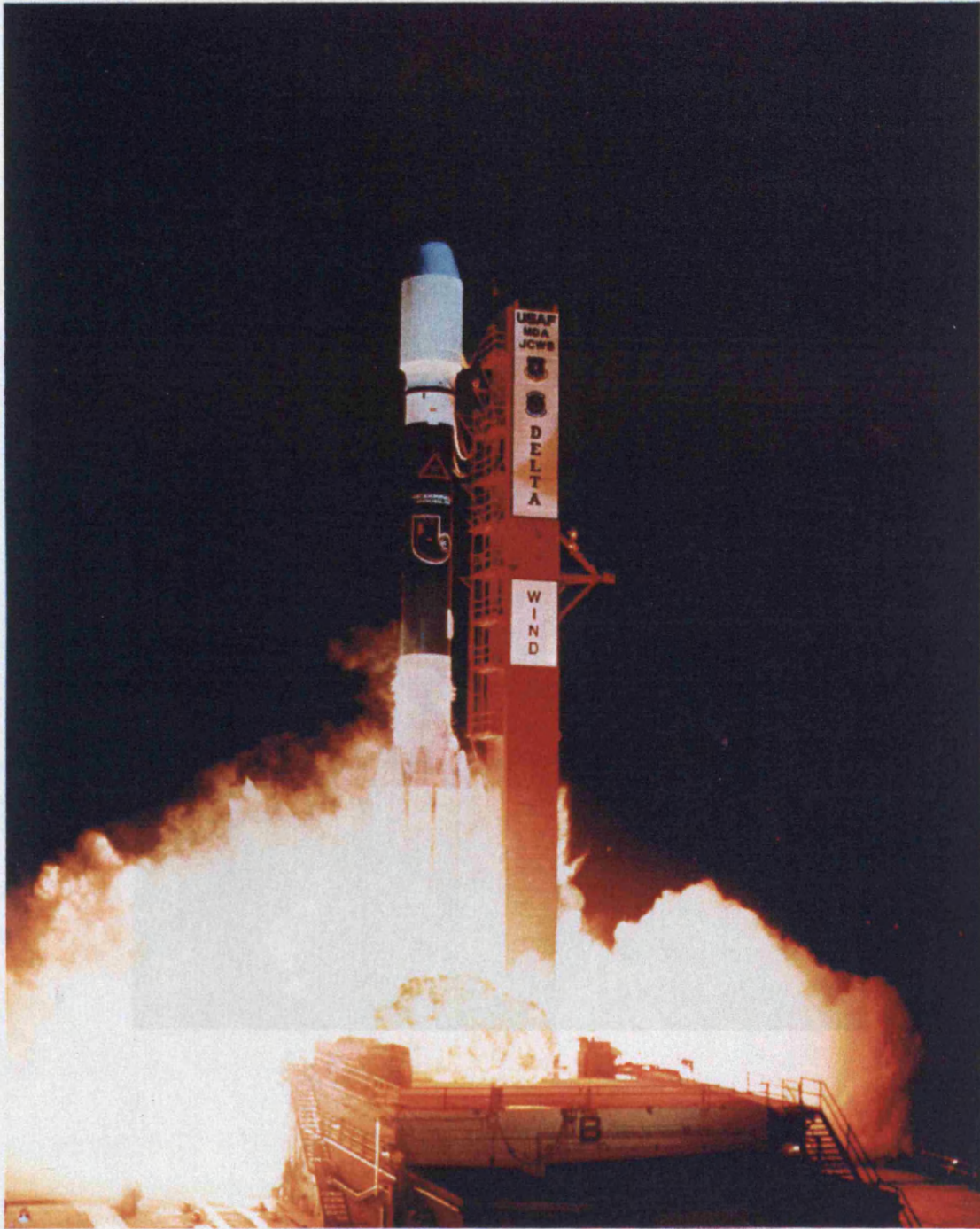


FIGURE 3.11: The launch of the Wind spacecraft. Wind was mated to Delta 227, a 7925 Delta II launch vehicle at the Kennedy Space Center in Florida. Launch occurred on-time at 04:31:00.057 EST on November 1st, 1994, from Launch Complex 17, Pad B.

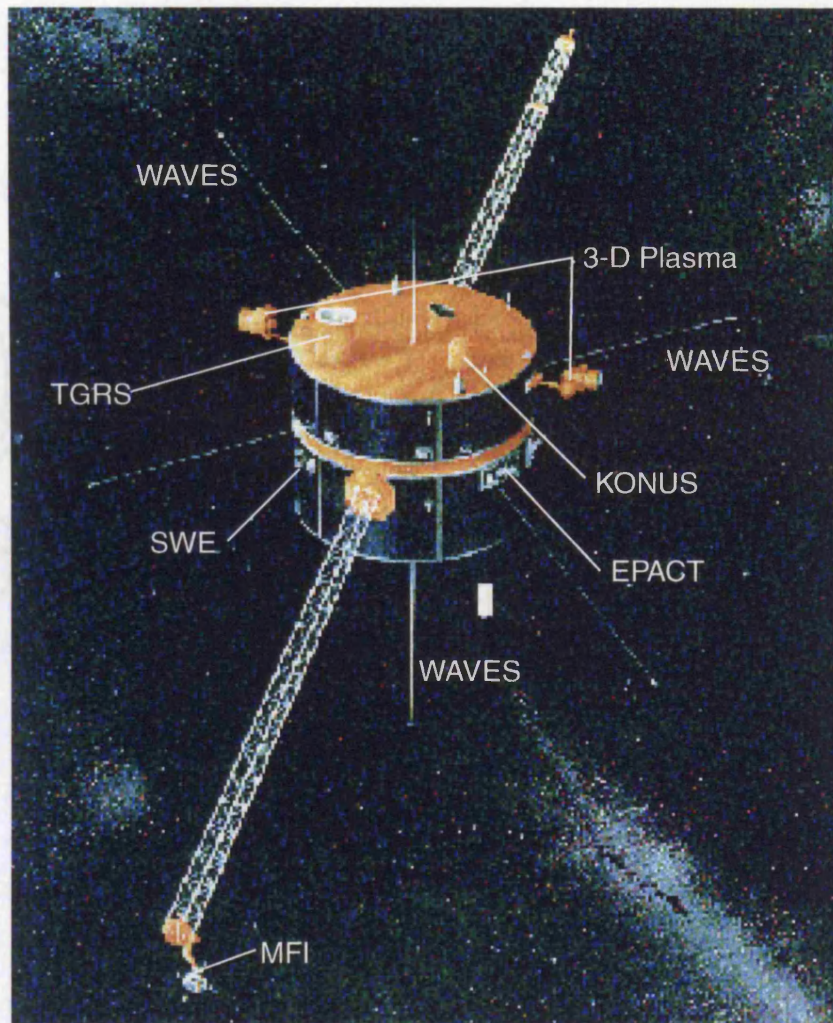


FIGURE 3.13: The selected orbit for the Wind spacecraft (taken from Acuña *et al.*, 1995). Periodic encounters with the Moon are used to maintain apogee near the Earth-Sun line, resulting in a "halo" orbit around the L1 libration point.

FIGURE 3.12: Schematic of the Wind spacecraft, with the locations of the main instruments. SUMS, a series of spectrometers, is on the far side of the spacecraft and so not shown on this diagram.

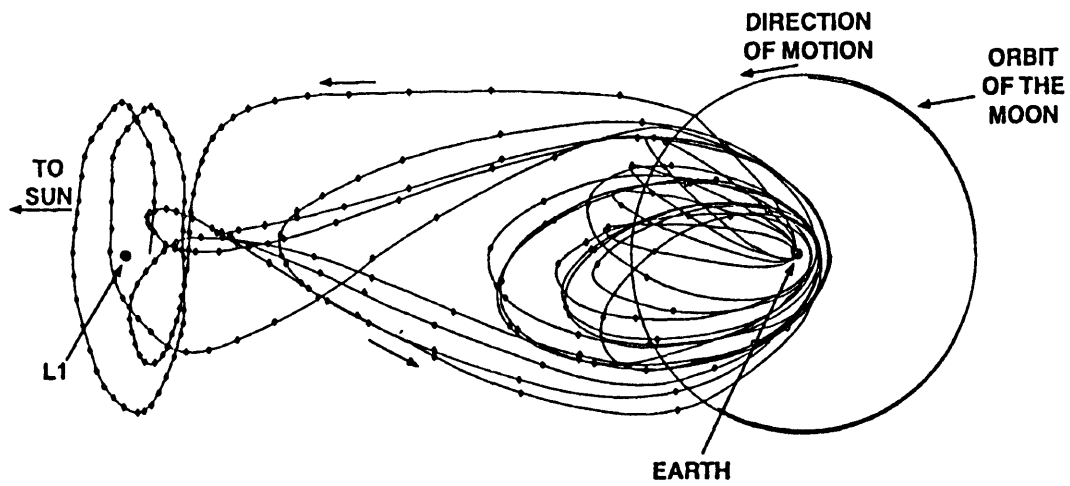


FIGURE 3.13: The selected orbit for the Wind spacecraft (taken from *Acuña et al.*, 1995). Periodic encounters with the Moon are used to maintain apogee near the Earth-Sun line, finishing in a "halo" orbit around the L1 libration point.

range of values of the ambient magnetic field, from ± 0.001 nT to $\pm 65,536$ nT. The MFI instrument provides the IMF magnitude and direction at a point upstream from the Earth.

3.3.2 The Solar Wind Experiment (SWE)

The SWE is a comprehensive, integrated set of sensors designed to determine and investigate several crucial parameters of the solar wind with respect solar-terrestrial relations (*Ogilvie et al.*, 1995). These parameters include velocity, density and temperature of the plasma, and electron and ion distributions. The instrument consists of two Faraday Cup (FC) sensors; a vector electron and ion spectrometer (VEIS); a strahl sensor, which measures the electron "strahl" (a narrow beam of electrons formed along the interplanetary magnetic field in the solar wind associated with solar coronal holes); and an on-board calibration system (*Ogilvie et al.*, 1995). The data used for this study is from the 3-dimensional measurements made by the FC system.

The FC system is used to determine distribution functions and basic flow parameters of the ion component of the solar wind. Each FC sensor consists of a cup containing a set of planar grids and two semi-circular collector plates. Figure 3.14a shows a cross-section of one sensor. The velocity distribution function of ions is measured by applying a sequence of voltages to the "modulator" grid, shown in the cross-sectional schematic in Figure 3.14b. With voltage V applied to the grid, only particles having energy/charge, E/Q , greater than V will be able to pass through the grid and continue on to strike the collector plate where they produce a measurable current. As normally operated, the grid voltage is varied between two voltages, V_1 and V_2 at a frequency of a few hundred Hz. Thus particles normally incident on the grid and having E/Q between V_1 and V_2 , will produce a current on the collector plate that varies at the modulation frequency and can easily be detected with an appropriate phase-sensitive measurement system. By choosing an increasing sequence of values for the modulation voltage, e.g. V_2 and V_3 , the E/Q spectrum of the particles can be explored, unlike that of an electrostatic analyser (ESA). The flow direction can also be determined to an accuracy of greater than 1 degree. Furthermore, the FC is ideally suited to high temporal resolution measurements, even on a spinning spacecraft such as Wind. A large (and sensitive) acceptance angle (approximated by a 60 half-angle cone, shown in Figure 3.14c), and the fact that the two FCs are pointing in opposite directions allows measurement of the solar wind 2/3 of the time. It is also particularly suitable for absolute density determinations in the supersonic solar wind since it can encompass the whole distribution and has no energy-

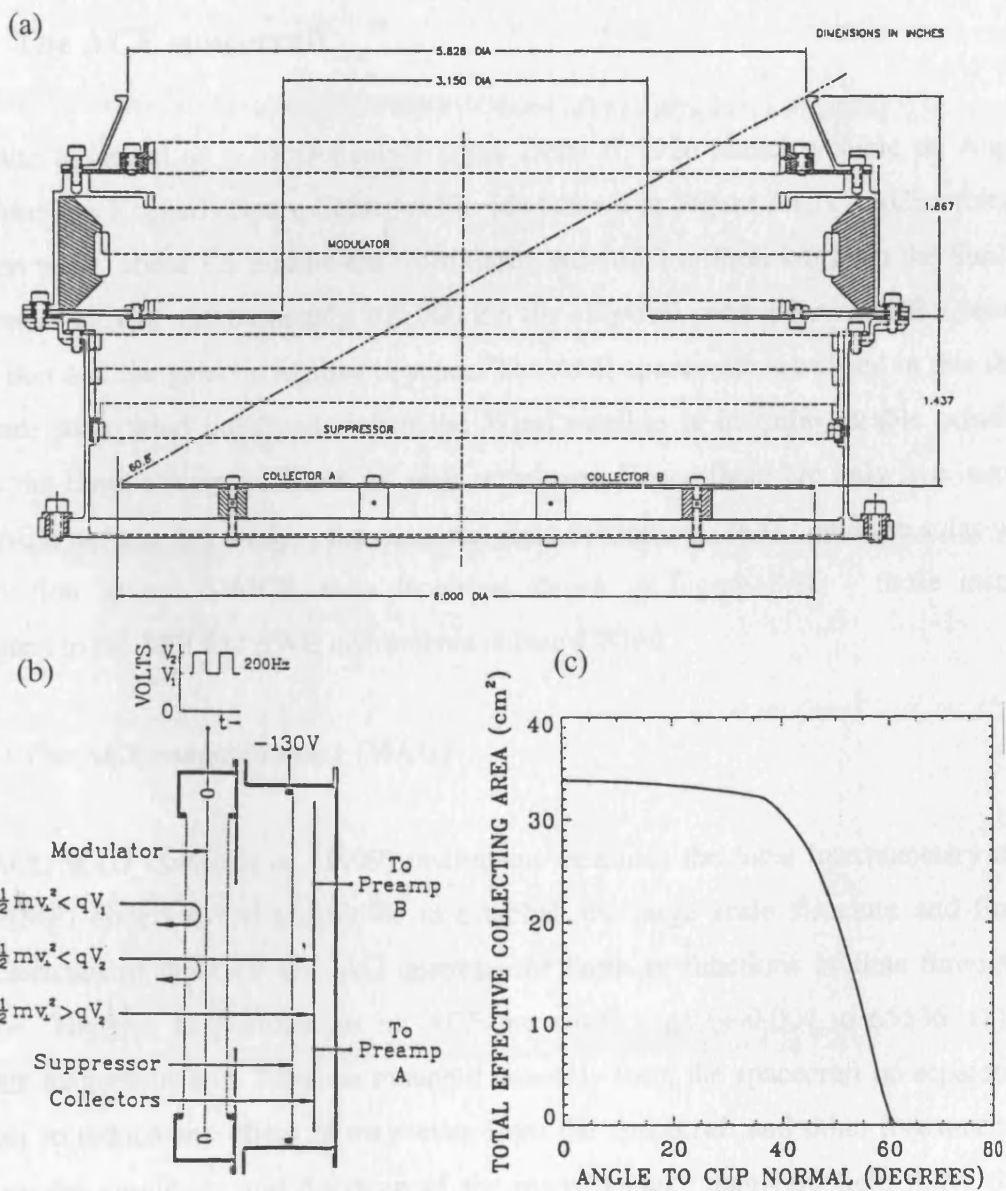


FIGURE 3.14: (a) a cross-section of a Faraday Cup sensor. (b) A schematic of the cross-section of a Faraday Cup, showing the principle of operation, and (c) the effective area of the Faraday Cup as a function of the incoming angle of a cold beam of electrons.

The Solar Wind Ion Composition Spectrometer determines the elemental and isotopic composition of the solar wind by measuring the mass-to-charge ratio of the ions.

dependent efficiency corrections. The SWE instrument provides many plasma parameters, including solar wind velocity and dynamic pressure, which is used to predict the time delay between Wind and the Earth's magnetopause, magnetosphere and ionosphere.

3.4 The ACE spacecraft

ACE was launched on a McDonnell-Douglas Delta II 7920 launch vehicle on August 25, 1997 from the Kennedy Space Center in Florida (shown in Figure 3.15). ACE orbits the L1 libration point, about 1.5 million km from Earth and 148.5 million km from the Sun. With a semi-major axis of approximately 200,000 km the elliptical orbit affords ACE a prime view of the Sun and the galactic regions beyond. The ACE spacecraft is utilised in this thesis for upstream solar wind conditions when the Wind satellite is in unfavourable positions i.e. within the Earth's magnetosheath or magnetosphere. Hence there are only two instruments from ACE used in this study – the magnetic field instrument, MAG, and the solar wind ion composition sensor, SWICS, their locations shown in Figure 3.16 – those instruments analogous to the MFI and SWE instruments onboard Wind.

3.4.1 The ACE magnetometer (MAG)

The ACE/MAG (*Smith et al.*, 1999) instrument measures the local interplanetary magnetic field (IMF) direction and magnitude to establish the large scale structure and fluctuation characteristics of the IMF at 1 AU upstream of Earth as functions of time throughout the mission. The two Magnetometers on ACE are wide-range (+0.004 to 65536 nT) triaxial fluxgate magnetometers. They are mounted remotely from the spacecraft on separate booms in order to reduce any effect of magnetics from the spacecraft and other instruments. They measure the amplitude and direction of the interplanetary magnetic field thirty times per second and can do Fast Fourier Analysis on these measurements to get the frequency spectrum of fluctuations in the magnetic field. The ACE/MAG instrument is very similar in nature to the MFE experiment onboard Polar and MFI on Wind.

3.4.2 The ACE Solar Wind Ion Composition Sensor (SWICS)

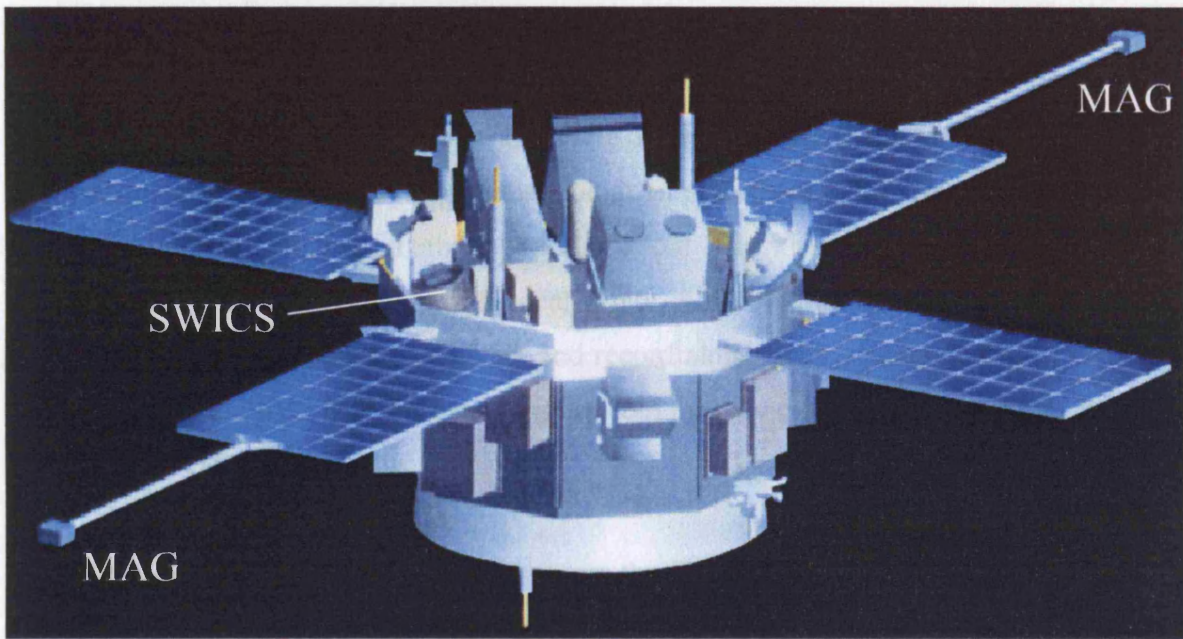
The Solar Wind Ion Composition Spectrometer determines the elemental and ion-charge composition, and the temperature and mean speeds of all major solar wind ions from



FIGURE 3.15: The launch of the ACE satellite from the Kennedy Space Center, Florida on August 25, 1997.

hydrogen through iron at solar wind speeds ranging from a minimum of 145 km/sec to 1532 km/sec. This instrument, which covers an energy-per-charge range of 0.11 keV/Q to 66.7 keV/Q in about 13 minutes, combines an electrostatic analyzer with post-acceleration, followed by time-of-flight and energy measurements, much the same as the SWE instrument onboard Wind. The active area is 0.009 CSR.

3.5 The DMSP satellite network



electrostatic analyzers that record electrons and ions between 30 eV and 30 keV as they flow past the spacecraft toward the Earth. The curved pass detectors allow precipitating electrons and ions to enter through an aperture of about 30 by 100 mm (FWHM). Electrons and ions of the selected energy are deflected toward the target by an imposed electric field applied across the two plates. The two low energy detectors consist of 10 channels centered on 34, 49, 71, 101, 130, 175, 220, 260, 370, and 960 eV. The high energy detector accepts particles in 10 channels from 10 to 29.3 keV. Each detector dwells at each channel for 0.09 seconds from high energy channel to low. A complete cycle is sampled each second. The nominal response efficiency is 50% at a value of 10% of the central energy for this channel. *Harley et al. (1984)* provides greater detail concerning these detectors. The DMSP satellite fleet provides the low-altitude link between the mid-altitude observations made by Polar, and the ground-based CUTLASS observations.

FIGURE 3.16: An artist's impression of the ACE satellite, with the locations of the magnetometer booms of MAG and the SWICS instrument marked.

hydrogen through iron at solar wind speeds ranging from a minimum of 145 km/sec to 1532 km/sec. This instrument, which covers an energy-per-charge range of 0.11 keV/Q to 66.7 keV/Q in about 13 minutes, combines an electrostatic analyzer with post-acceleration, followed by time-of-flight and energy measurements, much the same as the SWE instrument onboard Wind. The active area is 0.009 cm².

3.5 The DMSP satellite network

The Defence Meteorological Satellite Program (DMSP) is a Department of Defence (DoD) program run by the Air Force Space and Missile Systems Centre (SMC). DMSP satellites are in a near polar orbiting, sun synchronous orbit at an altitude of approximately 830 km above the earth. Each satellite has an orbital period of about 101 minutes. The space environmental sensors (SSJ/4) always point towards local zenith, which at the latitudes of interest means only precipitating particles are detected, and record along track plasma densities, velocities, composition and drifts. Electrons and ions are both measured in the range 32 eV to 30 keV in 20 logarithmically spaced steps.

The SSJ/4 instrument was designed to measure the flux of charged particles as they enter the Earth's upper atmosphere from the near-Earth space environment. It consists of four electrostatic analysers that record electrons and ions between 30 eV and 30 keV as they flow past the spacecraft toward the Earth. The curved plate detectors allow precipitating electrons and ions to enter through an aperture of about 20 by 100 mm (FWHM). Electrons and ions of the selected energy are deflected toward the target by an imposed electric field applied across the two plates. The two low energy detectors consist of 10 channels centred on 34, 49, 71, 101, 150, 218, 320, 460, 670, and 960 eV. The high-energy detector measures particles in 10 channels centred at 1.0, 1.4, 2.1, 3.0, 4.4, 6.5, 9.5, 14.0, 20.5 and 29.5 keV. Each detector dwells at each channel for 0.09 seconds from high-energy channel to low. A complete cycle is sampled each second. The nominal response efficiency is 50% at a value of 10% of the central energy for that channel. *Hardy et al.* [1984] provides greater detail concerning these detectors. The DMSP satellite fleet provides the low-altitude link between the mid-altitude observations made by Polar, and the ground-based CUTLASS observations.

3.6 The Co-Operative Twin Located Auroral Sounding System (CUTLASS)

3.6.1 The CUTLASS HF radar system

CUTLASS is a bi-static coherent HF radar system, with stations in Finland (located at Hankasalmi, 62.3°N, 26.6°E) and Iceland (located at Þykkvibær, 63.9°N, 19.2°E), the sites of which are shown in Figures 3.17a and b respectively. CUTLASS is part of the international SuperDARN chain of HF radars (*Greenwald et al.*, 1995). Each radar of the system is a frequency agile (8-20 MHz) radar, routinely measuring the line-of-sight (l-o-s) Doppler velocity and the spectral width of, and the backscattered power from, ionospheric plasma irregularities. The radars each form 16 beams of azimuthal separation 3.24°. Each beam is gated into 75 range bins, each of length 45 km in standard operations, with the dwell time on each beam 7s. This creates a full 16 beam scan which covers 52° in azimuth and over 3000 km in range (which is an area of over 4×10^6 km²) every 2 minutes. Common volume data can be combined to provide the convection velocities perpendicular to the magnetic field. Figure 3.18 illustrates the viewing areas of the CUTLASS radar pair.

The data presented in this thesis, however, is from a non-standard scan pattern. During this period, CUTLASS operated in a scan pattern that sequentially sampled the radar's 16 beams every 2 seconds, giving a full scan approximately every 32 seconds. Each beam is still gated into 75 range cells, but now each of length 30 km, and the lag to the first range was 630 km.

3.6.2 HF propagation

HF radio waves are transmitted at frequencies close to the local ionospheric plasma frequency, such that these waves are continually refracted as they negotiate the ionosphere. As a direct result of this, HF radio waves are capable of achieving orthogonality with the ambient magnetic field in both the E- and F-regions of the ionosphere. Figure 3.19 is a schematic representation of several propagation modes which can result in a signal being returned to the radar (*Milan et al.*, 1997). Ground backscatter is represented by the number of "hops" the ray has made and the ionospheric region it has passed through. For example, a 1F mode represents a ray that has reflected off the ground after passing through the F-region, and a 2F mode is one that has bounced off the ground twice after refracting from the F-region etc. Ionospheric backscatter is represented as originating half way between groundscatter

(a)



(b)



FIGURE 3.17: The CUTLASS (a) Finland and (b) Iceland antenna arrays. Also shown in (b) is the Iceland Interferometer array (on the right). Sixteen antennas form a phased array beam pattern in each radar case.

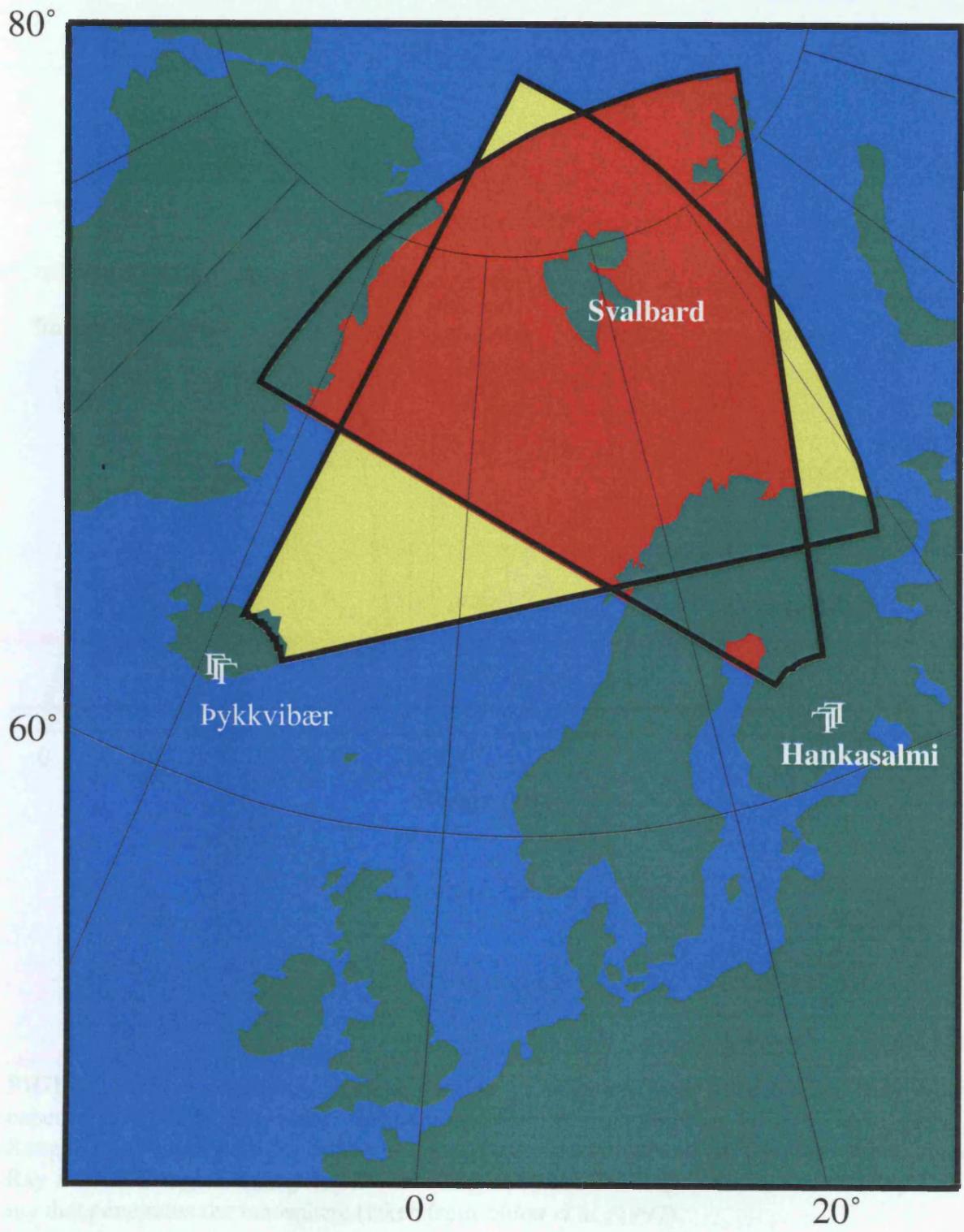


FIGURE 3.18: The fields-of-view of the CUTLASS HF radar pair

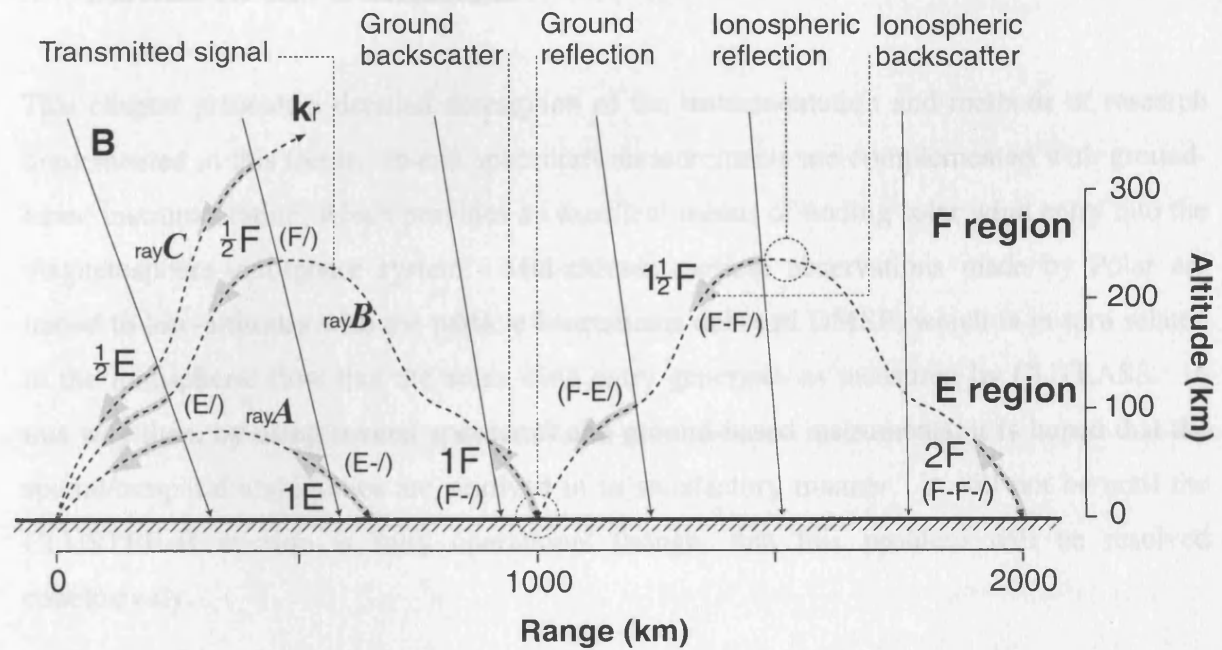


FIGURE 3.19: A schematic of some possible propagation modes and regions from which coherent backscatter can occur. Mode nomenclature in parentheses follows *Davies* [1967]. Ranges and altitudes are dependent on ionospheric conditions and are therefore approximate. Ray A is an E-region mode; Ray B producing near- and far-range backscatter; and Ray C is a ray that penetrates the ionosphere (taken from *Milan et al.*, 1997).

hops, and so denoted by half-integer numbers. For example, ionospheric backscatter denoted by $\frac{1}{2}E$ would represent a signal that has achieved orthogonality in the E-region and scattered without reflecting off the ground, a $1\frac{1}{2}F$ signal would be one that has reflected off the ground once, and scattered off ionospheric irregularities.

3.7 Discussion and Conclusions

This chapter presents a detailed description of the instrumentation and methods of research implemented in this thesis. In-situ spacecraft measurements are complemented with ground-based instrumentation, which provides an excellent means of tracing solar wind entry into the magnetosphere-ionosphere system. Mid-altitude particle observations made by Polar are traced to low-altitudes with the particle instruments onboard DMSP, which is in turn related to the ionospheric flow that the solar wind entry generates as measured by CUTLASS. In this way then, by using several spacecraft and ground-based instruments, it is hoped that the spatial/temporal ambiguities are resolved in as satisfactory manner. It will not be until the CLUSTER-II mission is fully operational though, that this problem will be resolved conclusively.

CHAPTER 4

Polar observations of the time-varying cusp

4.1 Introduction

This chapter presents insight into the mid-altitude cusp region as sampled by the Polar spacecraft. As discussed in Section 2.4.2, the mid-altitude cusp has not been sampled with the regularity of, for example the magnetopause, and in order to fully understand solar wind-magnetosphere-ionosphere coupling processes all aspects of the system have to be investigated, preferably concurrently. The three intervals presented in this chapter provide the basis to investigate this system by first defining the characteristics and plasma populations in the mid-altitude cusp observed by Polar. These observations are then related to the processes that must be occurring at the magnetopause, with specific reference to transient magnetic flux transfer. Utilising these definitions and characteristics, similar observations made by Polar can then be placed in terms of low-altitude and ground-based observations in later Chapters to investigate the solar wind-magnetosphere-ionosphere coupling fully. This Chapter is based upon work detailed in *Rae et al.* [2000].

4.2 Observations – 29th October 1996

The observations in the mid-altitude cusp are put into context with the upstream interplanetary conditions as measured by the Wind spacecraft which is ~ 75 - $120 R_E$ upstream from the Earth. An illustration of its position during October 1996, with position during each of the three case studies (where x_1 , x_2 and x_3 are the positions of Wind on the 12th, 20th and 29th October 1996 respectively) is shown in Figure 4.1.

4.2.1 The Interplanetary Magnetic Field (IMF)

Data from the Wind satellite are displayed in Figure 4.2. In this case study, Wind is situated upstream of the Earth at [$122 R_E$, $-43 R_E$, $28.5 R_E$] in X, Y, Z GSM co-ordinates. Assuming

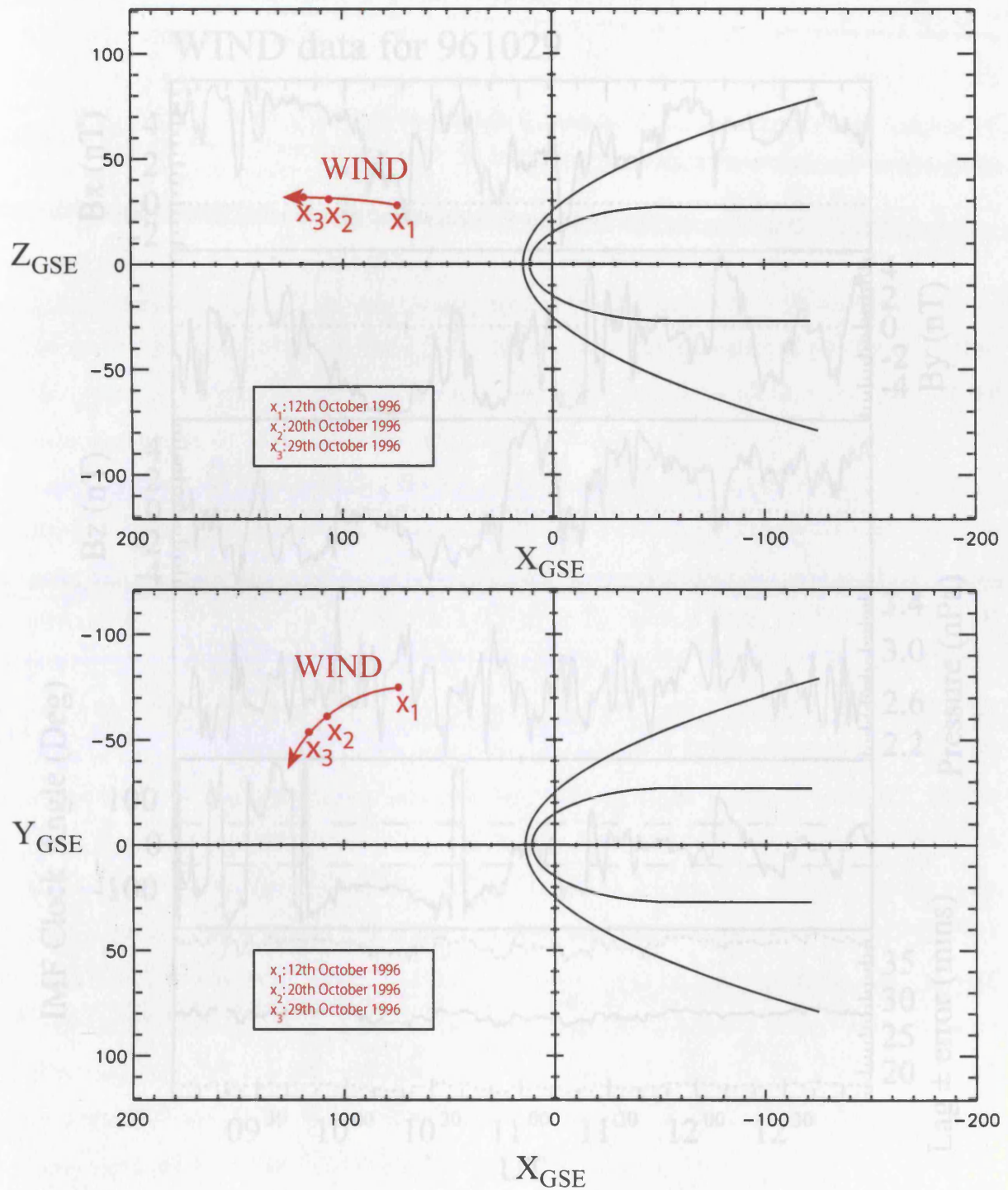


FIGURE 4.2: WIND MPI and SWE data for the 29th October 1996 09-13 UT. The bottom panel shows the calculated time lag between the features observed by the spacecraft and their effect in the ionosphere. Also included is the lag plus and minus the estimated error, shown by the dotted lines.

FIGURE 4.1: The position of the WIND spacecraft during the three case study intervals in October 1996 in GSE coordinates. A model bow shock and magnetopause is shown based on *Roelof and Sibeck [1993]* and $p=2.1$ nPa, IMF $B_z=0$ nT conditions.

planar IMF plane: first, dropping a perpendicular from the spacecraft to the Sun-earth line and using the solar wind velocity, a simple time delay to the magnetopause can be estimated.

Correction is made for the curvature of the interplanetary field within the bow shock. Two

examples are shown in Figure 4.1. The velocity of the solar wind is measured by the velocity

of the spacecraft relative to the Sun-earth line. The velocity of the solar wind is measured by the

velocity of the spacecraft relative to the Sun-earth line. The velocity of the solar wind is measured by

the velocity of the spacecraft relative to the Sun-earth line. The velocity of the solar wind is measured

by the velocity of the spacecraft relative to the Sun-earth line. The velocity of the solar wind is

measured by the velocity of the spacecraft relative to the Sun-earth line. The velocity of the solar

wind is measured by the velocity of the spacecraft relative to the Sun-earth line. The velocity of

the solar wind is measured by the velocity of the spacecraft relative to the Sun-earth line. The

velocity of the solar wind is measured by the velocity of the spacecraft relative to the Sun-earth

line. The velocity of the solar wind is measured by the velocity of the spacecraft relative to the

velocity of the solar wind is measured by the velocity of the spacecraft relative to the Sun-earth

line. The velocity of the solar wind is measured by the velocity of the spacecraft relative to the

velocity of the solar wind is measured by the velocity of the spacecraft relative to the Sun-earth

line. The velocity of the solar wind is measured by the velocity of the spacecraft relative to the

velocity of the solar wind is measured by the velocity of the spacecraft relative to the Sun-earth

line. The velocity of the solar wind is measured by the velocity of the spacecraft relative to the

velocity of the solar wind is measured by the velocity of the spacecraft relative to the Sun-earth

WIND data for 961029

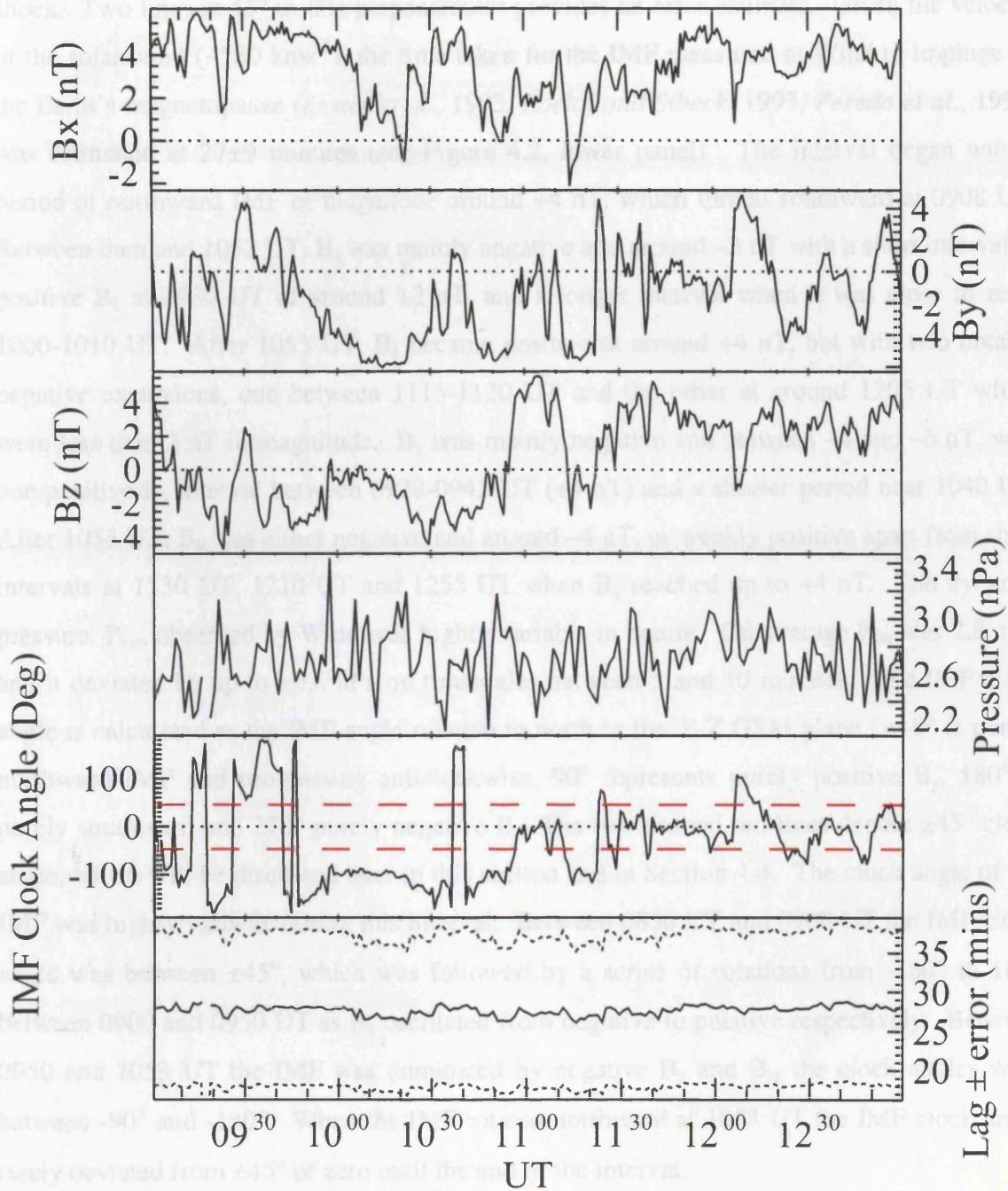


FIGURE 4.2: WIND MFI and SWE data for the 29th October 1996 09-13 UT. The bottom panel shows the calculated timelag between the features observed by the spacecraft and their effect in the ionosphere. Also included is the lag plus and minus the estimated error, shown by the dotted lines.

planar IMF phase fronts, dropping a perpendicular from the spacecraft to the Sun-earth line and using the solar wind velocity, a simple time delay to the magnetopause can be estimated. Correction is made for the slowing and compression of the interplanetary field within the bow shock. Two lines at 45° to this perpendicular provides an error estimate. Given the velocity of the solar wind ($\sim 580 \text{ km s}^{-1}$), the time taken for the IMF measured at Wind to impinge on the Earth's magnetopause (Lester *et al.*, 1993, Roelof and Sibeck, 1993, Peredo *et al.*, 1995) was estimated at 27 ± 9 minutes (see Figure 4.2, lower panel). The interval began with a period of northward IMF of magnitude around $+4 \text{ nT}$, which turned southward at 0908 UT. Between then and 1053 UT, B_z was mainly negative and around -3 nT with a short interval of positive B_z at 0930 UT of around $+2 \text{ nT}$, and a longer interval when it was close to zero, 1000-1010 UT. After 1053 UT, B_z became positive at around $+4 \text{ nT}$, but with two notable negative excursions, one between 1115-1120 UT and the other at around 1205 UT which were less than 2 nT in magnitude. B_y was mainly negative and between -4 and -6 nT , with one positive B_y interval between 0928-0942 UT ($+4 \text{ nT}$) and a shorter period near 1040 UT. After 1053 UT, B_y was either negative and around -4 nT , or weakly positive apart from short intervals at 1130 UT, 1210 UT and 1255 UT when B_y reached up to $+4 \text{ nT}$. The dynamic pressure, P_{sw} , observed by Wind was highly variable in nature. On average P_{sw} was 2.8 nPa , and it deviated by up to $\pm 0.6 \text{ nPa}$ on timescales between 5 and 10 minutes. The IMF clock angle is calculated as the IMF angle relative to north in the Y-Z GSM plane i.e. 0° is purely northward IMF and progressing anticlockwise, 90° represents purely positive B_y , 180° is purely southward and 270° purely negative B_y . The two dashed red lines denote $\pm 45^\circ$ clock angle, which will be discussed later in this section and in Section 4.4. The clock angle of the IMF was highly variable during this interval. Between 0830 UT and 0900 UT the IMF clock angle was between $\pm 45^\circ$, which was followed by a series of rotations from -180° to 180° between 0900 and 0950 UT as B_y oscillated from negative to positive respectively. Between 0950 and 1053 UT the IMF was dominated by negative B_y and B_z , the clock angles were between -90° and -180° . When the IMF rotated northward at 1053 UT the IMF clock angle rarely deviated from $\pm 45^\circ$ of zero until the end of the interval.

4.2.2 Polar spacecraft data

The orbit of the Polar spacecraft on the 29th October 1996 is given in Figure 4.3 in SM coordinates where the arrows, from 0900-1300 UT, mark the period of interest in this case study. During this interval, Polar was traversing the dayside magnetosphere away from apogee over the northern polar cap through the nominal mid-altitude cusp region and onto

closed toroidal field lines. Figure 4.4 presents data from CAMMICE MICS (Figure 4.4, panels 1 and 2) for the interval 0900-1306 LT. Panels 3 and 4 are energy spectrograms of ions and electrons respectively as measured by the MFE instrument. The time axis in panel 3 is the same as in panel 1. The time axis in panel 4 is the same as in panel 2.

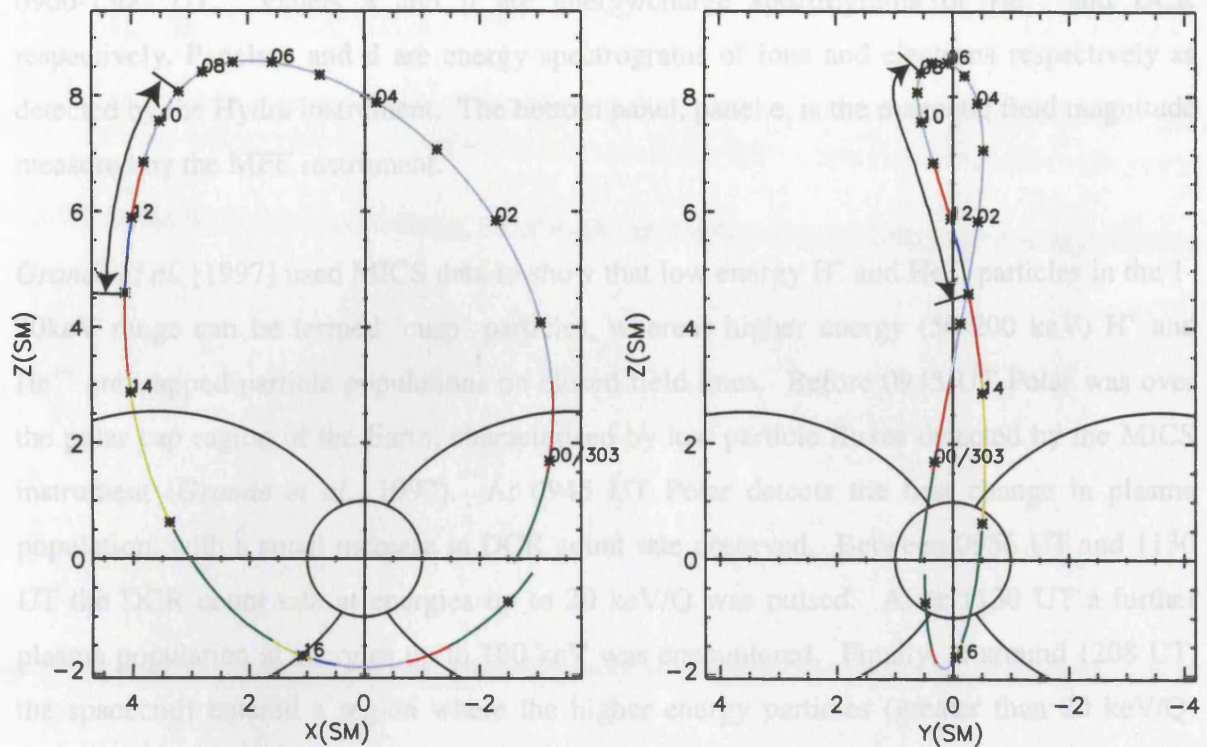


FIGURE 4.3: The orbit of the Polar spacecraft on the 28th and 29th October 1996 in SM coordinates.

electrons). The ion population detected by Hydras occurred at higher energies (10^3 - 10^4 eV) than the electrons (10 - 10^2 eV). While Hydras detected the large-scale pulsed behaviour observed by MICS, there was also a shorter timescale pulsing - a 'pulse-within-a-pulse' - with a timescale of 2-4 minutes. The 'pulse-within-a-pulse' events were energy-dispersed features with the detectors measuring the higher energy particles first in both ions and electrons. It is noted that the higher-energy (10-100 keV/Q) particles were also detected by the CEPPAD instrument (Blake *et al.*, 1995), and observed to pulse at approximately the 2-20 minute repetition rate. The CEPPAD data will be discussed later in this section.

In order to quantify the two discrete time-scales involved in this interval, a fast Fourier transform (FFT) was performed through the centre of the pulsed particle features, the 1keV Hydras ion channel, between 1000-1200 LT. Figure 4.5 shows the normalised power as a function of frequency of this FFT spectrum. Two dominant periodicities are evident from this analysis, one at ~21 minutes and one at 3-4 minute (composed of two similar peaks).

closed terrestrial field lines. Figure 4.4 presents data from CAMMICE MICS (Figure 4.4, panels a, b), Hydra (Figure 4.4, panels c, d), and MFE (Figure 4.4, panel e) for the interval 0900-1300 UT. Panels a and b are energy/charge spectrograms of He^{++} and DCR respectively. Panels c and d are energy spectrograms of ions and electrons respectively as detected by the Hydra instrument. The bottom panel, panel e, is the magnetic field magnitude measured by the MFE instrument.

Grande et al. [1997] used MICS data to show that low energy H^+ and He^{++} particles in the 1-30keV range can be termed ‘cusp’ particles, whereas higher energy (50-200 keV) H^+ and He^{++} are trapped particle populations on closed field lines. Before 0945 UT Polar was over the polar cap region of the Earth, characterised by low particle fluxes detected by the MICS instrument (*Grande et al.*, 1997). At 0945 UT Polar detects the first change in plasma population, with a small increase in DCR count rate observed. Between 0956 UT and 1130 UT the DCR count rate at energies up to 20 keV/Q was pulsed. After 1130 UT a further plasma population at energies up to 100 keV was encountered. Finally, at around 1208 UT, the spacecraft entered a region where the higher energy particles (greater than 20 keV/Q) were dominant and the lower energy particles decreased in flux. The population between 20 and 100 keV is consistent with closed field line particle populations (*Grande et al.*, 1997). Similar features were seen in panel a, the He^{++} population, though the particle count rate was lower. The plasma at energies below 20 keV between 0957-1206 UT pulsed on timescales of 12-20 minutes. The two Hydra panels show similar pulsed behaviour in both ions and electrons. The ion population detected by Hydra occurred at higher energies (10^2 - 10^4 eV) than the electrons (10 - 10^3 eV). While Hydra detected the large-scale pulsed behaviour observed by MICS, there was also a shorter timescale pulsing - a ‘pulse-within-a-pulse’ - with a timescale of 2-4 minutes. The ‘pulse-within-a-pulse’ events were energy-dispersed features with the detectors measuring the higher energy particles first in both ions and electrons. It is noted that the higher-energy (10-100 keV/Q) particles were also detected by the CEPPAD instrument (*Blake et al.*, 1995), and observed to pulse at approximately the 12-20 minute repetition rate. The CEPPAD data will be discussed later in this section.

In order to quantify the two discrete time-scales involved in this interval, a fast fourier transform (FFT) was performed through the centre of the pulsed particle features, the 1keV Hydra Ion channel, between 1000-1200 UT. Figure 4.5 shows the normalised power as a function of frequency of this FFT spectrum. Two dominant periodicities are evident from this analysis, one at ~21 minute and one at 3-4 minute (composed of two similar peaks).

POLAR Ion and Electron Energy Spectra

CAMMICE MICS, HYDRA and MFE

29/10/1996

0900-1300 UT

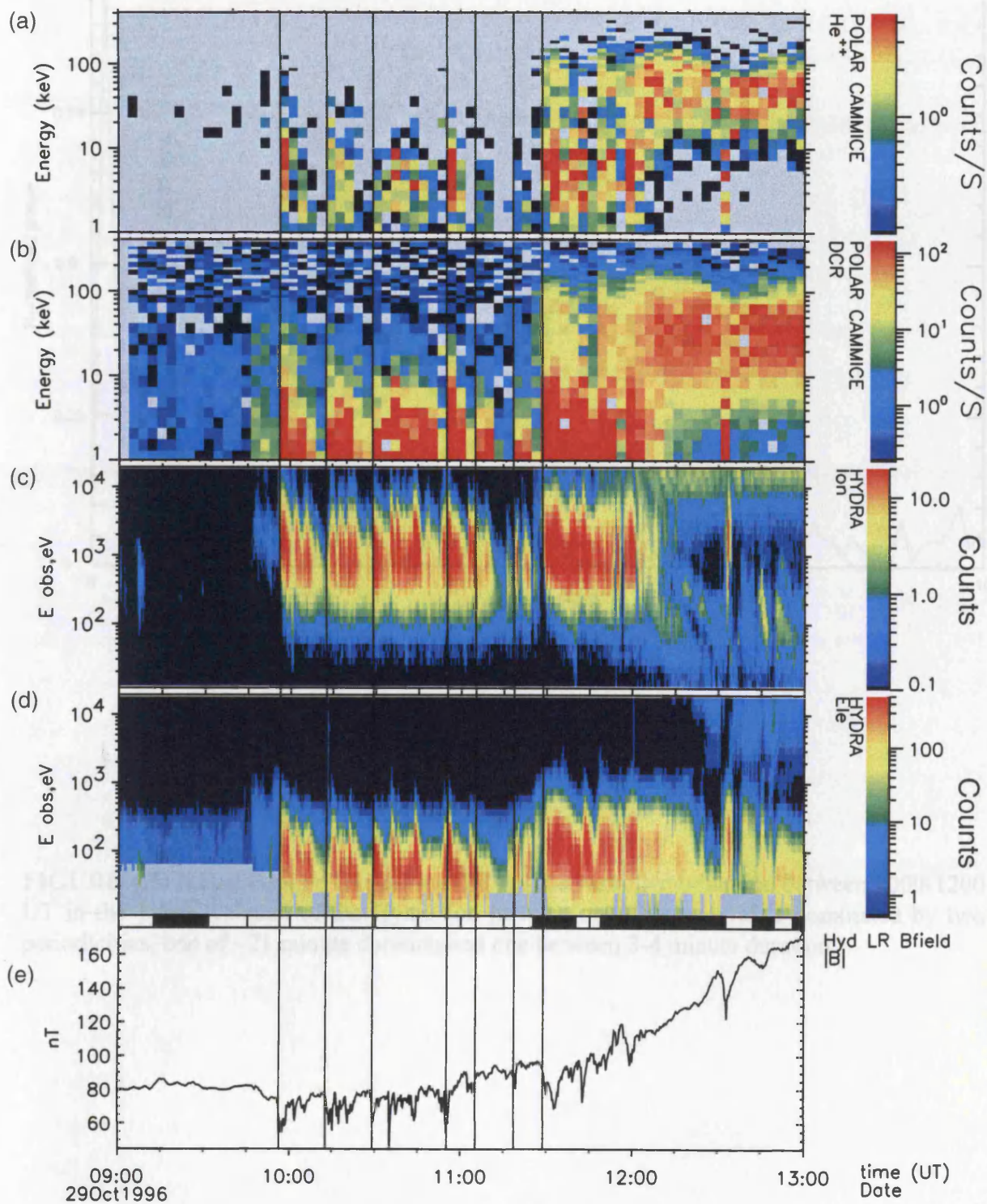


FIGURE 4.4: Polar Ion and Electron energy spectra for the 29th October 1996 09-13 UT.

It is noted that there is a "burst" of plasma detected in the closed field line region, at ~1235 UT, picked up by all four panels of Figure 4.4. The calculated delay for the IMF measured at Wind to reach the magnetopause is ~100 minutes. Taking the two usual

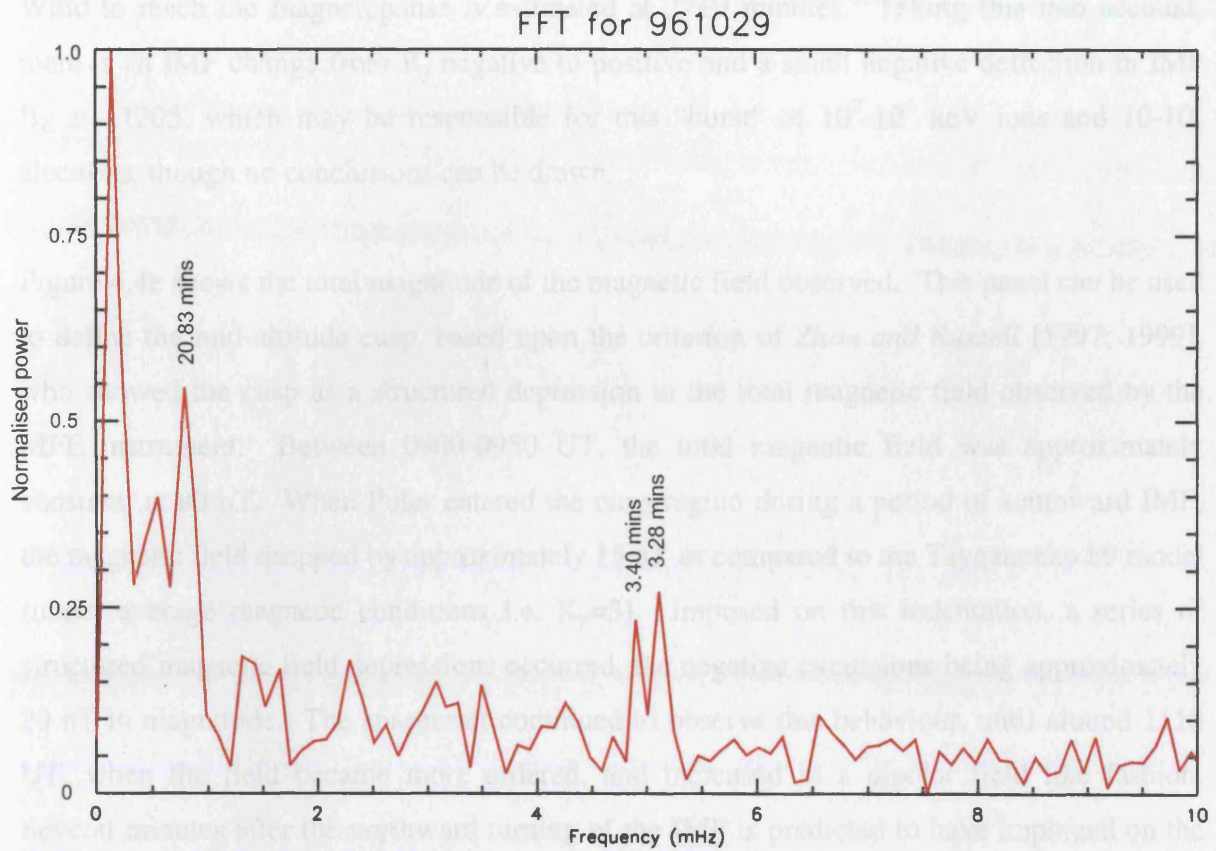


FIGURE 4.5: A Fast Fourier Transform (FFT) of the particle modulation between 1000-1200 UT in the 1 keV channel of the Hydra Ion instrument. This interval is dominated by two periodicities, one of ~21 minute duration and one between 3-4 minute duration.

assumed β_{\perp} oscillates and returns back to its original value. This behaviour is ultimately superposed onto a background dipolar-like field. There is also a good correspondence between the 3-4 minute cusp and the IMF oscillations, though not always on a 1:1 basis. A number of these intervals are also associated with a drop of ~20% in the local magnetic field.

Figure 4.6 shows the ion data from three separate instruments combined to produce an effective energy range of 10 eV-1 MeV from Hydra (Figure 4.6a), CASMIC (Figure 4.6b), and CERAD (Figure 4.6c). It can be seen in this Figure that these pulsed particle features

It is noted that there is a “burst” of plasma detected in the closed field line region, at ~1235 UT, picked up by all four panels of Figure 4.4. The calculated delay for the IMF measured at Wind to reach the magnetopause is estimated at 27 ± 9 minutes. Taking this into account, there is an IMF change from B_y negative to positive and a small negative deflection in IMF B_z at ~1205, which may be responsible for this “burst” of 10^2 - 10^4 keV ions and 10 - 10^3 electrons, though no conclusions can be drawn.

Figure 4.4e shows the total magnitude of the magnetic field observed. This panel can be used to define the mid-altitude cusp, based upon the criterion of *Zhou and Russell* [1997; 1999], who showed the cusp as a structured depression in the total magnetic field observed by the MFE instrument. Between 0900-0950 UT, the total magnetic field was approximately constant, at 80 nT. When Polar entered the cusp region during a period of southward IMF, the magnetic field dropped by approximately 15 nT as compared to the Tsyganenko 89 model (under average magnetic conditions i.e. $K_p=3$). Imposed on this indentation, a series of structured magnetic field depressions occurred, the negative excursions being approximately 20 nT in magnitude. The spacecraft continued to observe this behaviour, until around 1110 UT, when the field became more ordered, and increased in a dipolar field like fashion. Several minutes after the northward turning of the IMF is predicted to have impinged on the magnetopause i.e. ~1120 UT, there was a secondary series of structured depressions of 20 nT in depth, until the spacecraft exited the cusp at around 1205 UT, and the field becomes predominantly dipole-like. *Zhou and Russell* [1997] and *Zhou et al.* [1999] associated structured depressions in the total magnetic field such as these observed in Figure 4.4e with the entry into the cusp region, as *Chen et al.* [1997] also showed with Hawkeye spacecraft data at higher altitudes. The structure in the magnetic field depression appears also to be linked to the pulsed particle signature events observed by CAMMICE MICS. At the onset of each pulsed particle event measured by MICS the local magnetic field strength drops by around 20 nT, oscillates and recovers back to its original value. This behaviour is ultimately superposed onto a background dipolar-like field. There is also a good correspondence between the 2-4 minute pulses and the MFE oscillations, though not always on a 1:1 basis. A number of these intervals are also associated with a drop of ~20 nT in the local magnetic field.

Figure 4.6 shows the ion data from three separate instruments combined to produce an effective energy range of 10 eV-1 MeV from Hydra (Figure 4.6c), CAMMICE (Figure 4.6b), and CEPPAD (Figure 4.5a). It can be seen in this Figure that these pulsed particle features

POLAR Ion Energy Spectra

CEPPAD, CAMMICE MICS and HYDRA

29/10/1996
0900-1300 UT

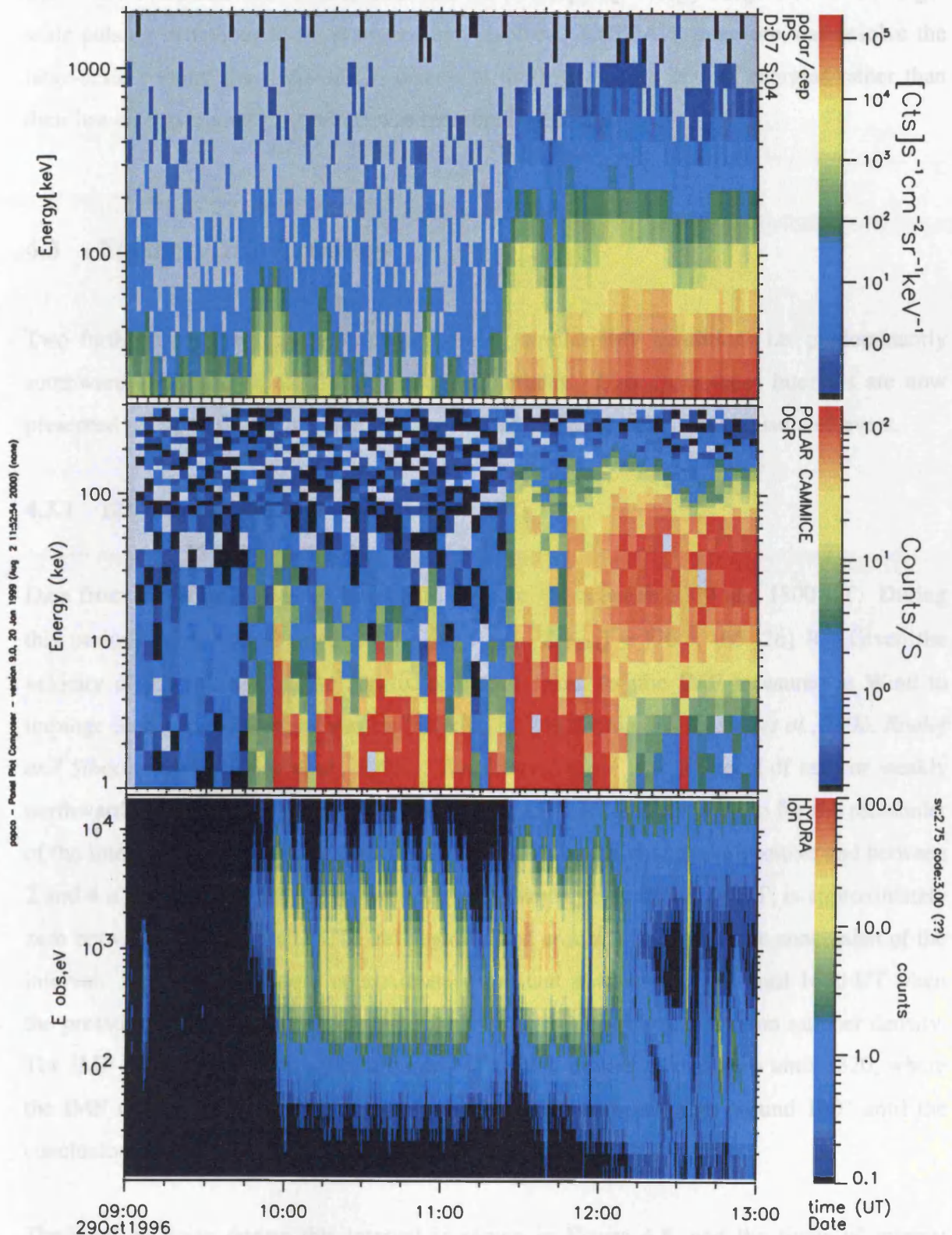


FIGURE 4.6: Polar Ion Spectra from the CEPPAD, CAMMICE MICS and HYDRA instruments for the 29th October 1996 09-13 UT.

extend from ~ 100 eV up to around 100 keV in energy. The increased temporal resolution of CEPPAD, compared with CAMMICE and the overlapping energy range allows the large-scale pulsing behaviour to be examined and resolved. CEPPAD, therefore, can resolve the large-scale pulsing that CAMMICE detects at the high-energy cut-off energies rather than their low-energy counterpart which was measured by Hydra.

4.3 Further Cusp Crossings

Two further cusp crossings were chosen during similar IMF conditions i.e. predominantly southward IMF, and similar local times and latitudes. Data from these intervals are now presented to establish that the case study presented in Section 4.2 is not an isolated event.

4.3.1 12th October 1996

Data from the Wind spacecraft is shown in Figure 4.7 between 1200 and 1800 UT. During this period, Wind was situated at $[X_{\text{GSM}}, Y_{\text{GSM}}, Z_{\text{GSM}}] \approx [76.5, -65, 26]$ R_E . Given the velocity of the solar wind, the approximate time taken for the IMF measured at Wind to impinge on the magnetopause was estimated to be 24 ± 17 minutes (*Lester et al.*, 1993, *Roelof and Sibeck*, 1993, *Peredo et al.*, 1995). The interval starts with a period of zero or weakly northward IMF, which turns southward at around 1322 UT and remains so for the remainder of the interval. B_y starts the interval around zero also which changes to positive and between 2 and 4 nT at around 1320 UT as well. B_x starts negative at around -4 nT, is approximately zero between 1330 and 1433 UT, and negative and around -2 nT until the conclusion of the interval. Dynamic pressure is approximately constant at around 1.7 nT until 1640 UT when the pressure almost doubles to around 3.2 nT through a doubling of the ion number density. The IMF clock angle starts off at around -90° which hovers around zero until 1320, where the IMF rotates and the clock angle approaches 150° and settles to around 100° until the conclusion of the interval.

The orbit of Polar during this interval is shown in Figure 4.8, and the times of interest between 1200 UT and 1700 UT marked with the blue lines. Figure 4.9 shows the Polar particle data for this interval in the same format as Figure 4.4. Before approximately 1300 UT, Polar was on open field lines characteristic of the polar cap, and hence dominated by low-energy low-flux ions (Figures 4.9b and c). Polar entered the closed field line region

WIND data for 961012

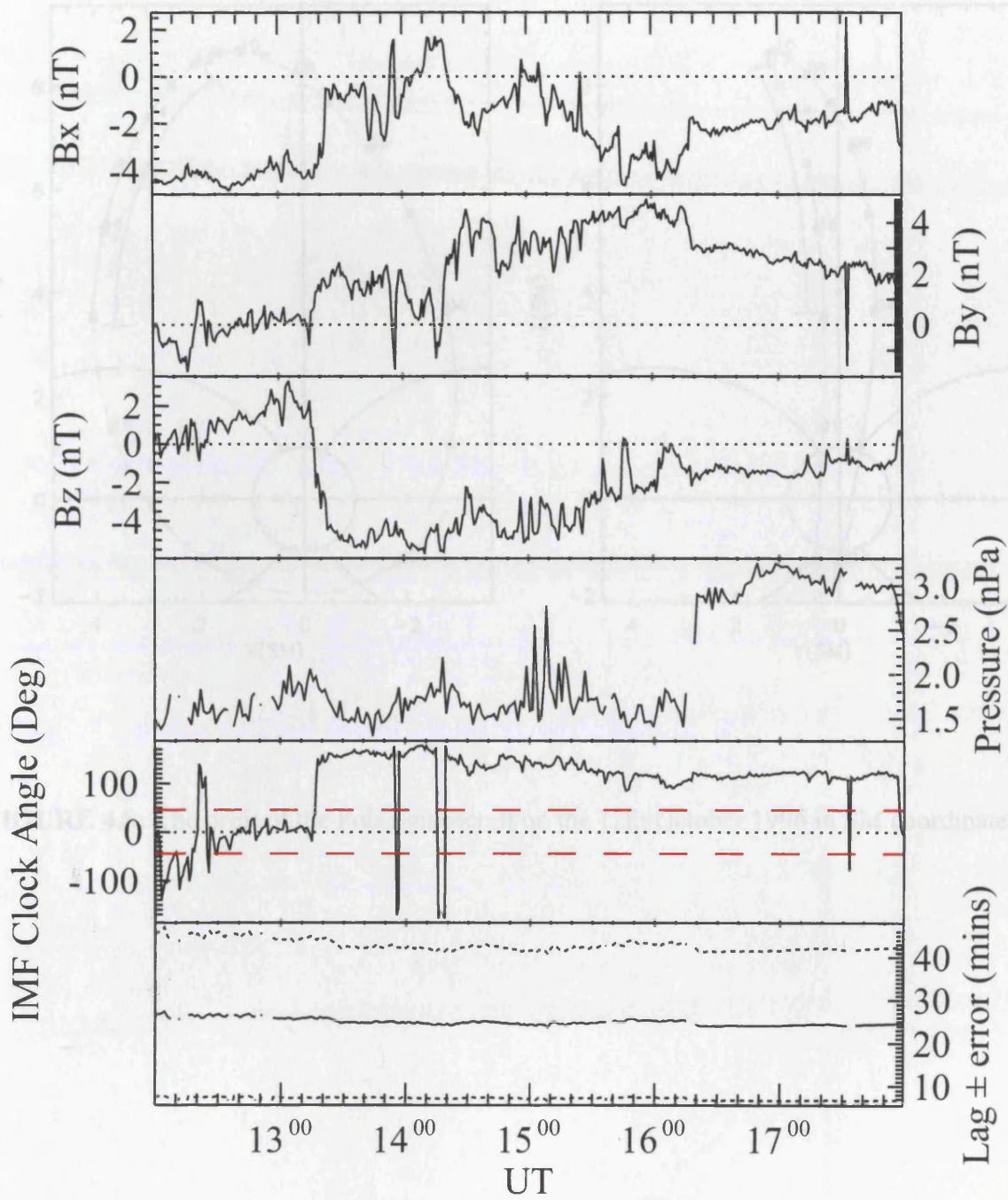


FIGURE 4.7: WIND MFI and SWE data for the 12th October 1996 12-18 UT.

POLAR orbit 1996 286 (10/12) 02:30 UT to 1996 286 (10/12) 20:30 UT

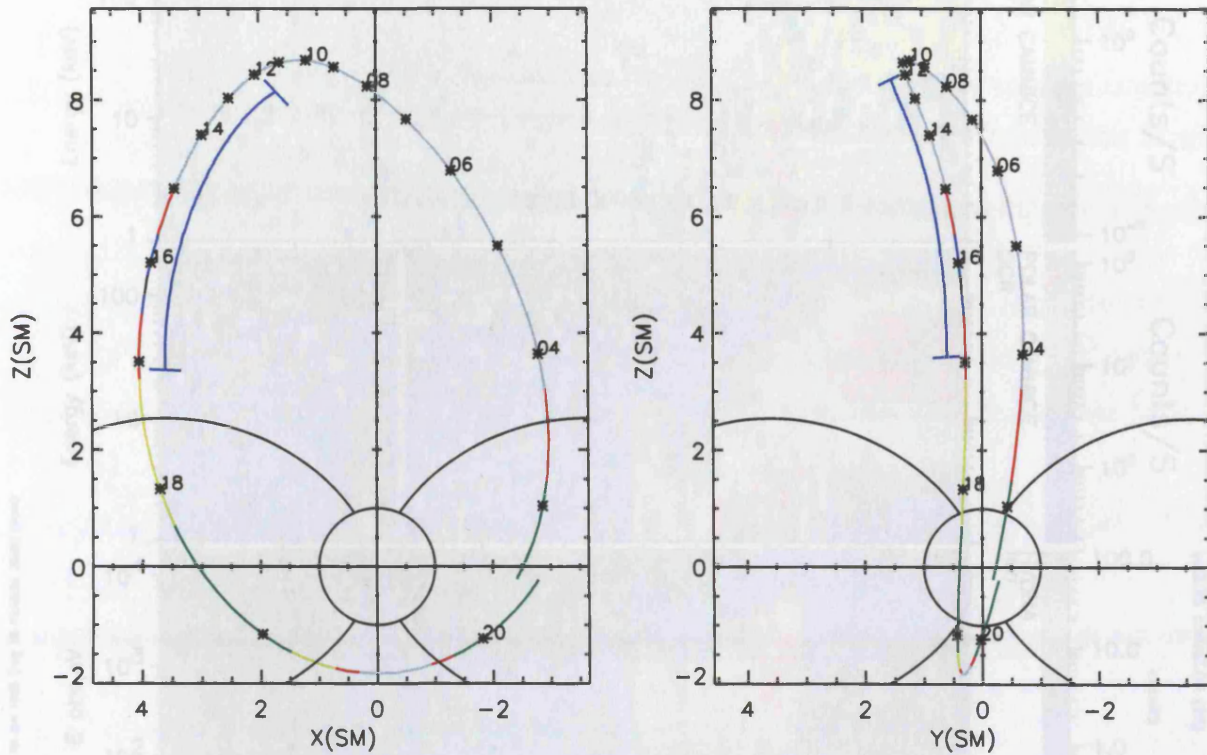


FIGURE 4.8: The orbit of the Polar spacecraft on the 12th October 1996 in SM coordinates.

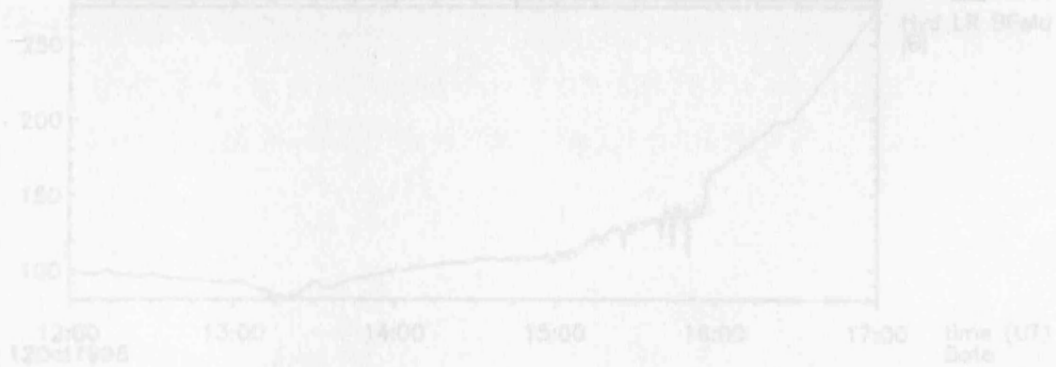


FIGURE 4.9: Polar Ion and Electron energy spectra for the 12th October 1996 12-17 UT

POLAR Ion and Electron Energy Spectra

CAMMICE MICS, HYDRA and MFE

12/10/1996
1200-1700 UT

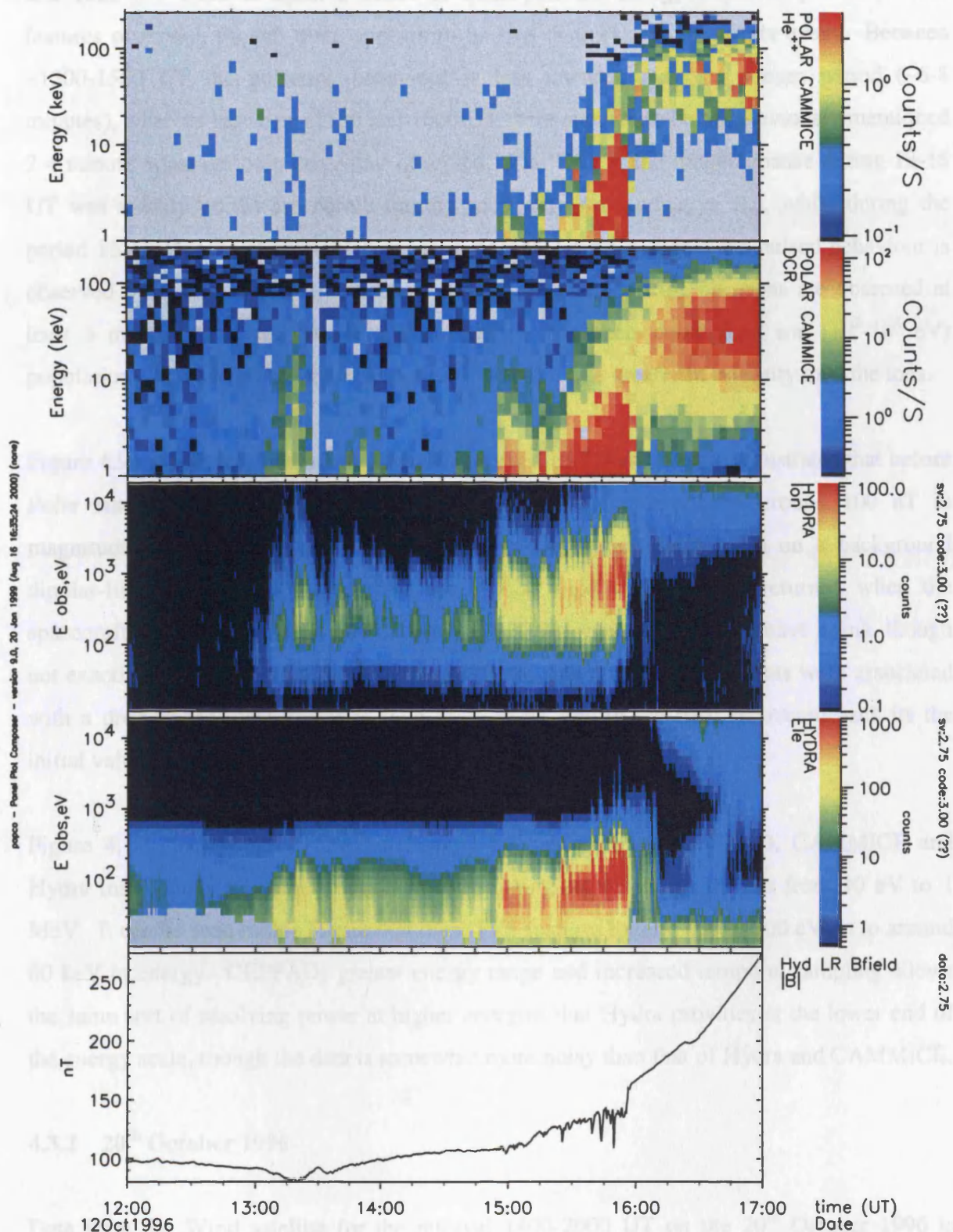


FIGURE 4.9: Polar Ion and Electron energy spectra for the 12th October 1996 12-17 UT.

characterised by high energy ($\sim 20\text{-}100$ keV/Q) high-flux ions near ~ 1600 UT. Between 1300 and 1600 UT there is again a series of quasi-periodic energy-dispersed pulsed particle features observed, though there appears to be two distinct regions to this event. Between $\sim 1300\text{-}1500$ UT the pulsating behaviour is less intense, and of a longer period ($\sim 6\text{-}8$ minutes), whereas between ~ 1500 and 1600 UT there appears to be the previously mentioned 2-4 minute quasi-periodic behaviour observed. The IMF at the magnetopause during 13-15 UT was weakly northward before turning southward (and negative B_y), while during the period 15-16 UT it was southward directed IMF of ~ 5 nT. Again the pulsed behaviour is observed by Hydra in both the electron and ion data, though the electrons are observed at least a magnitude lower ($10\text{-}10^3$ eV) in energy than their counterpart ion ($10^2\text{-}10^4$ eV) population. The electrons are also detected at a magnitude greater in intensity than the ions.

Figure 4.9e shows the total magnetic field observed by Polar. This demonstrates that before Polar entered the cusp region the magnetic field was ordered and around 100 nT in magnitude, while through the cusp a structured depression superposed on a background dipolar-like field was observed, and the dipolar field configuration returned when the spacecraft entered closed field lines. Again the PPS signatures appear to have a link, though not exactly 1:1, with these depressions in the field. Many of the PPS events were associated with a drop in the local magnetic field of ~ 20 nT before the field recovered back its the initial value.

Figure 4.10 displays solely the Ion Energy Spectra from the CEPPAD, CAMMICE and Hydra instruments to again produce an overlapping set of energy ranges from 10 eV to 1 MeV. It can be seen in this Figure that these PPS features extend from ~ 100 eV up to around 60 keV in energy. CEPPADs greater energy range and increased temporal sampling allows the same sort of resolving power at higher energies that Hydra provides at the lower end of the energy scale, though the data is somewhat more noisy than that of Hydra and CAMMICE.

4.3.2 20th October 1996

Data from the Wind satellite for the interval 1400-2000 UT on the 20th October 1996 is displayed in Figure 4.11. At this time, Wind was situated some $[X_{\text{GSM}}, Y_{\text{GSM}}, Z_{\text{GSM}}] \approx [76.5, -65, 26]$ R_E upstream from the Earth. Given the velocity of the solar wind, the approximate delay that the IMF is subject to in order to reach the Earth's magnetopause (*Lester et al.*, 1993, *Roelof and Sibeck*, 1993, *Peredo et al.*, 1995) was 29 ± 14 minutes.

POLAR Ion Energy Spectra

CEPPAD, CAMMICE MICS and HYDRA

12/10/1996
1200-1700 UT

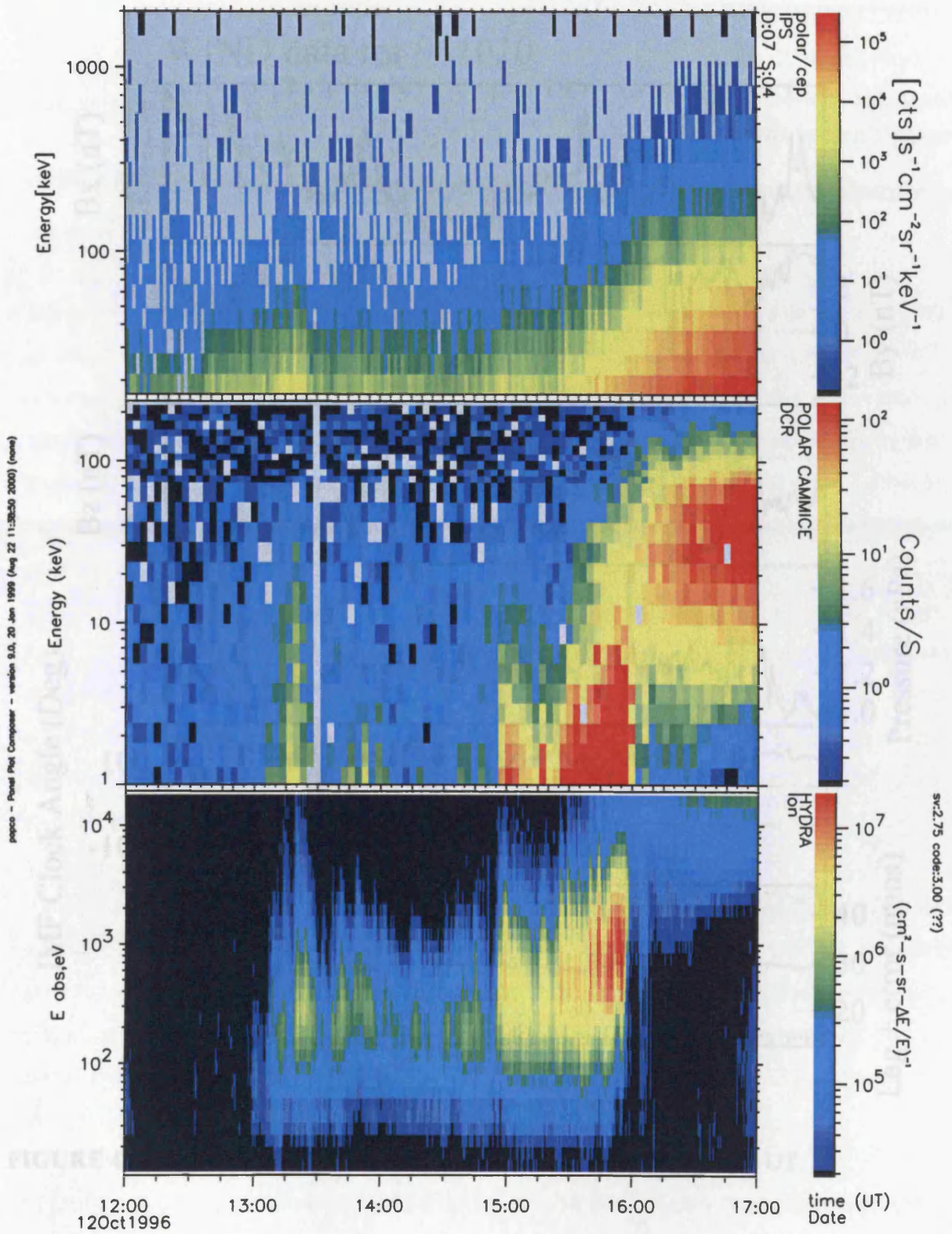


FIGURE 4.10: Polar Ion Spectra from the CEPPAD, CAMMICE and HYDRA instruments for the 12th October 1996 12-17 UT.

During the interval in question the IMF B_z was predominantly negative, though there are several positive excursions such as 1640-1702 UT and 1805-1822 UT. B_z was also fairly constant and positive at around +2 nT, though did extend negative on occasions, such as 1640-1716, and 1520-1540 UT. B_z was weakly

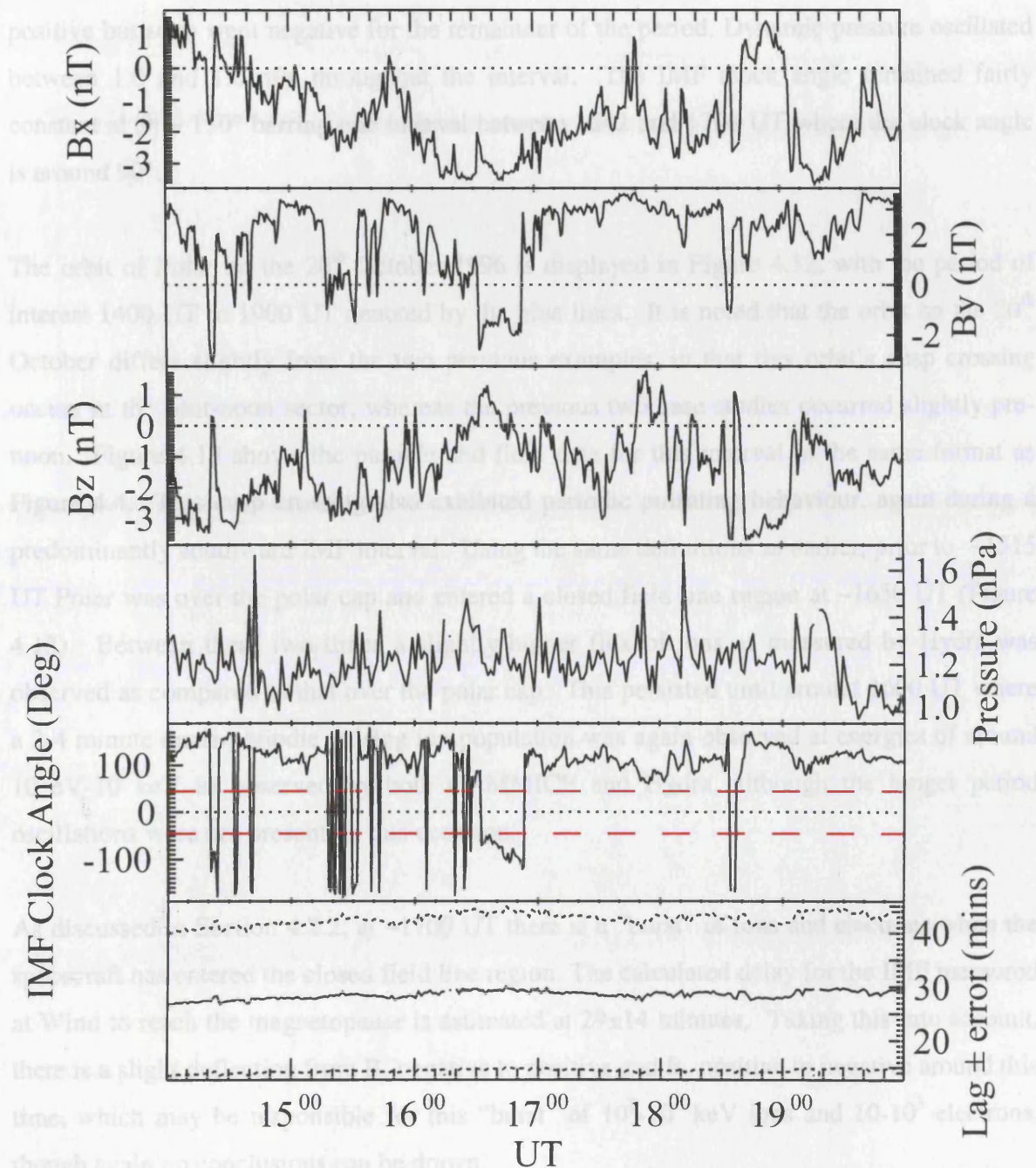


FIGURE 4.11: WIND MFI and SWE data for the 20th October 1996 14-20 UT.

Figure 4.13e shows the total magnetic field for this interval. Again during this interval the local magnetic field over the polar cap was oriented and around -180 nT until ~ 1900 UT where again a structured magnetic field depression was detected superposed on a dipolar-like field. This occurred until ~ 1650 where the field once again becomes dipolar-like when the

During the interval in question the IMF B_z was predominantly negative, though there are several positive excursions such as 1640-1702 UT and 1805-1822 UT. B_y was also fairly constant and positive at around +2 nT, though did extend negative on occasions, such as 1640-1710, and hovered around zero between around 1520-1540 UT. B_x starts weakly positive but soon went negative for the remainder of the period. Dynamic pressure oscillated between 1.0 and 1.6 nPa throughout the interval. The IMF clock angle remained fairly constant at $|\theta| \sim 150^\circ$ barring one interval between 1642 and 1708 UT where the clock angle is around 90° .

The orbit of Polar on the 20th October 1996 is displayed in Figure 4.12, with the period of interest 1400 UT to 1900 UT denoted by the blue lines. It is noted that the orbit on the 20th October differs slightly from the two previous examples, in that this orbit's cusp crossing occurs in the post-noon sector, whereas the previous two case studies occurred slightly pre-noon. Figure 4.13 shows the particle and field data for this interval in the same format as Figure 4.4. This cusp crossing also exhibited periodic pulsating behaviour, again during a predominantly southward IMF interval. Using the same definitions as earlier, prior to ~1515 UT Polar was over the polar cap and entered a closed field line region at ~1650 UT (Figure 4.13). Between these two times a slightly higher flux of ions as measured by Hydra was observed as compared to that over the polar cap. This persisted until around 1600 UT where a 2-4 minute quasi-periodic pulsing ion population was again observed at energies of around 10 eV-10 keV as observed by both CAMMICE and Hydra, although the longer period oscillations were not present on this occasion.

As discussed in Section 4.2.2, at ~1700 UT there is a "burst" of ions and electrons when the spacecraft has entered the closed field line region. The calculated delay for the IMF measured at Wind to reach the magnetopause is estimated at 29 ± 14 minutes. Taking this into account, there is a slight deflection from B_z negative to positive and B_y positive to negative around this time, which may be responsible for this "burst" of 10^2 - 10^4 keV ions and 10 - 10^3 electrons, though again no conclusions can be drawn.

Figure 4.13e shows the total magnetic field for this interval. Again during this interval the local magnetic field over the polar cap was ordered and around ~100 nT until ~1600 UT where again a structured magnetic field depression was detected superposed on a dipolar-like field. This occurred until ~1650 where the field once again becomes dipolar-like when the

POLAR orbit 1996 294 (10/20) 04:00 UT to 1996 294 (10/20) 22:00 UT

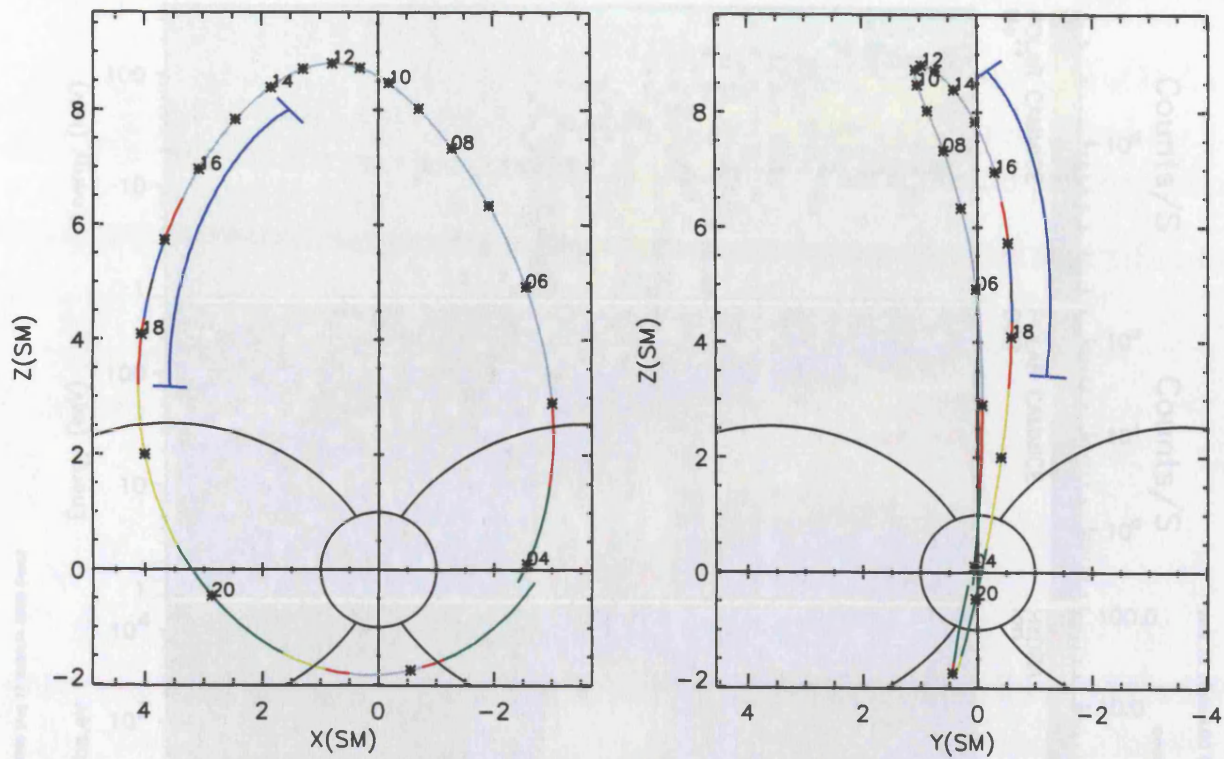


FIGURE 4.12: The orbit of the Polar spacecraft on the 20th October 1996 in SM coordinates.



FIGURE 4.13: Polar ion and electron energy spectra for 20th October 1996 1400-1830 UT.

POLAR Ion and Electron Energy Spectra

CAMMICE MICS, HYDRA and MFE

20/10/1996
1400-1830 UT

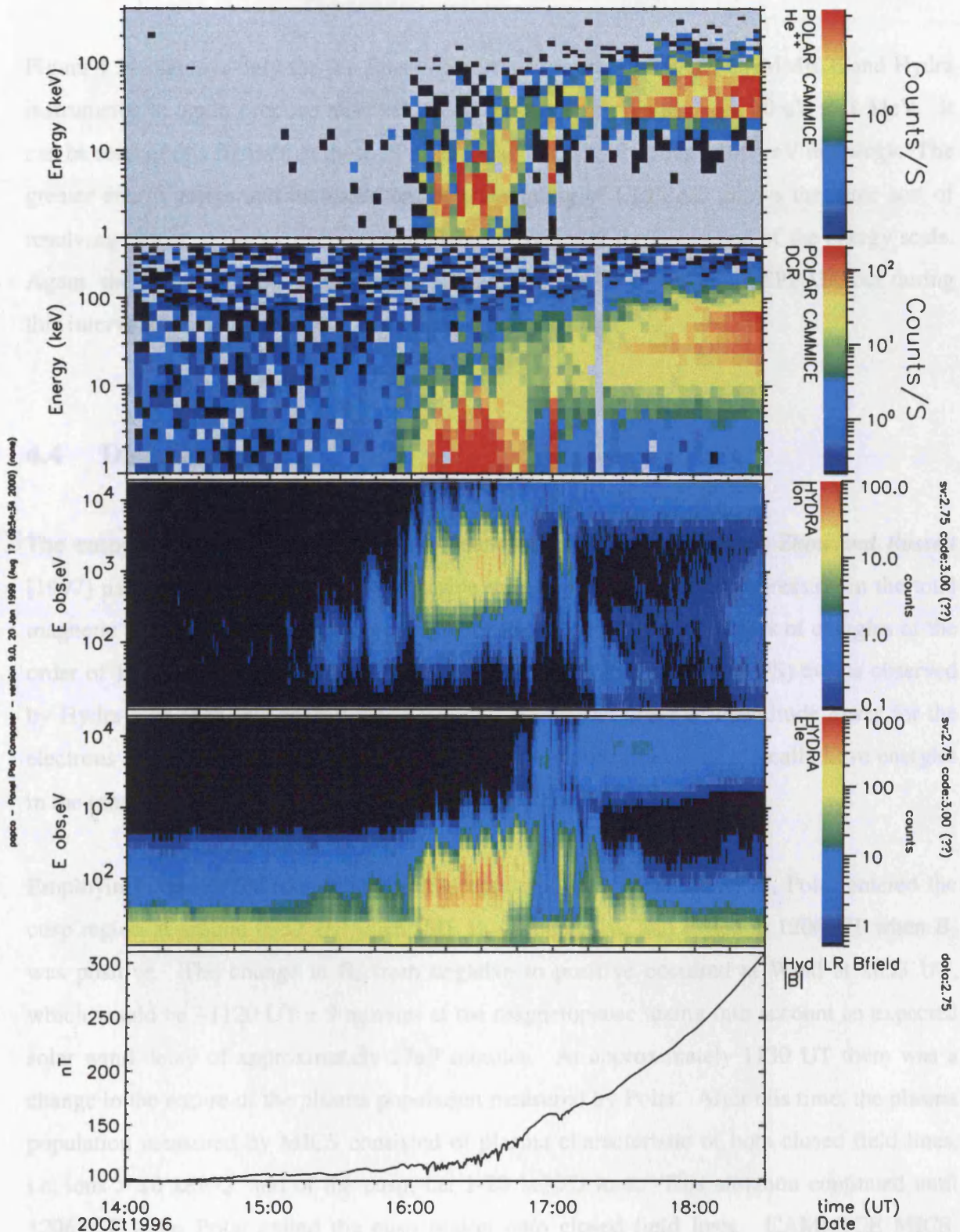


FIGURE 4.13: Polar Ion and Electron energy spectra for 20th October 1996 1400-1830 UT.

spacecraft is on closed field lines. Once more the structured depressions, though not all, are correlated with the onset of several PPS events.

Figure 4.14 displays only the Ion Energy Spectra from the CEPPAD, CAMMICE and Hydra instruments to again produce an overlapping set of energy ranges from 10 eV to 1 MeV. It can be seen in this figure that these PPS features extend up to around 100 keV in energy. The greater energy range and increased temporal sampling of CEPPAD allows the same sort of resolving power at higher energies that Hydra provides at the lower end of the energy scale. Again, the shorter period perturbations can be resolved in Hydra and CEPPAD, but during this interval there is no evidence of the large-scale pulsing.

4.4 Discussion

The cusp region observed by Polar has been defined in several ways. *Zhou and Russell [1997]* used the MFE instrument to describe the cusp as a structured depression in the total magnetic field. In MICS data the cusp is defined as being a region of ions of energies of the order of 1-20 keV/Q (*Grande et al., 1997*). Pulsed particle signatures (PPS) events observed by Hydra also span this energy range for ions, but are an order of magnitude lower for the electrons detected. In contrast, trapped particles on closed field lines typically have energies in the range 50-200 keV/Q and approximately uniform fluxes.

Employing these definitions for the initial case study, October 29, 1996, Polar entered the cusp region at around 0957 UT when IMF B_z was negative and exited at 1206 UT when B_z was positive. The change in B_z from negative to positive occurred at Wind at 1053 UT, which would be $\sim 1120 \text{ UT} \pm 9$ minutes at the magnetopause taking into account an expected solar wind delay of approximately 27 ± 9 minutes. At approximately 1130 UT there was a change in the nature of the plasma population measured by Polar. After this time, the plasma population measured by MICS consisted of plasma characteristic of both closed field lines, i.e. ions $> 20 \text{ keV/Q}$, and of the cusp, i.e. 1-20 keV/Q ions. This situation continued until 1206 UT when Polar exited the cusp region onto closed field lines. CAMMICE MICS, CEPPAD and the Hydra instruments observed pulsing of the particles on a timescale of 12-20 minutes between 0958 UT and 1120 UT. Furthermore, Hydra's increased temporal resolution demonstrates a shorter period component, $\sim 2-4$ minutes, within the large time-

POLAR Ion Energy Spectra

CEPPAD, CAMMICE MICS and HYDRA

20/10/1996
1400-1900 UT

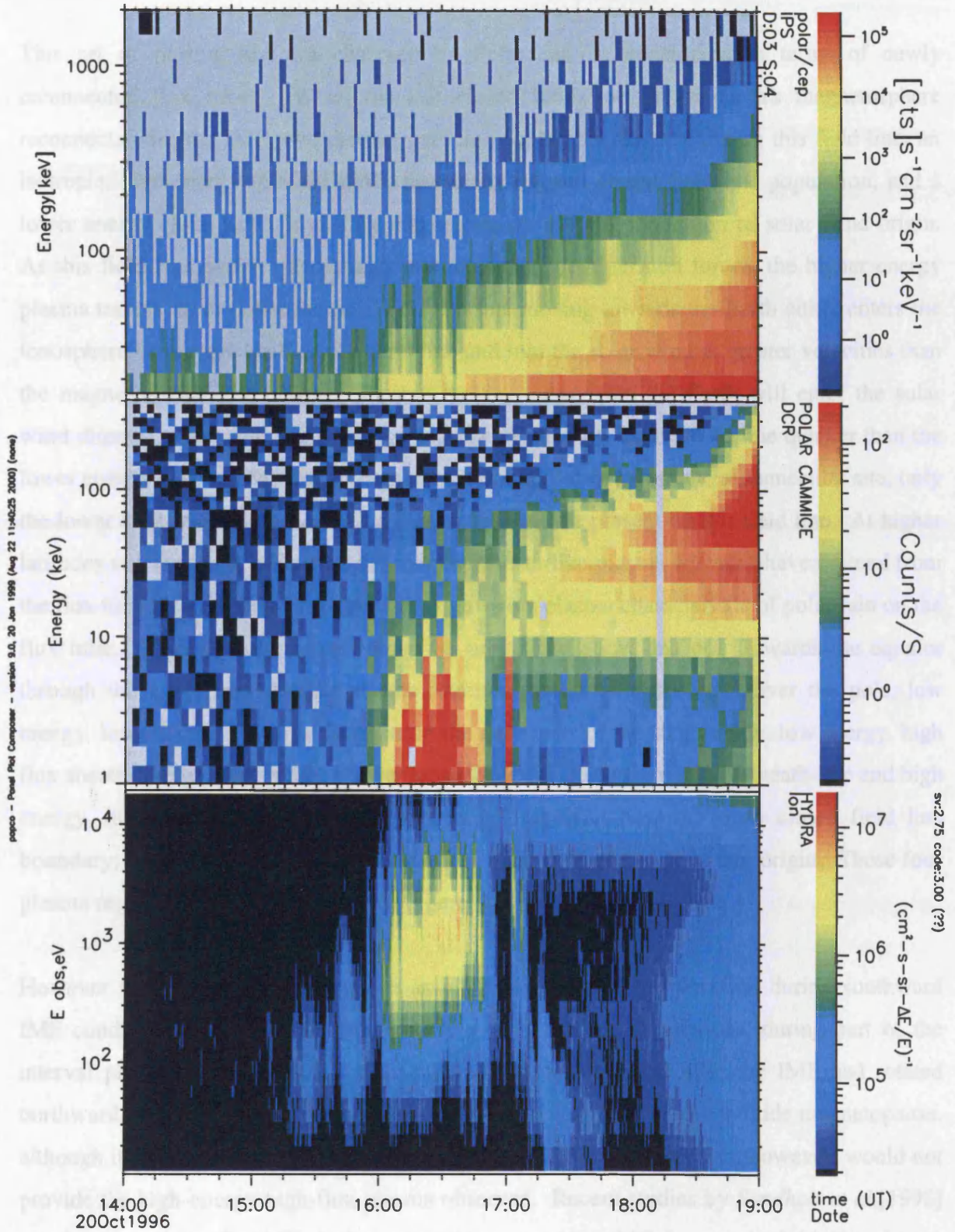


FIGURE 4.14: Polar Ion Spectra from the CEPPAD, CAMMICE and HYDRA instruments for the 20th October 1996 14-19 UT.

scale structures. We have termed these combined high and low frequency particle signatures as “pulsed particle signatures” or PPS.

This set of plasma regimes observed by Polar can be considered in terms of newly reconnected flux tubes. When the last closed field line of the earth's magnetosphere reconnects with the IMF, two distinct particle populations can co-exist on this field line; an isotropic, high-energy (50-200 keV), previously-trapped closed field line population, and a lower energy (1-20 keV), high flux magnetosheath plasma population of solar wind origin. As this field line evolves and straightens under magnetic tension forces, the higher energy plasma travels up or down the field line. Plasma moving towards the Earth either enters the ionosphere or mirrors back up the field line and into the solar wind at greater velocities than the magnetosheath-like plasma. Plasma moving away from the Earth will enter the solar wind directly. Thus, the higher energy plasma will drain from the field line quicker than the lower energy plasma. Moving to higher latitudes i.e. further from the reconnection site, only the lower energy magnetosheath-like plasma will still be present on this field line. At higher latitudes still (over the polar cap) the magnetosheath-like plasma will also have drained from the flux tube also, leaving very low energy, low flux plasma characteristic of polar rain on the flux tube. Thus as Polar moves along its orbit from above the pole towards the equator through the cusp, four distinct plasma regimes should be observed. Over the pole, low energy, low flux polar rain is detected; in the outer part of the cusp region, low energy, high flux sheath-like plasma; while at lower latitudes within the cusp a mix of sheath-like and high energy, high flux closed field line plasma will co-exist near the open closed field line boundary; and finally a high energy, high flux plasma of closed field line origin. These four plasma regimes are those illustrated in Figure 4.4.

However the scenario outlined above assumes low-latitude reconnection during southward IMF conditions, and, while it explains the mix of plasma populations, during part of the interval presented, the mixed particle populations are observed after the IMF had rotated northward. At this time, reconnection is believed to cease at the low latitude magnetopause, although it can occur at higher latitudes in the lobes. Lobe reconnection, however, would not provide the high-energy high-flux plasma observed. Recent studies by *Sandholt et al.*[1998] have suggested that for IMF clock angles of between 45 and 90 degrees, both high- and low-latitude reconnection could take place concurrently. Following the northward turning of the IMF at 1120±9 UT minutes at the magnetopause, however, the IMF clock angle is predominantly between -45° and 45°, and so it is not likely that low-latitude reconnection

was still occurring. There were two brief intervals starting at 1132 ± 9 UT and 1227 ± 9 UT when the IMF clock angle did exceed 45° in the magnetosphere. The start of the former interval corresponds to the time when the two populations were present on the same field line for the first time. This interval of higher clock angle is too short (~ 15 mins), however, to explain the whole interval of two populations. The second interval occurred when Polar was on closed field lines. If low-latitude reconnection was occurring then it could be postulated that the higher energy (50-200 keV) pulsed particles observed by Polar during northward IMF are simply the high-energy tail of the trapped field line particles that occupy the newly reconnected field lines during low-latitude reconnection. As low-latitude reconnection cannot be occurring then it is not evident as to how the mix of sheath-like and closed field line origin plasma can exist on the same field lines.

Several processes may be responsible for the modulation of particle signatures in the dayside magnetosphere. Firstly, transient reconnection, or flux transfer events can occur on a range of timescales. Reconnection between the IMF and the geomagnetic field at the low-latitude magnetopause results in flux tubes with a mixture of sheath and "trapped" plasma. These reconnected flux tubes appear to have plasma which is energy-dispersed due to the velocity filter effect. The large- and small-scale features observed by CAMMICE MICS and Hydra can therefore be interpreted in terms of FTEs: the large-scale pulsing has a repetition rate of 12-20 minutes, and the small-scale energy-dispersed "pulse-within-a-pulse" features have repetition rates of 2-4 minutes, both of which are within the expected repetition frequencies of transient and patchy-reconnection. It is generally assumed that FTEs have a repetition rate of between 8 and 10 minutes as observed in the ionosphere. However, *Lockwood and Wild (1993)* suggest that while the recurrence rate of FTEs (or inter-FTE period) is indeed found to have a median value of around 8 minutes, that the distribution of the inter-FTE intervals have a mode of 3 minutes, and lower and upper decile values of 1.5 minutes and 18.5 minutes respectively. *Kuo et al (1995)* also show that, although the median repetition rate of FTEs is between 7 and 8 minutes, the mode is significantly less than 8 minutes, at around 4 minutes.

Solar wind dynamic pressure pulses can also modulate plasma entry into the Earth's magnetosphere. When a pressure pulse impacts on the nose of the magnetopause then it is envisaged to compress the front of the magnetopause and produce a travelling indentation of the magnetopause that propagates in all directions (*Sibeck, 1990, 1992*). However, this scenario is unlikely to introduce plasma of magnetosheath origin into the magnetosphere, as this model assumes no reconnection ensues, and so the plasma taking part in this type of

modulation will be of high-energy closed field line origin. Figure 4.15 shows a cross-correlation analysis of solar wind dynamic pressure with the modulated particle populations observed by Polar over ± 24 minutes. From Figure 4.15 it is evident that no significant statistical peak is observed in this cross-correlation analysis, which indicates that there is no clear correlation of solar wind dynamic pressure variations with the particle modulations observed by Polar. A third mechanism that can result in the modulation of plasma populations is ULF wave activity. ULF wave activity, usually standing magnetohydrodynamic waves on resonant field lines, can perturb particles in the equatorial magnetosphere and cause modulation of precipitating fluxes. The period of such waves is dependent on the mode of oscillation and the length of the field lines, though is generally of the order of 5-10 minutes at high latitudes. Shorter periods have been observed, for example *Milan et al.* [1999] interpreted 2 minute period wave-like modulations of optical auroral features observed from the ground as the interaction between a ULF wave and magnetospheric particle populations. Figure 4.16 shows data from 10-12 UT of three ground magnetometer stations on Svalbard, situated close to the magnetic footprint of the spacecraft during this interval. From Figure 4.16, it can be seen that although there was modulation of the ground magnetic field during this interval, perturbations of similar frequencies to the PPS were not observed. Thus we conclude that the features observed in this case study are unlikely to be attributed to ULF wave activity. ULF waves of this nature would be expected to occur on closed magnetic field lines but Polar observes the PPS prior to entry into the closed field line region of the magnetosphere, as defined by higher-energy (50-200keV) ion populations (*Grande et al.*, 1997). Finally *Trattner et al.* [1999] showed that plasma populations can be modulated due to spatial structures existing in the cusp region. In the intervals presented by *Trattner et al.*, plasma populations were shown to be modulated on timescales of less than 2 minutes, shorter than those observed in this case study. In addition to this, spatial structures in the cusp region are indicative of a trapped plasma population, which would not exhibit the energy-dispersed signatures that Hydra observes during this interval, unless the events were isolated and gradient curvature drifting around from the flanks. The features presented in this case study exhibit energy dispersion, whereas those presented by *Trattner et al.* do not. Also, these features observed are not isolated events, and therefore it appears unlikely that there exists a spatial structure in the cusp region at this time.

The 12th October case study occurred during predominantly negative B_z and positive B_y conditions. The cusp pass by Polar was approximately three hours in length, but with great variability within this time. Between 13 and 15 UT the short-period pulsed behaviour (PPS)

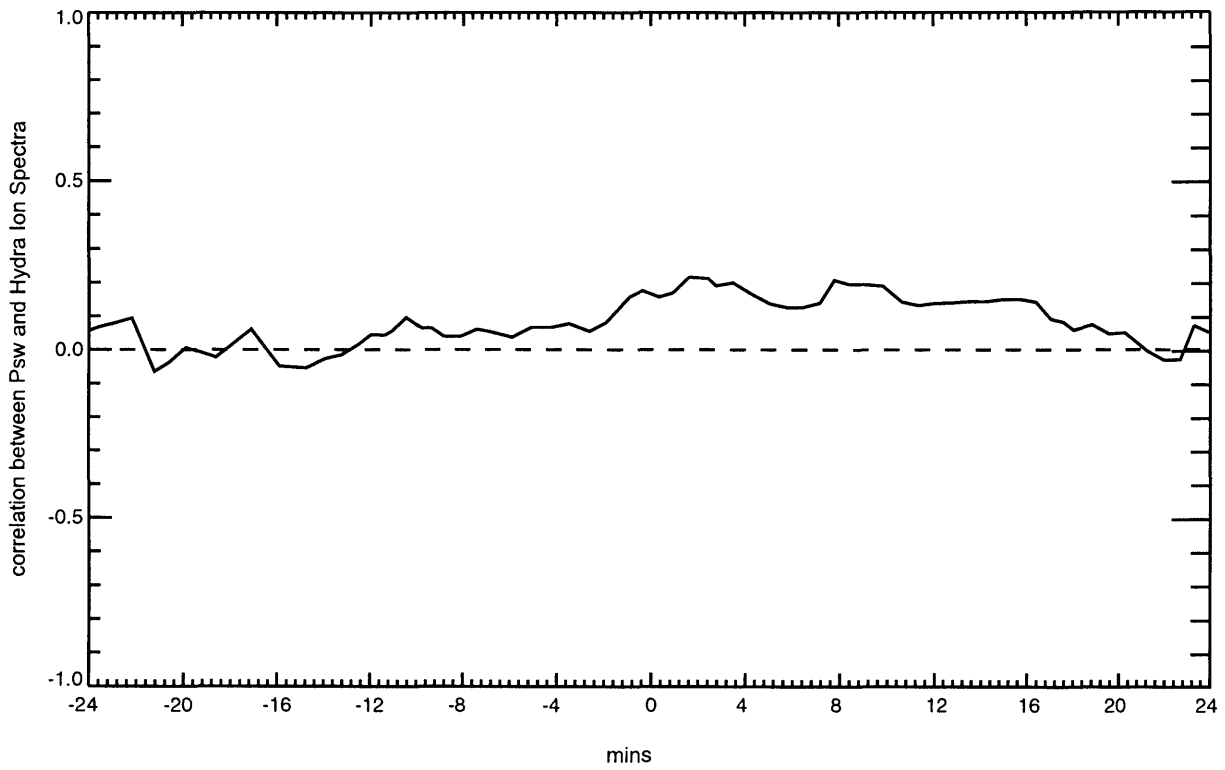


FIGURE 4.15: A cross-correlation analysis of the 1 keV Hydra Ion channel and the solar wind dynamic pressure. The Psw data has been lagged to the magnetopause before this analysis.

IMAGE Magnetometer Data - Svalbard

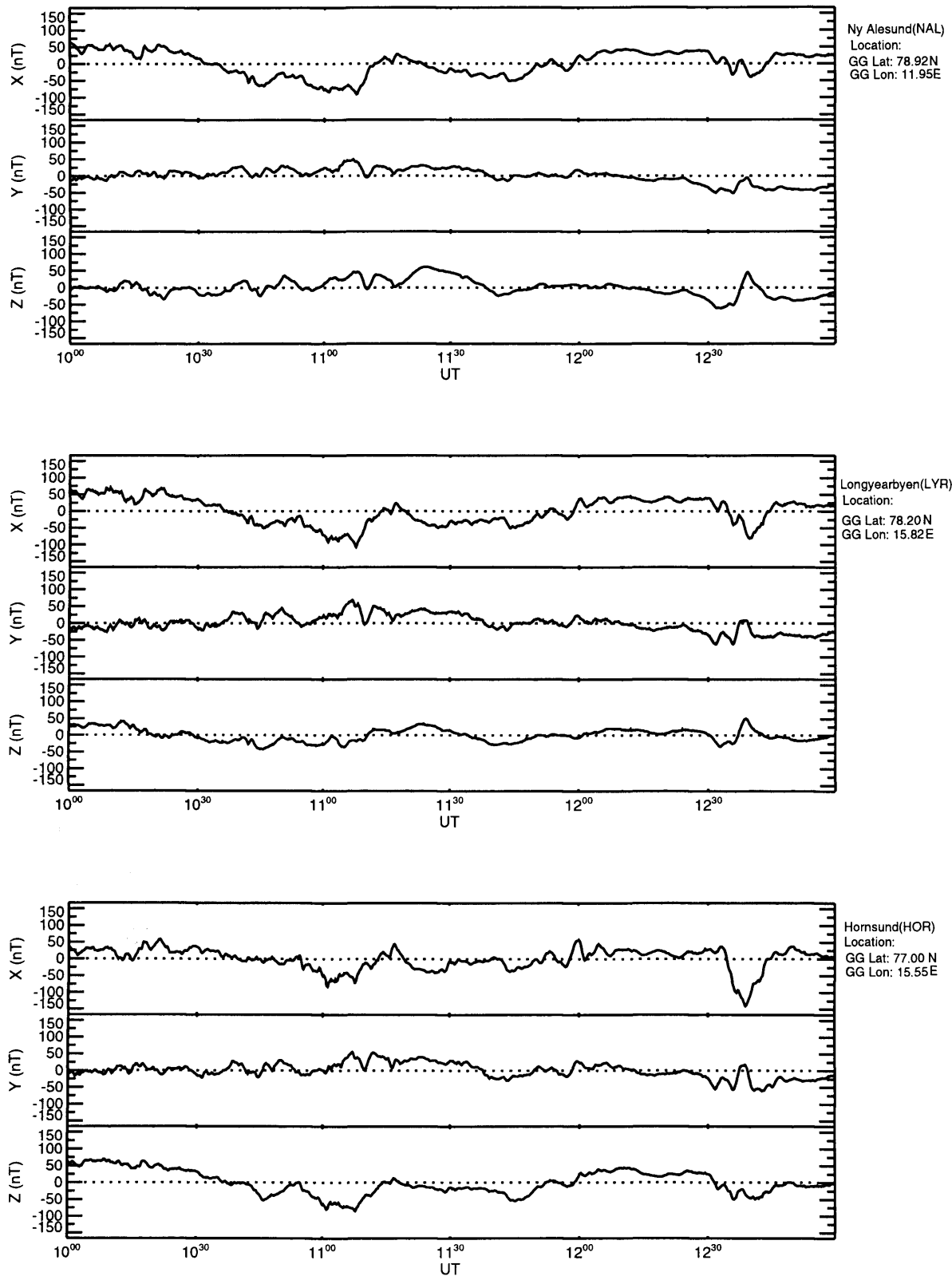


FIGURE 4.16: Magnetograms (X-, Y-, and Z-components) from three ground magnetometer stations close to the ionospheric footprint of Polar during 1000-1200 UT on 29th October 1996.

observed by CAMMICE MICS and Hydra is less intense than the 29th October cusp pass, and of a longer inter-PPS period (~2-6 minutes), though the features are still energy-dispersed. However, the period between 15 and 16 UT exhibits more intense energy-dispersed quasi-periodic perturbations of 2-4 minute duration, much like the 29th October case study.

The 20th October 1996 cusp pass also occurred during predominantly negative B_z and positive B_y conditions, though did not last for the same length of time, approximately an hour. During this time, PPS were observed on a quasi-periodic 2-4 minute timescale. These PPS also increased slightly with energy as the open-closed field line boundary approached. It is noted that the orbit of Polar during this pass differed slightly from the other two orbits in that this pass occurred in the post-noon sector, whereas the previous two case studies occurred slightly pre-noon. This may be responsible for the shorter time that the spacecraft was in the nominal mid-altitude cusp, or it may be simply that reconnection did not occur for such a long duration.

In the instances of the two further examples, both have been subject to the same rigorous testing that the first case study enjoyed. Both further examples did not show any correlation with solar wind pressure pulses or ULF wave activity. Neither did they show any indication that these PPS features are spatial in extent; the two further case studies also exhibit energy dispersion.

There are similarities and differences between the case studies. The similarities are that in all three examples, short-scale periodic pulsed particle signatures (PPS) are observed at a repetition rate of 2-4 minutes, and occur during predominantly southward IMF. In all three cases, Polar enters the mid-altitude cusp from the polar cap and exits onto closed field lines.

The noticeable difference between these three intervals is the duration of each event. This could be a consequence of three things; that non-steady or transient reconnection is taking place, that the spacecraft is not sampling exactly the same MLT/MLAT each orbit, or that the IMF is controlling the location of the PPS events. One of the main reasons that these three examples were chosen is because they all occurred during similar MLT/MLAT conditions thereby removing that likelihood. The magnitude and direction of the IMF B_y component can and will shift the location of the polar cusps merely by altering the location of the reconnection site on the magnetopause (*Gosling et al.*, 1990); a positive (negative) B_y will shift the reconnection site duskwards (dawnwards). Recent work by *Milan et al.* [2000] has

shown that the ionospheric footprint of the reconnection X-line can extend over a wide range of local times in the post-noon sector during positive B_y and southward IMF conditions. During the 20th and 29th October events the IMF B_y component is positive, thus shifting the reconnection site location duskwards, whereas the 12th October event was under negative B_y conditions thus shifting the reconnection site dawnwards. Therefore Polar is likely to be sampling the cusp at different locations, and so the time spent in the cusp by the spacecraft will differ. It may also be that as reconnection is transient and patchy, Polar will also be sampling a different number of reconnected flux tubes each time. In the 29th October case study, there is also a mixed magnetosheath/magnetospheric plasma population existing on the same flux tubes, whereas in the two other instances this is not the case. The 20th October case study also does not exhibit the same longer period pulsed signature as the other two examples.

4.5 Summary

This chapter first presents a multi-instrument case study of the signatures associated with the cusp observed by the CAMMICE, CEPPAD, Hydra and MFE instruments onboard the Polar satellite between 0900-1300 UT on the 29th October 1996. Characteristic signatures of the mid-altitude cusp include ions of energies 10^2 - 10^4 eV, and electrons of energy 10 - 10^3 eV, and a structured depression in the local magnetic field. During this particular passage through the cusp, ion fluxes in the 1-20 keV range were modulated quasi-periodically on a time scale of between 12 and 20 minutes, while energy dispersed ion count rates were observed close to the boundary between open and closed magnetic flux. The particle populations on the cusp field lines are dominated by H^+ and He^{++} ions (characteristic of magnetosheath-like plasma), and on closed field lines by uniform fluxes of high-energy (50-200 keV) protons, which are not pulsed. The pulsed particle events during this case study occur during both southward and northward IMF, with a significant, predominantly negative B_y component, but differ slightly in nature. After a northward turning of the IMF, Polar still observes the pulsed particle events, but magnetosheath-like particles and higher energy particles characteristic of closed field lines co-exist on the same magnetic flux tubes. It is not evident at this time as to how this mix of plasma regimes can exist on the same field line during this period of northward IMF. There is also a series of higher frequency (shorter period) pulsing detected, observed by Hydra of 3-4 minute duration, which, it is hypothesised, is caused by transient magnetic reconnection occurring at the low-latitude magnetopause. The simultaneous

observation of two different frequency components has not been previously reported in spacecraft observations of the mid-altitude cusp. To demonstrate that these observations are not unique, two further cusp passes during similar conditions (predominantly southward IMF and similar local times and latitudes) are presented. The short-period pulsed particle signatures were observed in all three examples, and the longer-period pulsing observed in two. The events differed in duration which is most likely due to the effect of IMF B_y on the location of the reconnection site, and hence the location of the polar cusp. There is also a slight difference in the orbital characteristics of these three cusp passes, in that the 12th and 29th October cusp passes were pre-noon and the 20th October cusp pass was post-noon, again affecting the sampling of the mid-altitude cusp.

The definitions employed in this chapter concerning the characteristics of the PPS observed by Polar will be employed in Chapters 5 and 6 in order to relate these signatures to plasma flows in the conjugate ionosphere, and to classify these PPS in terms of location and occurrence statistics respectively.

CHAPTER 5

Pulsed cusp particles and their ionospheric flow signatures

5.1 Introduction

This chapter presents a multi-instrument case study of the northern polar cusp from a variety of altitudes. The Polar spacecraft observed pulsed particle signatures (PPS) in the mid-altitude cusp, similar to those discussed in Chapter 4. During this period, the DMSP F13 satellite flew through the low-altitude cusp and through the ionospheric footprint of Polar immediately subsequent to measuring the low-altitude signature of transient reconnection. The ionospheric flows that reconnection at the dayside magnetosphere excites was sampled in the ionosphere by the CUTLASS HF radar system. CUTLASS measured the previously identified ionospheric signature of transient reconnection some several degrees of magnetic latitude poleward of the ionospheric footprints of these two spacecraft. The conclusions drawn in, and evidence presented by, Chapter 4 - that the PPS observed by Polar are most likely caused by transient magnetic flux transfer - can now be employed in tracing these signatures to lower altitudes and ultimately into the ionosphere. The unique nature of this experimental set-up allows the near-simultaneous sampling of the cusp at these three different altitudes, and provides an invaluable diagnostic of the cusp, and the tracing of solar wind plasma into the near-Earth environment.

5.2 Instrumentation Set-up

The locations of the instruments and spacecraft involved in this interval are outlined in this section to put the observations presented in Section 5.3 into context. The entire period of interest in this case study occurred between 0600 UT and 1300 UT on the 24th April 1999. At this time, Wind travelled from approximately $[X_{\text{GSM}}, Y_{\text{GSM}}, Z_{\text{GSM}}] \approx [4, -18, 23.5]$ to $[8.5, -16.5, 26]$ R_E between 0600 and 1200 UT respectively. The orbit of the Polar spacecraft on the 24th April 1999 is given in Figure 5.1 in SM co-ordinates. The arrow marks the period of

the orbit for the whole interval from 0600-1230 UT, when Polar was traversing the dayside magnetosphere, is marked by the black arrows and over the solar cap.

POLAR orbit 1999 114 (04/24) 02:39 UT to 1999 114 (04/24) 19:45 UT

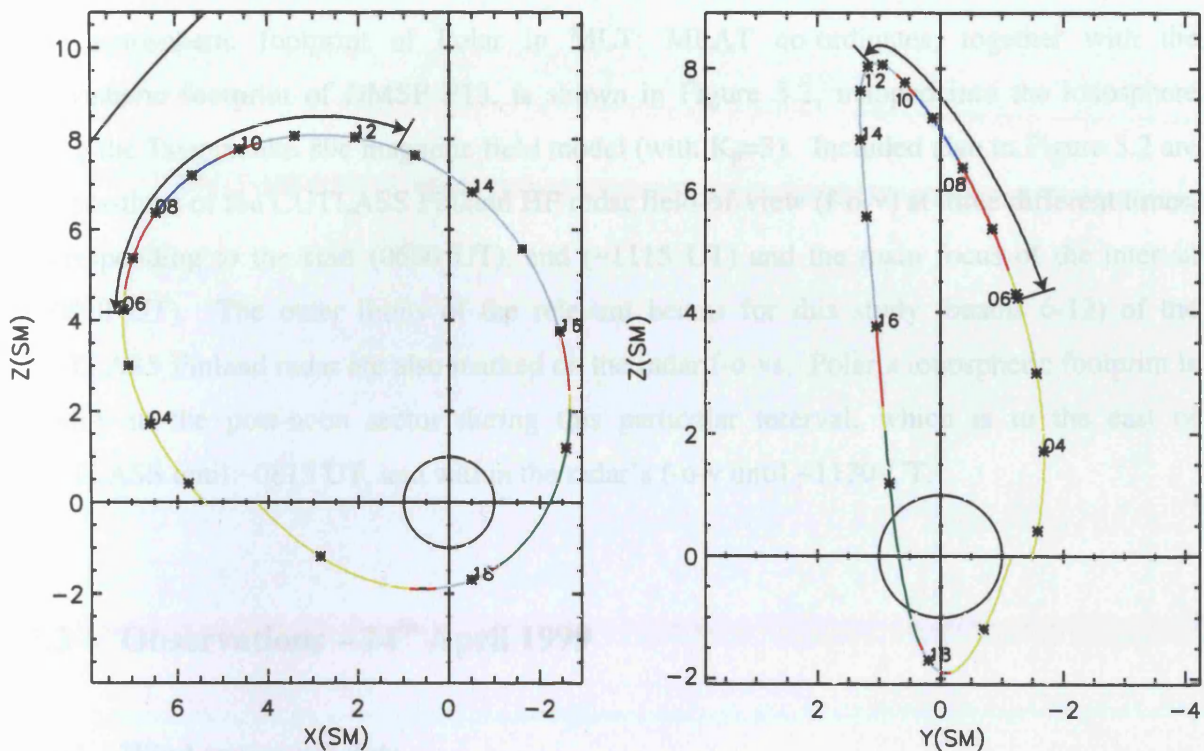


FIGURE 5.1: The orbit of the Polar spacecraft on the 24th April 1999 0240-1945 UT in SM coordinates. The period of interest 0600-1230 UT is marked by the black arrows.

What are the Magnetic Field (MF) and Solar Wind (SW) parameters? The observations are presented in Figure 5.1. Time delays in the interval are calculated by the method of Chen and Conner (1999) which is a more complex method than the one used here. The delay takes into account the actual orientation of the IMF plane. Given the solar wind velocity, a delay of approximately 8 ± 3 minutes is predicted. The interval occurs during a period of predominantly $B_z < 0$ of up to -3 nT and $B_y > 0$ of around $+5$ nT with low velocity approaching zero. B_z however, oscillates between 2.5 nT the interval during the B_z positive condition. Between 0625-0933 UT B_z is predominantly negative, though there is a positive excursion between 0650-0706 UT and an interval of $B_z > 0$ at 0710-0745 UT. Between 0745-1100 UT B_z again returns predominantly positive for approximately an hour until around 1100 UT when B_z returns negative. Solar wind velocity (data not shown) varies between 430-1400 km/s. The dynamic pressure, P_{sw} , starts at around 3 nPa and is highly variable with the maximum value at the end of the interval of around 7.3 nPa. The IMF clock angle θ is predominantly greater than 45° (during 11:00-11:45 UT).

interest for the whole interval from 0600-1230 UT, when Polar was traversing the dayside magnetosphere, through the nominal mid-altitude cusp and over the polar cap.

The ionospheric footprint of Polar in MLT: MLAT co-ordinates, together with the ionospheric footprint of DMSP F13, is shown in Figure 5.2, mapped into the ionosphere using the Tsyganenko 89c magnetic field model (with $K_p=3$). Included also in Figure 5.2 are the positions of the CUTLASS Finland HF radar field-of-view (f-o-v) at three different times, corresponding to the start (0600 UT), end (~1115 UT) and the main focus of the interval (~0830 UT). The outer limits of the relevant beams for this study (beams 6-12) of the CUTLASS Finland radar are also marked on the radar f-o-vs. Polar's ionospheric footprint is mainly in the post-noon sector during this particular interval, which is to the east of CUTLASS until ~0815 UT, and within the radar's f-o-v until ~1130 UT.

5.3 Observations – 24th April 1999

5.3.1 Wind spacecraft data

The Wind spacecraft Magnetic Fields Investigation (MFI) and Solar Wind Experiment (SWE) observations are presented in Figure 5.3. Time delays in this instance are calculated via the method of *Khan and Cowley* [1999] which is a more complex method than that utilised in Chapter 4 and documented by *Lester et al.* [1993], *Roelof and Sibeck* [1993], and *Peredo et al.* [1995]. Instead of assuming planar IMF phase fronts oriented perpendicular to the Sun-Earth line, the time delay takes into account the actual orientation of the IMF phase fronts. Given the solar wind velocity, a delay of approximately 8 ± 2 minutes is predicted between any features observed at Wind impinging on the magnetopause. The interval occurs during a period of predominantly $B_x < 0$ of up to -5 nT and $B_y > 0$ of around $+5$ nT with few excursions approaching zero. B_z however, oscillates between ± 4 nT, the interval starting under B_z positive conditions. Between 0625-0832 UT B_z is predominantly negative, though with a positive excursion between 0650-0706 UT and an interval of $B_z \approx 0$ at 0730-0745 UT. At 0832 UT B_z again returns predominantly positive for approximately an hour until around 0932 UT when B_z returns negative. Solar wind velocity (data not shown) varies between 430 and 460 ms^{-1} . The dynamic pressure, P_{sw} , starts at around 3 nPa and is highly variable between this value and the value at the end of the interval of around 2.3 nPa. The IMF clock angles throughout this period were predominantly greater than 45° (barring 1120-1145 UT

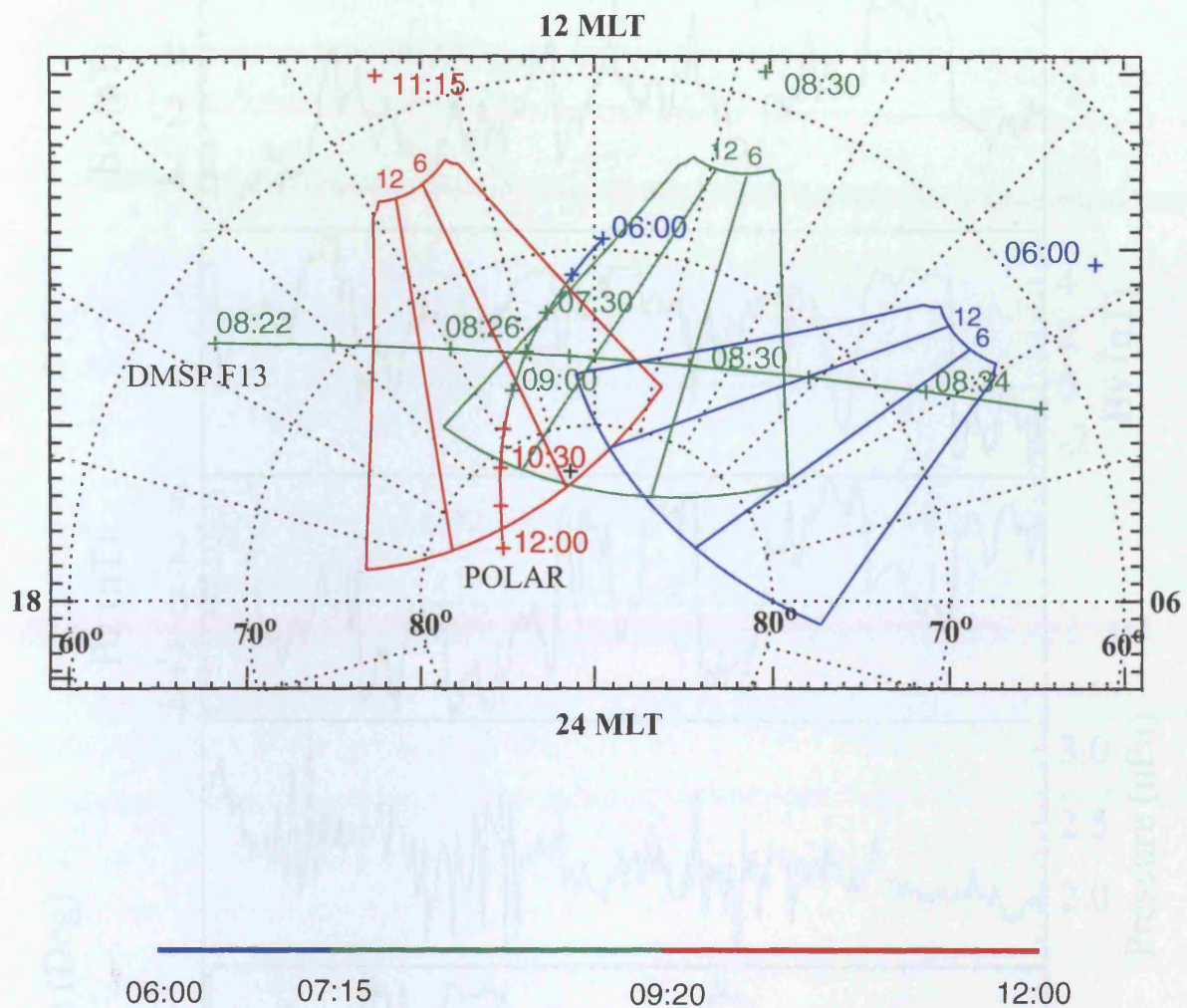


FIGURE 5.2: The ionospheric footprints of Polar (blue-green-red) and DMSP F13 (green) during the interval 0600-1200 UT. The CUTLASS Finland radar field-of-views are outlined for three times; 0600 (blue), 0830 (green) and 1115 (red) UT.

WIND data for 990424

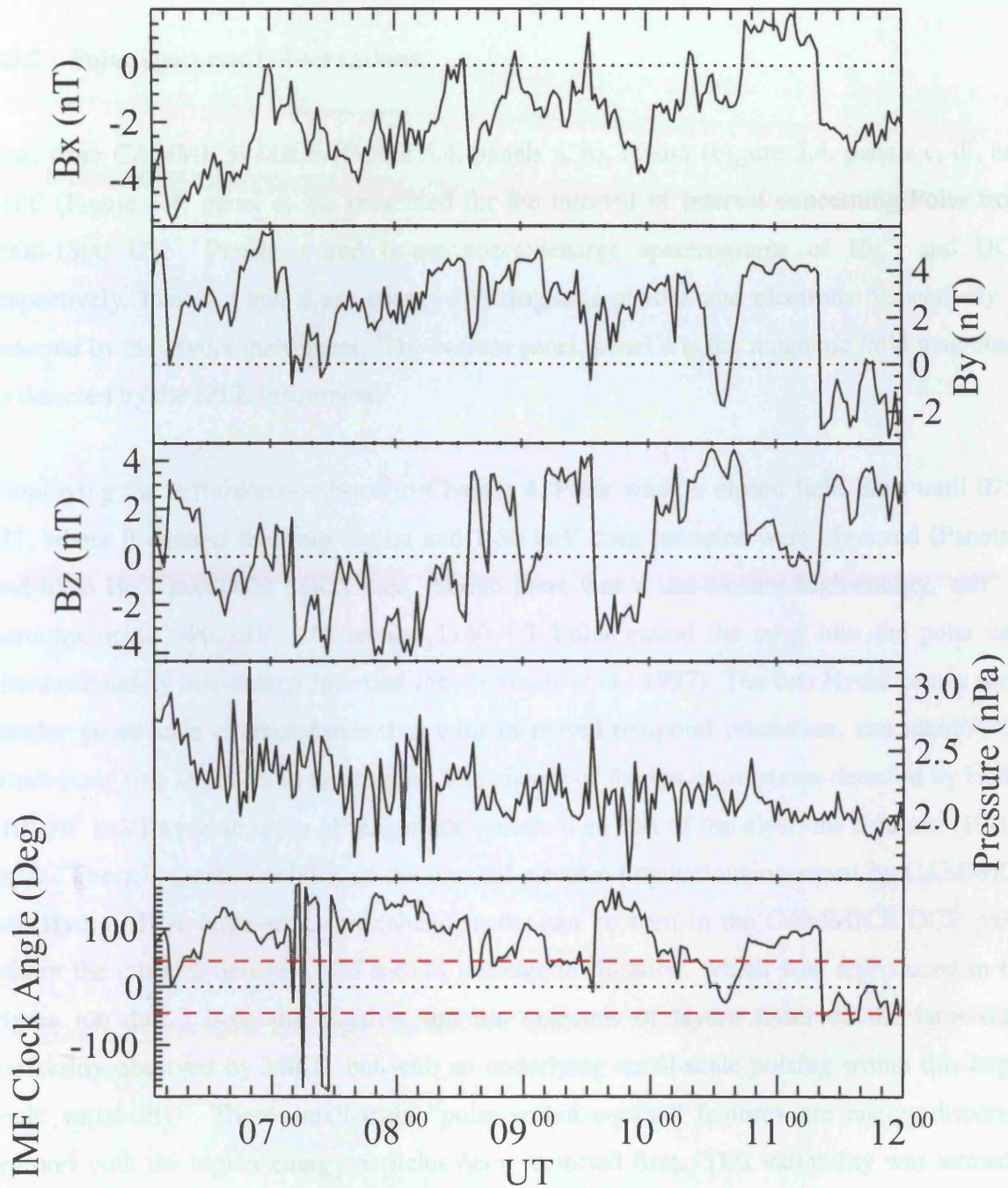


FIGURE 5.3: WIND MFI and SWE data for the 24th April 1999 06-12 UT.

and 1120-1200 UT) and greater than 90° between 0630 UT and 0830 UT, and 0930 UT to 1000 UT.

5.3.2 Polar spacecraft observations

Data from CAMMICE MICS (Figure 5.4, panels a, b), Hydra (Figure 5.4, panels c, d), and MFE (Figure 5.4, panel e) are presented for the interval of interest concerning Polar from 0900-1300 UT. Panels a and b are energy/charge spectrograms of He^{++} and DCR respectively. Panels c and d are energy spectrograms of ions and electrons respectively as detected by the Hydra instrument. The bottom panel, panel e is the magnetic field magnitude as detected by the MFE instrument.

Employing the definitions outlined in Chapter 4, Polar was on closed field lines until 0757 UT, where it entered the cusp region and 1-30 keV cusp particles were observed (Panels a and b) in He^{++} and DCR MICS data, though there was a less-intense high-energy “tail” of particles up to ~ 80 keV. At around 1140 UT Polar exited the cusp into the polar cap, characterised by low-energy low-flux ions (*Grande et al.*, 1997). The two Hydra panels show similar gross-scale characteristics, but with increased temporal resolution, can identify the small-scale fine structure in this region. The energy of the ion populations detected by Hydra (10^2 - 10^4 keV) were an order of magnitude greater than that of the electrons detected (10 - 10^3 keV). There is great variability in the ion and electron populations observed by CAMMICE and Hydra. Five large-scale ion enhancements can be seen in the CAMMICE DCR panel within the cusp of between ~ 20 and 40 minutes in duration, which was reproduced in the Hydra ion data. Both the electron and ion channels of Hydra observed the large-scale variability observed by MICS, but with an underlying small-scale pulsing within this large-scale variability. These small-scale “pulse-within-a-pulse” features are energy-dispersed features with the higher energy particles being detected first. This variability was termed a pulsed particle signature (PPS) in Chapter 4.

Figure 5.4e shows the total magnetic field observed, and the structured depression of the cusp during this interval, from around 0757 UT to 1130 UT, imposed on the background dipolar field. These negative excursions, of the order of 20 nT in magnitude, are associated with the PPS events; each individual particle pulse is associated with a decline in the local magnetic field of 20 nT which oscillates and recovers back to its original value superposed on a background dipolar-like field. Figure 5.5 displays the ion and energy spectra and magnetic

POLAR Ion and electron spectra

CAMMICE MICS, HYDRA and MFE

24/04/1999
0600-1230 UT

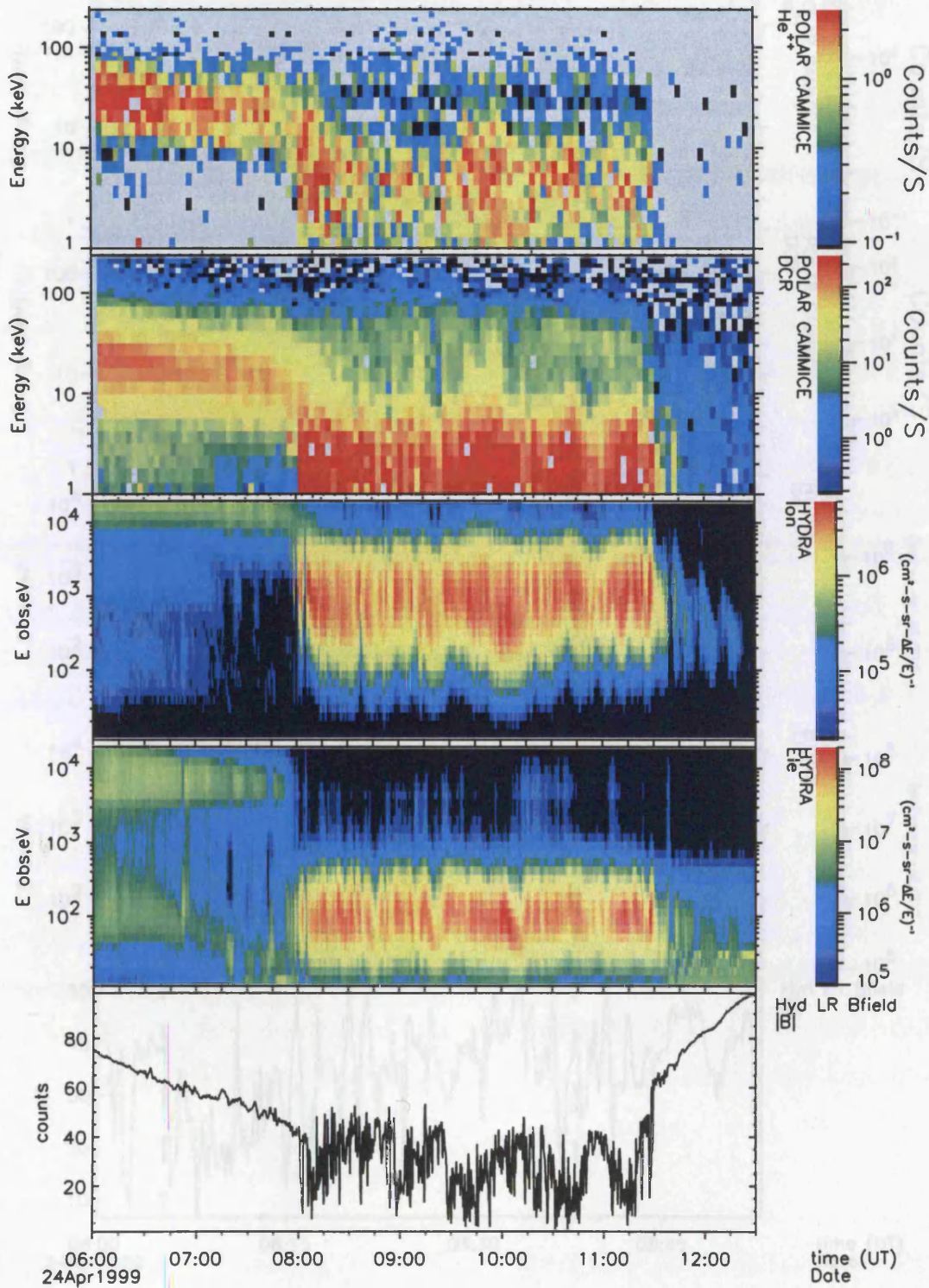


FIGURE 5.4: Polar Ion and Electron Energy spectra and magnetic field data for the 24th April 1999 0600-1230 UT.

POLAR Ion and electron spectra
 CAMMICE MICS, HYDRA and MFE

24/04/1999
 0800-0855 UT

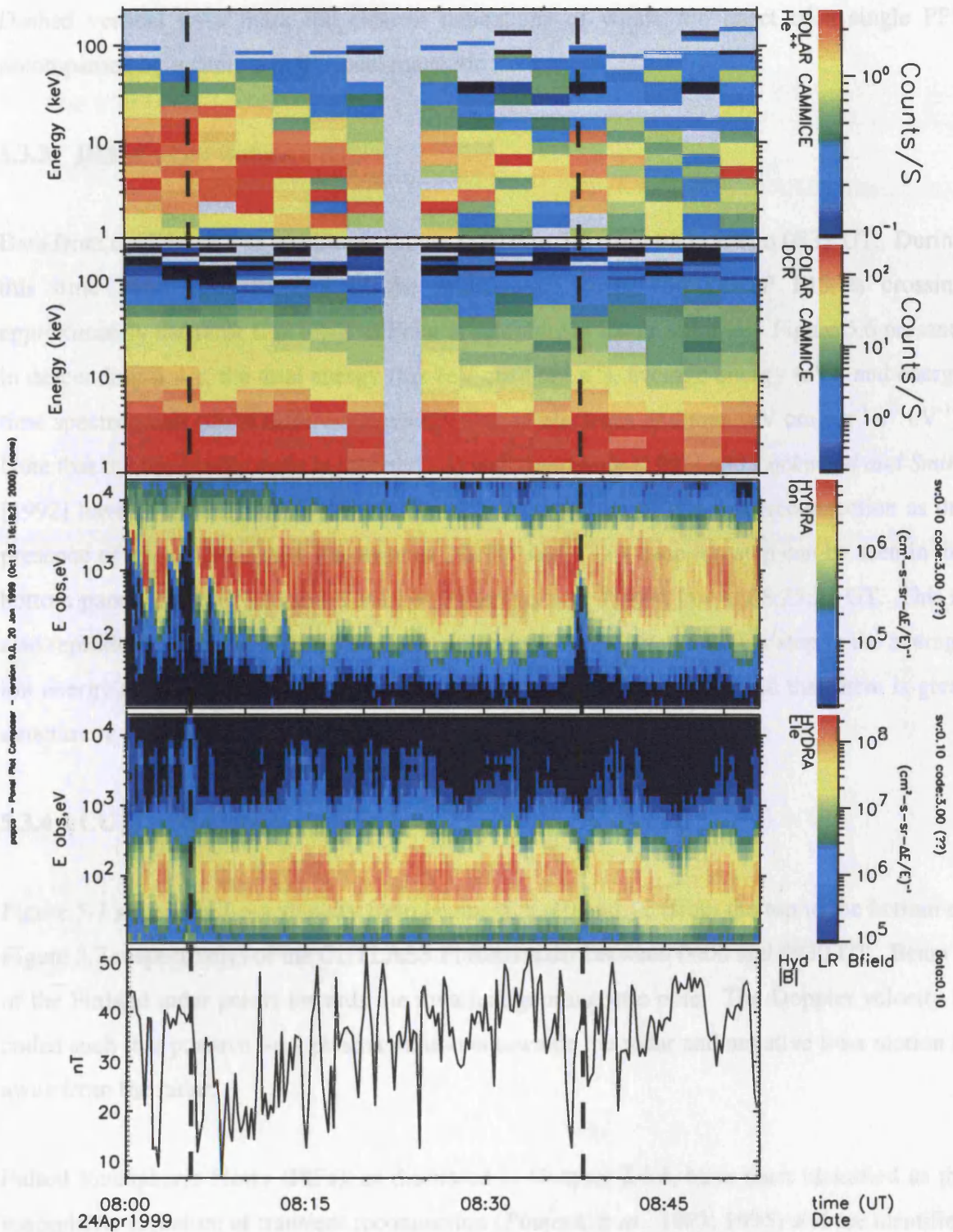


FIGURE 5.5: Polar ion and electron energy spectra over 0800-0855 UT on the 24th April 1999. Vertical dashed lines mark the clearest PPS enhancements concurrent with declines in the local magnetic field.

field observations over a shorter period spanning 08-09 UT in the same format as Figure 5.4. The small-scale variations in the total magnetic field are more clearly apparent in Figure 5.5e. Dashed vertical lines mark the clearest indications of where the onset of a single PPS accompanied by a decline in the local magnetic field.

5.3.3 DMSP observations

Data from the DMSP F13 satellite is shown in Figure 5.6 from 0822 UT to 0832 UT. During this time Polar detected PPS in the mid-altitude cusp, and DMSP F13 is crossing approximately the same flux tubes as Polar is sampling at lower altitudes. Figure 5.6 presents in descending order, the total energy flux ($\text{eV cm}^{-2} \text{sr}^{-1} \text{s}^{-1}$), average energy (eV), and energy time spectrograms of the differential energy flux of electrons and ions ($\text{eV cm}^{-2} \text{sr}^{-1} \text{s}^{-1} \text{eV}^{-1}$). Note that the ion energy scale is inverted. *Newell and Meng* [1991] and *Lockwood and Smith* [1992] have previously identified the low-altitude signature of transient reconnection as the presence of one or more cusp ion steps in DMSP data. This cusp ion step can be seen in the bottom panel of Figure 5.6, and is marked by the vertical dashed line at 08:25:23 UT. This is also reproduced noticeably in the average ion energy, which shows a clear step in the average ion energy from 10 keV to 500 eV around this time also. It is also noted that there is great structure in the electron spectrogram.

5.3.4 CUTLASS Finland observations

Figure 5.7 shows the l-o-s velocity from beams 6, 8, 10 and 12 (from the top to the bottom of Figure 5.7 respectively) of the CUTLASS Finland radar between 0600 and 0930 UT. Beam 5 of the Finland radar points towards the invariant geomagnetic pole. The Doppler velocity is coded such that positive l-o-s plasma motion is towards the radar and negative l-o-s motion is away from the radar.

Pulsed Ionospheric Flows (PIFs), as discussed in Chapter 2.4.4, have been identified as the ionospheric signature of transient reconnection (*Pinnock et al.*, 1993; 1995) and are identified as poleward moving transients with large negative l-o-s velocities in HF radar data. However, *McWilliams et al.*, 2000 proposed a stringent method of investigating backscatter that does not necessarily exhibit large l-o-s velocities. Through the technique of fast fourier transforming (FFT-ing), periodic velocity perturbations with frequencies similar to the visible PIF events can be detected in other beams of the radar. This effectively allows the

SUPERDARN PARAMETER PLOT 24 Apr 1999⁽¹¹⁴⁾

Hankasalmi: vel

unknown scan mode (-6314)

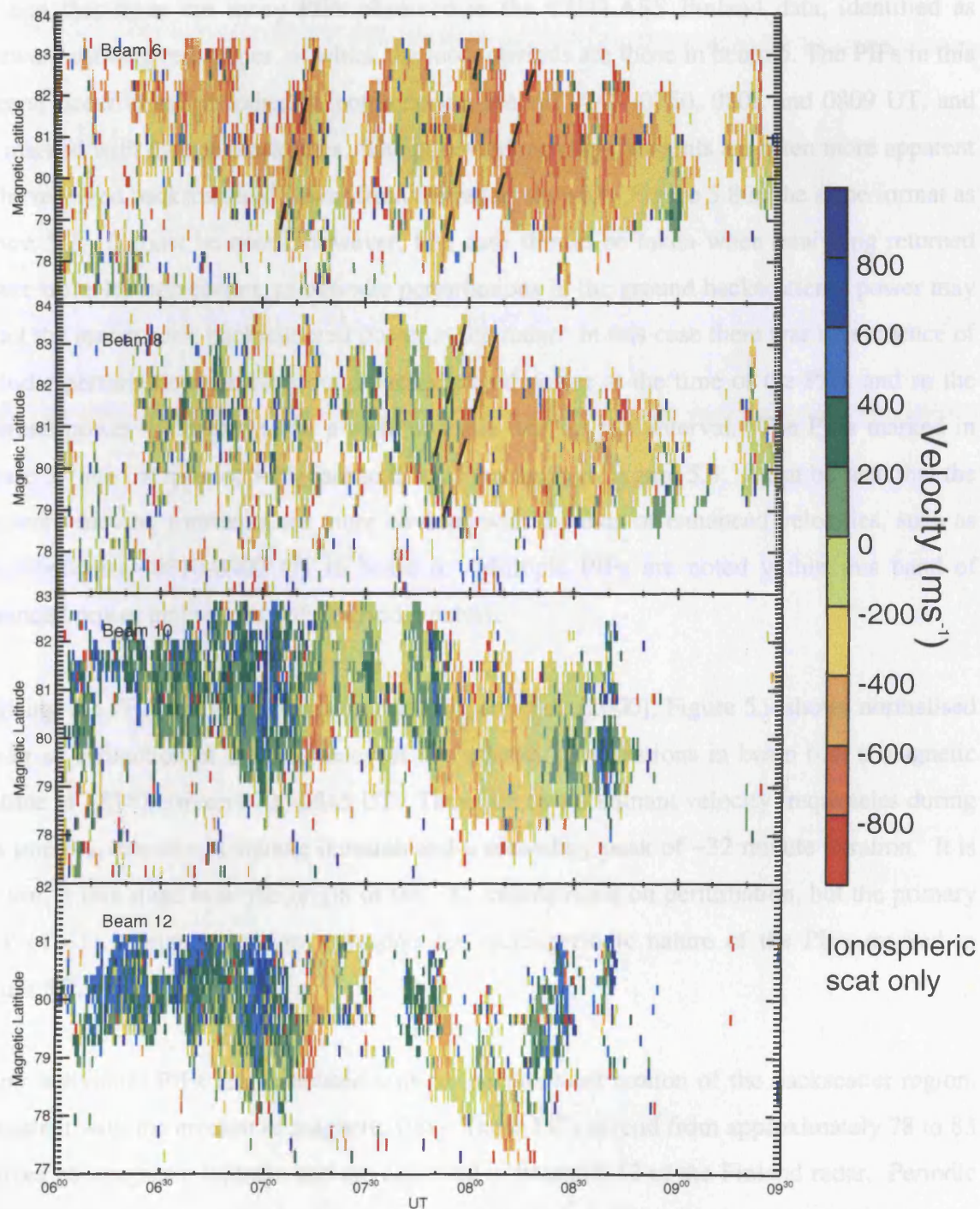


FIGURE 5.7: CUTLASS Finland Latitude Time Velocity (LTV) plots for beams 6, 8, 10, and 12 between 0600-0930 UT on the 24th April 1999. Several PIFs are marked with overplotted dashed black lines in beams 6 and 8, where the PIFs are more visually apparent. The periodic velocity perturbations in beams 10 and 12 are identified using FFT techniques (after *McWilliams et al.*, 2000.)

identification of PIFs even when the radar beams point in a direction in which the l-o-s velocity does not have a significant poleward component. Poleward propagating backscatter was first observed in beams 6 and 8 of the Finland radar several minutes after a southward turning of the IMF is calculated to impinge in the magnetopause (~0625 UT). Beams 10 and 12 observed strong flows towards the radar prior to, and after the southward turning. It can be seen that there are many PIFs observed in the CUTLASS Finland data, identified as poleward moving red stripes, of which the most obvious are those in beam 6. The PIFs in this interval occur quasi-periodically, commencing around 0740, 0750, 0802 and 0809 UT, and are marked with dashed black lines. The poleward moving transients are often more apparent in the received backscattered power from the radar, shown in Figure 5.8 in the same format as Figure 5.7. It must be noted, however, that care should be taken when analysing returned power from 1½-hop scatter, as periodic perturbations in the ground backscattered power may affect the ionospheric backscattered power at the radar. In this case there was no evidence of periodic perturbations in the ground backscattered power at the time of the PIFs and so the returned power is deemed to be a valid analysis tool for this interval. The PIFs marked in Figure 5.7 are overplotted with dashed black lines again in Figure 5.8. It can be seen that the poleward moving transients are more obvious within bands of enhanced velocities, such as those between ~0810-0900 UT in beam 6. Multiple PIFs are noted within this band of enhanced power and velocity of a periodic nature.

Utilising the FFT analysis detailed in *McWilliams et al.* [2000], Figure 5.9 shows normalised power as a function of the frequency of the *velocity* perturbations in beam 6 at a magnetic latitude of ~81° between 0700-0845 UT. There are two dominant velocity frequencies during this interval, one of ~11 minute duration and a secondary peak of ~32 minute duration. It is unclear at this stage as to the origin of the ~32 minute duration perturbation, but the primary peak of ~11 minute repetition represents the quasi-periodic nature of the PIFs marked in Figure 5.7.

Many individual PIFs are associated with an equatorward motion of the backscatter region, consistent with the erosion of magnetic flux. These PIFs extend from approximately 78 to 83 degrees geomagnetic latitude, and are observed in beams 0-12 of the Finland radar. Periodic velocity perturbations in beams 10-12 were observed, though not so visually obvious as those in beams 5-8, but have been subject to Fourier Analysis techniques (*McWilliams et al.*, 2000) in order to quantify their quasi-periodic behaviour. The signal measured by the radar from these poleward-moving transients strongly depends on the direction of the plasma flow with

SUPERDARN PARAMETER PLOT

24 Apr 1999⁽¹¹⁴⁾

Hankasalmi: pwr_l

unknown scan mode (-6314)

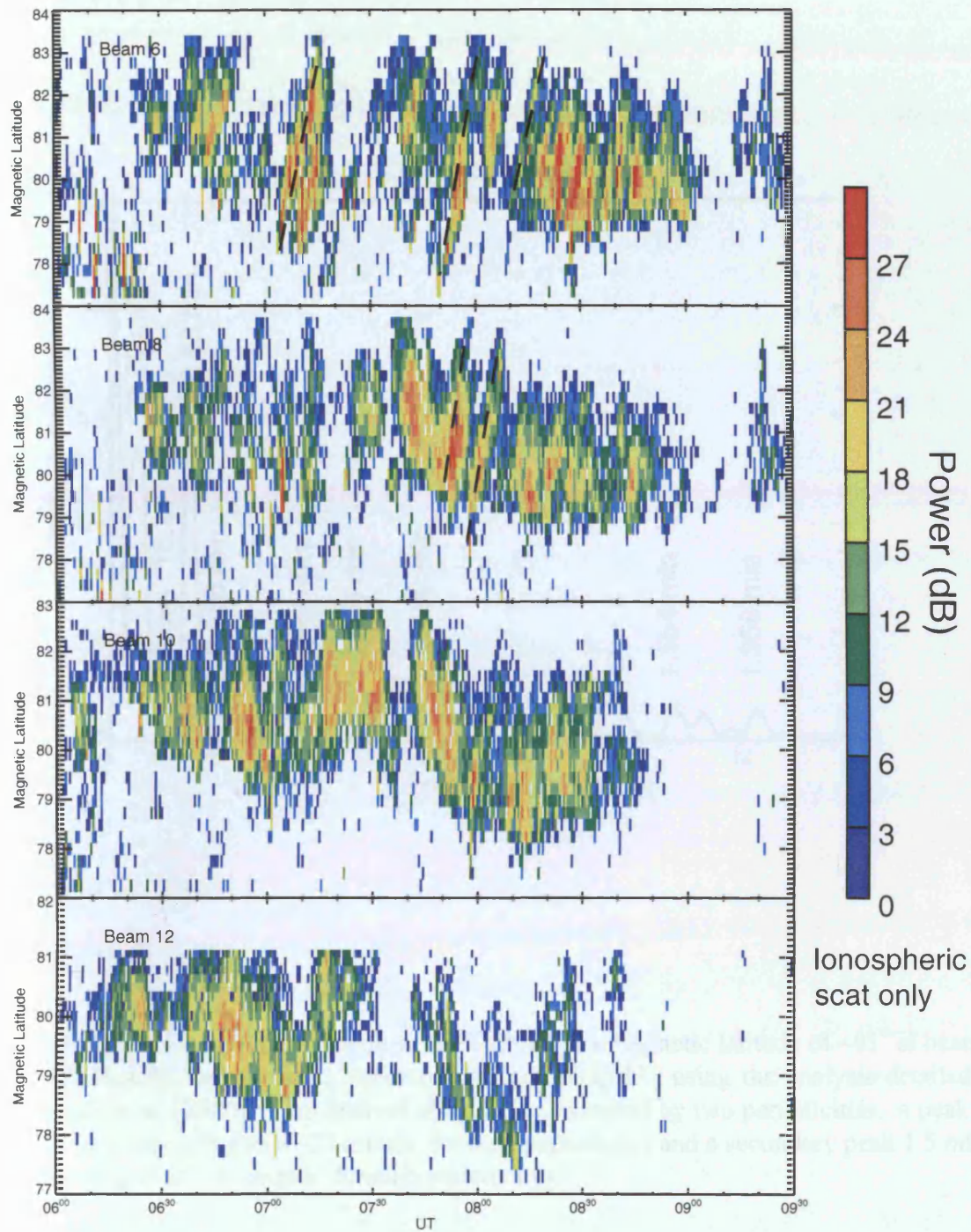


FIGURE 5.8: The complementary CUTLASS Finland Latitude-Time Power plots for beams 6,8,10 and 12 between 0600-0930 UT on the 24th April 1999. The poleward-moving features are more clearly seen in the returned power than the Doppler velocity shown in Figure 5.6.

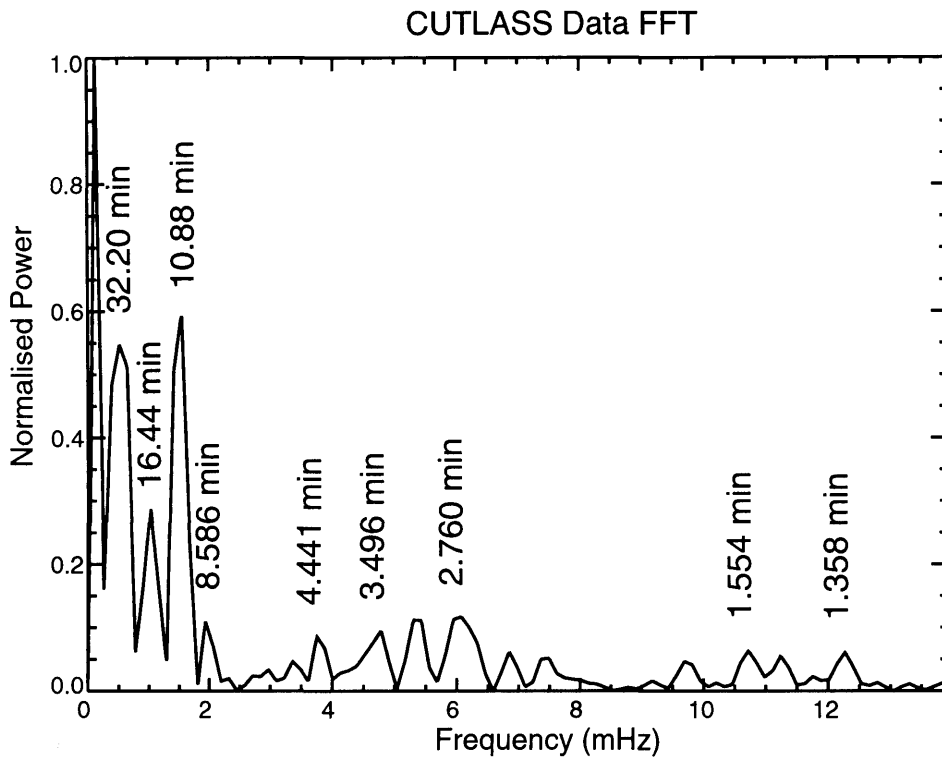


FIGURE 5.9: A Fast Fourier Transform (FFT) through a magnetic latitude of $\sim 81^\circ$ of beam 6 of the CUTLASS Finland radar between 0700 and 0845 UT using the analysis detailed in *McWilliams et al.* [2000]. This interval of study is dominated by two periodicities, a peak at 0.5 mHz (corresponding to a ~ 32 minute duration periodicity) and a secondary peak 1.5 mHz, corresponding to an ~ 11 minute duration periodicity).

respect to the radar beam direction. Beam 5 of CUTLASS Finland, for example, may have the most obvious pulsed signature as it points toward the geomagnetic pole. If these flux tubes were being dragged anti-sunward then plasma motion naively should have a significant component towards the geomagnetic pole. Of course, this motion of the flux tubes strongly depends upon the IMF direction and any IMF B_y will append a significant east-west component to the plasma flow, but still with a significant anti-sunward component.

There are also several changes in the direction of the l-o-s velocity within these Latitude Time Velocity (LTV) plots, which may be attributed to variations in the IMF. From top to bottom, Figure 5.10 displays two LTV plots for beams 8 and 10, and IMF B_x , B_y and B_z time-shifted by 8 minutes from the Wind satellite into the ionosphere. Dashed lines mark the significant IMF changes in B_y and B_z . At ~0614 UT the effects of a brief period of $B_z \sim 0$ calculated to occur in the ionosphere, which is concurrent with an enhancement (green to blue) in l-o-s velocity towards the radar. At 0630 UT a southward turning of the IMF is calculated to impinge on the magnetopause with the resultant effect of a flow change in beam 10 of the CUTLASS Finland radar from plasma flow strongly towards the radar (blue) to strongly away from the radar (orange-red). At ~0715 UT a change from IMF $B_z \sim 0$ and positive B_y to $B_z < 0$ and $B_y \sim 0$ precedes another enhancement of the l-o-s plasma flow, illustrated in beam 8 as increased flow away from the radar and in beam 10 as a flow reversal from towards to away from the radar. At ~0820 UT, another brief period of IMF $B_z \sim 0$ caused a l-o-s velocity change, from large negative velocities to strong positive l-o-s velocities. Finally, just after 0840 UT the IMF rotates northward which results in the loss of ionospheric backscatter.

Figure 5.11 illustrates 12 consecutive scans by the Finland radar in magnetic latitude: magnetic local time co-ordinates with the Polar spacecraft's ionospheric footprint, mapped into the ionosphere using the Tsyganenko 89c model, marked by the black cross. Polar is approximately 5° of MLAT and ~2 hours of MLT from the centre of the ionospheric activity. During this time period, 0800-0806 UT, there is a background l-o-s plasma flow away from the radar, with the evolution of a PIF marked by black arrows. The PIF "breaks off" the background flow at ~07:59:46 UT and traverses into the polar cap before dying away at ~08:03:20 UT, possibly as a result of the PIF passing beyond the radar f-o-v. A further PIF forms, breaks off at 08:05:42 UT, and evolves away from the radar again.

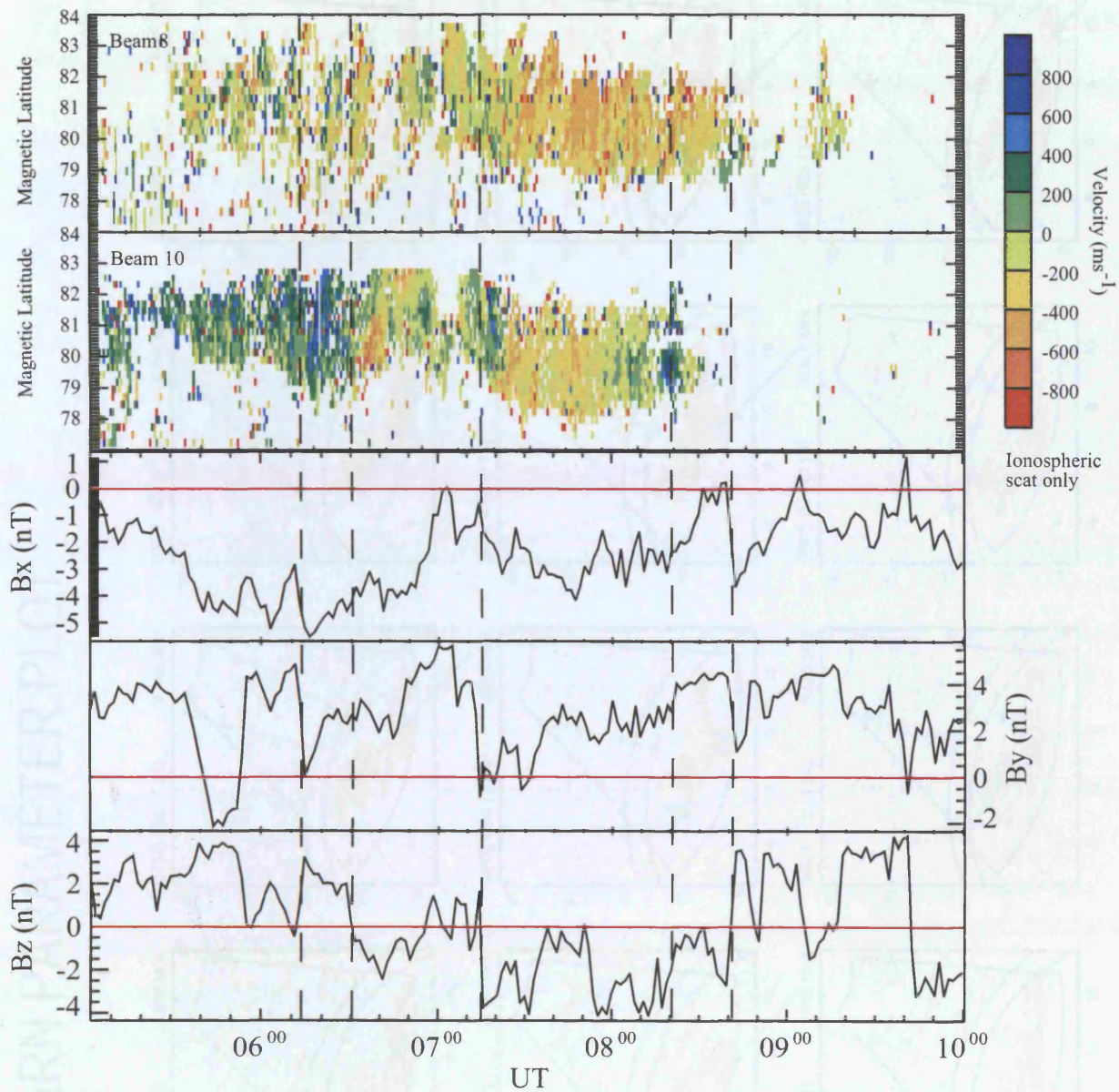


FIGURE 5.10: From the top in descending order CUTLASS Finland beams 8 and 10, and IMF B_x , B_y and B_z observed at WIND and time-shifted by 8 minutes for the IMF phase fronts to reach the ionosphere from the spacecraft. Significant IMF changes are marked by vertical dashed lines.

FIGURE 5.11: Twelve consecutive scans of the CUTLASS Finland radar in MUF-MI AC mode, showing the evolution of the ionospheric footprint of the radar (black dots) and the appropriate scans as a black trace. The evolution of an individual PFC is marked with the black arrow, with the start of a new PFC marked by a blue arrow.

SUPERDARN PARAMETER PLOT

Hankasalmi: vel

24 Apr 1999 (114)
unknown scan mode (-6314)

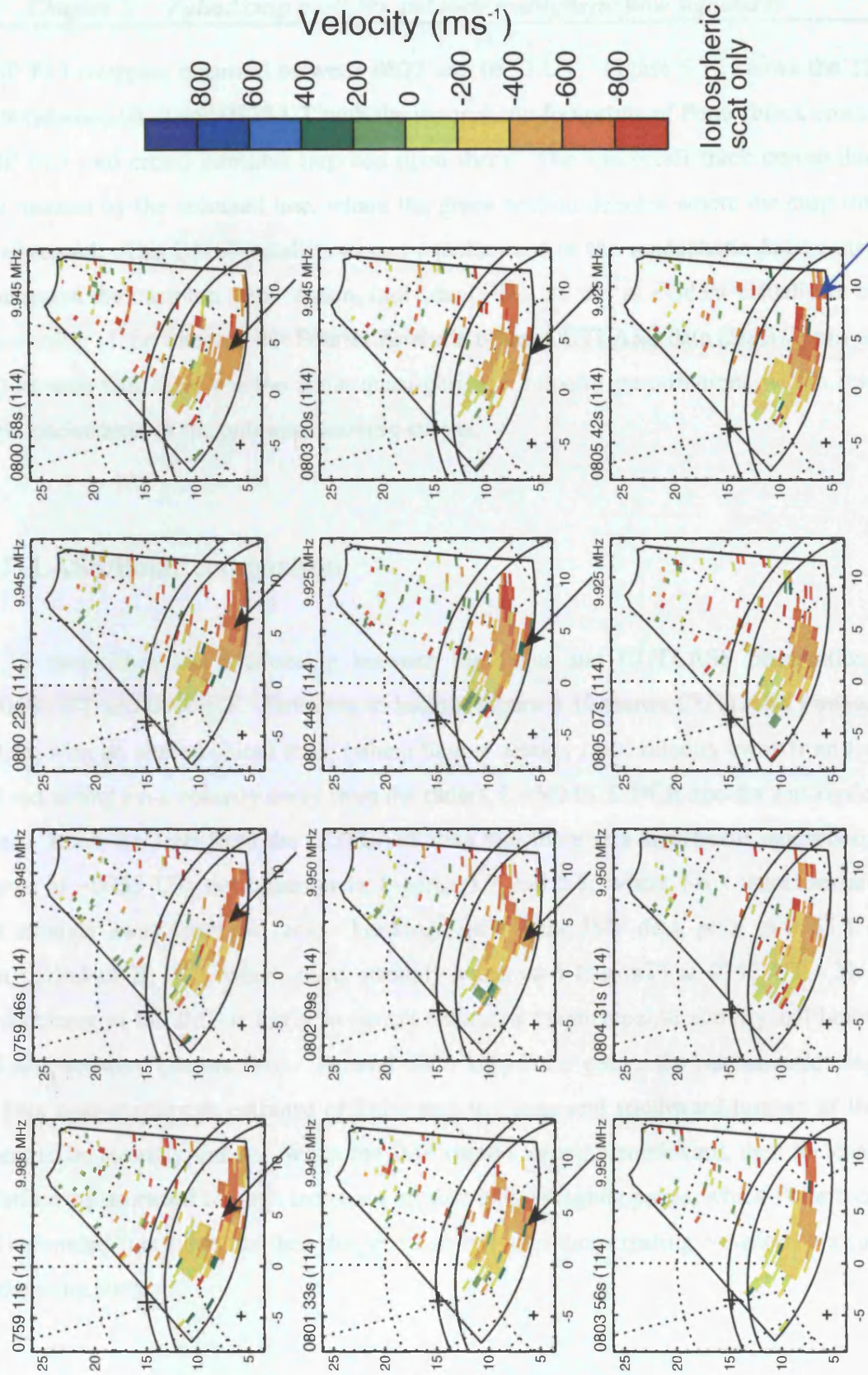


FIGURE 5.11: Twelve consecutive scans of the CUTLASS Finland radar in MLT: MLAT coordinates between 0800-0806 UT on 24th April 1999. The ionospheric footprint of the Polar satellite is imposed on the appropriate scans as a black cross. The evolution of an individual PIF is marked with the black arrow, with the start of a new PIF marked as a blue arrow.

The DMSP F13 overpass occurred between 0822 and 0830 UT. Figure 5.12 shows the 12 radar scans between 0822 and 0829 UT with the ionospheric footprints of Polar (black cross) and DMSP F13 (red cross) satellites imposed upon them. The spacecraft track during this interval is marked by the coloured line, where the green section denotes where the cusp ion step was observed. The DMSP satellite passes equatorward of the ionospheric backscatter whilst it detected the cusp ion step. Again, individual PIFs are not as evident visually as in the earlier section of the interval, but Fourier Analysis of the CUTLASS data (*McWilliams et al.*, 2000) reveals that there are the same quasi-periodic velocity perturbations within this ionospheric backscatter as the poleward moving stripes.

5.4 CUTLASS/Polar comparison

Figure 5.13 establishes the relationship between the Polar and CUTLASS observations between 0600 UT and 0900 UT. From top to bottom Figure 5.10 shows CUTLASS Finland beam 8 data, with an altered colour scale (where blue is weakly l-o-s velocity away from the radar and red strong l-o-s velocity away from the radar), CAMMICE DCR spectra and Hydra Ion spectra. It can be seen from the CUTLASS data that there is a significant ionospheric flow change at ~0755 UT, not apparent in Figures 5.7 and 5.8, where l-o-s velocities are enhanced strongly away from the radar. Looking again at the IMF data, prior to 0755 UT there is a period of $B_z \sim 0$, which turns strongly southward (~ -4 nT) at 0752 UT. This southward turning of the IMF is likely to permit enhanced magnetopause activity and hence increased anti-sunward plasma flow. Around 0800 UT, Polar enters the mid-altitude cusp region. This near-concurrent entrance of Polar into the cusp and southward turning of the IMF appear to be strongly linked. When the IMF rotates strongly southward, then the cusp may be shifted equatorward through increased erosion at the magnetopause, which Polar then enters. The eroded flux tubes are then dragged anti-sunward thus creating enhanced plasma flows in the ionosphere.

5.5 Discussion

A case study is presented of the pulsed particle signatures observed in the mid-altitude cusp during predominantly negative B_z conditions. Polar enters the cusp at 0757 UT concurrently with a negative B_z turning and exits the cusp at ~1140 UT when the IMF is northward. There

SUPERDARN PARAMETER PLOT

Hankasalmi: vel

24 Apr 1999⁽¹¹⁴⁾

unknown scan mode (-6314)

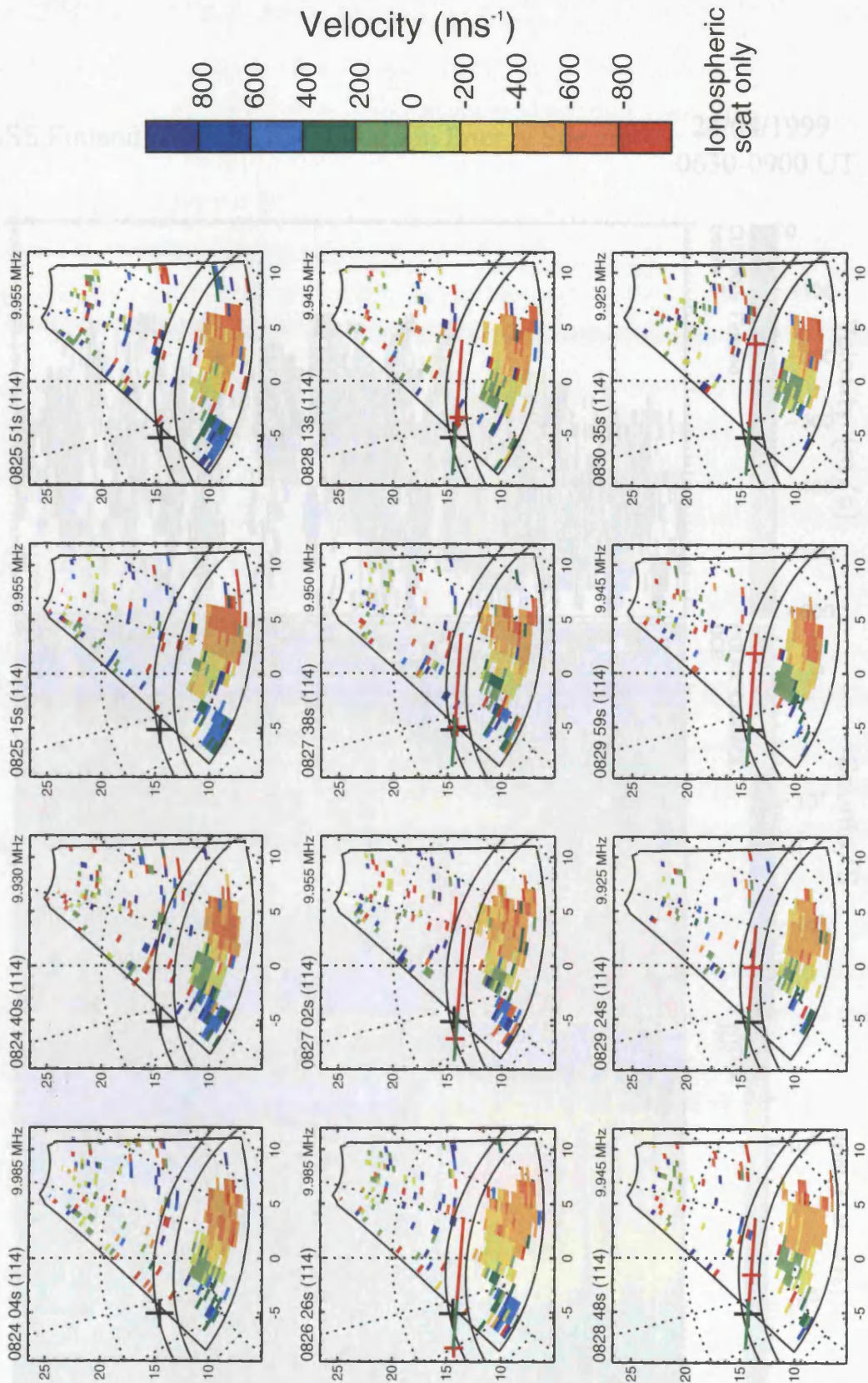


FIGURE 5.12: Twelve consecutive scans of the CUTLASS Finland radar in MLT: MLAT coordinates between 0824-0830 UT on 24th April 1999. The ionospheric footprints of the Polar (black cross) and DMSP F13 (red cross) satellites are imposed on the appropriate scans. The orbit of DMSP is denoted by the coloured line, where the green section denotes the location of the observed "cusp ion step".

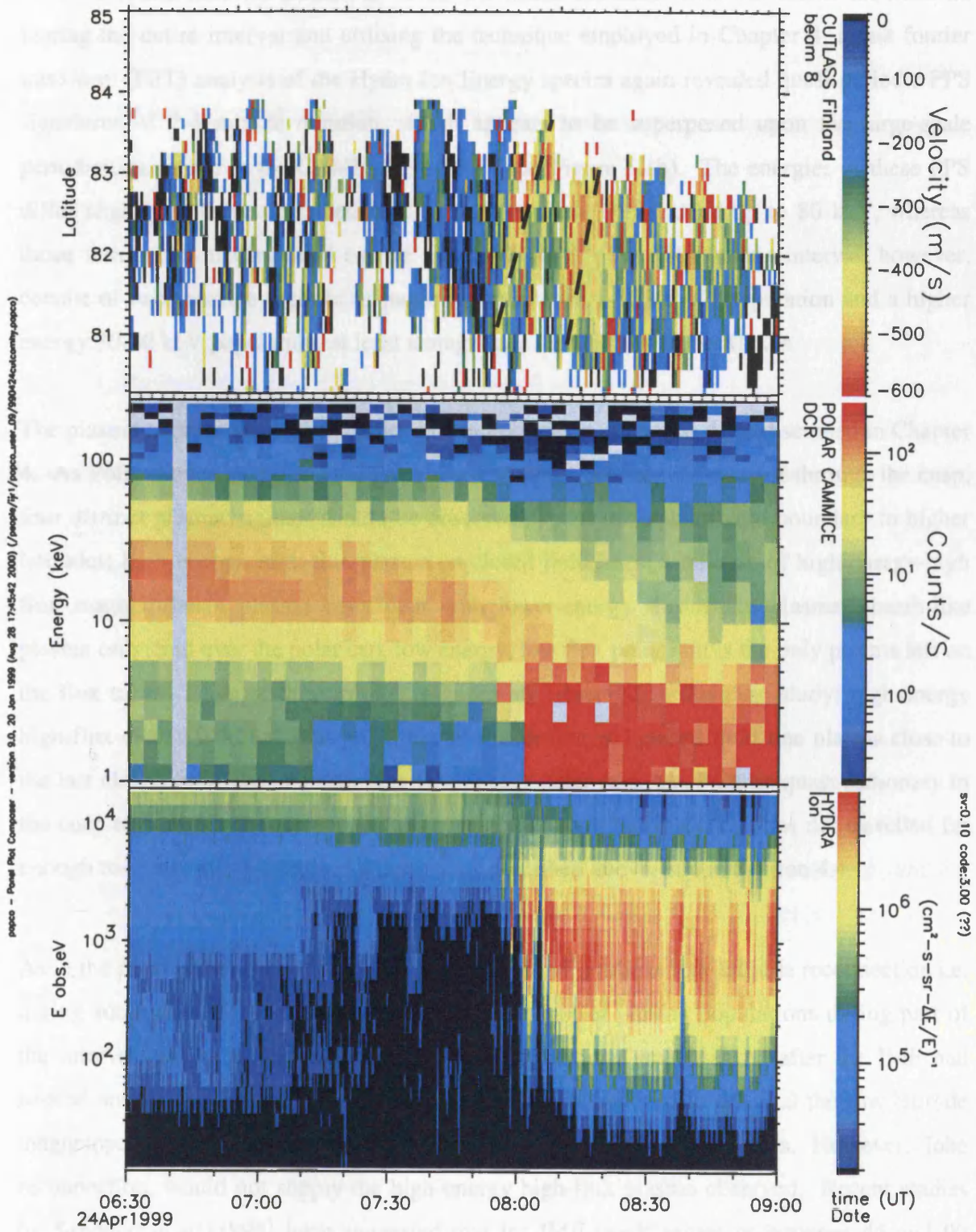


FIGURE 5.13: Comparison of CUTLASS Finland HF radar data and Polar Ion Energy spectra for 0630-0900 UT on the 24th April 1999.

are several IMF reversals within this interval with respect to B_z . Incorporating the time-delay calculated for the IMF phase fronts to reach the magnetopause from Wind, the IMF rotated northward from a southward configuration at ~0842 UT, back to a southward direction at ~0940 UT, and northward again at ~1010 UT which continues until the end of the interval. During the entire interval and utilising the technique employed in Chapter 4, a fast fourier transform (FFT) analysis of the Hydra Ion Energy spectra again revealed quasi-periodic PPS signatures of 2-4 minute duration, which appears to be superposed upon the large-scale periodicities visible in the CAMMICE MICS data (Figure 5.3b). The energies of these PPS differ slightly to those described in Chapter 4, as these PPS extend up to 80 keV, whereas those introduced in Chapter 4 extend up to 100 keV. The PPS in this interval, however, consist of two separate regimes of particles; an intense 1-30 keV/Q population and a higher energy 30-80 keV population, at least a magnitude less in the number fluxes.

The plasma regimes that Polar should encounter during a cusp pass were discussed in Chapter 4. As Polar moves along its orbit from above the pole towards the equator through the cusp, four distinct plasma regimes should be observed. From the equatorward boundary to higher latitudes; high-energy, high-flux plasma on closed field lines; a mixture of high-energy-high flux magnetosheath plasma coincident with lower-energy sheath-like plasma; sheath-like plasma only; and over the polar cap, low energy, low flux polar rain is the only plasma left on the flux tubes. Three of these plasma regimes are observed in this case study; high-energy high-flux closed field line plasma, a mix of sheath-like and closed field line plasma close to the last closed field line, and low-flux low-energy polar rain. As Polar is quasi-stationary in the cusp region then it is assumed that in this case study the spacecraft has not travelled far enough to detect solely sheath-like plasma, as described above, and in Section 4.4.

As in the previous chapter, the scenario outlined above assumes low-latitude reconnection i.e. during southward IMF, and, while it explains the mix of plasma populations during part of the interval presented, the concurrent plasma populations are observed after the IMF had rotated northward. In classical theory, reconnection is believed to cease at the low latitude magnetopause, although it can occur at higher latitudes in the lobes. However, lobe reconnection, would not supply the high-energy high-flux plasma observed. Recent studies by Sandholt *et al.*[1998] have suggested that for IMF clock angles of between 45 and 90 degrees i.e. B_y dominated, both high- and low-latitude reconnection could take place concurrently. If low-latitude reconnection was occurring then it could be postulated that the higher energy (~30-80 keV) pulsed particles observed by Polar during northward IMF are

simply the high-energy tail of the trapped field line particles that occupy the newly reconnected field lines during low-latitude reconnection. Following each northward turning of the IMF, the IMF clock angles are predominantly above 45° for the entire interval, barring brief periods, the most notable 1033-1040 UT, and 1127-1200 UT. Hence low-latitude reconnection may still be occurring and the high-energy plasma population on open field lines could simply be the high-energy tail of the trapped field line plasma that has been newly reconnected.

The 24th April 1999 case study was subjected to the same rigorous testing that the examples in Chapter 4 enjoyed, to demonstrate that there was no correlation between the PPS and solar wind pressure variations or ULF wave activity. It was noted that the MFE instrument provided the largest indication of variability on the approximate time-scales of P_{SW} . However, there was no significant correlation between P_{SW} and the MFE instrument over a large range of time lags ($-20 \leq \tau \leq 20$ mins). Neither did this case study show any indications that the PPS were a spatial feature, not a temporal one. This case study also exhibited energy-dispersed PPS signatures. The PPS are once more consistent with those generated by transient reconnection, with all other mechanisms capable of generating these features again excluded.

The ionospheric footprint of the DMSP F13 satellite crossed the ionospheric footprint of the Polar spacecraft at around 08:26:30 UT, thus effectively capturing a “snapshot” of the flux tube on which Polar was situated. At 08:25:15 UT DMSP detected the leading edge of the cusp ion step which maps close to the open-closed field line boundary (OCFLB). This cusp ion step is energy-dispersed and exists until 08:28:42 UT where this step fades out, and the satellite has crossed the flux tube that Polar is situated upon. Using a simple reconnection model (*Lockwood and Davis, 1996*) to calculate the travel time for any feature observed by Polar to reach DMSP, it was hoped that a single pulsed particle enhancement at Polar could be matched to the cusp ion step observed by DMSP. Unfortunately the cusp ion step was calculated to occur during an indiscernible period of overlapping pulsed particle detection, shown in detail in Figure 5.5. This could be due to one of two reasons; that there is in fact no one to one relationship between these signatures; or that because DMSP flew through the Polar’s footprint (and the flux tube that it was situated on) quickly and it did indeed view a snapshot of the continuous plasma injection. However, this null result is still an important one, in that though there was no exact 1:1 relationship arising from this study, the fact still remains that Polar also observed dispersed ion signatures at mid-altitudes prior to and after,

DMSP observed a dispersed ion signatures at low altitudes. This, then is a topic for further research, to either prove or disprove the relationship between these two signatures at different altitudes.

Both satellites pass several geomagnetic degrees equatorward of the PIFs observed in the ionosphere by the CUTLASS Finland HF radar, though this could be due to a number of factors; one being inherent inaccuracies in the Tsyganenko 89c model. Recent work has shown that the Tsyganenko model may not be as accurate in the cusp as it is in other places, perhaps due to absence of open field lines within the model. The most obvious place that this is inaccurate is the cusp region (Fenrich *et al.*, 2000). However, altering the input values of K_p did not alter the ionospheric tracing locations significantly and so it is thought that (at least in this case) the Tsyganenko 89c model is reasonably accurate. As DMSP flies a mere 830 km above the ground and is traced to 100 km altitude then there are no significant errors in these calculations, despite the model used.

The ionospheric signatures of FTEs in HF radar data have been identified by many as poleward moving transients (Pinnock *et al.*, 1993; 1995, Rodger and Pinnock, 1997, Provan *et al.*, 1998, 1999a, b). During this interval, numerous bands of poleward moving transients have been identified, the most obvious starting at 0740, 0750, 0802 and 0809 UT, thus giving a quasi-periodic repetition rate of ~11 minutes. The interval starting at ~0810 UT concealed a number of periodic velocity perturbations within beams 5-8, which, when subject to FFT analysis reveals a repetition rate of 6-8 minutes.

The I-o-s ionospheric plasma velocities respond to the discontinuities in the IMF on a near 1:1 basis. At ~0625 UT plasma velocities are enhanced following a southward turning of the IMF, are retarded as the IMF rotates towards zero B_z at 0655 UT, and enhanced again as B_z returns negative at ~0715 UT. At 0755 UT the IMF B_z rotates from around zero again to strongly negative, which enhances convection away from the radar and creates another series of PIFs, which is concurrent with Polar entering the mid-altitude cusp. At ~0842 UT the IMF returns northward, which signals the cessation of ionospheric backscatter in beams 5-8, which had already terminated at ~0830 UT in beams 9-12 when IMF $B_z \sim 0$.

The near-stationary nature of Polar's orbit through the northern polar cusp provides an insight into the evolution of flux tubes over the spacecraft, which in this case study is complemented by the snapshot through these flux tubes by the near-conjugate pass of the DMSP F13

spacecraft. Both satellites unfortunately were situated equatorward of the excited ionospheric flows during this interval. However, whilst Polar was sampling PPS in the mid-altitude cusp, numerous pulsed ionospheric transients were observed by CUTLASS. These transients are seen to evolve at the poleward edge of the ionospheric backscatter, break off from the main band of scatter and propagate anti-sunward into the polar cap before dying away. During this time Polar was observing PPS events in the mid-altitude cusp and DMSP observed a cusp ion step as it crossed close to the flux tube that Polar was situated upon.

Comparison of the CUTLASS and Polar data reveals that after a turning of the IMF from $B_z \sim 0$ to B_z strongly negative ionospheric plasma convection is enhanced and strong pulsed ionospheric transients are observed. Only minutes later Polar enters the cusp region. The likely scenario is that the erosion of closed magnetic flux tubes shifts the cusp equatorward enough for Polar to enter this region.

5.6 Summary

This chapter presents a case study of pulsed particle signatures (PPS) in the mid-altitude cusp, based upon the criteria outlined in Chapter 4, together with near-conjugate observations of the low-altitude and ionospheric cusps. A southward turning of the IMF and the erosion of magnetic flux moves the cusp equatorward. Several minutes after this IMF turning, pulsed particle signatures are observed in the mid-altitude cusp, and enhanced plasma convection and PIFs were excited in the ionosphere and observed by the CUTLASS Finland HF radar. The DMSP F13 spacecraft cuts through the flux tube that Polar is situated upon and detects a cusp ion step immediately prior to this conjugate position of closest approach whilst Polar is observing PPS. The ionospheric footprints of Polar and DMSP are situated a number of magnetic degrees equatorward and slightly eastward of the pulsed ionospheric transients, though all three features are signatures of transient and patchy reconnection. Although in this case study, no exact 1:1 relationship between these individual elements of the three signatures exist, the two spacecraft observed dispersed ion signatures, indicative of ephemeral reconnection, close to the ionospheric footprint of a third signature of transient flux transfer, that of pulsed ionospheric flows.

Chapter 4 presented the first observations of pulsed particle signatures (PPS) of two discrete frequencies associated with ephemeral reconnection. This chapter has built upon these

observations in that these PPS have now been linked to the low-altitude signature of transient reconnection observed by DMSP, and the poleward moving transients observed in the ionosphere by the CUTLASS radar system. It is hoped that future studies would envisage the spacecraft footprints closer to the poleward edge of the backscatter observed by CUTLASS, and that some relationship, 1:1 or otherwise, may arise between these three signatures at different altitudes.

CHAPTER 6

Pulsed Particle Signature Statistics

6.1 Introduction

This Chapter presents a statistical study of the pulsed particle signatures (PPS) observed by Polar in the mid-altitude northern polar cusp region. The definitions of PPS developed and refined in Chapters 4 and 5 are used to compile a stringent set of criteria to determine the exact nature and location of PPS events. A statistical database was compiled from a subset of over half of the orbits from May 1996 to November 1999. This inherent limitation which is due to the continuous variation in the local time of the orbital apogee of the satellite will not affect the validity of the statistics gained. The location characteristics of PPS were investigated with respect to the prevailing IMF orientation and gross-scale variations in the solar wind dynamic pressure. From this study it is clear that PPS occur in large percentages (> 30%) over a wide range of latitudes and local times (50-75° MLAT and 9-15 MLT). It is also possible to conclude that the location of PPS is moderately controlled by the solar wind and IMF. Strong evidence is presented of a link between the IMF B_z component and the location of pulsed particle signatures which adds further weight to the conclusions of Chapters 4 and 5. In addition to IMF orientation control, solar wind dynamic pressure also affects the location and occurrence statistics of PPS. The evidence presented here provides further proof that mid-altitude PPS are the dispersed plasma features associated with the observation of newly-opened flux tubes generated by transient magnetic flux transfer.

6.2 Statistical criteria

The following definitions were used to classify the cusp passes made by Polar into those that exhibited PPS, and those that did not. Pulsed particle signature events required all of the following characteristics:

- a transition from a closed field line (50-200 keV) plasma to polar cap (low-energy low-flux) plasma with “cusp plasma” of 1-30 keV H^+ and He^{++} ions separating the two in the CAMMICE MICS data,
- variable intensity ion enhancements (pulses) of “cusp plasma” detected by CAMMICE MICS,
- small-scale “pulse-within-a-pulse” ion enhancements of approximately 2-6 minute duration detected by the Hydra ion channel within the “cusp plasma”,
- accompanying pulsed electron enhancements of similar duration detected by the Hydra electron channel,
- a structured depression of the total magnetic field superposed on a background dipolar-like field measured by the MFE instrument.

Two northern cusp passes by Polar selected at random from spring 1998 are shown in Figures 6.1 and 6.2. Both cusp passes occur in the post-noon sector between 13-14 MLT. Figure 6.1 is an example that satisfies the criteria detailed above for a PPS event. From top to bottom, Figure 6.1 shows energy spectrograms of CAMMICE MICS He^{++} , CAMMICE MICS DCR, Hydra ion spectrograms and Hydra electron spectrograms, and magnetic field magnitude for the 4th April 1998 1200-1800 UT. From Figure 6.1a and b, a clear transition between closed-cusp-polar cap field lines can be observed in both He^{++} and DCR spectrograms; ~ 10 -200 keV He^{++} and DCR indicative of plasma of closed field line origin before ~ 1445 UT, low-energy low-flux plasma characteristic of the polar cap after ~ 1730 UT and variable intensity enhancements of ~ 1 -30 keV H^+ and He^{++} ions between these two regimes. Figure 6.1c and d show the small-scale “pulse-within-a-pulse” behaviour of the ions and electrons of ~ 2 -6 minute duration detected within this “cusp plasma”. A structured depression of total magnetic field observed by the MFE instrument (Figure 6.1e) was also present during this cusp pass. It is precisely this category of cusp pass that forms the basis of this study.

Figure 6.2 shows a cusp pass from the 15th March 1998 from 1200-1800 UT in the same format as Figure 6.1. The Polar cusp pass shown in Figure 6.2 was discarded from the statistical study on several grounds. From Figure 6.2a and b, a plasma population of ~ 10 -100 keV is observed between 1230-1600 UT in CAMMICE DCR and He^{++} , and low-energy low-flux plasma characteristic of the polar cap is observed soon after. However, there is little evidence of the variable “cusp plasma” that is so typical within this region present during this orbit. There is a low-energy tail to the closed field line plasma between ~ 1345 -1615 UT but not enough to verify that “cusp plasma” is observed. Furthermore, Figure 6.2c shows no

POLAR Ion and Electron Energy Spectra

CAMMICE MICS and HYDRA

04/04/1998
1200-1800 UT

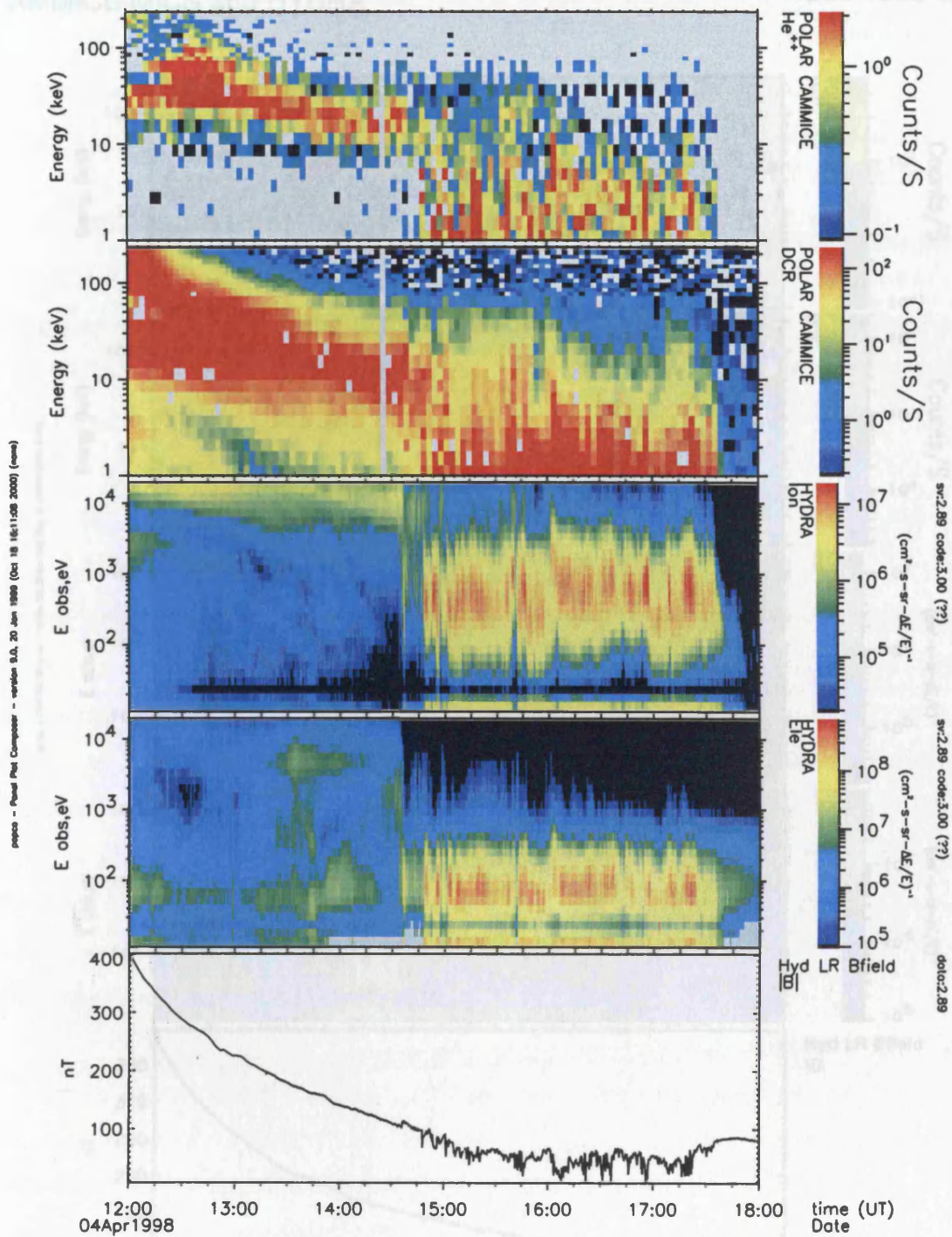


FIGURE 6.1: A typical interval included into the Polar PPS statistical study from the 4th April 1998 12-18 UT. Intervals that are included in the statistical study have both large-and small-scale perturbations in the CAMMICE DCR and Hydra ion channels respectively, as the spacecraft passes through the cusp region. The small-scale perturbations are also energy-dispersed. Also shown is the total magnetic field magnitude, which shows a structured depression superposed upon a background dipolar-like field.

POLAR Ion and Electron Energy Spectra

CAMMICE MICS and HYDRA

15/03/1998
1230-1800 UT

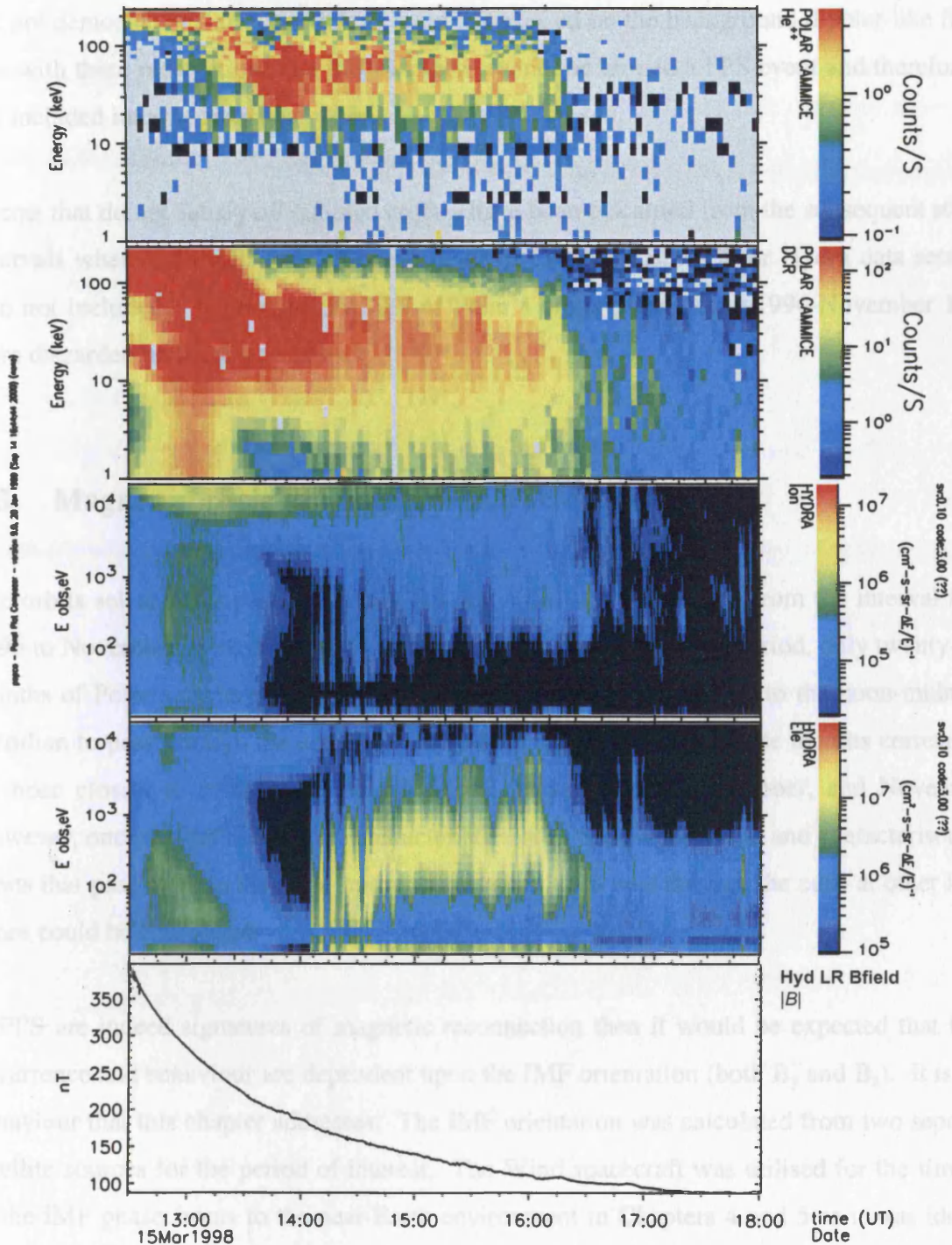


FIGURE 6.2: An example of a cusp pass which was not included in the PPS statistical study from the 15th March 1998 1230-1800 UT. This interval was not considered for inclusion due to the lack of a clear dispersed periodic ion signature observed in the Hydra ion channel. However, there is also an indication that there are no, or rather, few ions of magnetosheath (1-30 keV) origin, as *Grande et al.* [1997] defined. Also the magnetic field magnitude during this period exhibits no structured depression superposed on the observed dipolar field.

significant ion population of 10^2 - 10^4 keV associated with entry into the cusp region, though a weak and variable Hydra electron signature is observed during this time. In addition to the lack of “cusp ions” during this cusp pass the total magnetic field observed during this interval did not demonstrate a structured depression superposed on the background dipolar-like field. It is with these reservations that this cusp pass cannot be termed a PPS event and therefore is not included into the statistical study.

Events that do not satisfy *all* outlined criteria have been discarded from the subsequent study. Intervals where data gaps exist in one or both of CAMMICE MICS or Hydra data sets are also not included. Approximately 30% of Polar’s orbits during May 1996-November 1999 were discarded on these grounds.

6.3 Magnetospheric PPS location characteristics

The orbits selected for participation in this statistical study are taken from the interval May 1996 to November 1999, some forty-two months in duration. In this period, only twenty-two months of Polar’s orbits were deemed close enough (within ~4 hours) to the noon-midnight meridian to pass through the nominal mid-altitude cusp regularly. These months correspond to those closest to equinox i.e. March, April, May, September, October, and November. However, once the definitions and characteristics of PPS are understood and characterised for orbits that pass close to the noon-midnight meridian, then cuts through the cusp at other local times could be considered.

If PPS are indeed signatures of magnetic reconnection then it would be expected that their occurrence and behaviour are dependent upon the IMF orientation (both B_y and B_z). It is this behaviour that this chapter addresses. The IMF orientation was calculated from two separate satellite sources for the period of interest. The Wind spacecraft was utilised for the timings of the IMF phase fronts to the near-Earth environment in Chapters 4 and 5 as it was ideally positioned in these case studies to make such measurements. However, the Wind orbit is such that there are long intervals when Wind is actually situated in the Earth’s magnetosphere and is therefore not in a suitable location to measure upstream interplanetary conditions. The ACE satellite, however, was launched in late August 1997 into a constant halo orbit around the L1 libration point and can be utilised for the sections of the study that Wind was

unsuitable for. Hence for May 1996-November 1997, the upstream interplanetary conditions were provided by Wind, and from March 1998-November 1999 by ACE.

The IMF measurements, solar wind dynamic pressure and Polar data were averaged into 15 minute UT bins throughout the statistical study. Within any given 15 minute interval, Polar will move less than 1° in magnetic latitude and longitude. The time delay calculated for the IMF phase fronts to reach the Earth's magnetopause from the given spacecraft is taken from the approach taken in Chapter 4 and adopted by *Lester et al.*, 1993, *Roelof and Sibeck*, 1993, and *Peredo et al.*, 1995.

Intervals with gaps in data from either the upstream solar wind conditions or the Polar observations were disregarded from the sampled set for obvious reasons. Approximately one quarter of the available data set was removed due to data gaps from either Polar and/or Wind/ACE. Over half of these intervals are due to data gaps from the SWICS instrument onboard ACE.

As this approach truncated the available data somewhat, the bins in this statistical study were doubled in size in terms of the resolution of the data. This is especially relevant when the data was (roughly) split into four when each orientation of IMF B_y and B_z were considered together i.e. PPS dependence on IMF clock angle. Although the orbit and occurrence statistics can be binned in 1° latitude and 15 minutes of local time, each MLT bin in this study is 2° wide in latitude (magnetic or invariant) and 30 minutes wide in local time.

6.3.1 All IMF orientations

Figure 6.3 shows the distribution of pulsed particle signatures for all events where the IMF was determined and for complete intervals. All statistical data in Section 6.3 are shown in MLT: magnetic latitude (MLAT) co-ordinates, looking down on the northern pole with local noon at the top of the plot. Each concentric ring is 10° of magnetic latitude, and radial lines from the centre mark every third hour of MLT. The vast majority of the nightside magnetosphere is not considered, largely as low-latitude and lobe-reconnection processes are primarily dayside phenomena. From the top in descending order, Figure 6.3 presents the distribution of occurrence of the orbital location, PPS occurrence and normalized occurrence as a function of orbit. Inspection of the orbital occurrence reveals a wide coverage of latitudes and local times of the orbit, expected when half a year of precessing orbital

POLAR PPS location (all IMF)

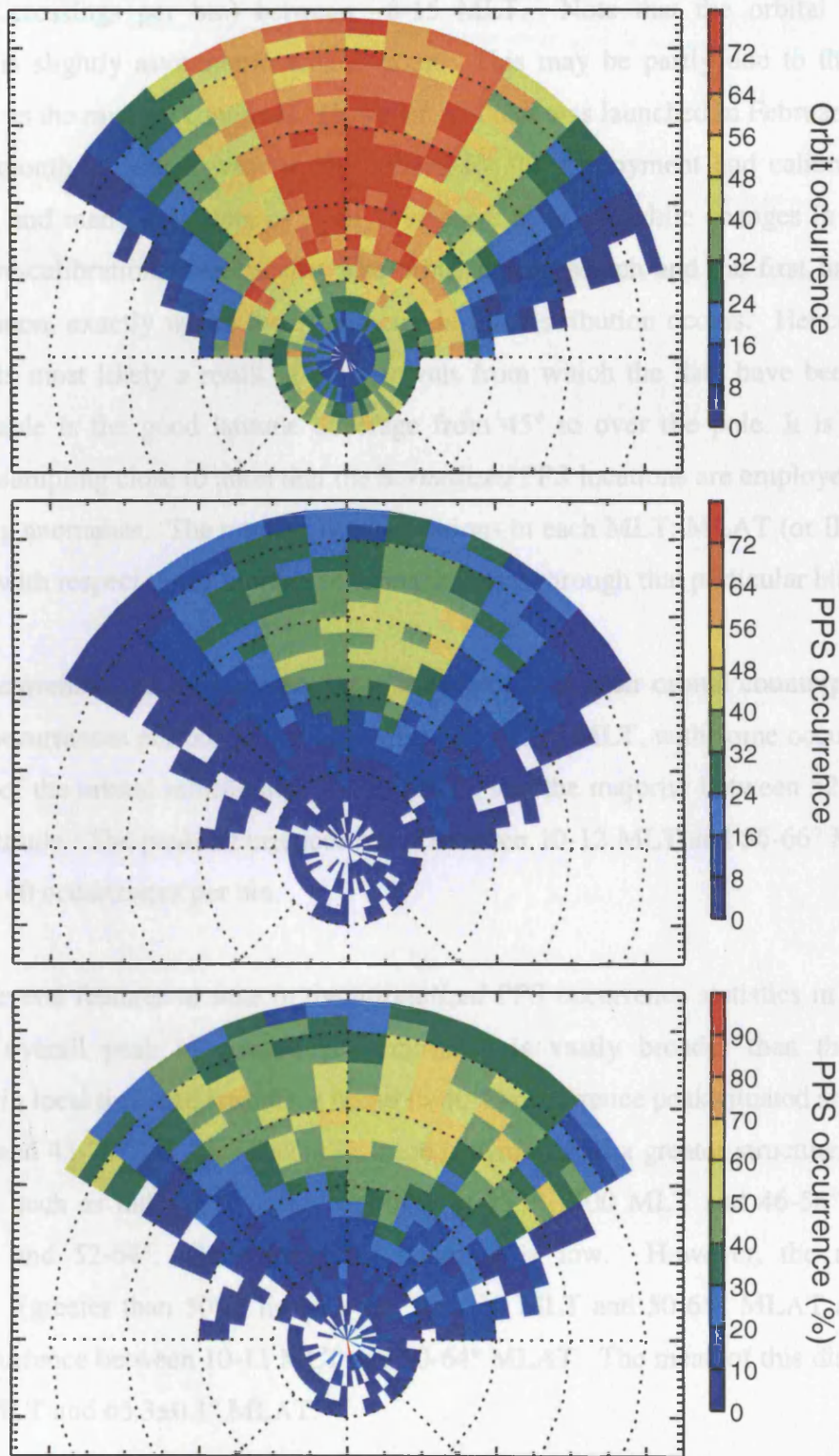


FIGURE 6.3: Pulsed particle signature location and orbital characteristics of Polar under all IMF conditions in MLT: MLAT co-ordinates. From top to bottom, Figure 6.3 shows the orbit occurrence, PPS occurrence and the normalised PPS occurrence in 30 minute and 2 degree bins.

as Figure 6.3. Note that the data set from Figure 6.3 is divided into 60% (40%) for southward (northward) IMF. The orbital occurrences therefore reach only 60 per orbital bin

information is utilised, from around 7-16 MLT over 45-90° MLAT with excellent coverage (> 24 orbit crossings per bin) between ~8-15 MLT. Note that the orbital occurrence distribution is slightly asymmetric around noon. This may be partly due to the decay of Polar's orbit as the mission continues. However, as Polar was launched in February 1996, the subsequent month of March was largely utilised for the deployment and calibration of its instruments, and many days data in April 1996 were also lost while changes in instrument modes and re-calibrations were made. The orbits during March and the first half of April occur post-noon, exactly where the asymmetry in the distribution occurs. Hence the slight asymmetry is most likely a result of the intervals from which the data have been selected. Also noticeable is the good latitude coverage from 45° to over the pole. It is due to the variation in sampling close to noon that the *normalized* PPS locations are employed to negate any sampling anomalies. The number of observations in each MLT: MLAT (or ILAT) bin is normalized with respect to the number of orbits that pass through that particular bin.

The PPS occurrences reside in a more localised region than their orbital counterparts. Most PPS (> 24 occurrences per bin) occur between ~1000-1330 MLT, with some occurrences out to the limit of the orbital information (~7-16 MLT), and the majority between 52 and 72° of magnetic latitude. The peak occurrences occur between 10-12 MLT and 56-66° MLAT with greater than 40 occurrences per bin.

There are several features to note in the *normalized* PPS occurrence statistics in Figure 6.3. Firstly the overall peak of percentage occurrence is vastly broader than the observed distribution in local time and latitude; a broad (> 40%) occurrence peak situated around 0900-1430 MLT and 45-70° MLAT. Secondly, there is evidence of a greater structure within this distribution, such as individual peaks occurring at 1530-1600 MLT and 46-56° and 0830-0900 MLT and 52-64°, where the orbit sampling is low. However, the majority of occurrences (greater than 50%) lie between 10-1230 MLT and 50-66° MLAT and peak at 60-70% occurrence between 10-11 MLT and 50-64° MLAT. The mean of this distribution is at 1050 ± 3 MLT and $65.3 \pm 0.1^\circ$ MLAT.

6.3.2 Effect of B_z on PPS location

Figure 6.4 displays the statistical data for Polar's cusp passes during IMF $B_z < 0$ in the same format as Figure 6.3. Note that the data set from Figure 6.3 is divided into 60% (40%) for southward (northward) IMF. The orbital occurrences therefore reach only 60 per orbital bin

POLAR PPS location (Bz -ve)

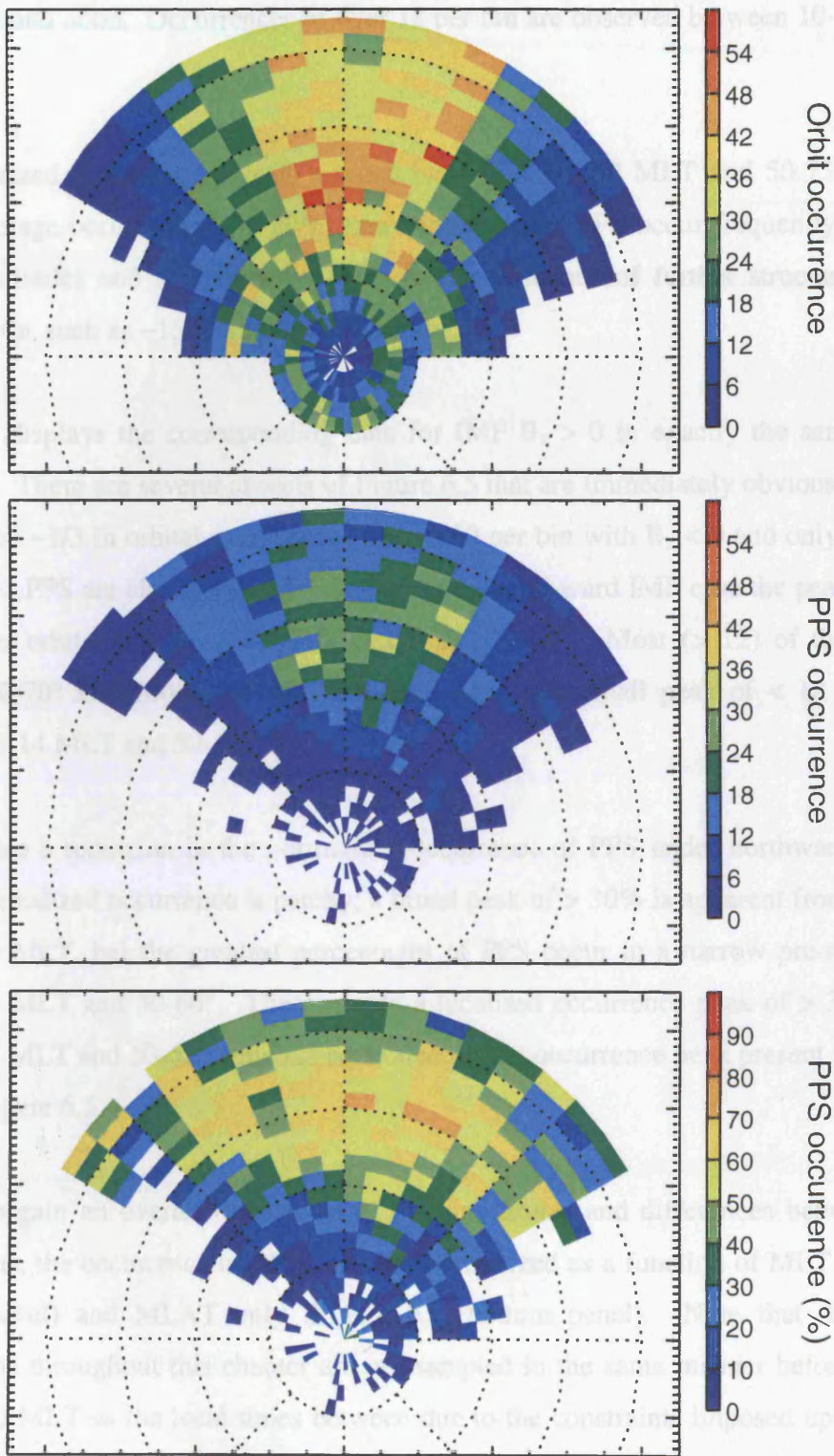


FIGURE 6.4: Pulsed particle signature statistics under negative Bz conditions, in MLT: MLAT in the same format as Figure 6.3.

maximum. The actual PPS occurrence statistics reveal a lower peak of occurrence, closely grouped around noon. Occurrences of over 18 per bin are observed between 10-13 MLT and $\sim 54-70^\circ$.

The normalized occurrence reveals a broad band (0900-1430 MLT and $50-75^\circ$ MLAT) of high percentage occurrences (50-80%), implying that that PPS occur frequently over a wide range of latitudes and local times. There is also evidence of further structure in regions sampled little, such as $\sim 1500-1530$ MLT and $46-52^\circ$.

Figure 6.5 displays the corresponding data for IMF $B_z > 0$ in exactly the same format as Figure 6.3. There are several aspects of Figure 6.5 that are immediately obvious. Firstly, the reduction by $\sim 1/3$ in orbital occurrences - up to 60 per bin with $B_z < 0$ and only < 48 during B_z positive. PPS are also reduced in number; in the northward IMF case the peak occurrence is < 24 per orbital bin at $\sim 1030-1100$ MLT and $72-74^\circ$. Most (> 12) of the PPS occur between $50-70^\circ$ and $1000-1230$ MLT, though there is a small peak of < 18 observations between $13-14$ MLT and $50-58^\circ$.

There is also a reduction in the normalized occurrence of PPS under northward IMF. The peak in normalized occurrence is patchy; a broad peak of $> 30\%$ is apparent from $45-72^\circ$ and $0800-1330$ MLT, but the greatest percentages of PPS occur in a narrow pre-noon band of $1000-1130$ MLT and $50-66^\circ$. There is also a localised occurrence peak of $> 30\%$ between $1300-1430$ MLT and $50-62^\circ$ which is equivalent to the occurrence peak present in the middle panel of Figure 6.5.

In order to gain an overall impression of the similarities and differences between the two distributions, the occurrence of PPS has been normalized as a function of MLT only (Figure 6.6, top panel) and MLAT only (Figure 6.6, bottom panel). Note that the integrated distributions throughout this chapter are not sampled in the same manner before ~ 0600 and after ~ 1700 MLT as the local times between due to the constraints imposed upon the study. The PPS occurrence is greater at most latitudes and local times under IMF $B_z < 0$ (red dashed lines) than $B_z > 0$ (blue dotted lines). The MLT dependence of PPS under negative B_z reveals a peak (mode) at 48% occurrence at $1030-1100$ MLT, though there is evidence for a secondary peak around $1200-1230$ MLT at 44%. The northward directed IMF case also reveals a primary peak at $\sim 39\%$ occurrence at $1030-1100$ MLT, with a secondary peak further towards dusk at $1300-1330$ (with 33% percentage occurrence).

POLAR PPS location (Bz +ve)

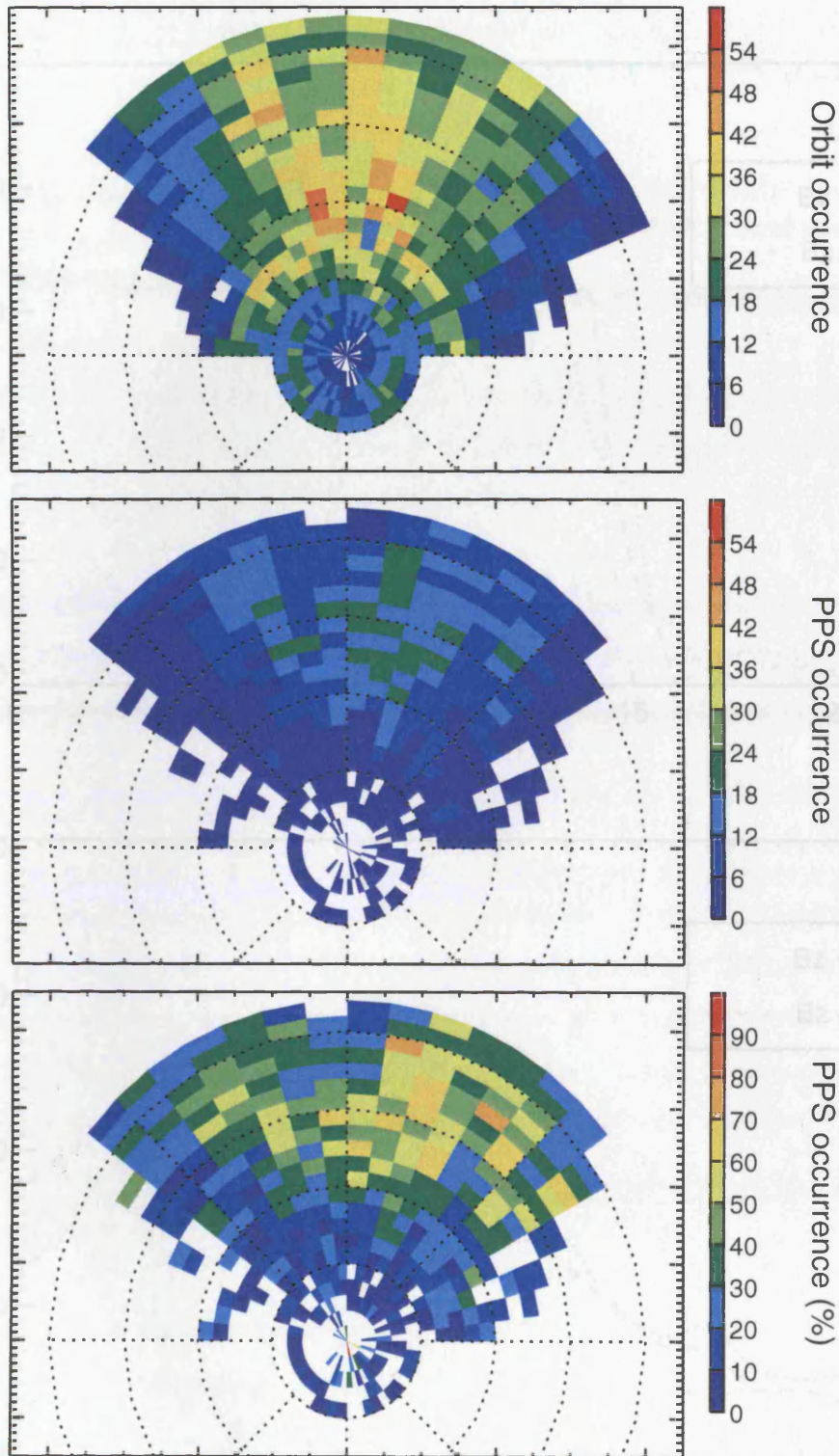


FIGURE 6.5: Pulsed particle signature statistics under positive Bz conditions, in MLT: MLAT in the same format as Figure 6.3.

Integrated MLT: MLAT PPS dependence on IMF Bz

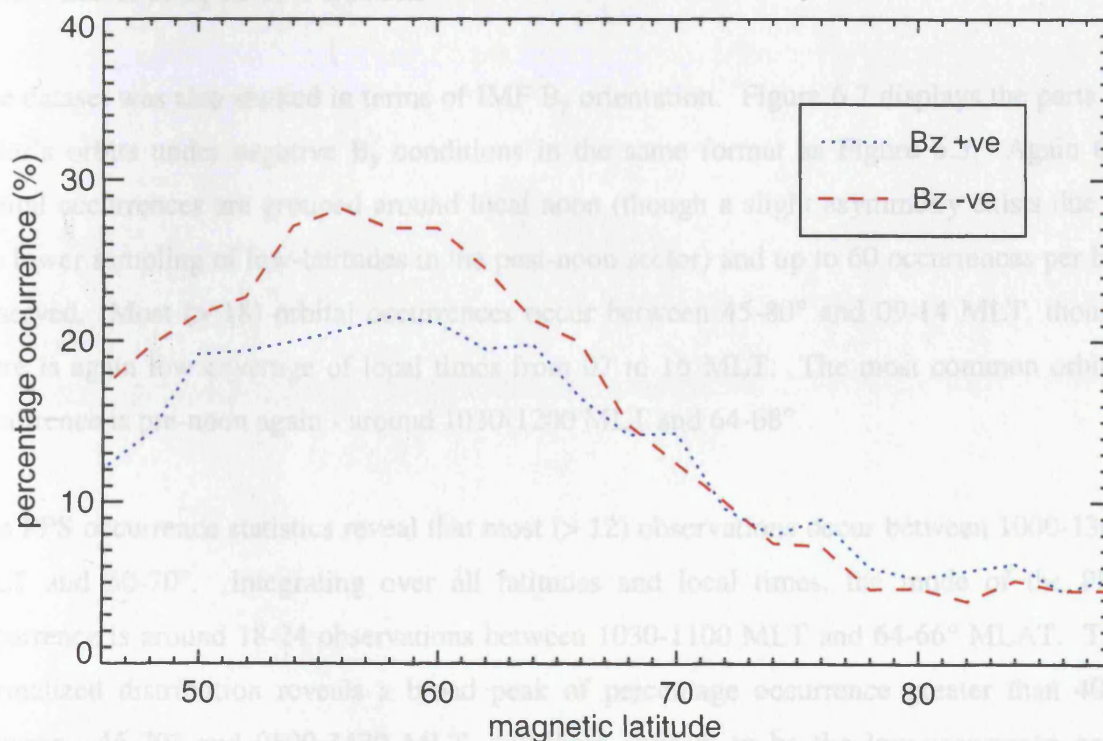
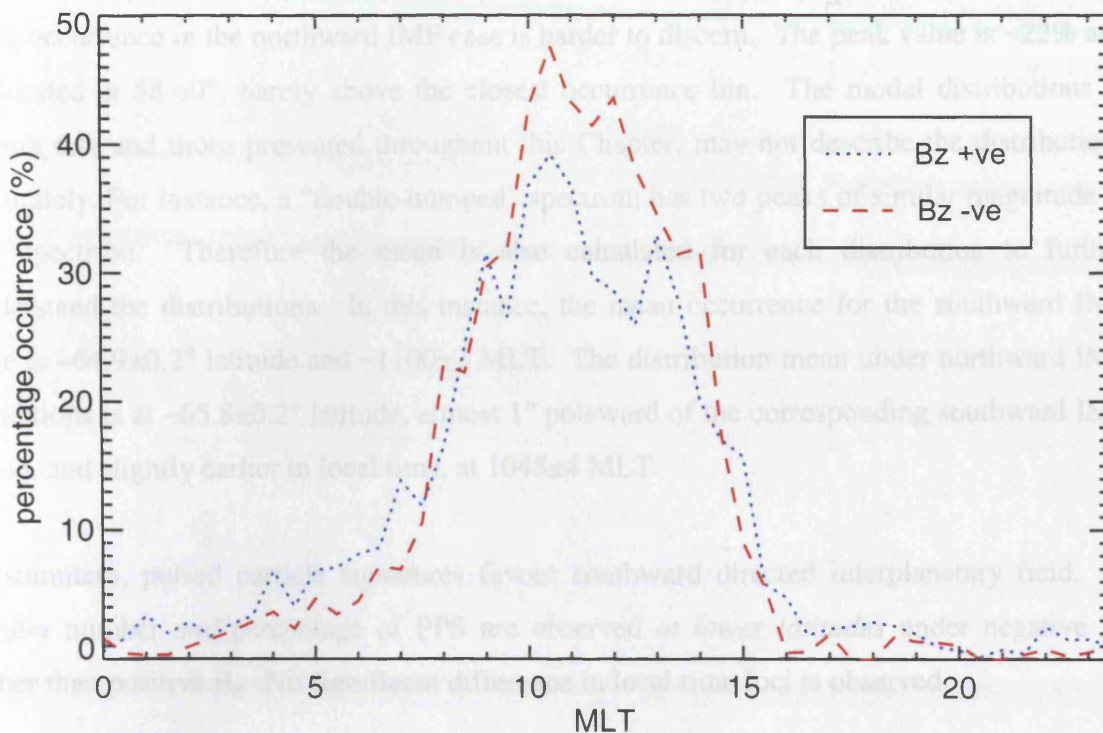


FIGURE 6.6: (top) MLT dependence of PPS location on IMF Bz integrated over all magnetic latitudes and (bottom) MLAT dependence of PPS location upon IMF Bz integrated over all MLTs

The orbital occurrence is more grouped around noon for positive B_z than negative B_z, as demonstrated by the top panel in Figure 6.8. The majority of PPS occurrences (> 18) occur

The integrated magnetic latitude occurrence distribution has smaller and wider peaks. For the southward IMF case, the peak is located in the 56-58° bin and boasts a 28% occurrence. The peak occurrence in the northward IMF case is harder to discern. The peak value is ~22% and is located at 58-60°, barely above the closest occurrence bin. The modal distributions in Figure 6.6, and those presented throughout this Chapter, may not describe the distributions accurately. For instance, a “double-humped” spectrum has two peaks of similar magnitude in its spectrum. Therefore the mean is also calculated for each distribution to further understand the distributions. In this instance, the mean occurrence for the southward IMF case is $\sim 64.9 \pm 0.2^\circ$ latitude and $\sim 1100 \pm 3$ MLT. The distribution mean under northward IMF conditions is at $\sim 65.8 \pm 0.2^\circ$ latitude, almost 1° poleward of the corresponding southward IMF mean, and slightly earlier in local time, at 1045 ± 4 MLT.

In summary, pulsed particle signatures favour southward directed interplanetary field. A greater number *and* percentage of PPS are observed *at lower latitudes* under negative B_z rather than positive B_z . No significant difference in local time foci is observed.

6.3.3 Effect of B_y on PPS location

The dataset was also studied in terms of IMF B_y orientation. Figure 6.7 displays the parts of Polar’s orbits under negative B_y conditions in the same format as Figure 6.3. Again the orbital occurrences are grouped around local noon (though a slight asymmetry exists due to the lower sampling of low-latitudes in the post-noon sector) and up to 60 occurrences per bin observed. Most (> 18) orbital occurrences occur between 45-80° and 09-14 MLT, though there is again low coverage of local times from 07 to 16 MLT. The most common orbital occurrence is pre-noon again - around 1030-1200 MLT and 64-68°.

The PPS occurrence statistics reveal that most (> 12) observations occur between 1000-1300 MLT and 50-70°. Integrating over all latitudes and local times, the mode of the PPS occurrence is around 18-24 observations between 1030-1100 MLT and 64-66° MLAT. The normalized distribution reveals a broad peak of percentage occurrence greater than 40% between $\sim 45-70^\circ$ and 0800-1430 MLT, and there appears to be the low-occurrence peak between 46-56° and 15-16 MLT.

The orbital occurrence is more grouped around noon for positive B_y than negative B_y , as demonstrated by the top panel in Figure 6.8. The majority of PPS occurrences (> 18) occur

POLAR PPS location (By -ve)

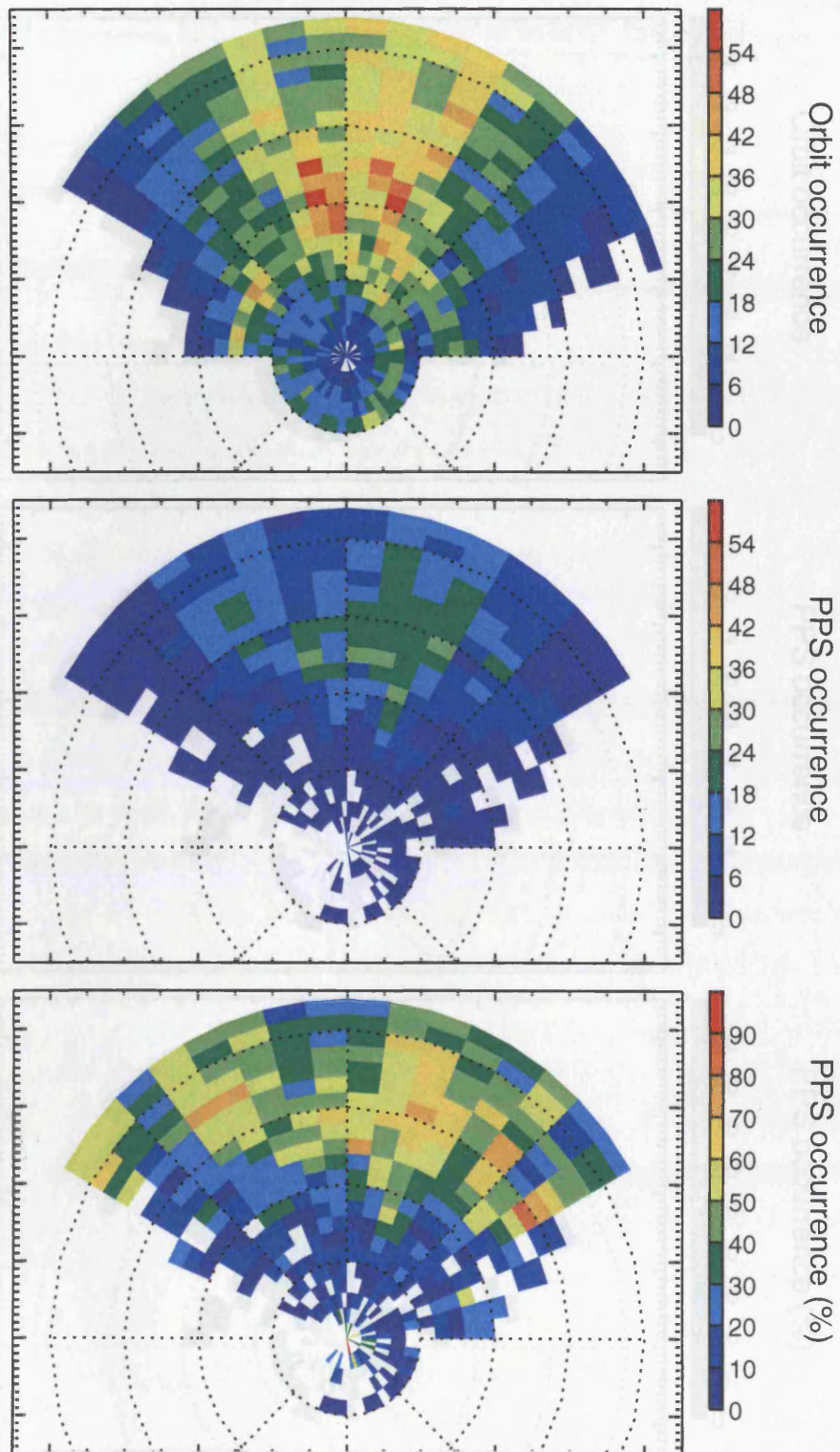


FIGURE 6.7: Pulsed particle signature statistics under negative B_y conditions, in MLT: MLAT in the same format as Figure 6.3.

POLAR PPS location (By +ve)

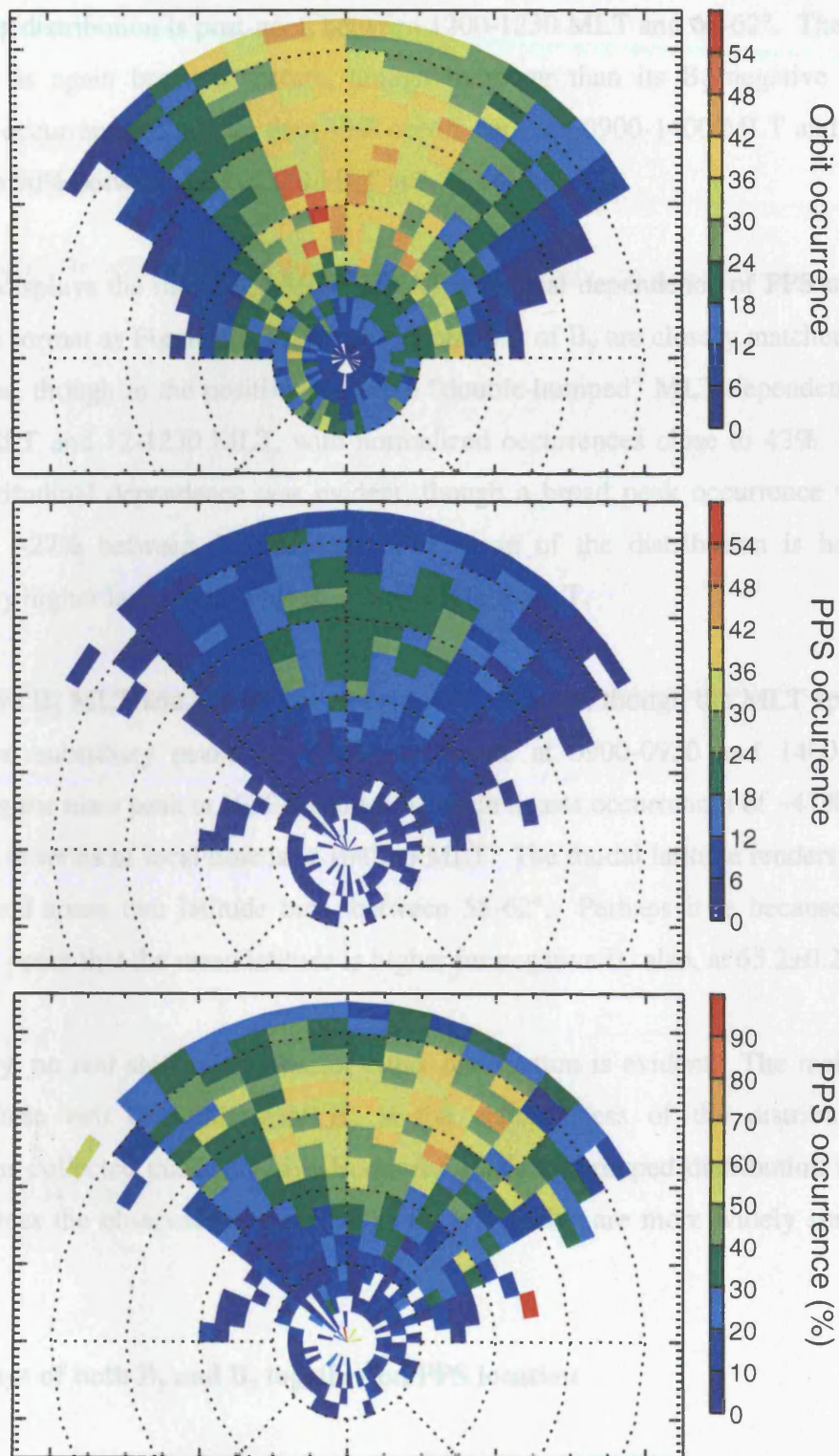


FIGURE 6.8: Pulsed particle signature statistics under positive B_y conditions, in MLT: MLAT in the same format as Figure 6.3.

between 10-13 MLT and $\sim 54-66^\circ$ and is skewed again towards pre-noon. However, the mode of this distribution is post-noon between 1200-1230 MLT and $60-62^\circ$. The normalized distribution is again broad in nature, though narrower than its B_y negative counterpart. Percentage occurrence of greater than 30% occurs between 0900-1400 MLT and $48-72^\circ$, and greater than 50% between 1000-1330 MLT and $56-66^\circ$ MLAT.

Figure 6.9 displays the integrated MLT: MLAT statistical dependence of PPS upon IMF B_y in the same format as Figure 6.6. The two orientations of B_y are closely matched in terms of distributions, though in the positive B_y case a “double-humped” MLT dependence exists, at 10-1030 MLT and 12-1230 MLT, with normalized occurrences close to 42%. No double-humped latitudinal dependence was evident, though a broad peak occurrence was present, peaking at $\sim 27\%$ between 56 and 58° . The mean of the distribution is however at a significantly higher latitude at $\sim 65.4 \pm 0.2^\circ$ and 1100 ± 4 MLT.

The negative B_y MLT and MLAT spectra are more ordered, though the MLT spectrum does possess two subsidiary peaks of $\sim 35\%$ occurrence at 0900-0930 and 1400-1430 MLT surrounding the main peak at 1030-1100 MLT which boasts occurrences of $\sim 47\%$. The mean occurrence in terms of local time is at 1045 ± 3 MLT. The modal latitude renders occurrences of $\sim 25\%$ and spans two latitude bins, between $58-62^\circ$. Perhaps it is because of the low occurrence peaks that the mean latitude is higher for negative B_y also, at $65.2 \pm 0.2^\circ$.

In summary, no real shift of the foci of either distribution is evident. The main difference between these two orientations of B_y is the cohesiveness of the distributions. The observations collected under positive B_y reveal a closely grouped distribution around local noon, whereas the observations made when B_y is negative are more widely spread in local time.

6.3.4 Effect of both B_y and B_z together on PPS location

Of course, testing this set of occurrence statistics against just one IMF orientation is not the sole intention of this Chapter. To fully understand the vagaries of the mid-altitude pulsed particle signature, the dependence of PPS location upon IMF B_y and B_z *together* must be performed. These statistics are presented in exactly the same format as those presented so far, in the magnetic latitude: magnetic local time frame. For the benefit of the reader, the orbital occurrences will not be discussed to the same extent as those that have gone before.

Integrated MLT: MLAT PPS dependence on IMF By

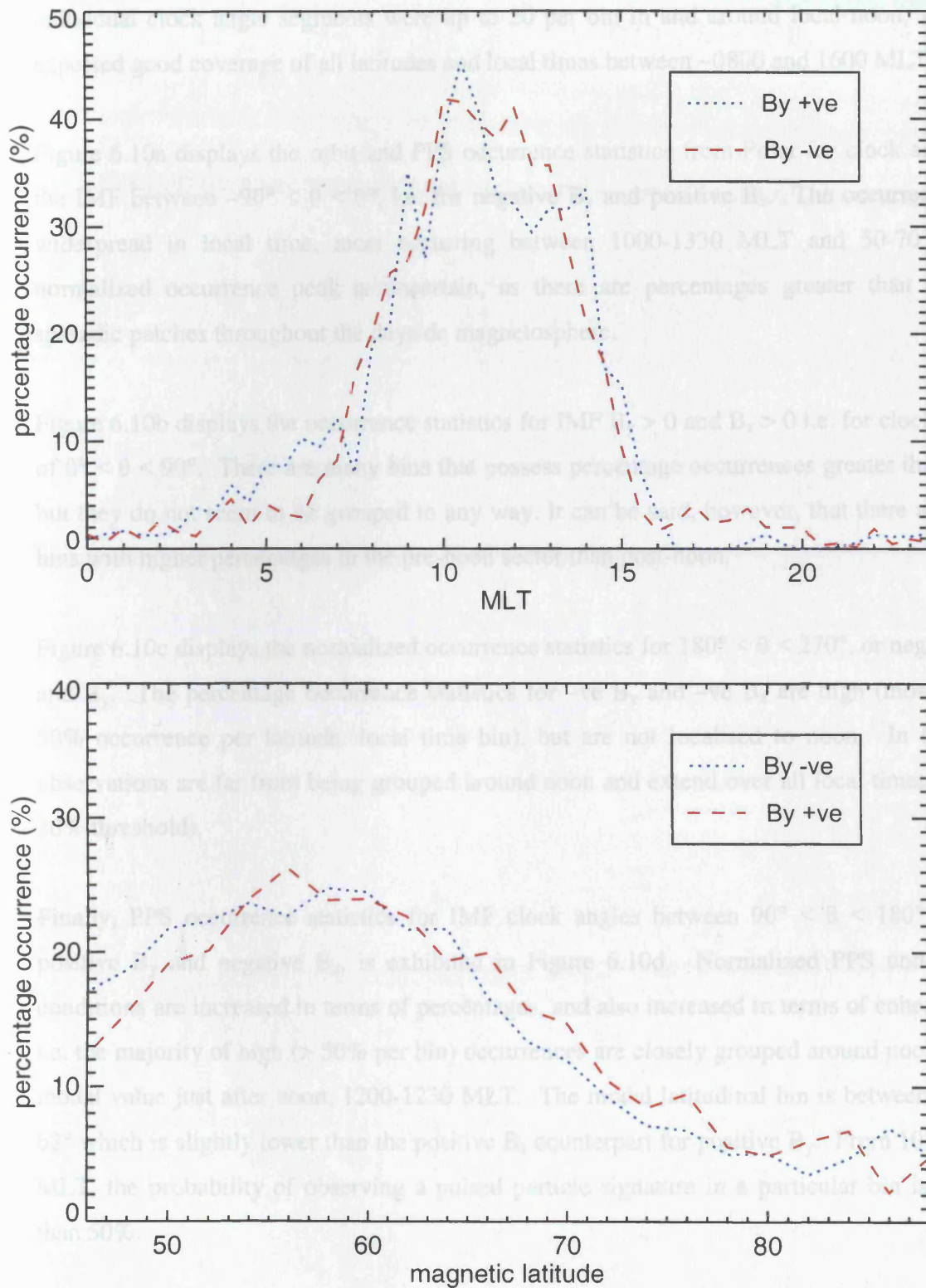


FIGURE 6.9: (top) MLT dependence of PPS location on IMF B_y integrated over all magnetic latitudes and (bottom) MLAT dependence of PPS location upon IMF B_y integrated over all MLTs

The normalized occurrence distributions for the four clock angle orientations alone are therefore presented in Figure 6.10. Suffice to say that the orbital occurrences for all individual clock angle segments were up to 20 per bin in and around local noon, with the expected good coverage of all latitudes and local times between ~0800 and 1600 MLT.

Figure 6.10a displays the orbit and PPS occurrence statistics from Polar for clock angles of the IMF between $-90^\circ < \theta < 0^\circ$, i.e. for negative B_y and positive B_z . The occurrences are widespread in local time, most occurring between 1000-1330 MLT and $50-70^\circ$. The normalized occurrence peak is uncertain, as there are percentages greater than 30% in sporadic patches throughout the dayside magnetosphere.

Figure 6.10b displays the occurrence statistics for IMF $B_y > 0$ and $B_z > 0$ i.e. for clock angles of $0^\circ < \theta < 90^\circ$. There are many bins that possess percentage occurrences greater than 50%, but they do not seem to be grouped in any way. It can be said, however, that there are more bins with higher percentages in the pre-noon sector than post-noon.

Figure 6.10c displays the normalized occurrence statistics for $180^\circ < \theta < 270^\circ$, or negative B_z and B_y . The percentage occurrence statistics for $-ve B_y$ and $-ve B_z$ are high (mostly over 50% occurrence per latitude: local time bin), but are not localised to noon. In fact, the observations are far from being grouped around noon and extend over all local times (over a 30% threshold).

Finally, PPS occurrence statistics for IMF clock angles between $90^\circ < \theta < 180^\circ$ i.e. for positive B_y and negative B_z , is exhibited in Figure 6.10d. Normalized PPS under these conditions are increased in terms of percentages, and also increased in terms of cohesiveness i.e. the majority of high ($> 50\%$ per bin) occurrences are closely grouped around noon with a modal value just after noon, 1200-1230 MLT. The modal latitudinal bin is between 60 and 62° which is slightly lower than the positive B_z counterpart for positive B_y . From 1030-1400 MLT, the probability of observing a pulsed particle signature in a particular bin is greater than 50%.

Figure 6.11 displays the integrated MLT: MLAT statistics for the four quadrants of IMF clock angle. The mode of the B_y - B_z distribution is around 45% chance of occurrence between 1030 and 1100 MLT and $64-66^\circ$ (the blue dot-dashed lines in Figure 6.11). The mean value is also pre-noon at 1045 ± 6 MLT and $65.6 \pm 0.2^\circ$ magnetic latitude.

Integrated MLT: MLAT PPS occurrence

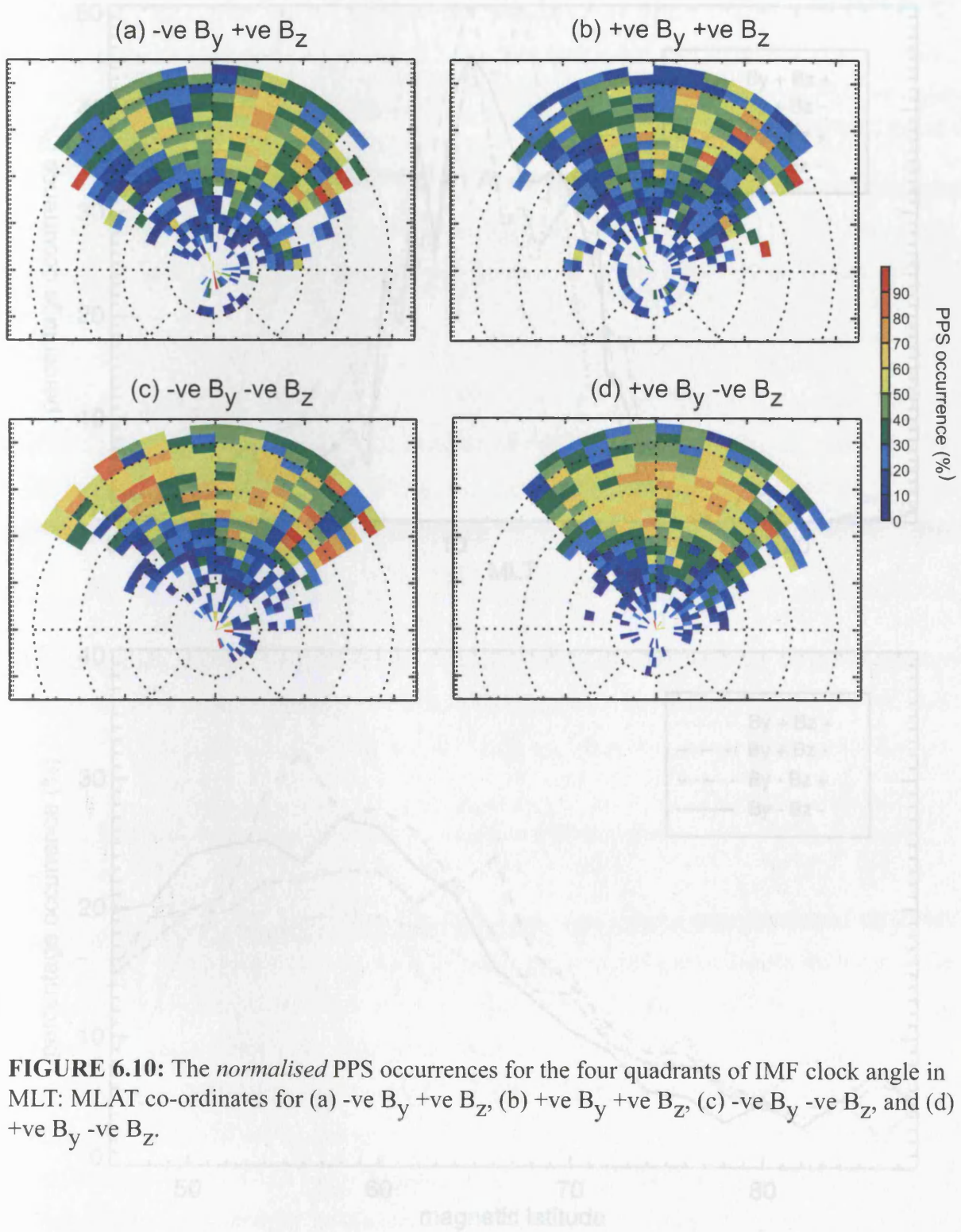


FIGURE 6.10: The *normalised* PPS occurrences for the four quadrants of IMF clock angle in MLT: MLAT co-ordinates for (a) -ve B_y +ve B_z , (b) +ve B_y +ve B_z , (c) -ve B_y -ve B_z , and (d) +ve B_y -ve B_z .

FIGURE 6.11: (top) MLT dependence of PPS location on IMF clock angle integrated over all magnetic latitudes and (bottom) MLAT dependence of PPS location upon IMF clock angle integrated over all MLTs.

Integrated MLT: MLAT PPS occurrence

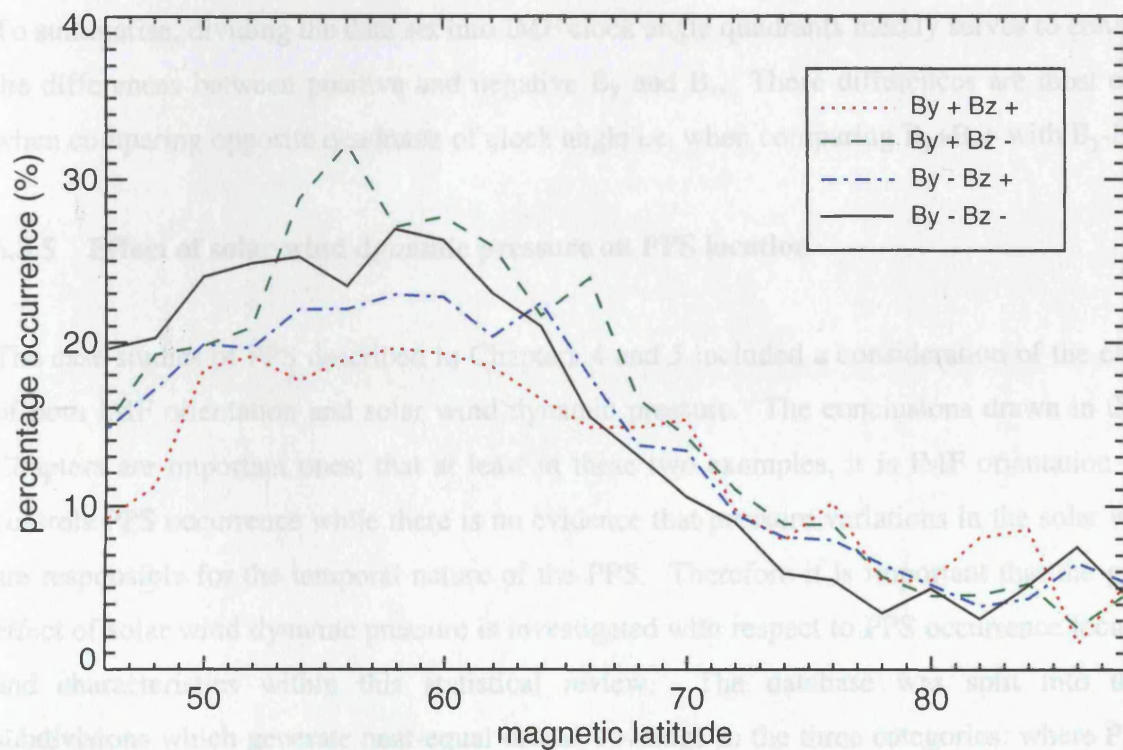
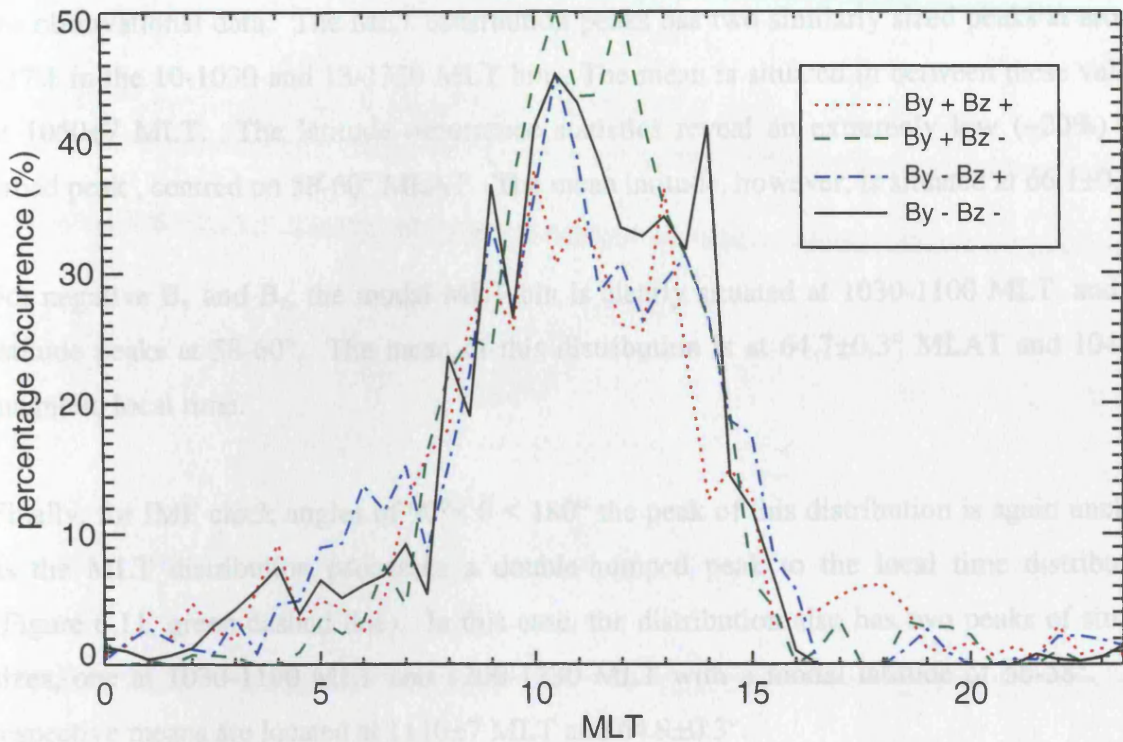


FIGURE 6.11: (top) MLT dependence of PPS location on IMF clock angle integrated over all magnetic latitudes and (bottom) MLAT dependence of PPS location upon IMF clock angle integrated over all MLTs

For $0^\circ < \theta < 90^\circ$ (Figure 6.11, red dotted line), the integrated MLT and latitude spectra possess a low, broad peak, implying that there is no one MLT or MLAT bin that dominates the observational data. The MLT distribution peaks has two similarly sized peaks at around $\sim 37\%$ in the 10-1030 and 13-1330 MLT bins. The mean is situated in between these values, at 1050 ± 7 MLT. The latitude occurrence statistics reveal an extremely low ($\sim 20\%$) and broad peak, centred on $58-60^\circ$ MLAT. The mean latitude, however, is situated at $66.1 \pm 0.3^\circ$.

For negative B_y and B_z , the modal MLT bin is clearly situated at 1030-1100 MLT, and the latitude peaks at $58-60^\circ$. The mean of this distribution is at $64.7 \pm 0.3^\circ$ MLAT and 1040 ± 7 magnetic local time.

Finally, for IMF clock angles of $90^\circ < \theta < 180^\circ$ the peak of this distribution is again unclear, as the MLT distribution possesses a double-humped peak to the local time distribution (Figure 6.11, green dashed line). In this case, the distribution also has two peaks of similar sizes, one at 1030-1100 MLT and 1200-1230 MLT with a modal latitude of $56-58^\circ$. The respective means are located at 1110 ± 7 MLT and $64.9 \pm 0.3^\circ$.

To summarise, dividing the data set into IMF clock angle quadrants merely serves to enhance the differences between positive and negative B_y and B_z . These differences are most clear when comparing opposite quadrants of clock angle i.e. when comparing B_y+B_z+ with B_y-B_z- .

6.3.5 Effect of solar wind dynamic pressure on PPS location

The case studies of PPS described in Chapters 4 and 5 included a consideration of the effect of both IMF orientation and solar wind dynamic pressure. The conclusions drawn in these Chapters are important ones; that at least in these two examples, it is IMF orientation that controls PPS occurrence while there is no evidence that pressure variations in the solar wind are responsible for the temporal nature of the PPS. Therefore it is important that the gross effect of solar wind dynamic pressure is investigated with respect to PPS occurrence location and characteristics within this statistical review. The database was split into three subdivisions which generate near-equal orbital coverage in the three categories: where $P_{sw} < 1.5$ nPa, $1.5 < P_{sw} < 2.5$ nPa and $P_{sw} > 2.5$ nPa.

Figure 6.12 shows PPS location and Polar orbital information for solar wind dynamic pressure of under 1.5 nPa presented in the same format as previous figures. What can be

POLAR PPS location ($P < 1.5$ nPa)

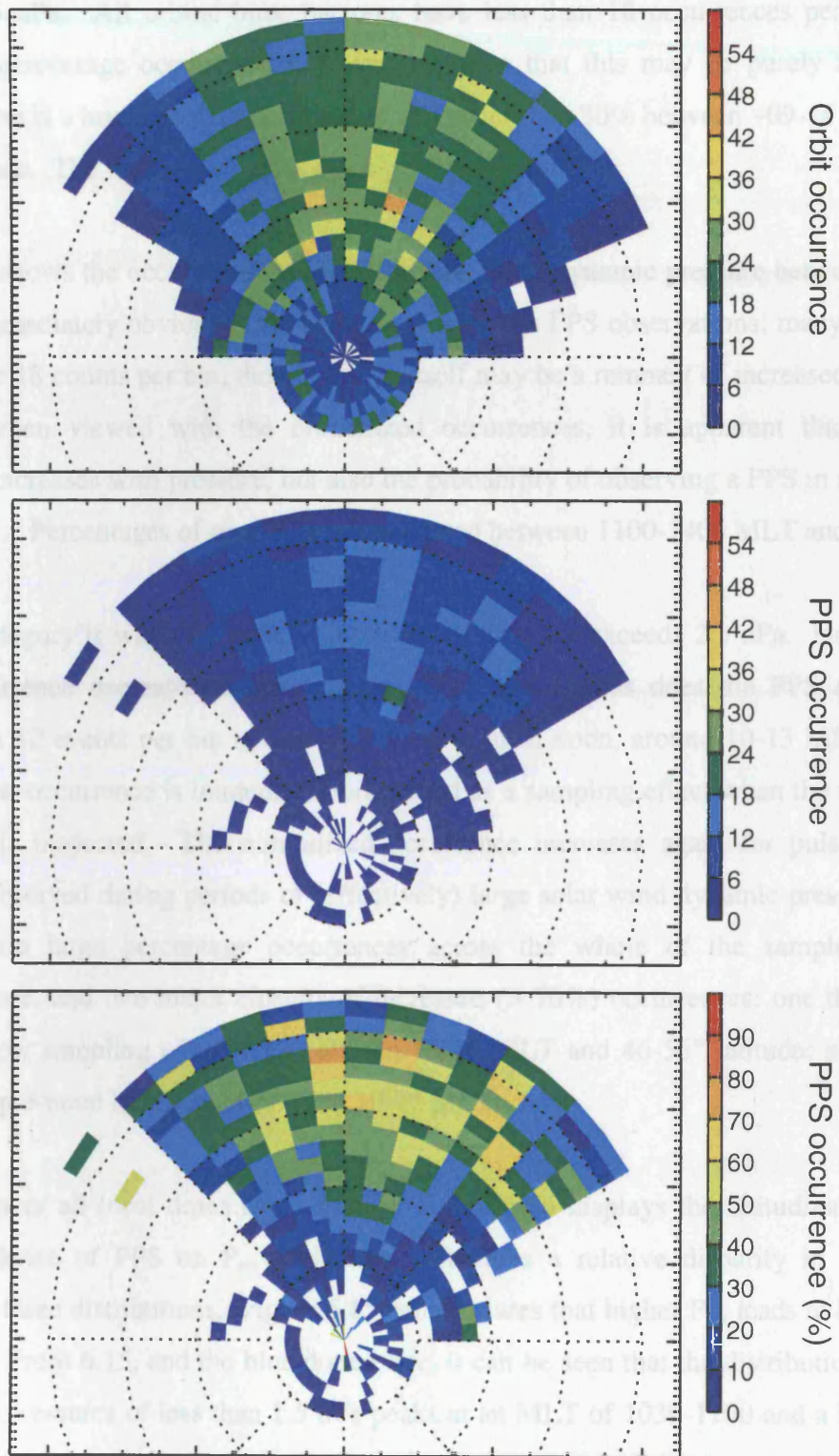


FIGURE 6.12: Pulsed particle signature statistics in MLT: MLAT co-ordinates, under solar wind dynamic pressures of less than 1.5 nPa.

immediately seen is the small occurrence of pulsed particle signatures for dynamic pressures of under 1.5 nPa. All orbital bins, bar one, have less than 18 occurrences per bin. The normalized percentage occurrence, however, suggests that this may be purely a sampling effect, as there is a broad peak in occurrences of greater than 30% between ~09-14 MLT band 50-70° latitude. The total occurrences again peak pre-noon.

Figure 6.13 shows the occurrence statistics for solar wind dynamic pressure between 1.5 and 2.5 nPa. Immediately obvious is the increase in absolute PPS observations; many more bins observe over 18 counts per bin, though this in itself may be a remnant of increased sampling. However, when viewed with the normalized occurrences, it is apparent that not only occurrence increases with pressure, but also the probability of observing a PPS in a particular bin per orbit. Percentages of over 50% are observed between 1100-1400 MLT and 50-66°.

The final category is when the solar wind dynamic pressure exceeds 2.5 nPa. Note that the orbital occurrence decreases in this category (Figure 6.14), as does the PPS occurrence. Greater than 12 events per bin is observed close to local noon, around 10-13 MLT and 54-70°. The low occurrence is immediately identified as a sampling effect when the normalized occurrence is inspected. The normalized occurrence increases again for pulsed particle signatures observed during periods of (effectively) large solar wind dynamic pressure. Note that there are large percentage occurrences across the whole of the sampled dayside magnetosphere, and two major clusters of increased (> 70%) occurrences: one that may be due to the low sampling of the area between 13-15 MLT and 46-56° latitude; and a larger distribution pre-noon between 54-66° and 10-12 MLT.

Integrating over all local times and latitudes, Figure 6.15 displays the latitudinal and local time dependence of PPS on P_{sw} variations. There is a relative disparity in occurrence between the three distributions. Figure 6.15 demonstrates that higher P_{sw} leads to higher PPS occurrence. From 6.15, and the blue dotted line, it can be seen that the distribution at ~45% for dynamic pressures of less than 1.5 nPa peaks at an MLT of 1030-1100 and a broad peak between 54-58° of ~20%. The mean values are higher than both of these modal values, at $63.8 \pm 0.3^\circ$ and 1115 ± 5 MLT.

For $1.5 < P_{sw} < 2.5$ nPa, the modal values of the distribution are around 1030-1100 MLT (with > 40% chance of occurrence) and 58-60° (with ~25% occurrence). Figure 6.15

POLAR PPS location ($1.5 < P < 2.5$ nPa)

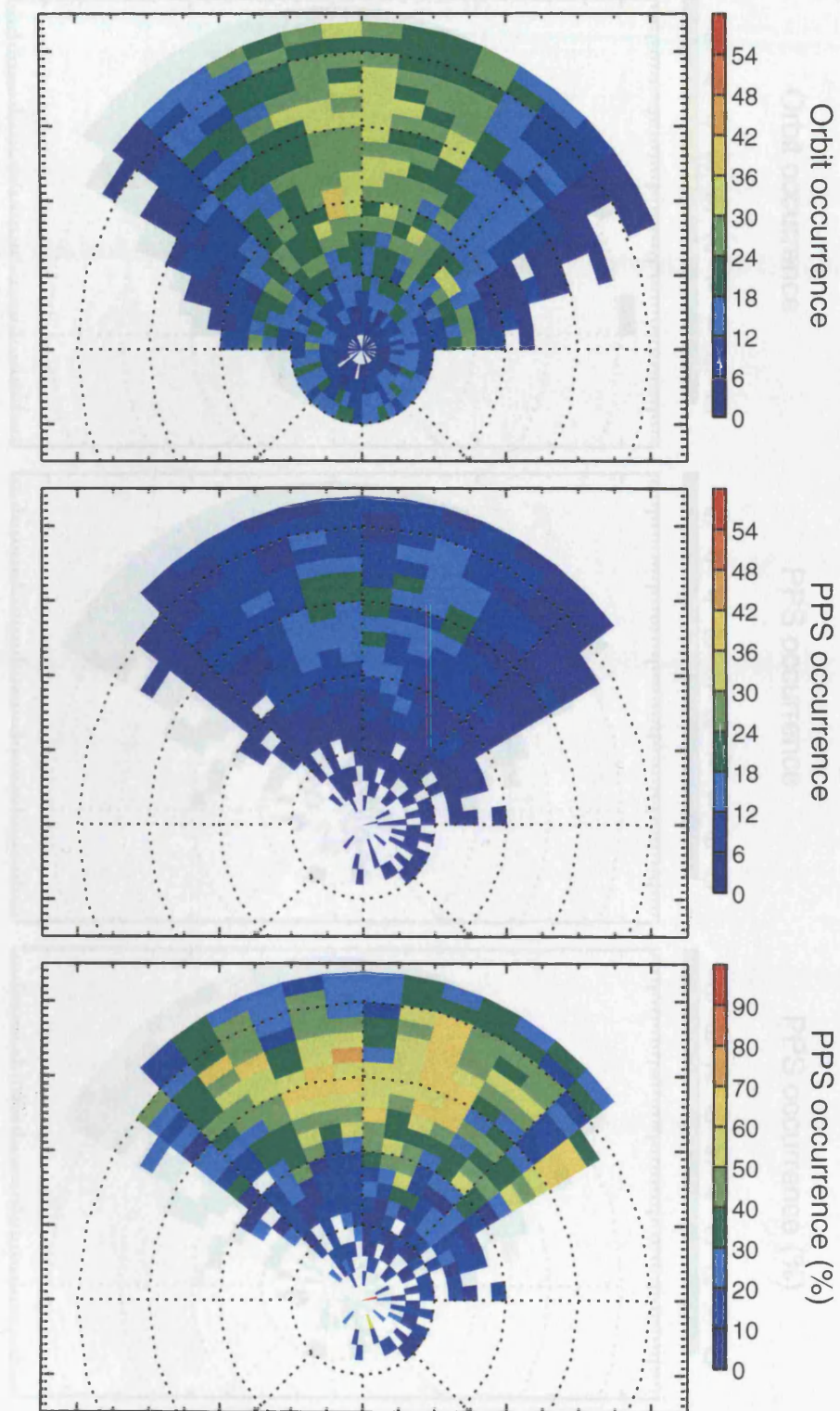


FIGURE 6.13: Pulsed particle signature statistics in MLT: MLAT co-ordinates, under solar wind dynamic pressures of between 1.5 and 2.5 nPa.

POLAR PPS location ($P > 2.5$ nPa)

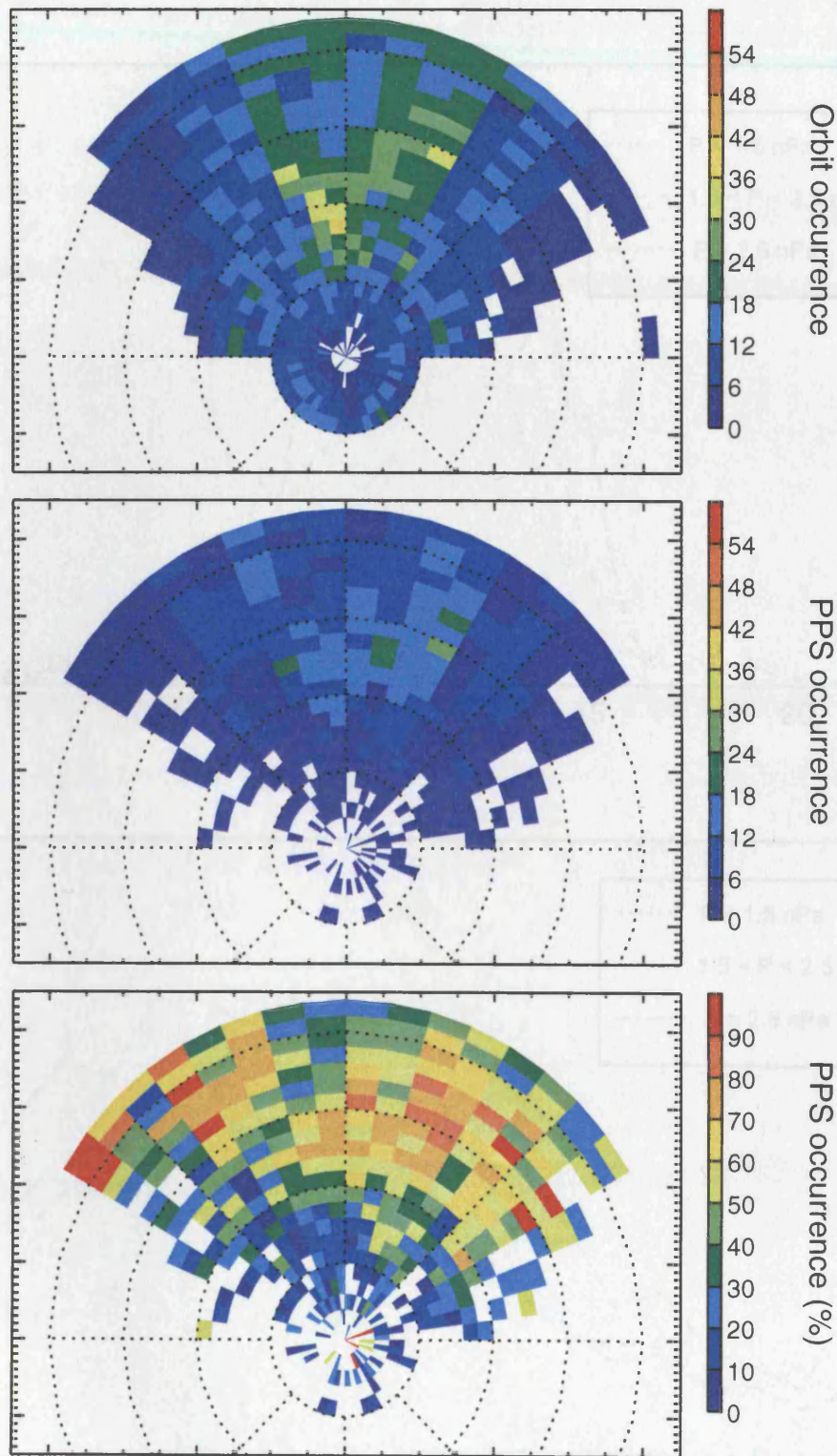


FIGURE 6.14: Pulsed particle signature statistics in MLT: MLAT co-ordinates, under solar wind dynamic pressures greater than 2.5 nPa.

Integrated MLT: MLAT PPS dependence on P_{sw}

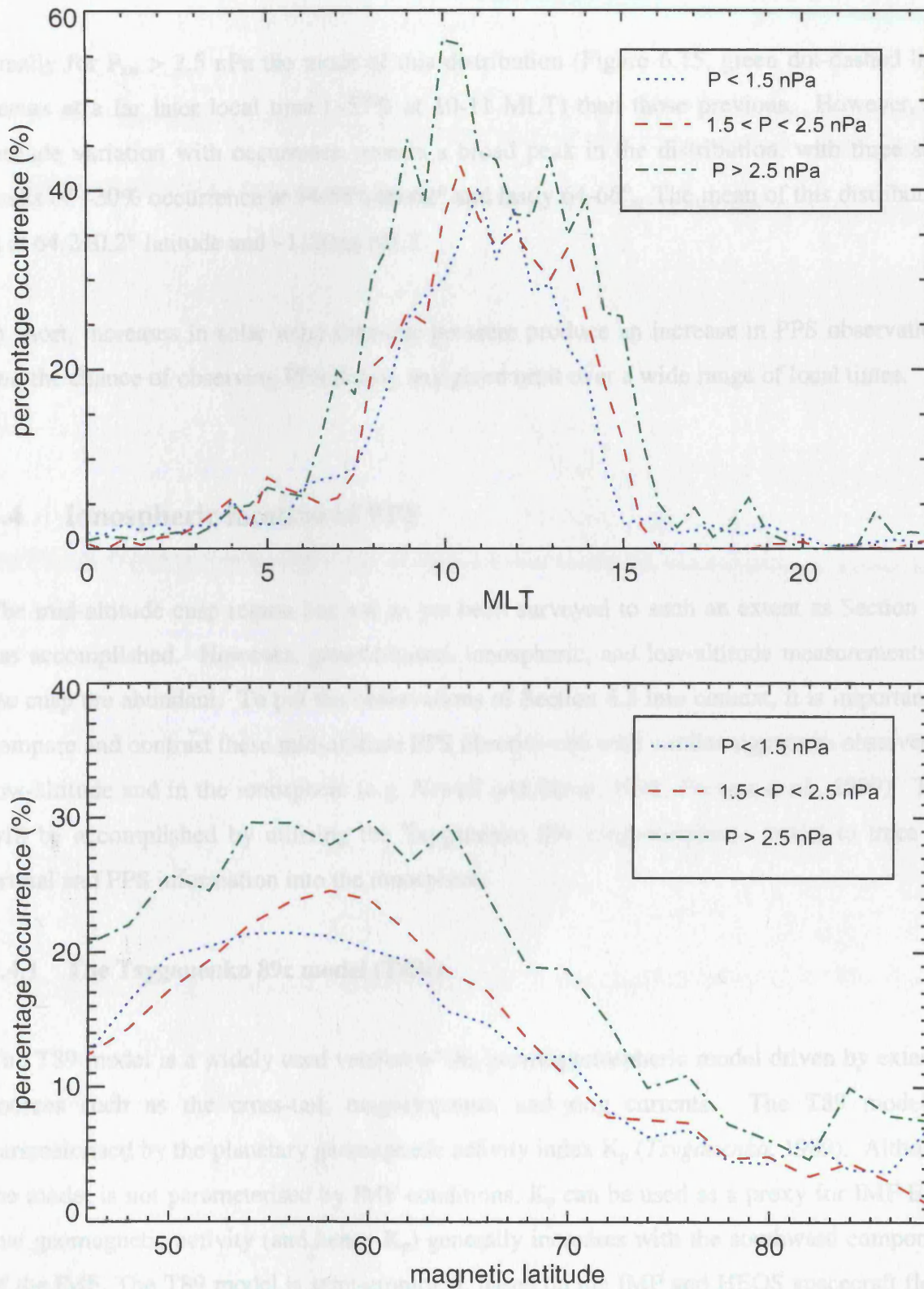


FIGURE 6.15: (top) MLT dependence of PPS location on solar wind dynamic pressure integrated over all magnetic latitudes and (bottom) MLAT dependence of PPS location upon solar wind dynamic pressure integrated over all MLTs.

demonstrates this also (red dashed line), insofar as the integrated distributions peak at higher values. The mean of this distribution is also $63.8 \pm 0.2^\circ$ latitude but at 1115 ± 4 MLT

Finally for $P_{sw} > 2.5$ nPa the mode of this distribution (Figure 6.15, green dot-dashed line) occurs at a far later local time ($\sim 57\%$ at 10-11 MLT) than those previous. However, the latitude variation with occurrence reveals a broad peak in the distribution, with three sub-peaks of $\sim 30\%$ occurrence at $54-58^\circ$, $60-62^\circ$ and lastly $64-66^\circ$. The mean of this distribution is at $64.2 \pm 0.2^\circ$ latitude and $\sim 1120 \pm 4$ MLT.

In short, increases in solar wind dynamic pressure produce an increase in PPS observations *and* the chance of observing PPS during any given orbit over a wide range of local times.

6.4 Ionospheric location of PPS

The mid-altitude cusp region has not as yet been surveyed to such an extent as Section 6.3 has accomplished. However, ground-based, ionospheric, and low-altitude measurements of the cusp are abundant. To put the observations of Section 6.3 into context, it is important to compare and contrast these mid-altitude PPS observations with similar signatures observed at low-altitude and in the ionosphere (e.g. *Newell and Meng, 1991; Provan et al., 1999*). This will be accomplished by utilising the Tsyganenko 89c magnetospheric model to trace the orbital and PPS information into the ionosphere.

6.4.1 The Tsyganenko 89c model (T89c)

The T89 model is a widely used version of the geomagnetospheric model driven by external sources such as the cross-tail, magnetopause, and ring currents. The T89 model is parameterised by the planetary geomagnetic activity index K_p (*Tsyganenko, 1989*). Although the model is not parameterised by IMF conditions, K_p can be used as a proxy for IMF B_z in that geomagnetic activity (and hence K_p) generally increases with the southward component of the IMF. The T89 model is semi-empirical, based on the IMP and HEOS spacecraft fleets and is deemed to be valid up to $70 R_E$ down the magnetotail. The Tsyganenko 89c model is merely empirically extended to include information from ISEE-1 and -2 spacecraft throughout their missions, with an extended range of K_p values available. The input values of K_p on which the T89c model is dependent are from $0 \leq K_p \leq 6$.

Figure 6.16 shows three examples of the Tsyganenko 89c magnetospheric model for (a) quiet conditions ($K_p=0, 0^+$), (b) average quiet conditions ($K_p=2^-, 2, 2^+$), and (c) for moderately disturbed ($K_p=4^-, 4, 4^+$) conditions for zero dipole tilt (taken from *Tsyganenko, 1989*). Of course in reality the Earth's dipolar field is at an 11° inclination to the Earth's rotation axis. What is also noticeable in these three figures is the magnetic latitude of the open closed field line boundary (OCFLB) in each case. Neglecting dipolar tilt, the OCFLB is calculated to lie at $\sim 78^\circ$ for $K_p=0$, at 76° for $K_p=2$ and at 74° for $K_p=4$ in magnetic latitude.

The Tsyganenko 89c model was utilised in this Chapter for two reasons. Firstly, this model is the most widely used in space physics and secondly later models such as the Tsyganenko 96 series are not as readily available as T89c. In view of these specifics, the Tsyganenko 89c model was utilised to trace the footprint of Polar into the ionosphere.

To judge the effect of parameterizing T89c by K_p , the tracing of the model was examined in detail with the case study detailed in Chapter 4. In particular the location of Polar when observing the OCFLB was traced using the T89c model to an altitude of 100 km in the ionosphere under varying K_p conditions. Table 6.1 summarises these results:

K_p	ILAT	ILON	MLT
0	80.9	102.6	1228
1	80.7	102.4	1227
2	80.5	102.0	1226
3	80.2	101.9	1225
4	80.0	101.7	1224
5	79.6	101.7	1224
6	78.6	100.6	1220

Table 6.1: Variation of the ionospheric footprint of the Polar spacecraft mapped into the ionosphere by the T89c model under varying K_p conditions in terms of invariant latitude (ILAT), invariant longitude (ILON) and MLT.

From Table 6.1, it is evident that even for the extreme values of K_p , the ionospherically traced field lines differ in invariant latitude by 2.3° and longitude by 2.6° . The occurrence of K_p values of 0 and 6 are rare and so for the majority of K_p conditions, the ionospheric

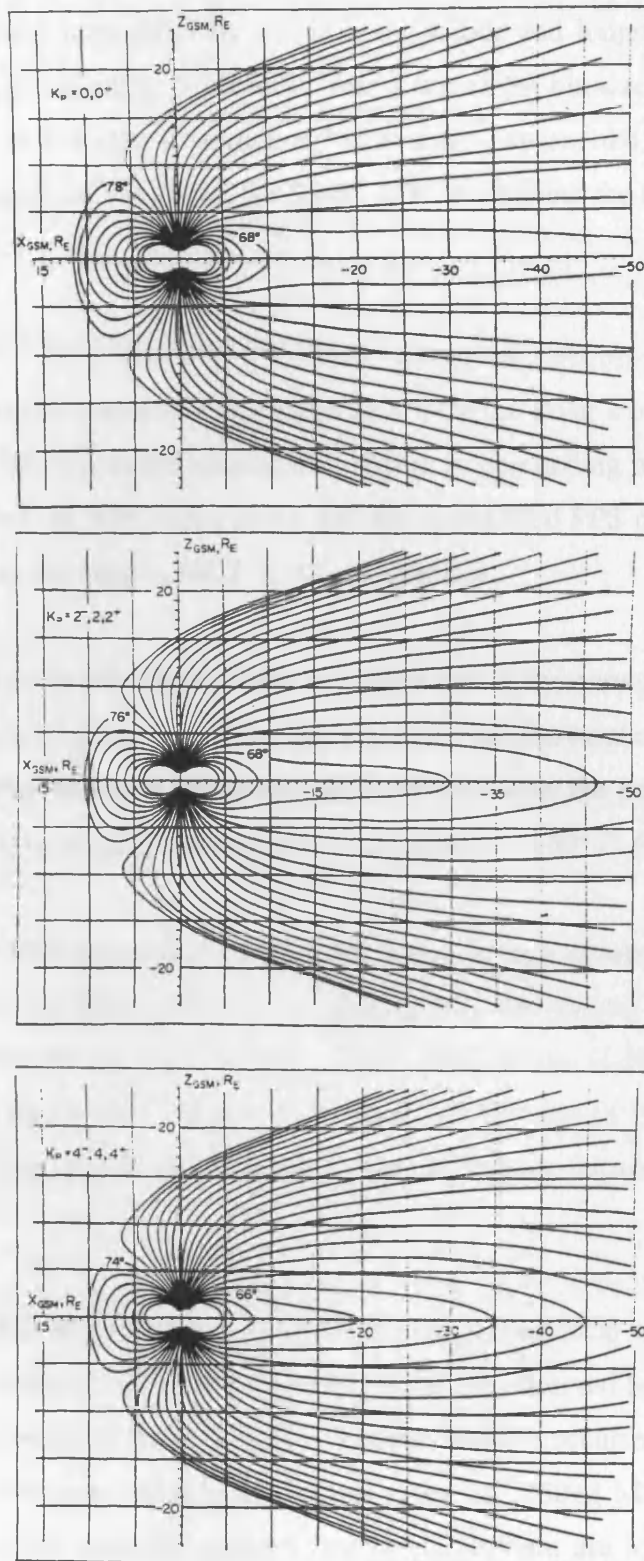


FIGURE 6.16: Three examples of the Tsyganenko 89c magnetospheric model for (a) quiet conditions ($K_p=0$), (b) average quiet conditions ($K_p=2$), and (c) for moderately disturbed ($K_p=4$) conditions for zero dipole tilt (taken from *Tsyganenko, 1989*).

footprint of the field lines differ by $\sim 1^\circ$ in both latitude and longitude, and ~ 5 minutes of MLT for varying geomagnetic conditions. This is within the bin size of 2° and 30 minutes of ILAT and MLT respectively. Consequently an average Tsyganenko model can be employed for average geomagnetic activity i.e. for $K_p=3^-, 3, 3^+$, throughout the statistical study.

6.4.2 All IMF

Figure 6.17 shows the ionospherically traced PPS location, Polar's orbital information traced to an altitude of 100 km in the ionosphere. Again, in descending order, Figure 6.17 shows the orbital occurrences, PPS occurrences, and the normalized PPS occurrence of PPS under all IMF conditions, this time in MLT: ILAT co-ordinates.

The orbital occurrence per bin is greatly increased due to the conversion between magnetic latitude and invariant latitude and also closely grouped around local noon. Over 55 orbits per bin occur between 0900-1430 MLT and 54° to 90° and over the polar cap. The maximum occurrences (> 99) occur close to magnetic noon between $70-80^\circ$ ILAT.

As expected, the PPS occurrence distribution is also closely grouped within three hours of local noon, and at far higher latitudes in keeping with the tracing of these features in the magnetosphere into the ionosphere. Only single observations of PPS during one orbit are observed outside 09-15 MLT and 60° to 90° and the majority (> 33) between $72-84^\circ$. The maximum occurrence is 108 observations per bin and occurs between 1130-1200 MLT and $76-78^\circ$.

The *normalized* distribution reveals similar grouping around local noon at similar latitudes. Significant percentages ($> 30\%$) of PPS observations are observed between 0830-1530 MLT and $72-84^\circ$. The mode of the distribution between 50-60% occurrence between 1030-1100 and $76-78^\circ$, and the mean value is around this range, at 1050 ± 3 MLT and $75.4 \pm 0.1^\circ$. The normalized occurrence statistics mapped into the ionosphere are lower in percentage than their magnetospheric counterparts. This is due to two factors. Many magnetospheric orbital bins fit into one ionospheric orbital bin. Further data losses also result due to the field line mapping of Polar into the ionosphere. In some instances, the Tsyganenko 89c model has some difficulty in mapping positions where a magnetic null point exists i.e. the heart of the cusp region, through simply being a closed field line model. Therefore, orbits where Polar is

POLAR PPS Ionospheric location (all IMF)

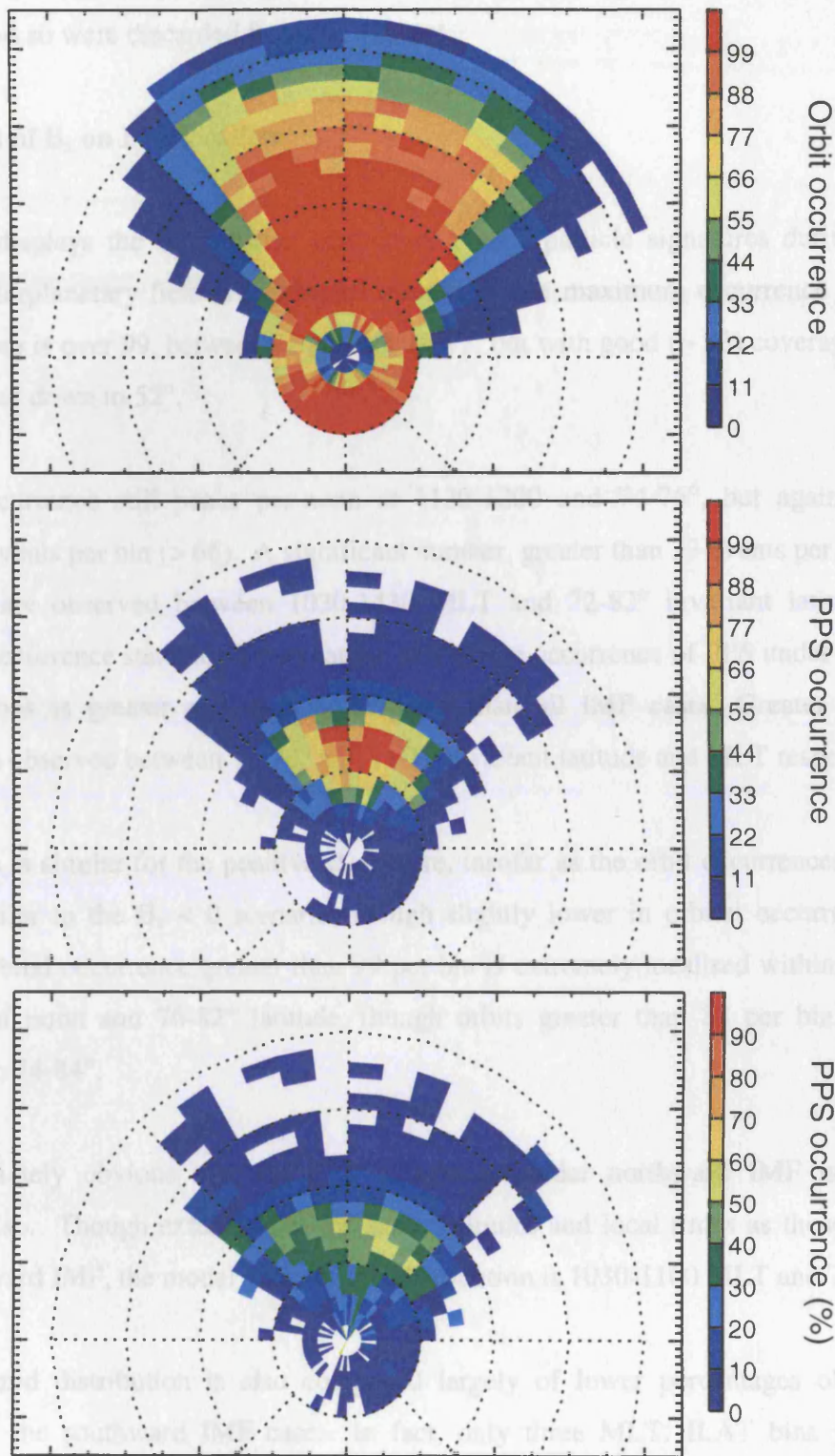


FIGURE 6.17: Pulsed particle signature location and orbital characteristics of Polar under all IMF conditions in MLT: ILAT co-ordinates. The features and orbital information were traced to an altitude of 100 km in the ionosphere using the Tsyganenko 89c model (with $K_p=3$). From top to bottom Figure 6.17 displays the orbit occurrence, PPS occurrence and the normalised PPS occurrence in 30 minute and 2 degree bins.

situated exactly at the magnetic null point in the model cannot be accurately traced into the ionosphere and so were discarded from the data set.

6.4.3 Effect of B_z on PPS location

Figure 6.18 displays the ionospheric location of pulsed particle signatures during periods where the interplanetary field is southward directed. The maximum occurrence of Polar's orbit in one bin is over 99, between 72 and 80° ILAT, but with good (> 33) coverage in those local times and down to 52°.

The PPS occurrence still peaks pre-noon at 1130-1200 and 74-76°, but again at lower numbers of events per bin (> 66). A significant number, greater than 33 events per bin, of the occurrences are observed between 1030-1430 MLT and 72-82° invariant latitude. The normalized occurrence statistics show that the percentage occurrence of PPS under southward IMF conditions is greater and more widespread than all IMF cases. Greater than 50% occurrence is observed between 74-78° and 11-13 invariant latitude and MLT respectively.

The situation is similar for the positive B_z picture, insofar as the orbit occurrences in Figure 6.19 are similar to the $B_z < 0$ scenario, though slightly lower in orbital occurrence. The maximum orbital occurrence greater than 99 per bin is extremely localised within two hours either side of noon and 76-82° latitude, though orbits greater than 88 per bin extend in latitude, from 74-84°.

It is immediately obvious that the PPS occurrence under northward IMF is lower in magnitude also. Though extending to the same latitudes and local times as those observed under southward IMF, the modal value of this distribution is 1030-1100 MLT and 74-6°.

The normalized distribution is also composed largely of lower percentages observed as compared to the southward IMF case. In fact, only three MLT: ILAT bins possess an occurrence of greater than 50%. Greater than 30% occurrence is spread from 09-15 MLT and 72-86° invariant.

From Figure 6.20, integrating over all local times and latitudes, it can be seen that the overall percentages of the ionospheric location of PPS are increased greatly over most latitudes and local times for IMF $B_z < 0$. The two similar peaks of the southward IMF distribution (red

POLAR PPS Ionospheric location (Bz -ve)

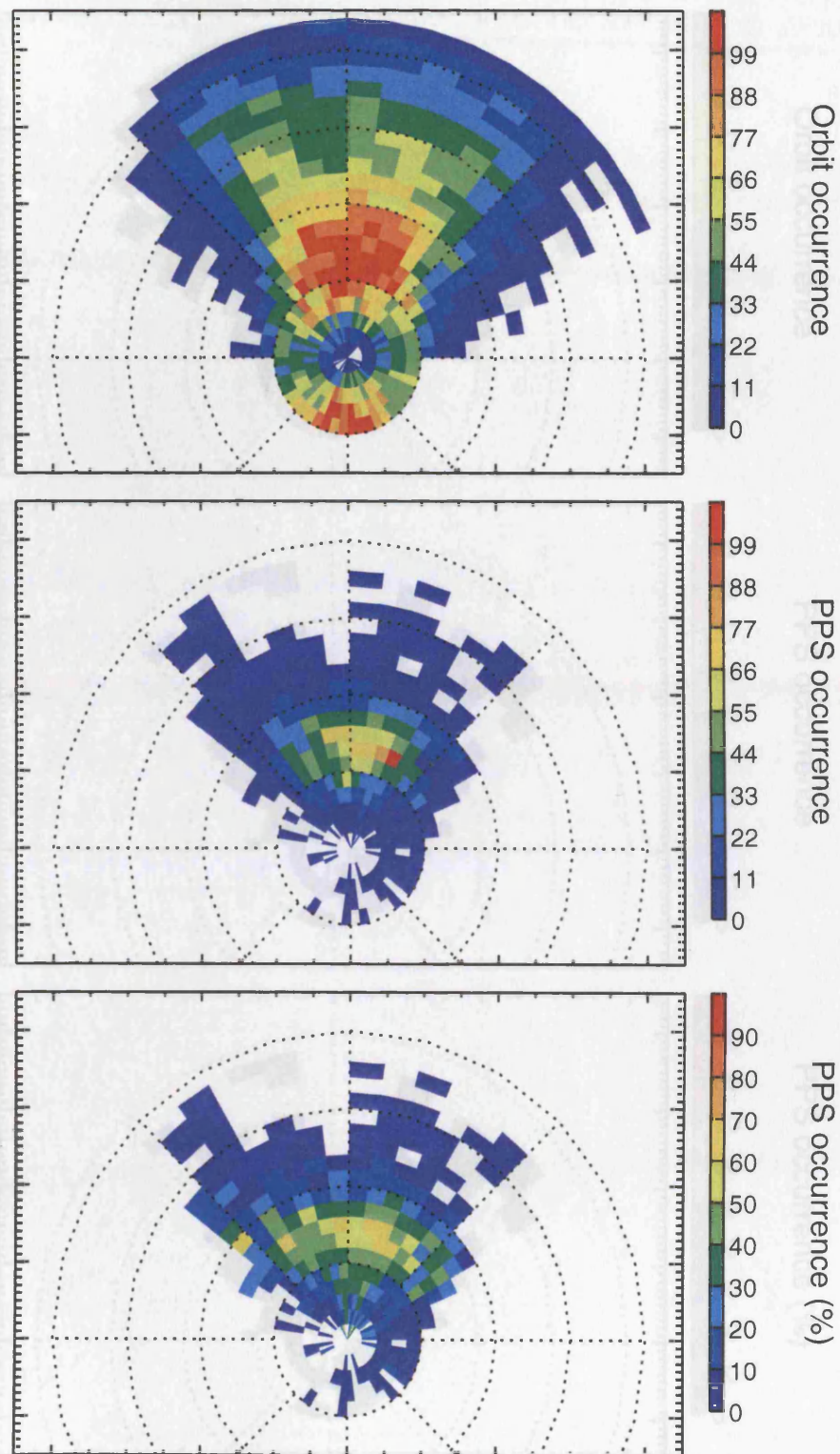


FIGURE 6.18: Pulsed particle signature statistics under negative Bz conditions, in MLT: ILAT co-ordinates in the same format as Figure 6.17.

POLAR PPS Ionospheric location (Bz +ve)

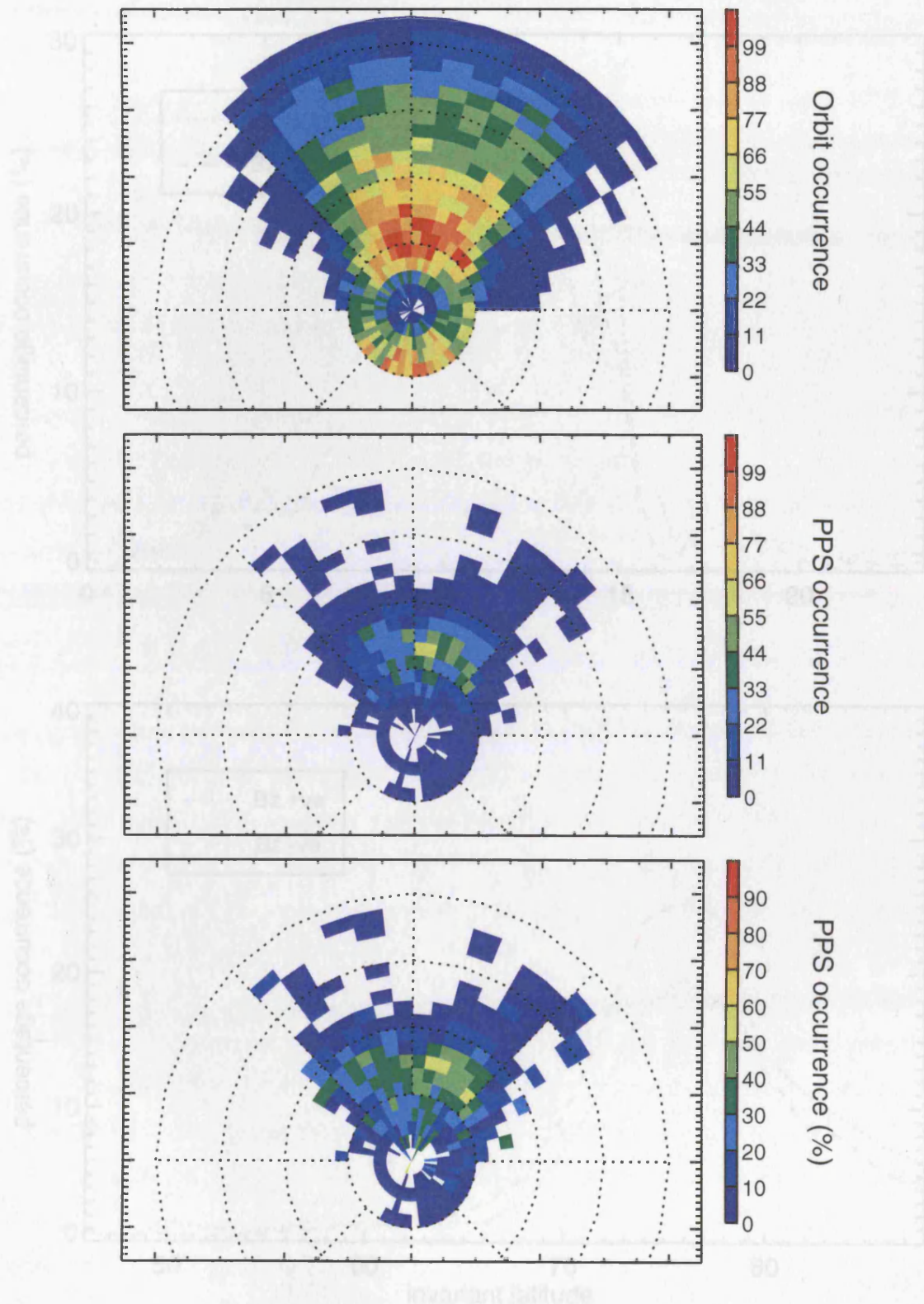


FIGURE 6.19: Pulsed particle signature statistics under positive Bz conditions, in MLT: ILAT co-ordinates in the same format as Figure 6.17.

Integrated MLT: ILAT PPS dependence on IMF Bz

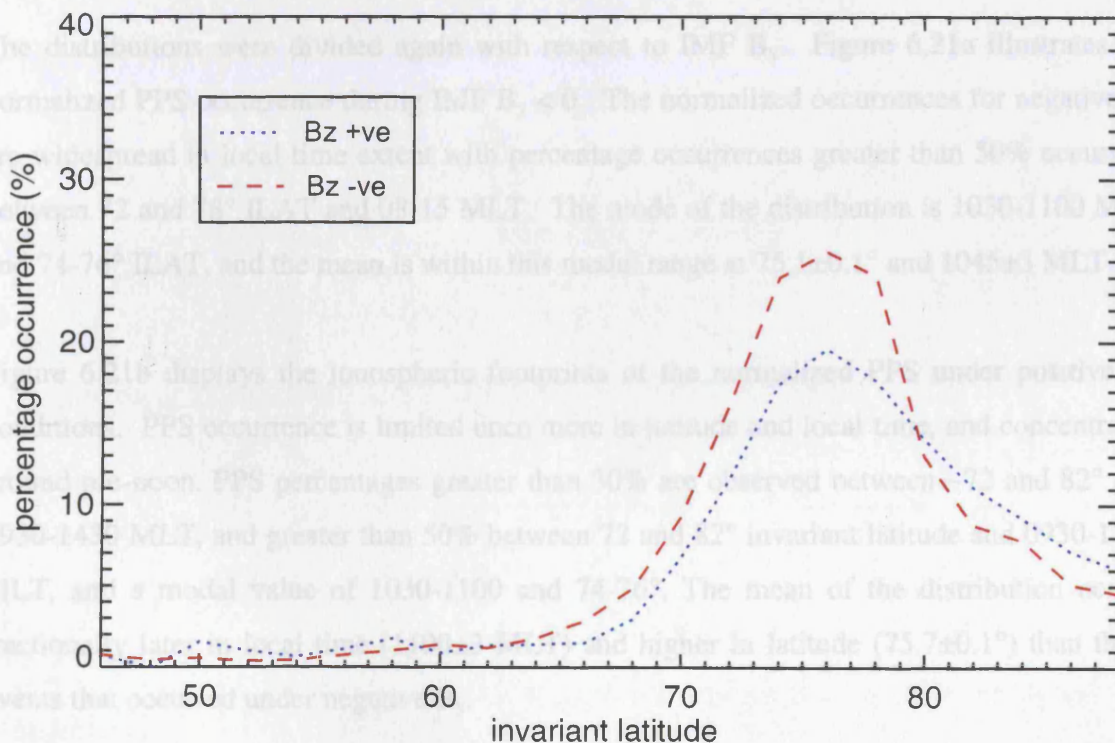
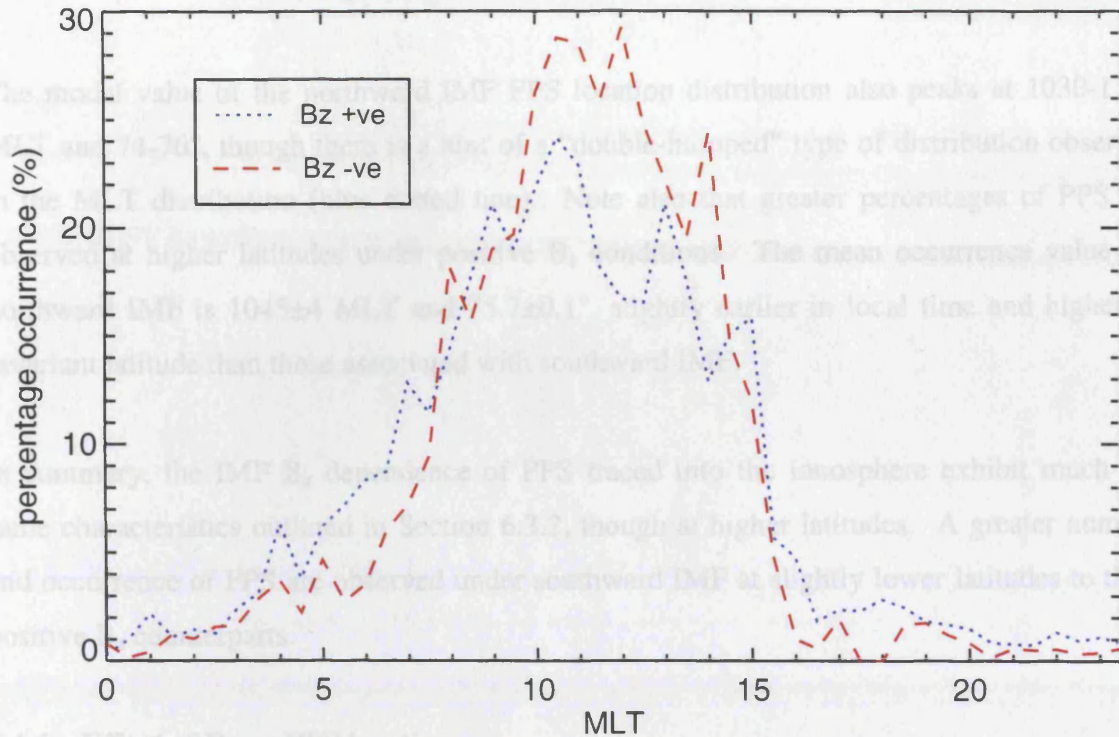


FIGURE 6.20: (top) MLT dependence of PPS location on IMF Bz integrated over all magnetic latitudes and (bottom) ILAT dependence of PPS location upon IMF Bz integrated over all MLTs.

The dynamic pressure dependence on the ionospheric footprint of PPS is traced from the mid-latitude magnetosphere to an altitude of 100 km in the ionosphere. Figure 6.22 displays the

dashed lines) are at 1030-1100 and 12-1230 MLT and $76-78^\circ$, whereas the mean is pre-noon, at 1100 ± 3 MLT and a slightly lower latitude at $75.2\pm 0.1^\circ$.

The modal value of the northward IMF PPS location distribution also peaks at 1030-1100 MLT and $74-76^\circ$, though there is a hint of a “double-humped” type of distribution observed in the MLT distribution (blue dotted line). Note also that greater percentages of PPS are observed at higher latitudes under positive B_z conditions. The mean occurrence value for northward IMF is 1045 ± 4 MLT and $75.7\pm 0.1^\circ$, slightly earlier in local time and higher in invariant latitude than those associated with southward IMF.

In summary, the IMF B_z dependence of PPS traced into the ionosphere exhibit much the same characteristics outlined in Section 6.3.2, though at higher latitudes. A greater number and occurrence of PPS are observed under southward IMF at slightly lower latitudes to their positive B_z counterparts.

6.4.4 Effect of B_y on PPS location

The distributions were divided again with respect to IMF B_y . Figure 6.21a illustrates the normalized PPS occurrence during IMF $B_y < 0$. The normalized occurrences for negative B_y are widespread in local time extent with percentage occurrences greater than 50% occurring between 72 and 78° ILAT and 08-15 MLT. The mode of the distribution is 1030-1100 MLT and $74-76^\circ$ ILAT, and the mean is within this modal range at $75.1\pm 0.1^\circ$ and 1045 ± 3 MLT.

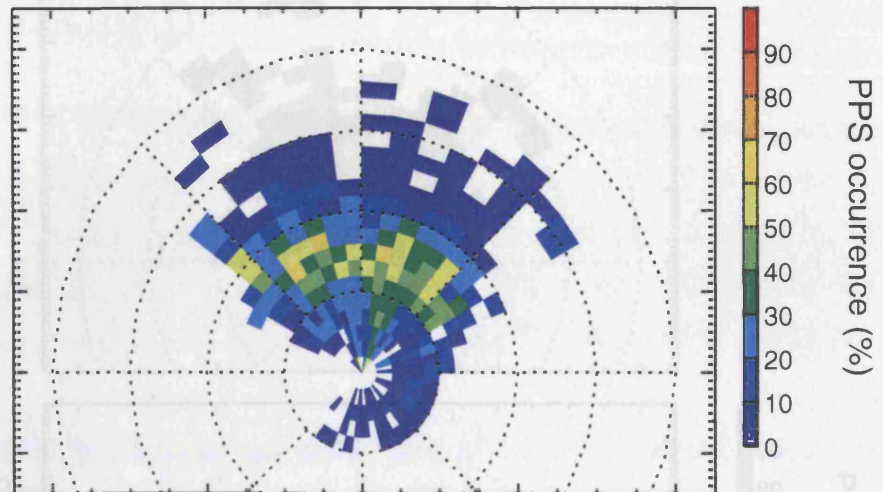
Figure 6.21b displays the ionospheric footprints of the normalized PPS under positive B_y conditions. PPS occurrence is limited once more in latitude and local time, and concentrated around pre-noon. PPS percentages greater than 30% are observed between ~ 72 and 82° and 0930-1430 MLT, and greater than 50% between 72 and 82° invariant latitude and 0930-1300 MLT, and a modal value of 1030-1100 and $74-76^\circ$. The mean of the distribution occurs fractionally later in local time (1100 ± 3 MLT) and higher in latitude ($75.7\pm 0.1^\circ$) than those events that occurred under negative B_y .

6.4.5 Effect of solar wind dynamic pressure on ionospheric PPS location

The dynamic pressure dependence on the ionospheric footprint of PPS is traced from the mid-altitude magnetosphere to an altitude of 100 km in the ionosphere. Figure 6.22 displays the

POLAR PPS Ionospheric location dependence upon B_y

(a) $B_y < 0$



(b) $B_y > 0$

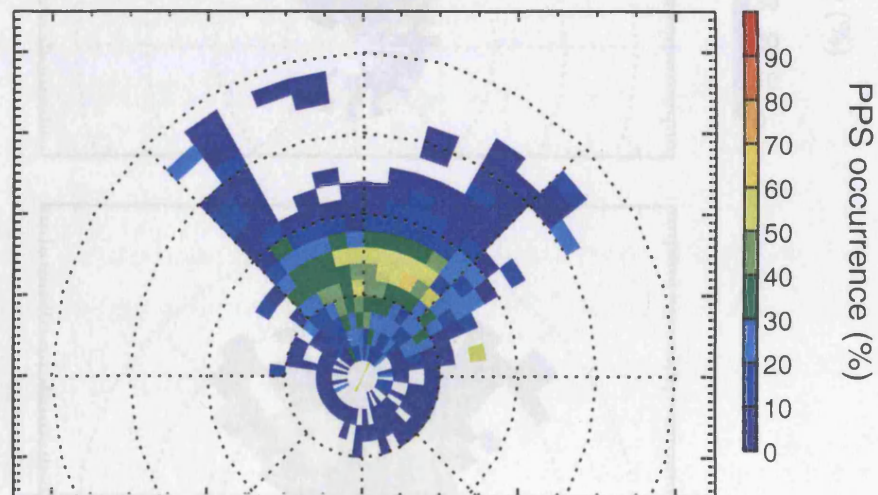
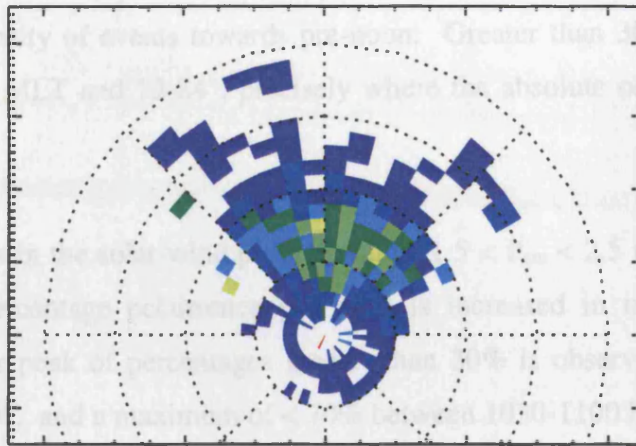


FIGURE 6.21: Normalised pulsed particle signature statistics under (a) negative B_y and (b) positive B_y conditions, in MLT: ILAT co-ordinates.

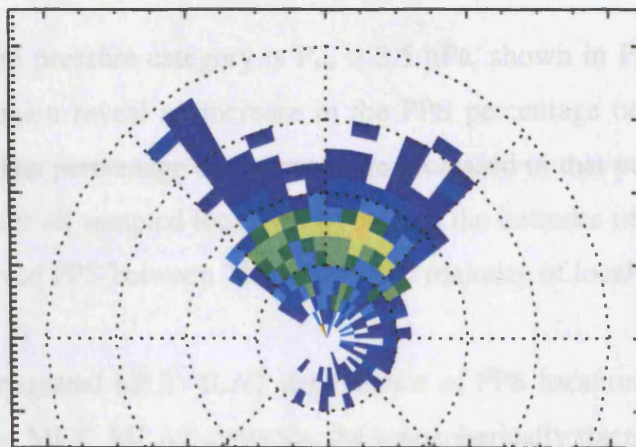
FIGURE 6.21: Pulsed particle signature statistics in MLT: ILAT co-ordinates, under solar wind dynamic pressures of (a) less than 1.5 nPa, (b) between 1.5 and 2.5 nPa, and (c) over 2.5 nPa.

Pressure dependence on ionospheric location of PPS

(a) $P < 1.5$ nPa



(b) $1.5 < P < 2.5$ nPa



(c) $P > 2.5$ nPa

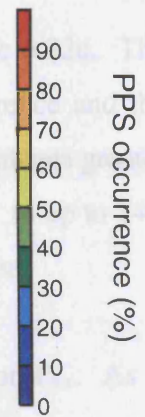
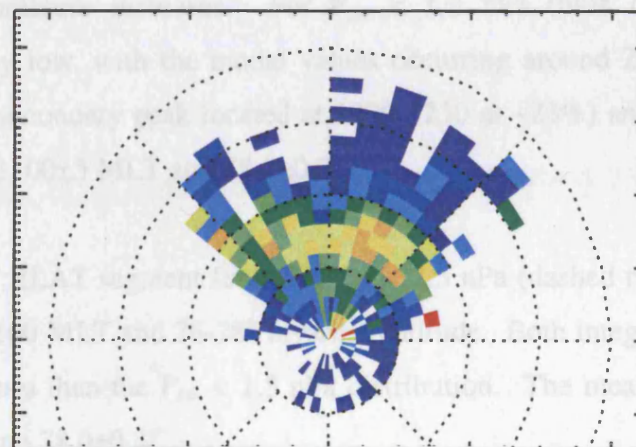


FIGURE 6.22: Pulsed particle signature statistics in MLT: ILAT co-ordinates, under solar wind dynamic pressures of (a) less than 1.5 nPa, (b) between 1.5 and 2.5 nPa, and (c) over 2.5 nPa.

ionospheric footprint of the normalized PPS occurrence for solar wind dynamic pressures, P_{sw} , (a) less than 1.5 nPa, (b) between 1.5 and 2.5 nPa, and (c) greater than 2.5 nPa (in descending order). The normalized occurrences in Figure 6.22a for $P_{sw} < 1.5$ nPa show a definite lean for the majority of events towards pre-noon. Greater than 30% occurrence is observed between 09-14 MLT and $72-84^\circ$, precisely where the absolute occurrence peaked (not shown).

The traced PPS footprints in the solar wind pressure range $1.5 < P_{sw} < 2.5$ nPa are displayed in Figure 6.22b. The percentage occurrence per orbit is increased in magnitude in this pressure range; a broader peak of percentages greater than 30% is observed between 1030 and 1500 MLT and $72-80^\circ$, and a maximum of $< 70\%$ between 1030-1100 MLT and $72-76^\circ$.

Finally, the last solar wind pressure category is $P_{sw} > 2.5$ nPa, shown in Figure 6.22c. The normalized occurrences again reveal an increase in the PPS percentage occurrence and the width of MLT location. The percentage occurrences are increased in that percentages greater than 30% are observed over all sampled local times between the latitudes of 70° to up to 84° . Over 50% of orbits observed PPS between $74-78^\circ$ over the majority of local times.

Figure 6.23 shows the integrated MLT: ILAT dependence of PPS location upon P_{sw} . As is the case with the observed MLT: MLAT statistics, the ionospherically traced PPS occurrence increases as dynamic pressure increases. For $P_{sw} < 1.5$ nPa (blue dotted lines), the occurrences are relatively low, with the modal values occurring around 25% at 1100-1130 MLT (though there is a secondary peak located at 1200-1230 at $\sim 23\%$) and $78-80^\circ$, and the mean of the distribution 1100 ± 5 MLT and $78.1 \pm 0.2^\circ$.

The most common MLT: ILAT segment for $1.5 < P_{sw} < 2.5$ nPa (dashed red lines in Figure 6.23) is between 1030-1100 MLT and $76-78^\circ$ invariant latitude. Both integrated peaks occur at higher percentage values than the $P_{sw} < 1.5$ nPa distribution. The mean of this pressure range is $\sim 1120 \pm 4$ MLT and $78.0 \pm 0.2^\circ$.

The mode of this data set is between $76-78^\circ$ and 1000-1030 MLT where percentage occurrence of pulsed particle signatures can be between up to 40%. There is a suggestion of a secondary peak between 1500 and 1530 local time also. The mean of the PPS distribution for solar wind pressures of over 2.5 nPa in magnitude is at 1130 ± 4 MLT and $77.7 \pm 0.2^\circ$.

Integrated MLT: ILAT PPS dependence on P_{sw}

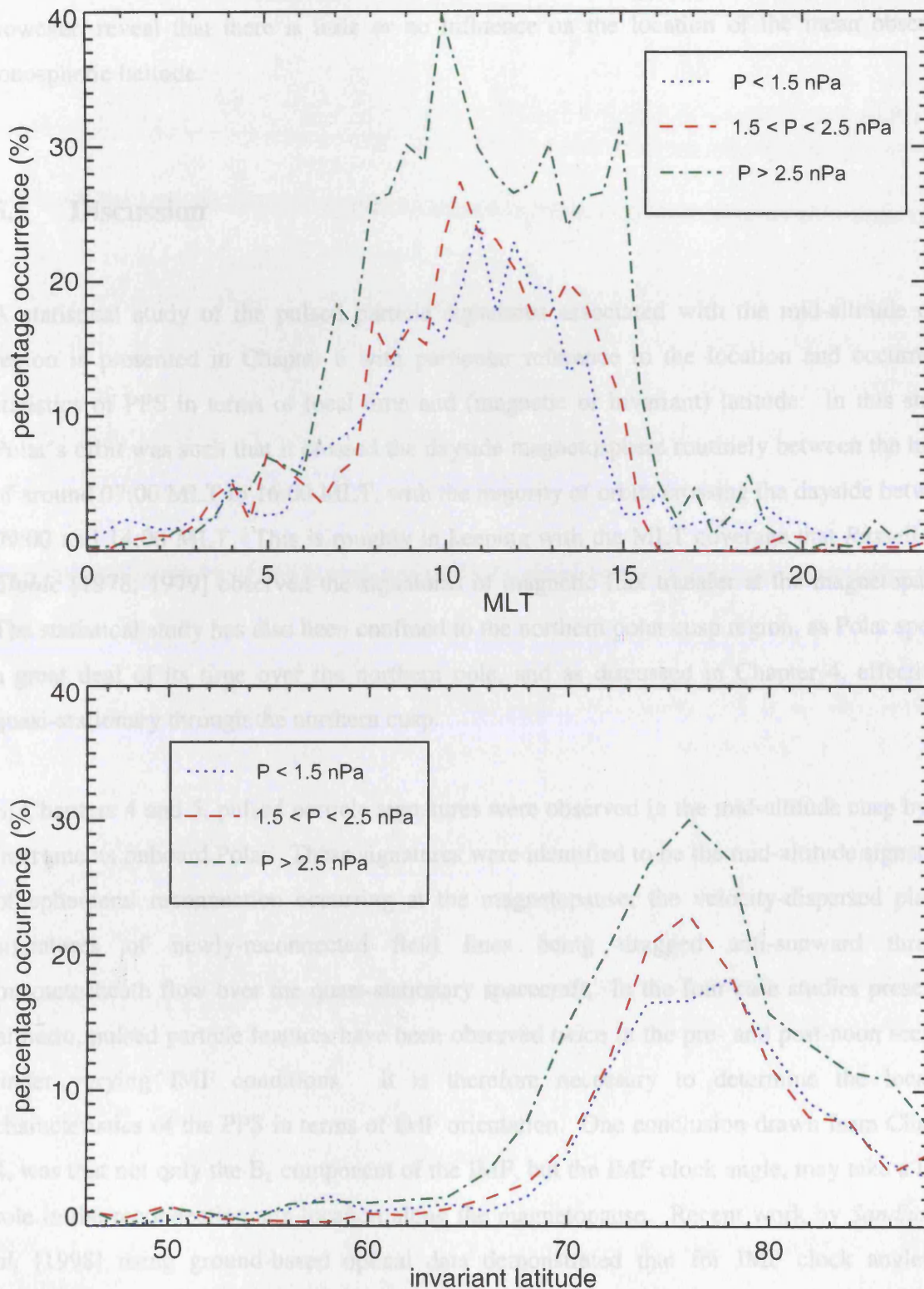


FIGURE 6.23: (top) MLT dependence of PPS location on solar wind dynamic pressure integrated over all magnetic latitudes and (bottom) ILAT dependence of PPS location upon solar wind dynamic pressure integrated over all MLTs.

Once again, enhanced solar wind dynamic pressure begets the observation of increased number and percentage observation of PPS traced into the ionosphere. Incorporating errors, however, reveal that there is little or no influence on the location of the mean observed ionospheric latitude.

6.5 Discussion

A statistical study of the pulsed particle signatures associated with the mid-altitude cusp region is presented in Chapter 6 with particular reference to the location and occurrence statistics of PPS in terms of local time and (magnetic or invariant) latitude. In this study, Polar's orbit was such that it crossed the dayside magnetosphere routinely between the hours of around 07:00 MLT to 16:00 MLT, with the majority of orbits crossing the dayside between 09:00 and 14:00 MLT. This is roughly in keeping with the MLT coverage that *Russell and Elphic* [1978; 1979] observed the signatures of magnetic flux transfer at the magnetopause. The statistical study has also been confined to the northern polar cusp region, as Polar spends a great deal of its time over the northern pole, and as discussed in Chapter 4, effectively quasi-stationary through the northern cusp.

In Chapters 4 and 5, pulsed particle signatures were observed in the mid-altitude cusp by the instruments onboard Polar. These signatures were identified to be the mid-altitude signatures of ephemeral reconnection occurring at the magnetopause; the velocity-dispersed plasma signatures of newly-reconnected field lines being dragged anti-sunward through magnetosheath flow over the quasi-stationary spacecraft. In the four case studies presented hitherto, pulsed particle features have been observed twice in the pre- and post-noon sectors, under varying IMF conditions. It is therefore necessary to determine the location characteristics of the PPS in terms of IMF orientation. One conclusion drawn from Chapter 4, was that not only the B_z component of the IMF, but the IMF clock angle, may take a large role in the reconnection site location along the magnetopause. Recent work by *Sandholt et al.* [1998] using ground-based optical data demonstrated that for IMF clock angles of between 45 and 90 degrees i.e. $|B_y| > |B_z|$, both high- and low-latitude reconnection could take place concurrently. In Chapter 4, PPS were detected when the IMF was $> 90^\circ$, between 45° and 90° , as well as $< 45^\circ$. Reconnection may be expected in the two former intervals, but the latter interval of $< 45^\circ$ clock angle PPS events cannot be explained at this juncture. Chapter 5 presented a similar mid-altitude series of PPS, in conjunction with low-altitude and ground-

based observations. The IMF clock angles during this event were $> 45^\circ$ barring two brief 20 minute spells and predominantly $> 90^\circ$, and so low-latitude reconnection can conceivably be responsible for the PPS observed during the entire interval. A statistical study of PPS signatures according to IMF orientation and more importantly IMF clock angle is vital to prove (or otherwise) the two concurrent reconnection site theory proposed by *Sandholt et al.* [1998] for the dispersed ion signatures observed by Polar.

In this statistical study the PPS were split into a total of 11,919 15-minute periods in the 22-month study period, totalling almost 2980 hours of pulsed particle signatures observed. This is equivalent to an average of almost $4\frac{1}{2}$ hours of PPS per day of the statistical study, or more importantly around 3 hours 20 minutes of pulsed particle signatures per orbit. This represents an extremely extended temporal period that Polar is effectively quasi-stationary in the mid-altitude cusp.

Pulsed particle signatures were presented irrespective of IMF orientation in MLT: MLAT coordinates, in order to characterise the spatial extent of the features in the dayside magnetosphere. The first conclusion that can be drawn from this study is that these PPS events occur over a huge range of latitudes and local times, whatever the upstream interplanetary conditions. Over 60% percentage occurrences were observed between 50 and 75° and 09-13 MLT, at a mean value of 65.3° and 1050 MLT. However, their occurrence statistics and location characteristics *do* vary with IMF orientation and solar wind dynamic pressure.

When the pulsed particle signatures are categorised with respect to IMF orientation, there are several points to note. Firstly there are several differences between the distributions when split in terms of IMF B_z . Not only is an increased number of PPS observed during southward IMF, but the *percentage* occurrence increases, implying that, although positive IMF B_z does not exclude the observation of PPS, southward IMF presents more favourable conditions for pulsed particle signatures. This is in keeping with the low-latitude reconnection scenario, in that flux transfer across the magnetopause occurs mainly during southward-directed interplanetary and magnetosheath field conditions (e.g. *Russell and Elphic*, 1978,1979; *Berchem and Russell*, 1984; *Rijnbeek et al.*, 1984; *Kawano and Russell*, 1997; *Neudegg et al.*, 2000). For southward IMF, low-latitude reconnection is presumed to dominate, whereas northward IMF allows lobe reconnection at higher latitudes to ensue. This is reflected in the mean latitudinal occurrence for both orientations, in that the southward IMF mean is situated

at 64.9° and the northward IMF mean at 65.8° . This is again an indication that a disparity exists between the location of negative B_z events and positive B_z events.

Subtle differences principally exist between the normalized occurrence distribution for positive and negative IMF B_y . Both modal values of B_y orientation were between 64 and 66° , but at differing local times; 1030-1100 MLT for B_y -ve and 1200-1230 MLT for B_y +ve. The positive B_y cases also are more closely grouped around local noon, whereas the negative B_y cases are greatly spread in both local time and latitudes. Mean values however, place the distributions at similar latitudes and local times. The similar mean values suggest no alteration of the foci under varying polarity of B_y . Theory (Gosling *et al.*, 1990, Cowley *et al.*, 1991a) proposes that for negative (positive) IMF B_y the reconnection site is shifted through the anti-parallel criteria towards dawn (dusk). There is no clear shift of the foci of local time under each B_y events in these directions.

It is difficult to envisage a reconnection scenario where there was no dependence of signature location upon IMF B_y . Figure 6.24 may illustrate one such possible scenario. Newell and Meng [1992] used DMSP to observe that the cusp is located in the same direction as the sense of B_y , whereas the CUTLASS radars (Provan *et al.*, 1999) observed the ionospheric flows associated with the cusp in the opposite direction to the sense of IMF B_y relative to noon. This is due to the region of the cusp that each instrument samples. The DMSP spacecraft cuts the reconnected flux tubes closer to the reconnection site location and so observes the direct signatures of reconnection, shown by the satellite in Figure 6.24. The CUTLASS radars measure the flow *excited* from reconnection that flows towards the opposite flank of the Earth, also shown in Figure 6.24. In the statistical study, Polar is situated close to the noon-midnight meridian. If Polar observes the signatures of reconnection and is located between the DMSP position and CUTLASS facility along the dotted blue line then Polar *may* not observe an IMF B_y dependence. It is stressed that this representation would only be possible if the average position of the mid-altitude cusp lies between that of the DMSP and CUTLASS averages. In this instance Polar would experience little or no IMF B_y effects.

The presentation of the various clock angles of IMF orientation with respect to PPS characteristics and occurrence merely serve to demonstrate that occurrence and mean latitude increase and decrease respectively for B_z negative conditions. This is highlighted chiefly by the distributions composed from opposite quadrants of clock angles i.e. between positive B_y and B_z and negative B_y and B_z , but can be seen in all four distributions. What is also

emphasised is the lack of real evidence of IMF B_y control of the mid-altitude cusp. This is also perhaps less than surprising, in the terms outlined above. The northern mid-altitude cusp is statistically a vast area, which Polar spends on average almost 15% of its highly elliptical orbit traversing. A polarity change in IMF B_y may shift the reconnection site significantly, but it remains to be seen whether this change in conditions will effect the exit of Polar from the mid-altitude cusp. Furthermore, recent studies by *Milan et al.* [2000] present UV observations of a bifurcated reconnection X-line that remains active over a wide range of local times along the dusk flank (Figure 2.18). An active X-line covering many hours of local time would not necessarily shift far enough in the Y-direction under varying IMF B_y polarities. If observations such as these are commonplace, then Polar may never observe a B_y dependence.

The influence of solar wind dynamic pressure variations on pulsed particle signature observation is puzzling. Events observed when $P_{sw} < 1.5$ nPa are localised around noon with maximum occurrences under 60%. For pressures between 1.5 and 2.5 nPa, the event occurrence is more widespread in latitude and local time. The occurrence percentages under these conditions are increased and up to 70% occurrence per orbital pass. For events observed when $P_{sw} > 2.5$ nPa there is almost no dependence on local time at all, in that high occurrence statistics are present at all local times. Percentages of up to 90% occur during increased dynamic pressure cusp passes. It is apparent from these statistics that the percentage occurrences per bin increase with increased dynamic pressure, and become extended in latitudes and local times.

This can be explained in terms of the confinement of the magnetosphere by the solar wind. Under low pressure exertion by the solar wind the Earth's magnetosphere is obviously extended in its occupying volume. Figure 6.25 shows three such possible sampled areas of the "mid-altitude cusp" under varying solar wind dynamic pressure regimes. Under low pressure the magnetosphere may be extended in volume, and the orbit of Polar will sample a narrower region of the cusp marked by the blue orbit. Under "normal" pressures, Polar will sample a larger cusp region marked by the green orbit, and under intense solar wind dynamic pressure, the magnetosphere may be confined to a smaller-than-average volume, thus allowing Polar to sample an extended cusp region marked by the red orbit.

The high-latitude ionospheric precipitation regions were first statistically characterised by *Newell and Meng* [1988; 1992], who described these regions in terms of magnetospheric

source regions to which they are believed to map. This was achieved by comparing thousands of meridional cuts through the ionosphere of the DMSP satellites to determine the high-altitude plasma characteristics (see Figure 2.11). They derived a statistical MLT-MLAT map of the dayside ionosphere according to the particle precipitation characteristics observed. Newell and Meng concluded that previous authors e.g. Heikkila and Wamington (1971) among others had not correctly identified the cusp region and that it could be separated into a deep proper cusp region to within 2.5 hours of MLT, dawn side, and a cleft LBL, which maps directly to the cleft just interior to the cusp proper. The cusp proper mapped directly to the cleft just interior to the cusp, consisting of a narrow region of high-energy particles of higher energy and lower flux to those in the cleft. The cleft LBL was identified as a region of lower energy particles. The acceleration mechanism for these particles is thought to be the interaction of two magnetopause Alfvén waves, which are generated by the interaction of the solar wind with the magnetopause. The boundary of the cleft LBL has been observed by the DMSP satellites. The cleft LBL is thought to be a region of lower energy particles and the motion of particles in this region is thought to be dominated by the magnetic field in their orbits. These authors therefore suggest a re-interpretation of the cleft LBL as a region of lower energy particles. Figure 6.26 illustrates two of the conclusions drawn from this study: (a) the cleft LBL is a region of lower energy particles and (b) the cleft LBL is a region of lower energy particles. Figure 6.26 illustrates two of the magnetospheric source regions: (a) a cleft LBL and (b) an open LBL. In either case the cusp is now significantly extended. This effectively maps to an extended X-line in both dimensions, marked by the black dotted line in both diagrams. Of course, this statistical study will be concerned with the magnetospheric source regions themselves, but nevertheless the cusp region identified by Lockwood will, to a certain extent, be analogous to a broader magnetospheric cusp identified by Polar. The features observed in the broader magnetospheric cusp, however, were traced down into the ionosphere using an empirical model, and may be analogous to the ionospheric footprints of the magnetospheric source regions identified by Lockwood (1971).

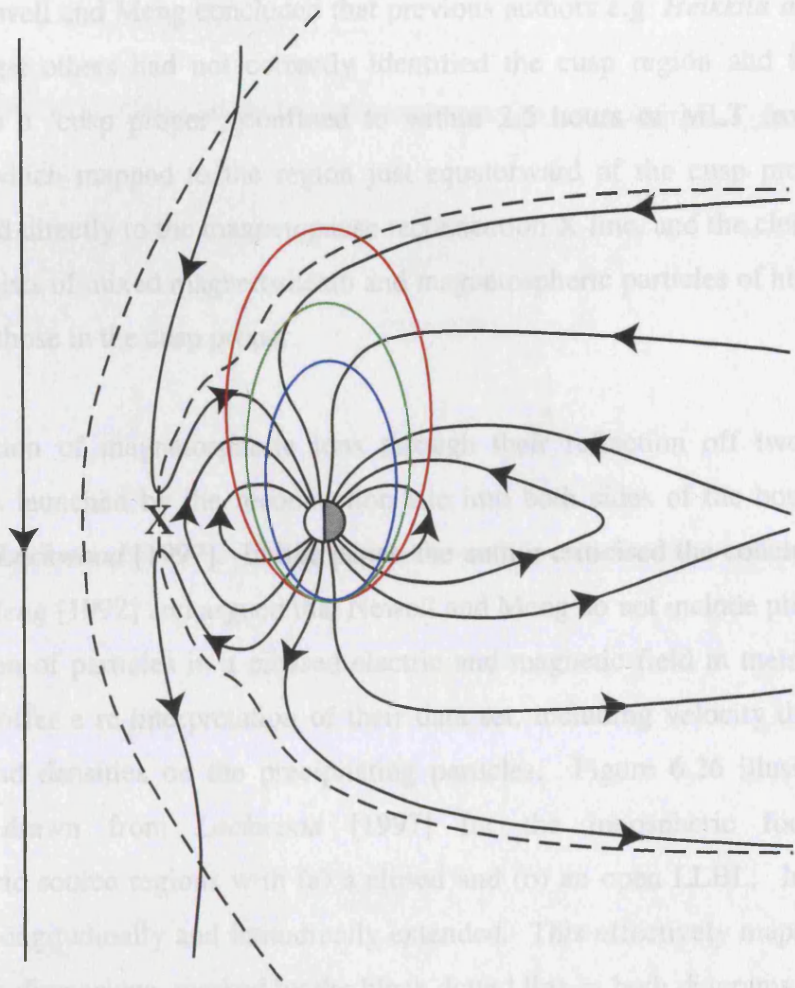


FIGURE 6.25: The dependence of the sampled section by Polar's orbit of the "mid-altitude cusp". Under low pressure the magnetosphere may be extended in volume, and the orbit of Polar will sample a narrower region of the cusp marked by the blue orbit. Under "normal" pressures, Polar will sample a larger cusp region marked by the green orbit, and under intense solar wind dynamic pressure, the magnetosphere may be confined to a smaller-than-average volume, thus allowing Polar to sample an extended cusp region marked by the red orbit.

source regions to which they are believed to map. This was achieved by comparing thousands of meridional cuts through the ionosphere of the DMSP satellites to determine the high-altitude plasma characteristics (see Figure 2.11). They derived a statistical MLT: MLAT map of the dayside ionosphere according to the particle precipitation characteristics observed. Newell and Meng concluded that previous authors e.g. *Heikkila and Winningham* [1971] amongst others had not correctly identified the cusp region and that it could be separated into a 'cusp proper', confined to within 2.5 hours of MLT from noon, and a cleft/LLBL, which mapped to the region just equatorward of the cusp proper. The cusp proper mapped directly to the magnetopause reconnection X-line, and the cleft just interior to the cusp, consists of mixed magnetosheath and magnetospheric particles of higher energy and lower flux to those in the cusp proper.

The acceleration of magnetospheric ions through their reflection off two magnetopause Alfvén waves launched by the reconnection site into both sides of the boundary has been discussed by *Lockwood* [1997]. In this paper, the author criticised the conclusions drawn by *Newell and Meng* [1992] and argued that Newell and Meng do not include plasma convection and the motion of particles in a crossed electric and magnetic field in their studies. These authors then offer a re-interpretation of their data set, including velocity dispersion effects and solar wind densities on the precipitating particles. Figure 6.26 illustrate two of the conclusions drawn from *Lockwood* [1997] for the ionospheric footprints of the magnetospheric source regions with (a) a closed and (b) an open LLBL. In either case the cusp is now longitudinally and latitudinally extended. This effectively maps to an extended X-line in both dimensions, marked by the black dotted line in both diagrams. Of course, this statistical study will be concerned with the magnetospheric source regions themselves, but nevertheless the cusp region identified by Lockwood will, to a certain extent, be analogous to a broader magnetospheric cusp identified by Polar. The features observed in the broader magnetospheric cusp, however, were traced down into the ionosphere using an empirical model, and may be analogous to the ionospheric footprints of the magnetospheric source regions identified by *Lockwood* [1997].

The PPS were classified in two ways; in terms of MLT: magnetic latitude (MLAT), and MLT: invariant latitude (ILAT), and both latitude parameters are illustrated in Figure 6.27. The angle λ is the magnetic latitude of a point on the field line, whereas Λ is the invariant latitude of the field line i.e. the latitude of the point where the field line intersects the Earth's surface. The magnetic latitude of a spacecraft can therefore alter without changing it's

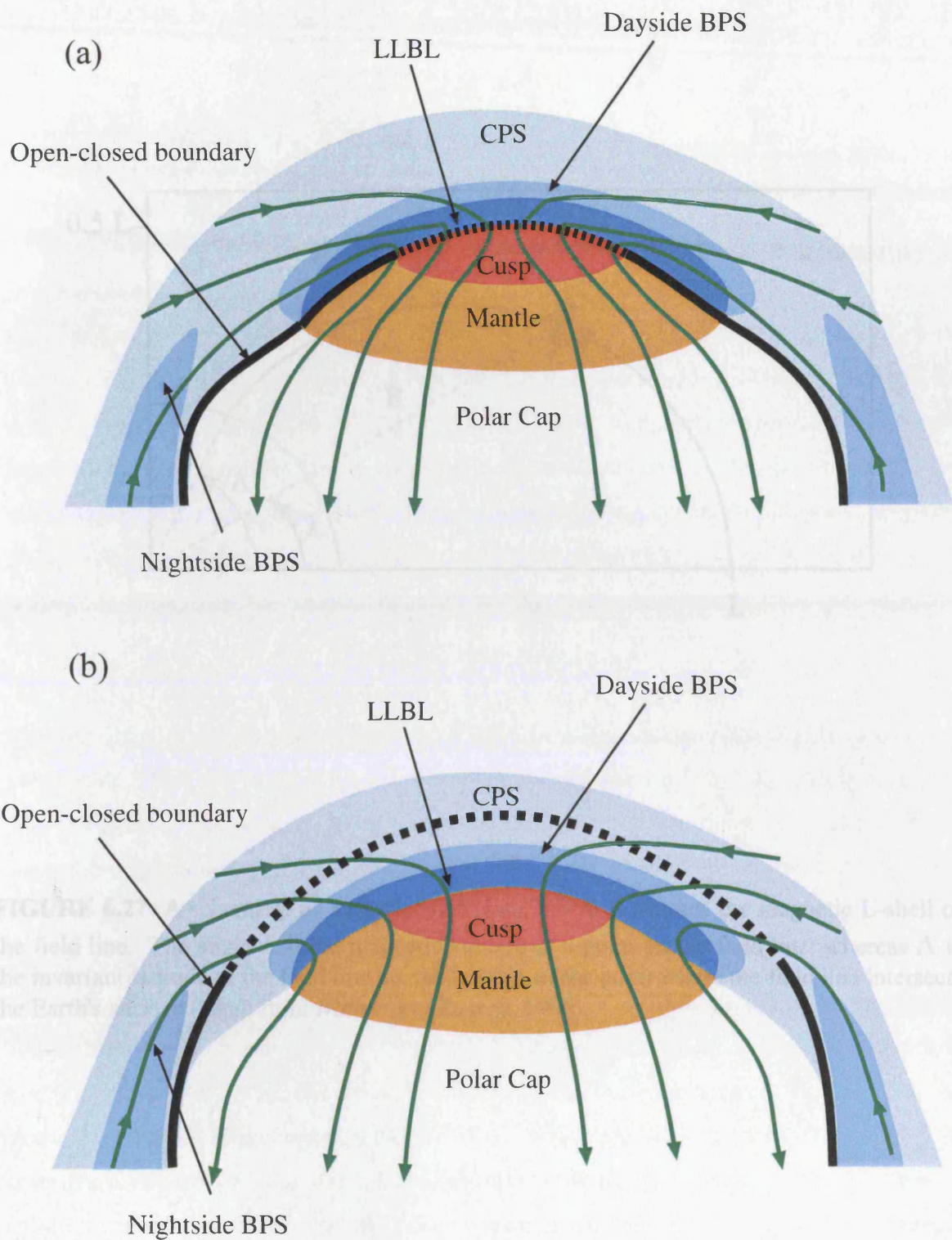


FIGURE 6.26: Two possible scenarios for possible relationships of the regions of dayside precipitation for (a) a closed low-latitude boundary layer (LLBL) and (b) an open LLBL. The OCFLB is shown as the thick black line when "adiarctic" and as a dashed black line at the merging gap. The convection pattern is shown as green arrowed lines (adapted from Lockwood, 1997).

invariant latitude location, depending on the distance R (effectively how far the satellite is above the field line), and L , the magnetic L-shell of the field line.

$$\Lambda = \cos^{-1}((L/R)^2)$$

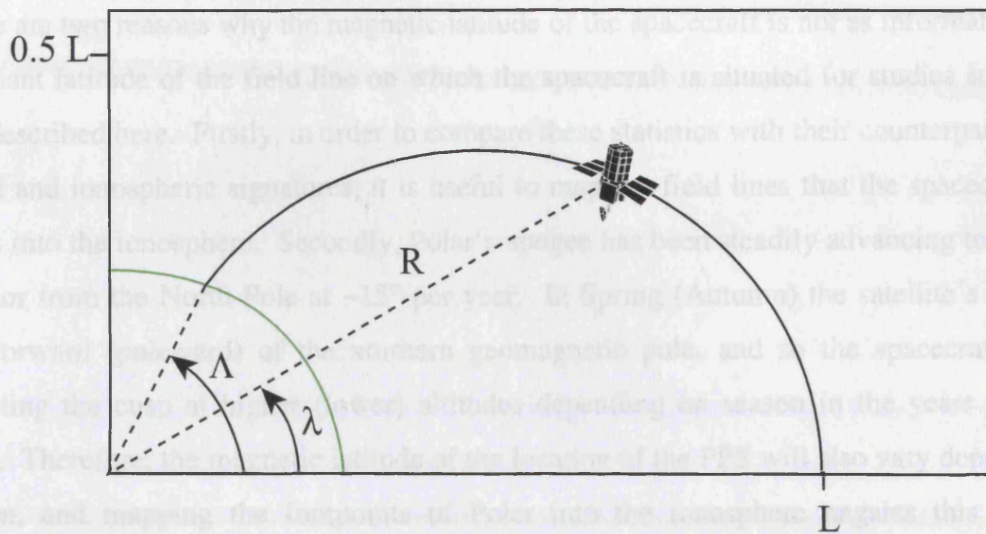


FIGURE 6.27: A schematic of a dipolar field line, where L denotes the magnetic L-shell of the field line. The angle λ is the magnetic latitude of a point on the field line, whereas Λ is the invariant latitude of the field line i.e. the latitude of the point where the field line intersects the Earth's surface (taken from Walker and Russell, 1995).

The ionospheric footprints of PPS during all IMF conditions are more closely grouped around local noon. Over 50% PPS occurrence is observed between -69 - 15 MLT and between 70 - 84° , confirming the wide spatial extent that these features are observed between in the ionosphere in addition to that in the magnetosphere. The main PPS occurrence is situated at

characteristics, in that the means (for both IMF directions) are observed at the same local time on. However, the main PPS latitude differs, around 75.2° for negative B_z , and 75.7° for positive B_z , which, although statistically small, difference does confirm the slight IMF-orientation dependence that the magnetospheric statistics demonstrated. It is useful to compare these results with previous observations of the ionospheric signature of transient magnetic flux transfer. Newell and Moyle [1988, 1992] showed that the "cusp proper" was situated within an hour of local noon between -77 - 78° , at higher latitudes than the mapping of the features observed in this study. Provan et al. [1998] demonstrated that pulsed ionospheric flows observed by the CUTLASS Finland radar occurred predominantly between 75 and 85° invariant latitude, with a mean at around 80 - 81° , again higher than this study. There are several potential sources for the discrepancies in average latitudes that must be

invariant latitude location, depending on the distance R (effectively how far the satellite is down the field line), and L, the magnetic L-shell of the field line.

$$\Lambda = \cos^{-1} (1/L)^{1/2}$$

There are two reasons why the magnetic latitude of the spacecraft is not as informative as the invariant latitude of the field line on which the spacecraft is situated for studies such as the one described here. Firstly, in order to compare these statistics with their counterpart ground-based and ionospheric signatures, it is useful to map the field lines that the spacecraft is on down into the ionosphere. Secondly, Polar's apogee has been steadily advancing towards the equator from the North Pole at $\sim 15^\circ$ per year. In Spring (Autumn) the satellite's apogee is equatorward (poleward) of the northern geomagnetic pole, and so the spacecraft will be sampling the cusp at higher (lower) altitudes depending on season in the years following 1996. Therefore, the magnetic latitude of the location of the PPS will also vary depending on season, and mapping the footpoints of Polar into the ionosphere negates this sampling variation.

The ionospheric footprints of PPS during all IMF conditions are more closely grouped around local noon. Over 50% PPS occurrence is observed between $\sim 09-15$ MLT and between $70-84^\circ$, confirming the wide spatial extent that these features are observed between in the ionosphere in addition to that in the magnetosphere. The mean PPS occurrence is situated at an invariant latitude of $\sim 75.4^\circ$ and 1050 local time.

The ionospheric footprints of the PPS events sorted in terms of IMF B_z reveal similar characteristics, in that the means of both IMF directions are observed at the same local time bin. However, the mean PPS latitude differs; around 75.2° for negative B_z and 75.7° for positive B_z which, although statistically small difference does confirm the slight IMF orientation dependence that the magnetospheric statistics demonstrated. It is useful to compare these results with previous observations of the ionospheric signature of transient magnetic flux transfer. *Newell and Meng* [1988; 1992] showed that the "cusp proper" was situated within an hour of local noon between $\sim 77-78^\circ$, at higher latitudes than the mapping of the features observed in this study. *Provan et al.* [1998] demonstrated that pulsed ionospheric flows observed by the CUTLASS Finland radar occurred predominantly between 75 and 85° invariant latitude, with a mean at around $80-81^\circ$, again higher than this study. There are several potential sources for the discrepancies in average latitudes that must be

discussed. One, that the Tsyganenko 89c model could be inaccurate, in particular in the vicinity of the cusp (*Fenrich et al.*, 2000). A more important consideration is that the field line tracing techniques do not include the anti-sunward motion of the flux tubes under magnetosheath flow. Pulsed particle signatures observed by Polar are observed at altitudes of up to 6 R_E . Employing the approximation, that the velocity of a proton, v_p (in kms^{-1}) is linked to the energy of the proton, E_p in keV, via

$$v_p \text{ (km/s)} \approx 440\sqrt{E_p \text{ (keV)}}$$

The time taken for a 10 keV proton, with a velocity ~ 1400 km/s to travel down the field line into the ionosphere would be ~ 30 seconds. During this time, the flux tube will be dragged anti-sunward at velocities of a few hundred metres per second, and will therefore travel \sim tens of kilometres maximum in the time taken for the incident protons to reach the ionosphere. A 1 keV proton will take ~ 90 seconds, and so the flux tube will travel a maximum of ~ 100 km, effectively 1° of invariant latitude, whereas the 10 keV proton will travel a fraction of a degree of magnetic latitude. The discrepancies in the results between data sets, therefore, cannot be attributed to merely the inclusion of time-of-flight characteristics of the ions and magnetosheath flow. Thirdly, the three data sets were taken over a different time interval. *Newell and Meng* [1992] took their low-altitude data set from December 1983-September 1990, a period that included solar minimum, and extended towards solar maximum. *Provan et al.* [1999a, b] presented data from March 1995-February 1997, spanning solar minimum, and this study presents data from May 1996-November 1999, extending towards solar maximum again. Studies have shown that during periods of increased geomagnetic activity, K_p , the auroral oval increases in width and extends equatorwards (*Feldstein and Starkov*, 1967). Of course, Polar and the DMSP satellites are measuring the in-situ particles at different parts and altitudes of the magnetosphere-ionosphere system, whereas the CUTLASS system measures the ionospheric flow *caused* by flux transfer, and by definition has to lie poleward of the OCFLB in the ionosphere. Furthermore, HF propagation, and therefore CUTLASS, is predisposed to lower values of K_p as during high K_p , increased absorption of the HF signal occurs. Taking into account the inaccuracies in the Tsyganenko model, ion time-of-flight effects and disparities in the phase of solar cycle and data sets, it is perhaps less than remarkable that the results of this statistical study lie on the low-latitude boundary of those performed closer to the Earth.

The ionospheric footprints of PPS under varying IMF B_y serve to highlight the differences outlined for the magnetospheric observations. High (> 50%) PPS percentages under negative B_y conditions occur sporadically throughout all sampled local times and between 72 and 80°, whereas positive B_y observations are more ordered, clustered within 2 hours of ~11 MLT over approximately the same latitudes. The mean latitudes and local times are approximately equal, the mean of negative B_y occurrence at 1045 MLT and 75.1° ILAT and that of the positive distribution at 1100 MLT and 75.7°.

The ionospheric footprint of PPS under gross-scale solar wind dynamic pressure variations also confirms that demonstrated by their magnetospheric counterparts, that increased P_{sw} increases the chances of Polar observing PPS in any given orbit, and at a wider range of local times. This can be thought of as merely sampling different altitudes of the magnetospheric cusp depending on the level of compression of the magnetosphere, as illustrated in Figure 6.25.

6.6 Summary

Chapter 6 documents a statistical study of the location and characteristics of the pulsed particle signatures observed by Polar in terms of magnetic local time and magnetic and invariant latitude. The statistics demonstrate that whatever the upstream interplanetary conditions, PPS can be observed over a wide range of latitudes and local times throughout the dayside magnetosphere. The statistics also demonstrate an IMF B_z dependence, in terms of increased occurrences and slightly lower average latitudes for southward IMF. The average latitude of PPS lies at the equatorward edge of previously reported statistical studies of signatures of transient reconnection (*Newell and Meng, 1992; Provan et al., 1999*). However, this may be resultant from a combination of three sources of discrepancy; ionospheric mapping errors, a time-of-flight effect, and the increased geomagnetic activity experienced in this study compared to those previous. No definitive conclusions can be drawn as to the exact driving mechanism of pulsed particle signatures from these statistics, though this chapter provides strong evidence that these signatures are the plasma signatures of ephemeral reconnection processes, largely occurring at the low-latitude magnetopause. Very little dependence on IMF B_y was established, though this again could be a sampling discrepancy due to the satellite's position relative to the noon-midnight meridian, or an extended active reconnection X-line expanding around the flanks of the magnetopause (*Milan et al., 2000*), as

discussed in Section 6.5. Solar wind dynamic pressure also participates in the location and characteristics of pulsed particle signatures. Increased solar wind pressure compresses the Earth's magnetosphere and hence an extended cusp region is observed. An increased number of PPS and occurrence percentages transpire as P_{sw} increases, perhaps also a consequence of the pseudo-increase in the sampled volume of the cusp region.

CHAPTER 7

Summary and Conclusions

7.1 Introduction

In this thesis, the effects of solar-terrestrial coupling have been explored in depth, with particular reference to the solar wind entry into the high-latitude magnetosphere-ionosphere system through the northern mid-altitude cusp. Since the discovery of the process of magnetic reconnection (*Dungey, 1961*), its role in magnetospheric and ionospheric convection has been studied and discussed at great length. When reconnection was revealed to be time-varying in nature (e.g. *Russell and Elphic, 1979*) this led to a wide debate on the spatial and temporal extent of these reconnected flux tubes, which has, as yet, not been fully resolved.

Many different signatures of this transient magnetic flux transfer have been reported over the last 25 years, though the evolution of these flux tubes through the mid-altitude magnetosphere has not been fully investigated. Satellite measurements have been routinely made of ephemeral reconnection processes in the dayside magnetosphere, chiefly at the low-latitude magnetopause (e.g. *Russell and Elphic, 1978, 1979; Berchem and Russell, 1984; Rijnbeek et al., 1984*). However, little observational evidence has been collected on the spatial extent and the temporal variability of these reconnection pulses, largely due to the single point nature of the spacecraft observations. The Polar spacecraft offers a different and unique perspective in this debate, in that its orbital characteristics effectively allow the routine study of the northern polar cusp whilst remaining quasi-stationary throughout this region. This means that reconnected flux tubes will be dragged across Polar, and so information on the extent of these flux tubes, and the time-scales involved in this flux transfer can be gleaned.

This thesis provides an in-depth analysis of the time-scales and extent of pulsed particle signatures (PPS) in the mid-altitude cusp, identified as the plasma signatures of transient magnetic reconnection. These PPS occur on two discrete time-scales; one of 2-6 minute

duration and one of the order of tens of minutes. Such observations have not been previously reported. A multi-instrument case study is also presented that associates signatures of reconnection processes at three different altitudes; at mid- and low-altitudes and in the ionosphere.

Furthermore, the location and occurrence statistics of PPS were investigated in terms of magnetic local time and (magnetic and invariant) latitudes and found to occur over a wide range of latitudes and local times. Their occurrence and behaviour were investigated with respect to the upstream interplanetary conditions, specifically B_y , B_z and solar wind dynamic pressure. Strong evidence is presented that these PPS features are dependent on IMF B_z and P_{sw} though do not alter significantly with IMF B_y . A summary detailing the main results in this thesis is presented in the following section.

7.2 Summary of results

7.2.1 29th October 1996

A multi-instrument case study is presented of the 29th October 1996 cusp pass by the Polar spacecraft. The spacecraft passes over the polar cap, through the mid-altitude cusp, and exits onto closed field lines. Within the cusp region, pulsed particle signatures are observed. The modulation of the particle count rates contained two predominant periodicities, one of 12 to 20 minutes duration, the other significantly shorter at 2-4 minutes. In many ways, such modulation of the particle count rates is consistent with transient and intermittent dayside reconnection (*Lockwood et al.*, 1998), or flux transfer events (*Lockwood and Wild*, 1993, and *Kuo et al.*, 1995). The simultaneous observation of two different frequency components has not been previously reported. *Lockwood et al.* [1998] observed a similar shorter period oscillation, but without the longer large-scale periodicity. Each pulse, and pulse-within-a-pulse is associated with a drop and oscillation in local magnetic field, which *Zhou and Russell* [1997] discussed in terms of field-aligned currents. The pulsed particle signatures (PPS) events also occur during both southward and northward IMF, but differ slightly in nature during the different B_z conditions. After the northward turning of the IMF, Polar still observes the pulsed particle events, but sheath-like particles and higher-energy particles characteristic of closed field lines co-exist. Particles of solar wind origin and higher energy magnetospheric particles can co-exist on the most newly reconnected flux tubes until the

higher energy particles escape into the ionosphere or solar wind. However, this can only be the case if low-latitude reconnection is occurring, which it does not appear to in this case. It is not therefore evident as to how the mix of sheath-like and closed field line origin plasma can exist on the same field lines.

Two further examples are presented at similar latitudes and local times during the same month of interest to confirm the conclusions drawn from the detailed case study, and are similar in nature to that first presented. However, there seems to be an IMF B_y dependence on the length of time that the spacecraft samples the cusp region, possibly as a result of an extended active X-line (*Milan et al.*, 2000).

7.2.2 24th April 1999

Chapter 5 presented a multi-instrument multi-altitude case study of the northern polar cusp region. In this case study, pulsed particle signatures (PPS) were observed by Polar, situated within the mid-altitude cusp, identified in all probability as the signature of pulsed magnetopause reconnection.

This chapter presents a case study of pulsed particle signatures (PPS) in the mid-altitude cusp, based upon the criteria outlined in Chapter 4, together with near-conjugate observations of the low-altitude and ionospheric cusps. A southward turning of the IMF and the erosion of magnetic flux moves the cusp equatorward. Several minutes after this IMF turning, pulsed particle signatures are observed in the mid-altitude cusp, and enhanced plasma convection and PIFs were excited in the ionosphere and observed by the CUTLASS Finland HF radar. The DMSP F13 spacecraft cuts through the flux tube that Polar is situated upon and detects a cusp ion step immediately prior to this conjugate position of closest approach whilst Polar is observing PPS. The ionospheric footprints of Polar and DMSP are situated a number of magnetic degrees equatorward and slightly eastward of the pulsed ionospheric transients, though all three features are signatures of transient and patchy reconnection. Although in this case study, no 1:1 relationship between these three signatures exist, the facts still remain that the two spacecraft observed dispersed ion signatures, indicative of ephemeral reconnection, close to the ionospheric footprint of a third signature of transient flux transfer, that of pulsed ionospheric flows.

Chapter 4 presented the first observations of pulsed particle signatures (PPS) of two discrete frequencies associated with ephemeral reconnection. This chapter has built upon these observations in that these PPS have now been linked to the low-altitude signature of transient reconnection observed by DMSP, and the poleward moving transients observed in the ionosphere by the CUTLASS radar system. It is hoped that future studies would envisage the spacecraft footprints closer to the poleward edge of the backscatter observed by CUTLASS, and that some relationship, 1:1 or otherwise, may arise between these three signatures at different altitudes.

7.2.3 PPS statistical study

Chapter 6 presents a statistical study of the location and characteristics of pulsed particle signatures within the mid-altitude cusp observed by Polar in terms of magnetic local time and (magnetic and invariant) latitudes. Pulsed particle signatures were observed over a wide range of latitudes and local times in the magnetosphere under all IMF conditions. However, several aspects of PPS location and occurrence statistics were shown to be dependent upon upstream interplanetary conditions. PPS were found to favour southward IMF conditions in terms of increased occurrence statistics, and also occurred at lower latitudes in comparison to their northward IMF counterparts. The average latitude of PPS mapped into the ionosphere is located at the equatorward edge of previously reported phenomena associated with ephemeral reconnection (*Newell and Meng, 1992; Provan et al., 1999*). However, this could be a consequence of one or more of three factors; errors in the mapping of Polar into the ionosphere using the Tsyganenko 89c model, time-of-flight effects, and increased geomagnetic activity in comparison to previous studies. Although a definitive conclusion cannot be drawn, Chapter 6 provides strong evidence that PPS are the energy-dispersed plasma signatures of transient reconnection, chiefly occurring at the low-latitude magnetopause.

Despite this indication of a B_z dependence, little B_y dependence was established, though this again could be a systematic sampling discrepancy due to the relative position of Polar to the noon-midnight meridian. This is an integral element of the entire statistical study, in that the spacecraft's orbits were constrained to within a few hours of noon, ergo any shift in the reconnection site due to a change in B_y may not affect the position of the cusp seen by Polar. Alternatively, an extended active X-line over many hours of local time (*Milan et al., 2000*)

may not necessarily shift far enough in the Y-direction under varying IMF B_y polarities for Polar not to observe pulsed particle signatures.

A dependence on variations in solar wind dynamic pressure was also noted from this study. It is perhaps not surprising that the statistics reveal that increased PPS observations and normalized occurrences occur for increased solar wind dynamic pressures. Under increased P_{sw} , the Earth's magnetosphere compresses, and thus Polar's orbit will effectively be sampling a different region of the cusp depending on the gross-scale solar wind dynamic pressure conditions.

However, it was also noted in this Chapter that a true IMF dependence may never arise from this statistical study, due to the initial criteria that this study was based around. The fundamental question that this study answered was "when the PPS occur, where do they occur and under what interplanetary conditions?" An inherent problem concerning this question is that the orbits that did not exhibit PPS have been discarded, and rightly so, to satisfy the outlined criteria. However, with the removal of these orbits from the database may have disappeared the true IMF dependence. This initial criteria may be revised in future studies to include those cusp passes that did not exhibit PPS more fully, and start with a question along the lines of "under which IMF conditions do the PPS occur, and if they *do* occur, *where* do they occur?" It is hoped that this revision of initial criteria will disclose a clearer IMF B_z dependence.

7.3 Suggestions for Future Work

There now exists a more rigorous means of examining the process of solar wind entry into the near-Earth environment; namely the CLUSTER-II mission. Inserted into their final orbits on the 14th August 2000, the 4 spacecraft will provide the direct means to accurately investigate three-dimensional and time-varying phenomena. Through their orbital characteristics (the four spacecraft will follow each other around their orbit for a significant portion of their lifetime) their configuration will also make it possible to distinguish between spatial and temporal variations in the cusp. Unfortunately, the author was one of those that would have benefited from the successful launch of the first CLUSTER mission several years ago. Early in March 2001, the apogee of the four CLUSTER spacecraft will pass through the high-altitude cusp whilst Polar is situated within the mid-altitude cusp. With the excellent suite of

low-altitude DMSP satellite and ground-based instruments this would provide an exceptional case study to investigate the spatial and time-varying nature of the cusp at all altitudes within the near-Earth environment.

The multi-instrument case study of the 24th April 1999 can be expanded to the extensive ground- and satellite-based datasets. The SuperDARN HF network covers almost the whole of the high-latitude ionosphere in the northern hemisphere, and a vast portion of the southern hemisphere ionosphere. Polar's ionospheric footprint maps into the ionospheric cusp and the CUTLASS fields-of-view in the Scandinavian ionosphere approximately every third orbit. However, studies do not have to be concentrated in this sector. Recent studies (*McWilliams et al.*, 2000) have shown that normal resolution (~2 minute scans) of the CUTLASS radars also reveal the characteristic quasi-periodic l-o-s velocity perturbations associated with transient magnetic flux transfer. Further studies could be performed over the range of SuperDARN radars in an attempt to uncover a conjunction between the ionospheric footprint of the spacecraft and the ionospheric flow signatures of FTEs within ~2 hours of MLT. Furthermore, Polar is quasi-stationary within the mid-altitude cusp for a number of hours every orbit. The DMSP satellites orbits' are designed pass through this region every day, and so a database of conjunctions could be compiled in an attempt to find clear 1:1 relationships between the PPS observed by Polar and "cusp ion steps" observed by DMSP. This modelling of PPS and cusp ion steps can be performed using the simple reconnection model proposed by *Lockwood and Davis* [1996].

From the statistical study of PPS signatures observed in Chapter 6 by Polar, there are many variations and classification studies that can be performed. Pulsed particle signatures in this thesis have been quantified and classified in terms of location and characteristics as functions of IMF B_z and B_y orientation, and the dynamic pressure variation. These studies could be furthered in terms of several parameters. *Sandholt et al.*[1999] showed that both high- and low-latitude reconnection could ensue for IMF clock angles of over 45°. This study concentrated merely on the quadrant of IMF clock angle, but an extension to this study would be to investigate PPS behaviour in terms of IMF clock angle to verify (or otherwise) this relationship. The statistical study also ended in November 1999. At this date, almost a year of additional data is available to incorporate into this study. Although this additional data may not greatly affect the distributions under IMF B_y or B_z or P_{sw} , it would vastly improve the statistics of the PPS events when the data was split into four when categorised by IMF clock angle quadrant. An additional addendum to this study is that pulsed particle signatures

have now been categorised in terms of occurrence and location statistics. Stringent criteria were formed to define the gross-scale characteristics of pulsed particle signatures which can now be utilised in the investigation of Polar cusp passes at other local times. It is envisioned that future work would entail the inclusion of the residual six months of orbital information to obtain a complete magnetic local time and (magnetic or invariant) latitudinal dependence.

It is noted that the ionospheric mapping of the statistical study did not provide as great an insight as would be hoped. The PPS observed in the mid-altitude cusp lie at the equatorward edge of the average latitudes of signatures of transient reconnection in previous studies (*Newell and Meng, 1991; Provan et al., 1999*). However, these results were taken during differing epochs, spanning over more than an entire solar cycle. To be directly equivalent, low-altitude or ground-based measurements must be taken during the same months and years, or at least a conversion factor for average K_p values over which the statistics were taken obtained. Notwithstanding this disparity, the ionospheric measurements may still not be co-located with spacecraft measurements of transitory reconnection processes simply because CUTLASS measures the flow *excited* from the reconnection, which is by definition poleward of the open closed field line boundary.

References

- Acuña, M. H., K. W. Ogilvie, D. N. Baker, S. A. Curtis, D. H. Fairfield and W. H. Mish,** The Global Geospace Science Program and Its Investigations, *Space Sci. Rev.*, **71**, 5-21, 1995.
- Axford, W. I., and C. O. Hines,** A Unifying theory of high-latitude Geophysical phenomena and Geomagnetic Storms, *Can. J. Phys.*, **39**, 1433-1464, 1961.
- Bartels, J., N. H. Heck, and H. F. Johnston,** The three-hour-range index measuring geomagnetic activity, *J. Geophys. Res.*, **44**, 411-, 1939.
- Berchem, J., and C. T. Russell,** Flux transfer events on the magnetopause: Spatial distribution and controlling factors, *J. Geophys. Res.*, **89**, 6689, 1984.
- Blake, J. B., J. F. Fennell, L. M. Friesen, B. M. Johnson, W. A. Kolasinski, D. J. Mabry, J. V. Osborn, S. H. Penzin, E. R. Schnauss, H. E. Spence, D. N. Baker, R. Belian, T. A. Fritz, W. Ford, B. Laubscher, R. Stiglich, R. A. Baraze, M. F. Hilsenrath, W. L. Imhof, J. R. Kilner, J. Mobilia, D. H. Voss, A. Korth, M. Gull, M. Grande and D. Hall,** Comprehensive Energetic Particle and Pitch-Angle Distribution experiment on Polar, *Space Sci. Rev.* **71**, 531, 1995.
- Chapman, S. and V. C. A. Ferraro,** A new theory of magnetic storms, *Nature*, 126-129, 1930.
- Chapman. S. and V. C. A Ferraro,** A new theory of magnetic storms, *Nature*, **126**, 129, 1931
- Chapman. S. and V. C. A Ferraro,** A new theory of magnetic storms. *Terr. Magn. Atmosph. Elec.*, **36**, 171-186, 1932.
- Chen, S. -H., S. A. Boardsen, S. F. Fung, J. L. Green, R. L. Kessel, L. C. Tan, T. E. Eastman, and J. D. Craven,** Exterior and interior polar cusps: Observations from Hawkeye, *J. Geophys. Res.*, **102**, 11355-11347, 1997.
- Cowley, S. W. H.,** The causes of convection in the Earth's magnetosphere: A review of developments during IMS, *Rev. of Geophysics*, **20**, 531-565, 1982.
- Cowley, S. W. H.,** Solar Wind control of magnetospheric convection, in Achievements of the International Magnetospheric Study, IMS, *Eur. Space Agency Spec.Publ., ESA SP-217*, 483-494, 1984.

- Cowley, S. W. H., J. P. Morelli, and M. Lockwood**, Dependence of convective flows and particle precipitation in the high-latitude dayside ionosphere on the X and Y components in the interplanetary magnetic field, *J. Geophys. Res.*, **96**, 5557, 1991a.
- Cowley, S. W. H., M. P. Freeman, M. Lockwood, and M. F. Smith**, The ionospheric signature of flux transfer events, in *CLUSTER Dayside Polar Cusp Spec. Publ., ESA SP-330*, edited by C. I. Barron, 105-112, *Eur. Space. Agency Publ.*, Noordwijk, Netherlands, 1991b.
- Cowley, S. W. H., and M. Lockwood**, Incoherent Scatter Observations Related to Magnetospheric Dynamics,, *Adv. Space. Res.*, **20**, 873, 1997
- Crooker, N. U.**, Reverse convection, *J. Geophys. Res.*, **97**, 19,363-19,372, 1992.
- Davies, K.**, A nomenclature for oblique ionospheric soundings and ray tracing, *Radio Sci.*, **2**, 1395-1396, 1967.
- Dungey, J. W.**, Interplanetary field and the auroral zones, *Phys. Rev. Lett.*, **40**, 47-48, 1961.
- Elphic, R. C., and D. J. Southwood**, Simultaneous measurements of the magnetopause and flux transfer events at widely separated sites by AMPTE, UKS and ISEE 1 and 2, *J. Geophys. Res.*, **92**, 13,666-13,672, 1987.
- Elphic, R. C., M. Lockwood, S. W. H. Cowley, and P. E. Sandholt**, Signatures of flux transfer events at the dayside magnetopause and in the ionosphere: Combined ISEE, EISCAT and optical observations, *Geophys. Res. Lett.*, **17**, 2241-2244, 1990.
- Fairfield, D.**, Average and unusual locations of the Earth's magnetopause and bow shock, *J. Geophys. Res.*, **76**, 6700, 1971.
- Farquhar, R. W.**, The Control and Use of Libration Point Satellites, *NASA Technical Report TR-R346*, 1970.
- Farquhar, R. W.**, A New Trajectory Concept for Exploring the Earth's Geomagnetic Tail, *J. Guidance and Control*, 1991.
- Farrugia, C. J., R. C. Elphic, D. J. Southwood and S. W. H. Cowley**, Field and flow perturbations outside the reconnected field line region in flux transfer events: Theory, *Planet. Space Sci.*, **35**, 227-240, 1987.
- Fasel, G. J., L. C. Lee, and R. W. Smith**, A mechanism for the multiple brightening of dayside poleward moving forms, *Geophys. Res. Lett.*, **20**, 2247-2250, 1993.

- Feldstein, Y. I., and G. V. Starkov**, Dynamics of auroral belt and polar geomagnetic disturbances, *Planet. Space Sci.*, **15**, 209-230, 1967.
- Fenrich, F. R., J. G. Luhmann, J. A. Fedder, S. P. Slinker, and C. T. Russell**, A Global MHD and empirical magnetic field model investigation of the magnetospheric cusp, *submitted to J. Geophys. Rev.*, 2000.
- Friis-Christensen, E., and J. Wilhelm**, Polar cap currents for different directions of the interplanetary magnetic field in the y-z plane, *J. Geophys. Rev.*, **80**, 1248, 1975.
- Gibson, E. G.**, The Quiet Sun, *NASA SP-303*, 1973.
- Glaßmeier, K.-H.**, Travelling magnetospheric convection twin-vortices: Observations and theory, *Ann. Geophys.*, **10**, 547-565, 1992.
- Gloeckler, G. J. Cain, F. M. Ipavich, E. O. Tums, P. Bedini, L. A. Fisk, T. H. Zurbuchen, P. Bochsler, J. Fischer, R. F. Wimmer-Schweingruber, J. Geiss, R. Kallenbach**, Investigation of the Composition of Solar and Interstellar Matter Using Solar Wind and Pickup Ion Measurements with SWICS and SWIMS on the ACE Spacecraft, *Space Sci. Rev.*, **86**, 497-539, 1998.
- Goertz, C. K., E. Nielsen, A. Korth, K.-H. Glaßmeier, C. Haldoupis, P. Hoeg, and D. Hayward**, Observations of a possible signature of flux transfer events, *J. Geophys. Rev.*, **90**, 4069-4078, 1985.
- Gosling, J.T, J. R Asbridge, S.J.Bame and W.C. Feldman**, Solar wind speed variations, 1962-1974, *J. Geophys. Rev.*, **81**, 5061, 1976.
- Gosling, J.T, J. R Asbridge, S.J.Bame and W.C. Feldman**, Solar wind stream interfaces, *J. Geophys. Rev.*, **83**, 1401, 1978.
- Gosling, J. T., M. F. Thomsen, S. J. Bame, R. C. Elphic, and C. T. Russell**, Plasma flow reversals at the dayside magnetopause and the origin of asymmetric polar cap convection, *J. Geophys. Rev.*, **95**, 8073-8084, 1990.
- Grande, M., J. Fennell., S. Livi., B. Kellett., C. Perry., P. Anderson., J. Roeder., H. Spence., T. Fritz., and B. Wilken.**, First Polar and 1995-034 observations of the midaltitude cusp during a persistent northward IMF condition, *Geophys. Res. Lett.*, **24**, 1475-1478, 1997.
- Greenwald, R. A., W. Weiss, E. Nielsen and N. R. Thomson**, STARE a new radar auroral backscatter experiment in northern Scandinavia, *Radio Sci.*, **13**, 1021-1039, 1978.

- Greenwald, R. A., K. B. Baker, J. R. Dudeney, M. Pinnock, T. B. Jones, E. C. Thomas, J.-P. Villain, J.-C. Cerisier, C. Senior, C. Hanuise, R. D. Hunsucker, G. Sofko, J. Koehler, E. Nielsen, R. Pellinen, A. D. M. Walker, N. Sato and H. Yamagishi,** Darn/Superdarn : A global view of the dynamics of high-latitude convection, *Space Science Reviews*, **71**, 761 - 796, 1995.
- Haerendel, G., G. Paschmann, N. Sckopke, H. Rosenbauer and P. C. Hedgecock,** The frontside boundary layer of the magnetopause and the problem of reconnection, *J. Geophys. Res.*, **83**, 3195, 1978.
- Hardy, D. A., L. K. Schmitt, M. S. Gussenhoven, F. J. Marshall, H. C. Yeh, T. L. Shumaker, A. Hube, and J. Pantazis,** Precipitating electron and ion sensors (SSJ/4) for the block 5D/flights 6-10 DMSP satellites: Calibration and data presentation, Rep. AFGL-TR-84-0317, Air Force Geophys. Lab., Hanscom Air Force Base, Mass., 1984.
- Hughes, W. J.,** The Magnetopause, Magnetotail and Magnetic Reconnection, in *Introduction to Space Plasma Physics*, ed. M. G. Kivelson and C. T. Russell, 1995.
- Kawano, H., and C. T. Russell,** Survey of flux transfer events observed with the ISEE 1 spacecraft: Dependence on the interplanetary magnetic field, *J. Geophys. Rev.*, **102**, 11,307-11,313, 1997.
- Khan, H., and S.W.H. Cowley,** Observations of the response time of high-latitude ionospheric convection to variations in the interplanetary magnetic field using EISCAT and IMP-8 data, *Ann. Geophys.*, **17**, 1306-1335, 1999.
- Kivelson, M. G., and D. J. Southwood,** Ionospheric travelling vortex generation by solar wind buffeting of the magnetosphere, *J. Geophys. Rev.*, **96**, 1661-1667, 1991.
- Klumpar, D. M., S. A. Fuselier, E. G. Shelley,** Ion composition measurements within magnetospheric flux transfer events, *Geophys. Res. Lett.*, **17**, 2305-2308, 1990.
- Kuo, H., C. T. Russell, and G. Le,** Statistical studies of flux transfer events, *J. Geophys. Rev.*, **100**, 3513-3519, 1995.
- Le, G., J. T. Gosling, C. T. Russell, R. C. Elphic, M. F. Thomsen, J. A. Newbury,** The magnetic and plasma structure of flux transfer events, *J. Geophys. Rev.*, **104**, 233-245, 1999.
- Lee, L. C., and Z. F. Fu,** A theory of magnetic flux transfer at the Earth's magnetopause, *Geophys. Res. Lett.*, **12**, 105-108, 1985.

- Lee, L. C.**, Magnetic flux transfer at the Earth's magnetopause, in *Solar Wind-Magnetosphere Coupling*, edited by Y. Kamide and J. A. Slavin, 297-314, Terra. Sci., Tokyo, 1986.
- Lepping, R. P., M. H. Acuña, L. F. Burlaga, W. M. Farrell, J. A. Slavin, K. H. Schatten, F. Mariani, N. F. Ness, F. M. Neubauer, Y. C. Whang, J. B. Byrnes, R. S. Kenyon, P. V. Panetta, J. Scheifele, and E. M. Worley**, The WIND Magnetic Field Investigation, *Space Sci. Rev.*, **71**, 207-229, 1995.
- Lester, M., O. de la Beaujardiere, J. C. Foster, M. P. Freeman, H. Luhr, J. M. Ruohonemi, and W. Swider**, The response of the large-scale Ionospheric convection pattern to changes in the IMF and substorms – Results from the SUNDIAL 1987 Campaign, *Ann. Geophysicae*, **11**, 556-571, 1993.
- Lester, M., and S. W. H. Cowley**, The Solar-Terrestrial Interaction and its importance for space weather, *Adv. Space. Res.*, **26**, 1, 79-88, 2000
- Lester, M.**, Magnetosphere of Earth: Substorms, In Encyclopedia of Astronomy and Astrophysics, to be published by IOP Publishing and Macmillan Publishers Ltd, in press, 2000.
- Levy, R. H., E. Petscheck, and G. L. Siscoe**, Aerodynamic aspects of the magnetospheric flow, *AIAA J.*, **2**, 2065-2076, 1964.
- Lockwood, M., S. W. H. Cowley, P. E. Sandholt, and R. P. Lepping**, The ionospheric signatures of flux transfer events and solar wind dynamic pressure changes, *J. Geophys. Rev*, **95**, 17,113-17,135, 1990.
- Lockwood, M.**, Modelling the high-latitude ionosphere for time-varying plasma convection, *Proc. I.E.E. (H)*, **140**, 2, 91-100, 1993.
- Lockwood M, and M. N. Wild.**, On the Quasi-Periodic Nature of Magnetopause Flux Transfer Events, *J. Geophys. Res.*, **98**, 5935-5940, 1993.
- Lockwood, M.**, Ionospheric signatures of pulsed magnetopause reconnection, in *Physical Signatures of Magnetopause Boundary Layer Processes*, NATO ASI Ser. C, vol. 425, edited by J. A. Holtet and A. Egeland, 229-243, Kluwer, Dordrecht, 1994.
- Lockwood, M.**, The location and characteristics of the reconnection X line deduced from low-altitude satellite and ground-based observations, 1, Theory, *J. Geophys. Rev*, **100**, 21,791-21,802, 1995.

- Lockwood, M., and C. J. Davis**, An analysis of the accuracy of magnetopause reconnection rate variations deduced from cusp ion dispersion characteristics, *Ann. Geophys.*, **14**, 149-161, 1996.
- Lockwood, M.**, Relationship of dayside auroral precipitations to the open-closed separatrix and the pattern of convective flow, *J. Geophys. Rev.*, **102**, 17,475-17,487, 1997.
- Lockwood, M.**, Identifying the open-closed field line boundary, in *Polar Cap Boundary Phenomena*, edited by J. Moen, A. Egeland, and M. Lockwood, 73-90, Kluwer Academic Publishers, Netherlands, 1998.
- Lockwood, M., and M. Hapgood**, On the cause of a magnetospheric flux transfer event, *J. Geophys. Res.*, **103**, 26453-26478, 1998.
- Lockwood, M., C. J. Davis, T. G. Onsager, and J. D. Scudder**, Modelling signatures of pulsed magnetopause reconnection in cusp ion dispersion signatures seen at middle altitudes, *Geophys. Res. Lett.*, **25**, 5, 591-594, 1998.
- Ma, Z. W., A. Otto, and L. C. Lee**, Core magnetic field enhancement in single X line multiple X line and patchy reconnection, *J. Geophys. Rev.*, **99**, 6125-6136, 1994.
- Mansurov, S. V.**, New evidence of a relationship between magnetic fields in space and on the Earth, *Geomag. Aeron. USSR*, **9**, 622-623, 1969.
- McWilliams, K. A., T. K. Yeoman, and G. Provan**, A statistical survey of dayside pulsed ionospheric flows as seen by the CUTLASS Finland HF radar, *Ann. Geophys.*, **18**, 445-453, 2000.
- Milan, S. E., T. K. Yeoman, M. Lester, E. C. Thomas and T. B. Jones**, Initial backscatter occurrence statistics from the CUTLASS HF radars, *Ann. Geophysicae*, **15**, 703-718, 1997
- Milan, S. E., T. K. Yeoman, M. Lester, J. Moen, and P. E. Sandholt**, Post-noon two-minute period pulsating aurora and their relationship to the dayside convection pattern, *Ann. Geophys.*, **17**, 877-891, 1999.
- Milan, S. E., M. Lester, S. W. H. Cowley, and M. Brittnacher**, Convection and auroral response to a southward turning of the IMF: Polar UVI, CUTLASS, and IMAGE signatures of transient magnetic flux transfer at the magnetopause, *J. Geophys. Rev.*, **105**, 15,741-15,756,2000.

- Neudegg, D. A., T. K. Yeoman, S. W. H. Cowley, G. Provan, G. Haerendel, W. Baumjohann, U. Auster, K.-H. Fornacon, E. Georgescu, and C. J. Owen**, A flux transfer event observed at the magnetopause by the Equator-S spacecraft and in the ionosphere by the CUTLASS HF radar, *Ann. Geophys.*, **17**, 707, 1999.
- Neudegg, D. A., S. W. H. Cowley, S. E. Milan, T. K. Yeoman, M. Lester, G. Provan, G. Haerendel, W. Baumjohann, B. Nikotowski, J. Büchner, U. Auster, K.-H. Fornacon, and E. Georgescu**, A survey of magnetopause FTEs and associated flow bursts in the polar ionosphere, *Ann. Geophys.*, **18**, 416-435, 2000.
- Newell, P. T., and C.-I. Meng**, The cusp and the cleft/boundary layer: Low altitude identification and statistical local time variation, *J. Geophys. Res.*, **93**, 14,549-14,566, 1988.
- Newell, P. T., and C.-I. Meng**, Ion acceleration at the equatorward edge of the cusp: Low altitude observations of patchy merging, *Geophys. Res. Lett.*, **18**, 1829-1832, 1991.
- Newell, P. T., and C.-I. Meng**, Mapping the Dayside Ionosphere to the Magnetosphere according to Particle Precipitation Characteristics, *Geophys. Res. Lett.*, **19**, 609-612, 1992.
- Newell, P. T., and D. G. Sibeck**, Upper limits on the contribution of flux transfer events to ionospheric convection, *Geophys. Res. Lett.*, **20**, 2829-2832, 1993.
- Ogilvie, K. W., D. J. Chornay, R. J. Fritzenreiter, F. Hunsaker, J. Keller, J. Lobell, G. Miller, J. D. Scudder, E. C. Sittler Jr., R. B. Torbert, D. Bodet, G. Needell, A. J. Lazarus, J. T. Steinberg, J. H. Tappan, A. Mavretic and E. Gergin**, SWE, A Comprehensive Plasma Instrument for the Wind Spacecraft, *Space Sci. Rev.*, **17**, 55-77, 1995.
- Parker, E. N.**, Dynamics of Interplanetary Gas and magnetic fields, *Astrophys. J.*, **128**, 664-76, 1958.
- Parker, E. N.**, *Interplanetary Dynamical Processes*, Wiley-Interscience, New York, 1963.
- Paschmann, G., G. Haerendel, I. Papamastorakis, N. Sckopke, S. J. Bame, J. T. Gosling, and C. T. Russell**, Plasma and magnetic field characteristics of magnetic flux transfer events, *J. Geophys. Res.*, **87**, 2159, 1982.
- Peredo, M., J. A. Slavin, E. Mazur, and S. A. Curtis**, 3-dimensional position and shape of the bow shock and their variation with Alfvénic Sonic and Magnetosonic Mach numbers and Interplanetary Field orientation, *J. Geophys. Res.*, **100**, 7907-7916, 1995.

- Petschek, H. E.**, Magnetic Field Annihilation, in *NASA Symposium on Physics of Solar Flares*, NASA SP 50, 425-429, 1964.
- Pinnock, M., A. S. Rodger, J. R. Dudeney, K. B. Baker, R. A. Greenwald, and M. Greenspan**, Observations of an enhanced convection channel in the cusp ionosphere, *J. Geophys. Res.*, **98**, 3767-3776, 1993.
- Pinnock, M., A. S. Rodger, J. R. Dudeney, F. Rich, and K. B. Baker**, High spatial and temporal resolution observations of the ionospheric cusp, *Ann. Geophys.*, **13**, 919-925, 1995.
- Priest, E. R.**, The Sun and its Magnetohydrodynamics, in *Introduction to Space Plasma Physics*, ed. M. G. Kivelson and C. T. Russell, 1995.
- Provan, G., T. K. Yeoman, and S. E. Milan.**, CUTLASS Finland radar observations of the ionospheric signatures of flux transfer events and the resulting plasma flows, *Ann. Geophys.*, **16**, 1411-1422, 1998.
- Provan, G., and T. K. Yeoman**, Statistical observations of MLT, latitude and size of pulsed ionospheric flows with the CUTLASS Finland radar, *Ann. Geophys.*, **17**, 855-867, 1999a.
- Provan, G., T. K. Yeoman and S. W. H. Cowley**, The influence of the IMF B_y component on the location of pulsed flows in the dayside ionosphere observed by an HF radar, *Geophys. Res. Lett.*, **26**, 521-524, 1999b.
- Rae, I. J., M. Lester, S. E. Milan, T. A. Fritz, M. Grande, and J. D. Scudder**, Polar observations of the time-varying cusp, *J. Geophys. Res.*, accepted August, 2000.
- Reiff, P. H., and J. L. Burch**, IMF B_y -Dependent Plasma Flow and Birkeland Currents in the Dayside Magnetosphere 2. A Global Model for Northward and Southward IMF, *J. Geophys. Res.*, **90**, 1595, 1985.
- Reiff, P. H., and J. G. Luhmann**, Solar Wind control of the polar cap voltage, in *Solar Wind-Magnetosphere Coupling*, edited by Y. Kamide, and J. A. Slavin, 453-472, Terra Scientific, Tokyo, 1986.
- Rijnbeek, R. P., S. W. H. Cowley, D. J. Southwood, and C. T. Russell**, A survey of dayside flux transfer events observed by the ISEE-1 and -2 magnetometers, *J. Geophys. Res.*, **89**, 786-800, 1984.
- Rodger, A. S., and M. Pinnock**, The ionospheric response to flux transfer events: the first few minutes, *Ann. Geophys.*, **15**, 685-691, 1997

- Roelof, E. C., and D. G. Sibeck**, Magnetopause shape as a bivariate function of Interplanetary Magnetic Field $B(z)$ and Solar Wind Dynamic Pressure, *J. Geophys. Res.*, **98**, 21421-21450, 1993.
- Russell, C. T.**, The configuration of the magnetosphere, in *Critical Problems of Magnetospheric Physics*, Ed. E. R. Dyer, National Academy of Sciences, Washington D. C., 1972.
- Russell, C. T.**, The configuration of the magnetosphere, in *Critical Problems of Magnetospheric Physics*, edited by E. R. Dyer, p. 1, Nat. Acad. Sciences, Washington, 1972.
- Russell, C. T., and R. L. McPherron**, The magnetotail and substorms, *Space Sci. Rev.*, **15**, 205, 1973.
- Russell, C. T., and R. C. Elphic**, Initial ISEE magnetometer results: magnetopause observations, *Space Science Review*, **22**, 681, 1978.
- Russell, C. T., and R. C. Elphic**, ISEE observations of flux transfer events at the dayside magnetopause, *Geophys. Res. Lett.*, **6**, 33, 1979.
- Russell, C. T., R. C. Snare, J. D. Means, D. Pierce, D. Dearborn, M. Larson, G. Barr, G. Le**, The GGS/POLAR Magnetic-fields Investigation, *Space Sci. Rev.*, **71**, 563, 1995.
- Safrankova, J., Z. Nemecek, D. G. Sibeck, L. Prech, J. Merka, and O. Santolik**, Two point observation of high-latitude reconnection, *Geophys. Res. Lett.*, **25**, 4301-4304, 1998.
- Sandholt, P. E., C. S. Deehr, A. Egeland, B. Lybekk, R. Viereck, and G. J. Romick**, Signatures in the dayside aurora of plasma transfer from the magnetosheath, *J. Geophys. Res.*, **91**, 10,063, 1986.
- Sandholt, P. E., M. Lockwood, T. Oguti, S. W. H. Cowley, K. S. C. Freeman, B. Lybekk, A. Egeland, and D. M. Willis**, Midday auroral breakup events and related energy and momentum transfer from the magnetosheath, *J. Geophys. Res.*, **95**, 1039, 1990.
- Sandholt, P. E., J. Moen, A. Rudland, D. Opsvik, W. F. Denig, and T. Hansen**, Auroral event sequences at the dayside polar cap boundary for positive and negative interplanetary magnetic field B_y , *J. Geophys. Res.*, **98**, 7737, 1993.
- Sandholt P. E., C. J. Farrugia, J. Moen, S. W. H. Cowley, B. Lybekk**, Dynamics of the aurora and associated convection currents during a cusp bifurcation event, *Geophys. Res. Lett.*, **25**, 4313-4316, 1998a.

- Sandholt, P. E., C. J. Farrugia, and S. W. H. Cowley**, Pulsating cusp aurora for northward IMF, *J. Geophys. Rev.*, **103**, 26507, 1998b.
- Sandholt, P. E., C. J. Farrugia, J. Moen, and S. W. H. Cowley**, Dayside auroral configurations: responses to southward and northward rotations of the interplanetary magnetic field, *J. Geophys. Rev.*, **103**, 20,279,1998c.
- Sandholt, P. E., C. J. Farrugia, J. Moen, Ø. Noraberg, B. Lybekk, T. Sten, and T. Hansen**, A classification of dayside auroral forms and activities as a function of IMF orientation, *J. Geophys. Rev.*, **103**, 23,325, 1998d.
- Sandholt P. E., C. J. Farrugia, B. Lybekk**, The dynamic cusp aurora on 30 November 1997: response to southward turning of the IMF, *Ann. Geophys.*, **17**, 1155-1165, 1999.
- Sanny, J., C. Beck, D. G. Sibeck**, A statistical study of the magnetic signatures of FTEs near the dayside magnetopause, *J. Geophys. Rev.*, **103**, 4683-4692, 1998.
- Saunders, M. A.**, Recent ISEE observations of the magnetopause and low-latitude boundary layer: A review, *J. Geophys. Rev.*, **52**, 190-198, 1983.
- Saunders, M. A., C. T. Russell, and N. Sckopke**, Flux transfer events, scale size and interior structure, in *Magnetic Reconnection in Space and Laboratory Plasmas*, *Geophys. Monogr. Ser.*, vol. 30, edited by E. W. Hones Jr., 145-152, AGU, Washington, D. C., 1984.
- Scholer, M, D. Hovestadt, F. M. Ipavich, and G. Gloeckler**, Energetic protons, alpha particles and electrons in magnetic flux transfer events, *J. Geophys. Rev.*, **87**, 2169, 1982
- Scholer. M.**, Magnetic Flux Transfer at the Magnetopause based on single line X Bursty Reconnection, *Geophys. Res. Lett.*, **15**, 291-294, 1988a.
- Scholer, M.**, Strong core magnetic fields in magnetopause flux transfer events, *Geophys. Res. Lett.*, **15**, 748-751, 1988b.
- Scholer, M.**, Asymmetric time-dependent and stationary magnetic reconnection at the dayside magnetopause, *J. Geophys. Rev.*, **94**, 15,099-15,111, 1989.
- Schunk, R. W.**, The Terrestrial Ionosphere, *Solar-Terrestrial Physics. Principles and Theoretical Foundations, Proceedings of the Theory Institute. Reidel.*, 609-676, 1983.

- Scudder, J., F. Hunsacker, G. Miller, J. Lobell, T. Zawistowski, K. Ogilvie, J. Keller, D. Chornay, F. Herrero, R. Fitzenreiter, D. Fairfield, J. Needell, D. Bodet, J. Googins, C. Kletzing, R. Torbert, J. Vandiver, R. Bentley, W. Fillius, C. McIlwain, E. Whipple and A. Korth**, Hydra a 3-dimensional electron and ion hot plasma instrument for the Polar spacecraft of the GGS mission, *Space Sci. Rev.*, **71**, 459, 1995.
- Sibeck, D.G.**, A model for the transient magnetic response to sudden solar wind dynamic pressure variations, *J. Geophys. Rev.*, **95**, 3755-3771, 1990.
- Sibeck, D. G.**, Transient events in the outer magnetosphere: Boundary waves or flux transfer events?, *J. Geophys. Rev.*, **97**, 4009-4026, 1992.
- Smith, M. F., and C. J. Owen**, Temperature anisotropies in a magnetospheric FTE, *Geophys. Res. Lett.*, **19**, 1907-1910, 1992.
- Smith, M. F., M. Lockwood, and S. W. H. Cowley**, The statistical cusp: A simple flux transfer event model, *Planet. Space Sci.*, **40**, 1251, 1992.
- Smith, M. F., and M. Lockwood**, Earth's Magnetospheric Cusps, *Rev. of Geophysics*, **34**, 233-260, 1996.
- Smith, C. W., J. L'Heureux, N. F. Ness, M. H. Acuna, L. F. Burlaga and J. Scheifele**, The ACE Magnetic Fields Experiment, *Space Sci. Rev.*, **86**, 611, 1999.
- Song, P., and C. T. Russell**, Model of the formation of the low-latitude boundary layer for strongly northward interplanetary magnetic field, *J. Geophys. Rev.*, **97**, 1411-1420, 1992.
- Southwood, D. J.**, Theoretical aspects of ionosphere-magnetosphere-solar wind coupling, *Adv. Space Res.*, **5(4)**, 7-14, 1985.
- Southwood, D. J.**, The ionospheric signature of flux transfer events, *J. Geophys. Rev.*, **92**, 3207-3213, 1987.
- Southwood, D. J., C. J. Farrugia., and M. A. Saunders**, What are flux transfer events?, *Planet Space Sci.*, **36**, 503-508, 1988.
- Svalgard, L.**, Sector Structures of the interplanetary magnetic field and daily convection pattern of geomagnetic fields at high latitudes, *Geophys. Pap.*, **R-6**, Dan. Meteor. Inst., Copenhagen, Denmark, 1968.

- Thompson, M. J., J. A. Stansberry, S. J. Barne, S. A. Fuselier, and J. T. Gosling**, Ion and electron velocity distributions within flux transfer events, *J. Geophys. Rev.*, **92**,12,127, 1987.
- Todd, H., B. J. I. Bromage, S. W. H. Cowley, M. Lockwood, A. P. van Eyken, and D. M. Willis**, EISCAT observations of bursts of rapid flow in the high latitude dayside ionosphere, *Geophys. Res. Lett.*, **13**, 909-912, 1986.
- Trattner, K. J., S. A. Fuselier, W. K. Peterson, J.-A. Savaud, H. Stnuit, N. Du bouloz, and R. A. Kovrazhkin**, On spatial and temporal structures in the cusp, *J. Geophys. Rev.*, **104**, 28411-28421, 1999.
- Tsyganenko, N. A.**, A magnetospheric magnetic field model with a warped tail sheel current, *Planet. Space Sci.*, **37**, 5-20, 1989.
- Van Eyken, A. P., H. Risbeth, and M. A. Saunders**, Initial observations of plasma convection at invariant latitudes of 70-77°, *J. Atmos. Terr. Phys.*, **46**, 635, 1984.
- Villante, U.**, Some remarks on the structure of the distant neutral sheet, *Planet. Space Sci.*, **28**, 723, 1975
- Walker, R. J. and C. T. Russell**, Solar-wind interactions with magnetised planets, in *Introduction to Space Plasma Physics*, ed. M. G. Kivelson and C. T. Russell, 1995.
- Wilken, B. W. Weiss, D. Hall, M. Grande, F. Sorass, J. F. Fennell**, Magnetospheric Ion Composition Spectrometer onboard the CRRES spacecraft, *Journal Spacecraft and Rockets*, **29**, 585-591, 1992.
- Yeoman, T. K., M. D. Burrage, M. Lester, T. R. Robinson and T. B. Jones**, Long term variations of radar auroral backscatter and the interplanetary sector structure, *J. Geophys. Rev.*, **95**, 14885, 1995.
- Yeoman, T. K., M. Lester, S. W. H. Cowley, S. E. Milan, J. Moen, and P. E. Sandholt**, Simultaneous observations of the cusp in optical, DMSP and HF radar data, *Geophys. Res. Lett.*, **24**, 2251-2254, 1997.
- Zhou. X. W., and C. T. Russell**, The location of the high-latitude polar cusp and the shape of the surrounding magnetopause, *J. Geophys. Rev.*, **102**, 105-110, 1997.
- Zhou, X. W., C. T. Russell, G. Le, S.A. Fuselier, and J. D. Scudder**, The polar cusp location and its dependence on dipole tilt, *Geophys. Res. Lett.*, **26**, 429-432, 1999.